Convection thermique dans un fluide visqueux hétérogène : phénoménologie, lois d'échelle et applications aux systèmes terrestres

Michael Le Bars

THÈSE de DOCTORAT

de l'INSTITUT DE PHYSIQUE DU GLOBE DE PARIS

Spécialité: GÉOPHYSIQUE INTERNE

présentée par

Michael LE BARS

pour obtenir le titre de

DOCTEUR DE L'INSTITUT DE PHYSIQUE DU GLOBE DE PARIS

Sujet de la thèse :

Convection thermique dans un fluide visqueux hétérogène : phénoménologie, lois d'échelle et applications aux systèmes terrestres.

Soutenue le 14 janvier 2003, devant le jury composé de

Madame Anne DAVAILLE .... co-Directrice de Thèse

Monsieur Claude JAUPART .... co-Directeur de Thèse

Madame Luce FLEITOUT .... Rapporteur

Monsieur Dominique SALIN .... Rapporteur

Monsieur Friedrich BUSSE .... Examinateur

Monsieur Grae WORSTER .... Examinateur

Laboratoire de Dynamique des Systèmes Géologiques

Institut de Physique du Globe de Paris

4, place Jussieu - 75252 Paris cedex 05

Un grand merci...

à Anne Davaille qui a dirigé cette thèse. Dès mon arrivée, Anne m'a fourni toutes les conditions nécessaires au bon déroulement de ce travail. Je la remercie pour la confiance et la grande liberté qu'elle m'a toujours accordées. Ses précieux conseils m'ont guidé tant pour l'approche expérimentale et la dynamique des fluides que pour les applications géophysiques. Ce travail doit beaucoup à sa rigueur, à son expérience de la recherche et à ses encouragements.

à Claude Jaupart, qui m'a accueilli dans son laboratoire et qui a toujours été disponible pour m'écouter et me conseiller.

aux membres de mon jury : Luce Fleitout et Dominique Salin qui ont bien voulu être rapporteurs, ainsi que Friedrich Busse et Grae Worster. Tous ont fourni un travail approfondi, rigoureux et minutieux qui a permis d'améliorer significativement ce manuscrit.

à Claude Froidevaux qui m'a communiqué sa passion pour la géophysique.

à 'tata' Catherine, Stéphanie et Gérard pour leur bonne humeur, leur gentillesse et leur efficacité à toute épreuve.

à Doudou pour les discussions passionnées et les conseils toujours avisés.

à Geneviève et à Damien pour la relecture attentive de ce manuscrit.

à tous les membres du laboratoire de Dynamique des Systèmes Géologiques et autres habitués des lieux, qui ont tous contribué de près ou de loin à l'aboutissement de ce travail.

à mes fidèles acolytes de ces dernières années : Jérémy, Titi, Bénédicte, Delphine, JB, Momo, Claudia, Valérie, Raf, Hugues, Riton, Laurent, Eric, Ben, Amaury, et tous les autres...

à ma famille, présente en force à ma soutenance, pour ses continuels encouragements.

à Mathieu, mon ami de toujours, pour les coups de fil, les mails, les soirées, les week-ends... bref, pour m'avoir épaulé jusqu'au jour J.

à Marie enfin et surtout, pour sa patience infinie et son soutien au jour le jour. Ce travail n'aurait jamais abouti sans son aide constante et sa confiance sans faille. Je lui dédie donc cette thèse.

Résumé

Les observations géochimiques démontrent que le manteau terrestre est hétérogène mais ne précisent ni la taille, ni la forme, ni les caractéristiques de ces réservoirs. Nous avons donc étudié un système simple, dans lequel deux couches de fluides miscibles de densités, de viscosités et d'épaisseurs différentes sont soumises à un contraste thermique déstabilisant. D'après l'analyse de stabilité marginale, le démarrage de la convection peut être stationnaire ou oscillatoire, selon la valeur du nombre de flottabilité B (rapport entre la stratification chimique et l'anomalie thermique de densité) : lorsque B est inférieur à une valeur critique fonction des rapports de viscosités et d'épaisseurs des deux couches, la convection se développe sur l'intégralité du système et l'interface se déforme ; lorsque B est supérieur à cette valeur critique, le régime stratifié prend place et les deux fluides convectent séparément au-dessus et en-dessous de l'interface plane. Les expériences sont conformes aux résultats de la stabilité marginale. À faible nombre de Rayleigh, la théorie linéaire indique les bonnes échelles de temps et de longueur. À haut nombre de Rayleigh, des structures purement thermiques de petite taille, dues à la convection à l'intérieur de chaque couche indépendamment, se superposent au régime thermochimique à grande échelle ; par ailleurs, le système évolue systématiquement vers la convection Rayleigh-Bénard à une couche en raison du mélange progressif. Cependant, les deux fluides peuvent demeurer isolés sur des durées très longues comparées à l'échelle de temps du mode thermique. De nombreux comportements transitoires sont possibles, parmi lesquels le régime pulsatif où l'une des deux couches donne naissance à de grands dômes oscillant sur toute l'épaisseur du système. Dans l'espace des paramètres approprié à la Terre, notre modèle analogique suggère que le régime du manteau évolue au cours de son histoire, en partant du modèle 'historique' à deux couches pour tendre vers le modèle 'historique' à une couche. Les lois d'échelle démontrent également qu'une dynamique pulsative serait susceptible de fournir une explication simple aux superswells observés actuellement sur Terre, et d'une manière plus générale aux grandes pulsations géologiques enregistrées sur les planètes de type terrestre.

Abstract

Geochemical observations demonstrate that the Earth's mantle is heterogeneous, but the sizes, forms and characteristics of these reservoirs are not constrained. We have thus studied a simple non-homogeneous system, where two layers of miscible fluids with different densities, depths and viscosities are subjected to a destabilizing temperature contrast. According to marginal stability analysis, the onset of convection can be either stationary or oscillatory depending on the buoyancy number B, the ratio of the stabilizing chemical density anomaly to the destabilizing thermal density anomaly: when B is lower than a critical value (a function of the viscosity and layer depth ratios), the whole-layer regime develops, with a deformed interface and convective patterns over the whole tank depth; when B is larger than this critical value, the stratified regime develops, with a flat interface and layers convecting separately. Experiments agree well with the marginal stability results. At low Rayleigh number, characteristic time- and length-scales are well predicted by the linear theory. At higher Rayleigh number, small-scale purely thermal features due to convection inside each layer independently are superimposed to the large-scale thermochemical regime; besides the system systematically evolves towards one-layer Rayleigh-Bénard convection because of stirring. However, the two isolated fluids can persist for very long time compared to the characteristic time-scale of thermal convection and give rise to numerous transient behaviours. Of particular interest is the pulsatory dynamics, where the interface between the two layers deforms in large domes moving up and down quasi-periodically. In the parameter range likely to be relevant to the Earth, our analogical model suggests that the mantle regime evolves through its history from the historical 'two-layered' model where the mantle is divided in two isolated layers towards the historical 'one-layer' model where the mantle is fully mixed. Scaling laws also demonstrate that a pulsatory dynamics could provide a simple and single explanation for the superswells observed at present on Earth, and more generally for the long-term episodicity in planetary interiors observed in geological records.

Table des matières

I   Convection thermique dans un système à deux couches : étude théorique et expérimentale.   **53**

Introduction générale.

La Terre est un système dynamique fascinant, mettant en jeu de multiples phénomènes sur une gamme d'échelles très étendue : de la seconde pour les tremblements de Terre aux centaines de millions d'années pour la dérive des continents, du dixième de millimètre pour les minéraux aux milliers de kilomètres pour les plaques tectoniques. Son étude se révèle donc particulièrement complexe, et implique l'intervention simultanée de deux disciplines scientifiques complémentaires : la géologie et la physique. La géologie permet de mettre en évidence la structure et le fonctionnement de la Terre : elle utilise pour cela des données directes provenant de l'étude des roches et des phénomènes de surface, mais également des données indirectes fournies par exemple par la sismologie et la géochimie. La physique cherche à comprendre les mécanismes et lois universels régissant notre monde : la Terre constitue alors un champ d'applications passionnant pour ses conclusions. La collaboration entre ces deux domaines est particulièrement enrichissante, puisqu'elle permet d'élaborer des modèles réalistes dynamiquement et tenant compte de l'ensemble des spécificités de notre planète : ainsi, le concept de 'tectonique des plaques' permet d'accorder le phénomène physique de convection thermique (Bénard 1901 ; Rayleigh 1916) avec les observations de dérive des continents (Wegener 1912), d'expansion océanique (Vine & Matthews 1963) et de ceinture volcanique.

L'étude de la Terre profonde s'est beaucoup développée au cours du XXe siècle, mais de multiples problèmes demeurent aujourd'hui encore irrésolus. Par exemple, le régime convectif du manteau terrestre, couche solide de la Terre s'étendant de 30 à 2900 kilomètres de profondeur, constitue toujours un thème de recherche important : la controverse provient essentiellement de l'apparente opposition entre les données géochimiques, imageant un manteau hétérogène, et les données sismiques, qui observent des mouvements à l'échelle globale, impliquant un mélange rapide. Plusieurs explications ont été proposées pour tenter de résoudre ce conflit, mais aucune ne semble totalement satisfaisante. Nous avons donc abordé ce problème d'un point de vue dynamique des fluides, en modélisant 'à l'échelle' la situation réelle par une expérience simple de laboratoire.

Les conclusions et implications de ce travail sont présentées ici. Dans cette introduc-

tion, nous rappelons brièvement les résultats fondamentaux de la convection Rayleigh-Bénard ainsi que les données géophysiques et géologiques disponibles pour le manteau, puis nous décrivons notre modèle analogique. La première partie de cette thèse est consacrée à l'étude théorique et expérimentale de la convection dans un système hétérogène constitué de deux couches de fluides miscibles visqueux. Ces résultats sont ensuite appliqués aux systèmes planétaires - et tout particulièrement à la Terre - dans la seconde partie : nous verrons qu'ils sont susceptibles de réconcilier qualitativement et quantitativement l'essentiel des observables actuellement disponibles.

Chapitre 1

La convection thermique.

1.1 Principe général.

Un fluide dilatable soumis à un chauffage suffisant se met en mouvement : c'est la convection thermique. L'exemple le plus simple est celui de l'eau que l'on fait bouillir sur une plaque chauffante : au voisinage de celle-ci, le fluide se réchauffe, devient plus léger et se met à monter, tandis qu'à la surface, au contact de l'air, il se refroidit, devient plus lourd et se met à descendre.

D'un point de vue physique, la convection thermique correspond à un transport de chaleur par transport de matière, et résulte de l'affrontement entre un phénomène moteur, la poussée d'Archimède, et deux phénomènes résistants, la diffusion de chaleur et la diffusion de vorticité (mesurée par la viscosité du fluide).

La convection thermique joue un rôle primordial dans de nombreux systèmes naturels (océan, atmosphère, lac de lave, manteau terrestre,...). Elle a donc été amplement étudiée au cours de ce siècle, depuis les premières expériences de Bénard (1901) et la première approche théorique de Lord Rayleigh (1916). Toutefois, en raison de la multiplicité des géométries et des propriétés des fluides naturels, ce thème de recherche demeure aujoud'hui encore d'actualité.
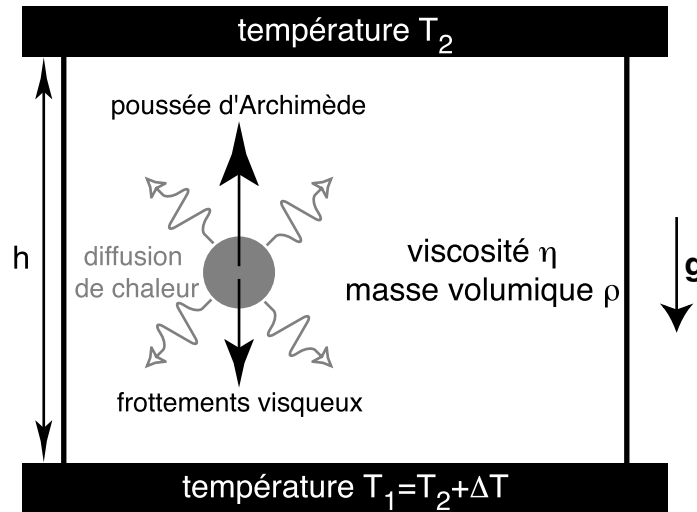
Fig. 1.1 – *Convection Rayleigh-Bénard dans un fluide simple.*

1.2 Convection Rayleigh-Bénard dans un fluide simple.

Nous allons dans un premier temps étudier le cas le plus classique de convection :
une couche de fluide Newtonien aux propriétés constantes est soumise à un chauffage par
le bas et un refroidissement par le haut (figure 1.1). Nous nous plaçons de plus dans le
cadre de l'approximation de Boussinesq (1903) : les variations de densité sont négligeables
partout, sauf dans l'expression de la poussée d'Archimède.

4 équations sont nécessaires pour décrire la dynamique du système :

– l'équation d'état du fluide

$$\rho = \rho_0(1 - \alpha(T - T_0)), \tag{1.1}$$

où ρ désigne la masse volumique du fluide à la température T (ρ_0 à la température
T_0) et α le coefficient de dilatation thermique du fluide.

– l'équation de conservation de la masse

$$\nabla \cdot \mathbf{u} = 0, \tag{1.2}$$

où $\mathbf{u}$ désigne le vecteur vitesse, $\mathbf{u} = (u, v, w)$.

– l'équation de conservation de la quantité de mouvement

$$\rho_0(\frac{\partial}{\partial t} + \mathbf{u}\cdot\nabla)\mathbf{u} = -\nabla p + \Delta\rho g\mathbf{k} + \eta\nabla^2\mathbf{u}, \tag{1.3}$$

où p désigne l'écart entre la pression réelle et la pression hydrostatique, g l'accélération de la pesanteur, $\mathbf{k}$ le vecteur vertical unitaire dirigé vers le haut, η la viscosité dynamique du fluide ($\nu = \eta/\rho$ la viscosité cinématique) et $\Delta\rho = \rho_0 - \rho$.

– l'équation de la température (conservation de l'énergie)

$$(\frac{\partial}{\partial t} + \mathbf{u}\cdot\nabla)T = \kappa\nabla^2 T. \tag{1.4}$$

où κ désigne le coefficient de diffusivité thermique du fluide.

Il faut de plus ajouter à ce système les conditions aux limites:

$$\mathbf{u} = \mathbf{0} \text{ pour des limites rigides,} \tag{1.5a}$$

$$w = 0, \frac{\partial u}{\partial z} = \frac{\partial v}{\partial z} = 0 \text{ pour des limites libres.} \tag{1.5b}$$

Pour adimensionnaliser les équations, nous utilisons l'épaisseur du fluide h, la différence totale de température ΔT, le temps typique de diffusion thermique h^2/κ, et l'échelle de pression visqueuse $\eta\kappa/h^2$. Les équations sans dimension sont alors

$$\nabla\cdot\mathbf{u} = 0, \tag{1.6}$$

$$\frac{1}{Pr}(\frac{\partial}{\partial t} + \mathbf{u}\cdot\nabla)\mathbf{u} = -\nabla p + Ra(T - T_0)\mathbf{k} + \nabla^2\mathbf{u}, \tag{1.7}$$

$$(\frac{\partial}{\partial t} + \mathbf{u}\cdot\nabla)T = \nabla^2 T, \tag{1.8}$$

où Ra et Pr représentent respectivement les nombres de Rayleigh et de Prandtl définis par

$$Ra = \frac{\alpha g\Delta T h^3}{\kappa\nu} \text{ et } Pr = \frac{\nu}{\kappa}. \tag{1.9}$$

Le nombre de Prandtl est égal au rapport entre le temps caractéristique de diffusion thermique h^2/κ et le temps caractéristique de diffusion mécanique h^2/ν : lorsque $Pr << 1$, la chaleur diffuse beaucoup plus vite que la vorticité, et le mouvement peut se poursuivre par inertie après disparition de la poussée d'Archimède. Par contre, à $Pr >> 1$, l'équation (1.7) montre que les effets inertiels sont négligeables : le mouvement résulte d'un équilibre entre forces visqueuses et poussée d'Archimède.

Le nombre de Rayleigh traduit quant à lui le rapport entre le phénomène moteur de la convection (la poussée d'Archimède) et les phénomènes résistants (diffusion de chaleur et de vorticité). La seule étude de Ra permet de savoir si un système convecte ou non (figure 1.2). Lorsque Ra est inférieur à une valeur critique Ra_c ($Ra_c = 1707.76$ pour des limites rigides, $Ra_c = 657.51$ pour des limites libres et $Ra_c = 1100.65$ pour des limites rigide-libre : Chandrasekhar 1961), l'énergie apportée au système n'est pas suffisante pour contrer les diffusions visqueuse et thermique : le fluide demeure immobile. Mais lorsque Ra est supérieur à la valeur critique Ra_c, le fluide se met en mouvement. Ensuite, à Pr fixé, la valeur de Ra détermine l'intensité et la forme de la convection (Krishnamurti 1970) : en augmentant progressivement Ra à partir de la valeur critique, on observe successivement (figure 1.2a)

- un régime permanent à deux dimensions sous forme de rouleaux de convection de taille comparable à la profondeur h du fluide (figure 1.2b).
- un régime permanent à trois dimensions sous forme de cellules de convection de taille comparable à h.
- un régime à trois dimensions dépendant du temps sous forme de petits panaches thermiques (figure 1.2c).
- un régime turbulent.

Il est important de noter que la dépendance en Pr disparaît à partir d'une valeur typique de 100 : les effets inertiels deviennent alors négligeables. Cette condition est systématiquement vérifiée dans toutes les expériences présentées dans ce travail ; dans les développements analytiques, elle sera implicitement supposée satisfaite.

(a)

(b)

(c)
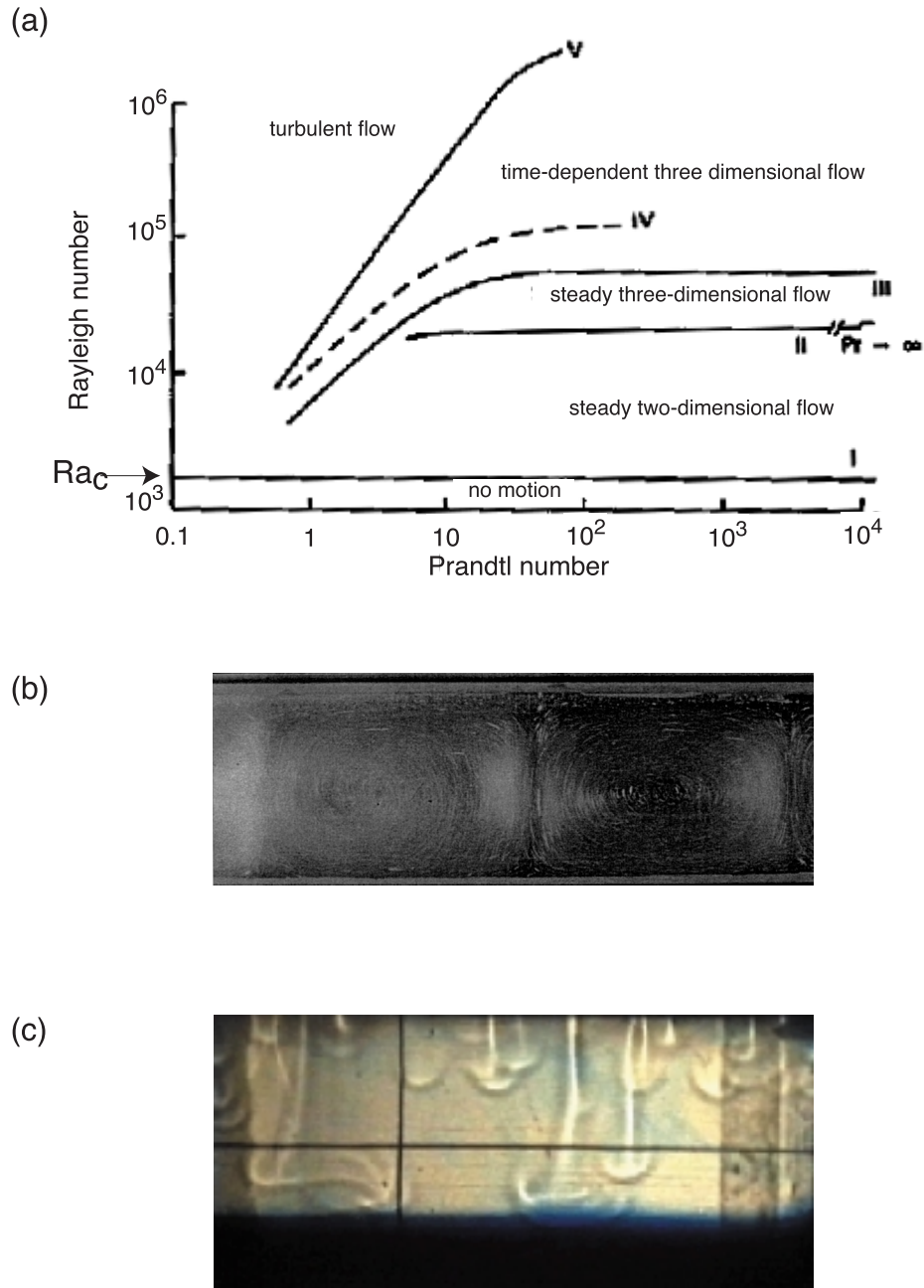
FIG. 1.2 – *(a) Régimes convectifs en convection Rayleigh-Bénard simple en fonction des deux nombres sans dimension Pr et Ra (Krishnamurti 1970). (b) Rouleaux de convection : $Ra = 1.1 \times 10^4$, $Pr > 100$ (photo de L. Guillou et C. Jaupart, IPGP). (c) Panaches thermiques se développant à partir de la plaque supérieure froide : $Ra = 1.3 \times 10^7$, $Pr = 880$ (expérience $n^o 13$).*

1.3   Résolution aux dimensions.

Lorsque les effets inertiels sont négligeables, l'équation du mouvement est donnée par l'équilibre entre la poussée d'Archimède et les forces visqueuses, donc 'aux dimensions' (Turner 1979, pp. 208)

$$\alpha \rho g \theta = \eta \frac{w}{h^2}, \tag{1.10}$$

où θ désigne le contraste de température entre le fluide chaud et le fluide environnant. Ce contraste évolue du fait de la diffusion thermique : au premier ordre,

$$\frac{\partial \theta}{\partial t} = -\kappa \frac{\theta}{h^2} \tag{1.11}$$

donc

$$\theta = \Delta T exp(-\frac{t}{h^2/\kappa}). \tag{1.12}$$

h^2/κ correspond au temps typique de diffusion thermique sur la hauteur h. En remplaçant (1.12) dans (1.10),

$$w = \frac{\alpha \rho g h^2 \Delta T}{\eta} exp(-\frac{t}{h^2/\kappa}). \tag{1.13}$$

Considérons une particule initialement située contre la plaque inférieure : sa position finale est donnée par

$$h_{finale} = \int_0^{\infty} w dt = \frac{\alpha \rho g \Delta T h^4}{\kappa \eta} = h \times Ra. \tag{1.14}$$

La convection consiste à transporter de la chaleur entre les deux limites du système. Dans notre modèle simple, cela implique qu'une particule initialement située contre la plaque inférieure soit capable d'atteindre la plaque supérieure, donc que $h_{finale} >> h$: d'après (1.14), le système convecte lorsque $Ra >> 1$.
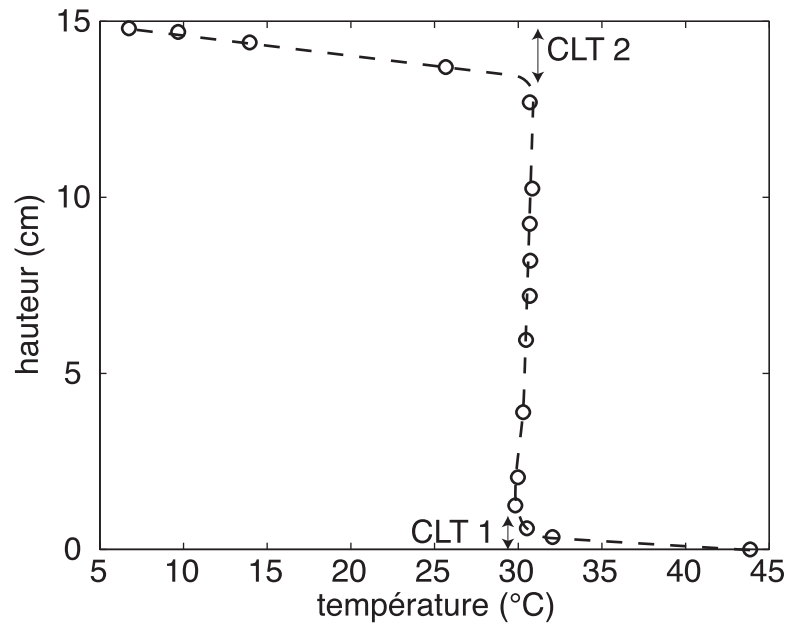
FIG. 1.3 – *Profil vertical de température typique d'une convection à haut nombre de Rayleigh (Ra = 2.6 × 10^6).*

1.4 Étude locale à haut nombre de Rayleigh.

La figure 1.3 présente le profil vertical de température typique d'une convection à haut nombre de Rayleigh ($Ra > 10^4 - 10^5$). À l'intérieur du système, les mouvements convectifs sont très rapides : les transferts de chaleur sont donc très efficaces, et la température quasi-constante. Toutes les variations thermiques sont concentrées dans de fines couches au voisinage immédiat des bords, où les mouvements sont freinés : ce sont les couches limites thermiques, où les transferts de chaleur se font par conduction.

Dans ce cas, il est possible de développer un raisonnement local (Howard 1964) donnant les caractéristiques spatiales et temporelles de la convection en fonction de Ra. Soit $\delta(t)$ l'épaisseur de la couche limite thermique à un instant t. Celle-ci grandit uniquement par diffusion de chaleur : au premier ordre, l'équation de la température donne donc une

dépendance en temps simple

$$\delta(t) = \sqrt{\pi \kappa t}.$$ (1.15)

On peut alors définir un nombre de Rayleigh local

$$Ra_{local} = \frac{\alpha g \Delta T_{local} \delta^3}{\kappa \nu},$$ (1.16)

où ΔT_{local} désigne la différence de température imposée à la couche limite thermique. Celle-ci se déstabilise et se vide lorsque le Rayleigh local atteint la valeur critique :

$$Ra_{local} = Ra_c.$$ (1.17)

On obtient ainsi une taille caractéristique des instabilités

$$\delta = h \left(\frac{\Delta T}{\Delta T_{local}} \times \frac{Ra_c}{Ra} \right)^{1/3}$$ (1.18)

et d'après (1.15), une période caractéristique de déstabilisation

$$\tau = \frac{h^2}{\pi \kappa} \left(\frac{\Delta T}{\Delta T_{local}} \times \frac{Ra_c}{Ra} \right)^{2/3}.$$ (1.19)

Cette loi d'échelle simple explique correctement nos résultats expérimentaux pour un coefficient critique $Ra_c = 1100 \pm 420$ (figure 1.4), proche de la valeur théorique $Ra_c = 1100.65$ pour des limites rigide-libre (Chandrasekhar 1961). Ce résultat peut paraître surprenant puisque dans nos expériences, les limites extérieures sont constituées par deux plaques de cuivre rigides ; toutefois, dans le cadre d'un raisonnement local, chaque couche limite est en fait en contact avec une plaque rigide d'un côté, et du fluide de l'autre.

1.5 Introduction d'une seconde couche.

La convection de Rayleigh-Bénard a donné lieu à de multiples études, y compris pour des systèmes plus complexes : nous pouvons par exemple citer, en raison de leur importance pour la Terre, l'introduction d'un chauffage interne qui modifie sensiblement les structures convectives (Sotin & Labrosse 1999), ou encore l'utilisation d'un
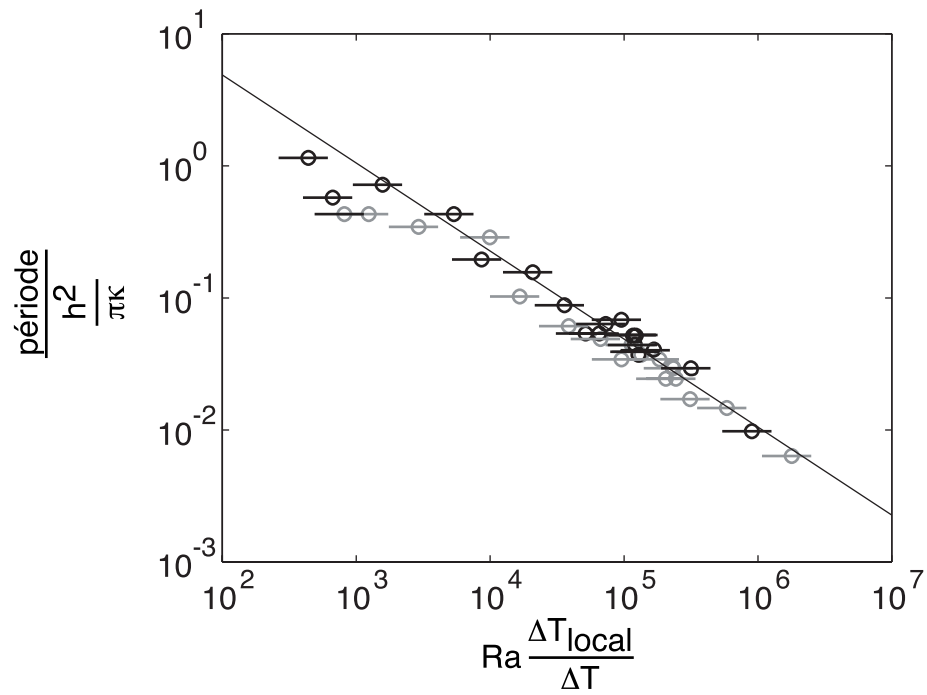
FIG. 1.4 – *Périodes typiques enregistrées dans les couches limites thermiques chaudes (cercles gris) et froides (cercles noirs) en fonction du nombre de Rayleigh : la droite représente la meilleure correspondance avec (1.19), obtenue pour $Ra_c = 1100 \pm 420$.*

fluide dont la viscosité dépend de la température, engendrant la formation d'un cou-
vercle stagnant (Stengel, Olivier & Broker 1982; Richter, Nataf & Daly 1983; Davaille
& Jaupart 1993). Cependant, de nombreuses situations ne sont encore que partiellement
comprises. Ainsi, le simple fait d'ajouter une seconde couche de fluide dont la densité
et éventuellement d'autres propriétés physiques diffèrent (viscosité, diffusivité,...) com-
plique considérablement le système et ouvre un vaste espace de paramètres qui n'a pu
être parcouru dans son intégralité (voir par exemple Richter & Johnson 1974 ; Rasenat,
Busse & Rehberg 1989 ; Davaille 1999b). Le travail présenté ici s'est ainsi focalisé sur l'in-
fluence des rapports de densité et de viscosité dans une configuration Rayleigh-Bénard à
deux couches, en raison de ses possibles applications à la dynamique complexe du man-
teau terrestre : nous utiliserons par la suite l'adjectif 'thermochimique' - par opposition
à 'purement thermique' - pour souligner la responsabilité simultanée des variations de
température et de composition chimique dans les changements de densité engendrant le
mouvement (mais aucune réaction chimique ne prend place dans notre système).

Chapitre 2

Le manteau terrestre.

2.1 Description globale.

2.1.1 Un fluide en convection.

Le manteau terrestre s'étend depuis la base de la croûte terrestre jusqu'au noyau liquide situé à 2900 km de profondeur (figure 2.1). Il est constitué de roches solides qui ne fondent que très localement, près de la surface, et en petite quantité. Toutefois, ce manteau solide se comporte comme un fluide à l'échelle des temps géologiques : il se déforme avec des vitesses typiques de l'ordre du centimètre par an, comme nous le montre la tectonique des plaques. Sa viscosité a été estimée en utilisant le rebond post-glaciaire (remontée de la surface des continents consécutive à l'allègement de la charge lors de la fonte des glaces) à 10^{21} Pa s (Peltier & Jarvis 1982).

Le manteau terrestre est soumis simultanément à deux types de chauffage : un chauffage basal provenant du noyau, et un chauffage interne consécutif à la désintégration d'éléments radioactifs. Ces deux contributions impliquent un contraste total de température entre le haut et le bas du manteau de l'ordre de 3500 K, dont 1000 K environ correspondent au gradient adiabatique et ne participent pas à l'instabilité convective. Les propriétés physiques des roches peuvent être évaluées à partir des échantillons
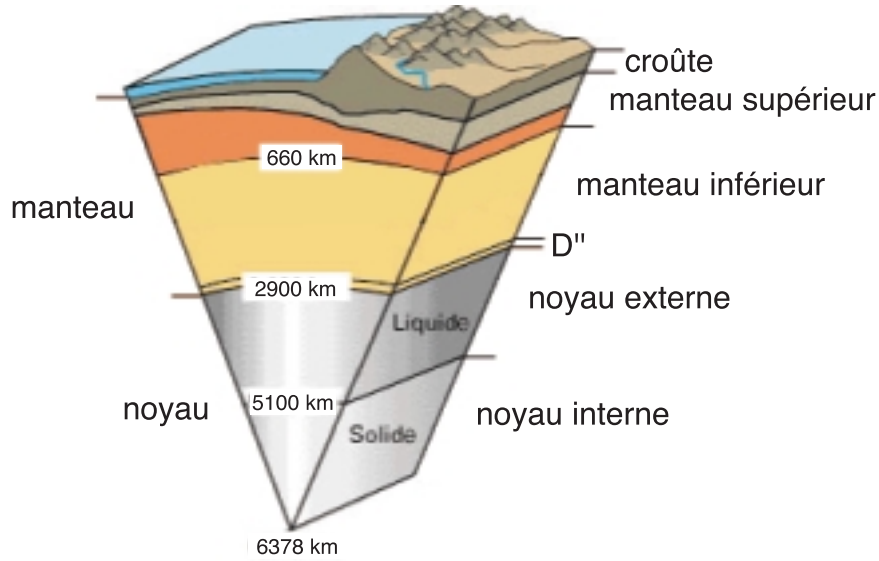
FIG. 2.1 – *Coupe verticale de la Terre (d'après une image USGS ; échelle non respectée).*

recueillis à la surface : les ordres de grandeur sont $\rho \sim 4000 \ \mathrm{kg\,m^{-3}}$, $\alpha \sim 3 \times 10^{-5} \ \mathrm{K^{-1}}$ et $\kappa \sim 10^{-6} \ \mathrm{m^2\,s^{-1}}$ (Poirier 1991).

Ces différentes valeurs nous permettent d'estimer les deux nombres fondamentaux de la convection pour le manteau :

$$Ra \sim 7.4 \times 10^7 \tag{2.1}$$

$$Pr \sim 2.5 \times 10^{23}. \tag{2.2}$$

D'après les résultats exposés au §1.2, le manteau terrestre convecte sous forme de panaches thermiques, et les effets inertiels y sont négligeables : sa dynamique est contrôlée par l'équilibre entre les forces visqueuses et la poussée d'Archimède.

2.1.2   Complications naturelles.

Il s'avère cependant difficile d'appliquer directement les lois théoriques simples de la convection Rayleigh-Bénard (§1.2) au système complexe terrestre. Tout d'abord, les conditions à la limite supérieure du manteau sont très différentes suivant que l'on se trouve sous

un continent ou un océan (Guillou & Jaupart 1995). Par ailleurs, les propriétés physiques du manteau (par exemple la viscosité) varient fortement avec la température et la profondeur (Karato & Wu 1993). Il existe de plus des transitions de phase à l'intérieur du manteau : ainsi, à 660 km de profondeur, les minéraux des roches subissent une réorganisation (Ito & Takahashi 1989), marquant la séparation entre le manteau 'supérieur' et le manteau 'inférieur' (figure 2.1). Il est donc indispensable, pour développer un modèle correct, de s'appuyer sur les différentes observations disponibles.

2.2 Données disponibles.

2.2.1 Plaques, points chauds, superswells : coexistence de différentes échelles.

La dynamique du manteau constitue le moteur de la tectonique des plaques (figure 2.2a), et est donc à l'origine des séismes et d'une grande partie du volcanisme. En suivant le modèle physique simple de la convection, les dorsales océaniques correspondent à la montée de matériel chaud, et les zones de subduction à la descente de matériel froid, formant ainsi dans le manteau un certain nombre de cellules de convection.

Cette vision 'à l'ordre 0' est toutefois insuffisante. En effet, certains volcans (comme par exemple Hawaii, figure 2.2b) apparaissent au milieu des plaques, indépendamment de toute structure tectonique. Ces points chauds (Wilson 1963) sont interprétés comme la trace en surface de panaches convectifs provenant des profondeurs du manteau (Morgan 1972) : un second type de structure convective à petite échelle (une centaine de kilomètres de diamètre) vient donc se superposer aux grandes cellules convectives mises en évidence par la tectonique des plaques.

Enfin, deux superswells ont été mis en évidence à la surface de la Terre, respectivement sous le sud-ouest de l'Afrique (Nyblade & Robinson 1994) et sous la Polynésie française (McNutt & Fisher 1987) (figure 2.2b) : ces superswells correspondent à des régions larges

(a)

(b)
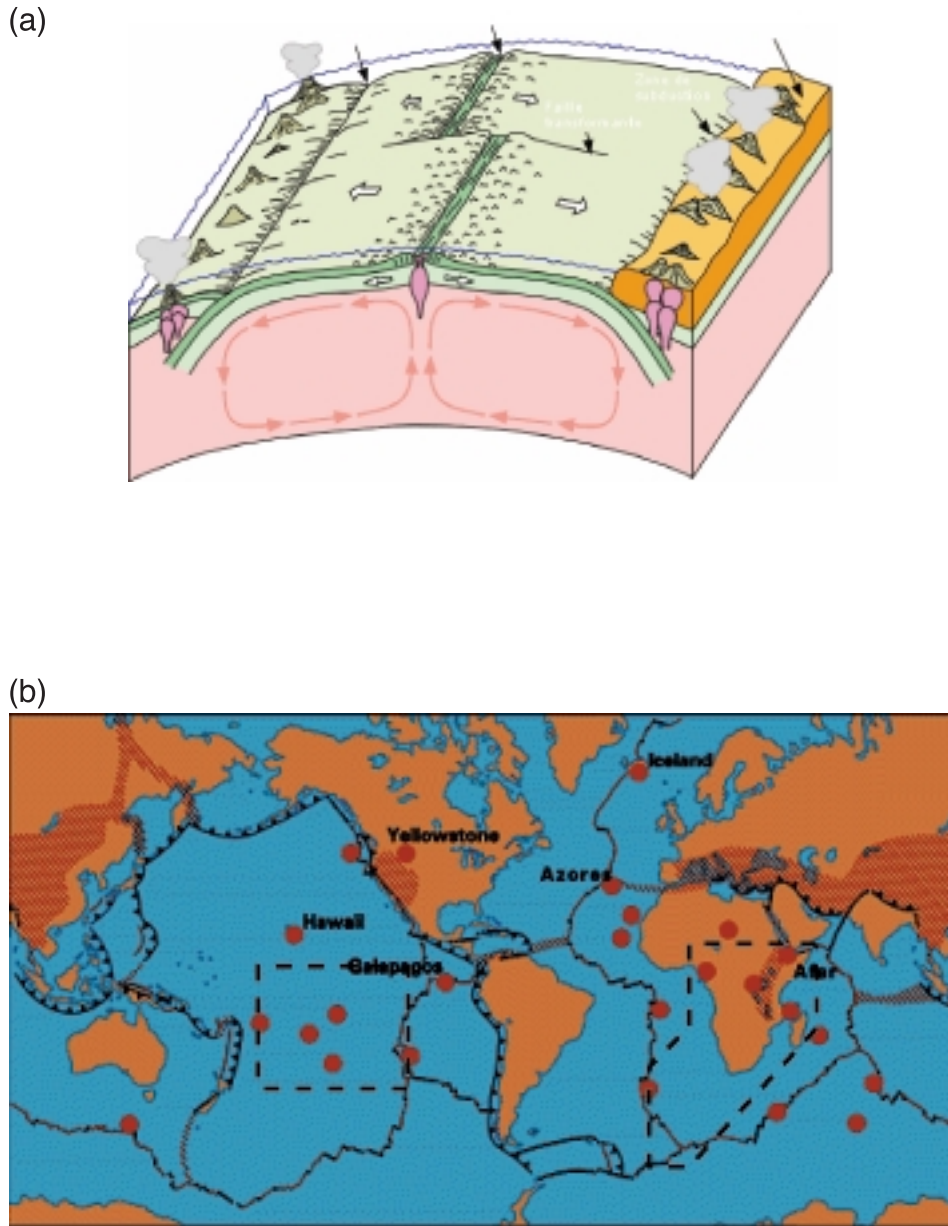
FIG. 2.2 – *(a) Mouvements des plaques océaniques (shéma de P.-A. Bourque, Univer-sité Laval, Québec). (b) Frontières de plaques (lignes continues, les triangles marquant les zones de convergence), localisation des points chauds les plus importants et des 2 super-swells (pointillés) à la surface de la Terre (modifié d'après une image USGS).*

de quelques milliers de kilomètres, caractérisées par un bombement topographique de 500 à 1000 m et par une concentration de points chauds. Ces superswells pourraient correspondre à un phénomène périodique (avec un temps caractéristique de l'ordre de 100 millions d'années), relié à la variation de production de croûte océanique ainsi qu'aux inversions du champ magnétique terrestre (Larson 1991). Les processus de surface à eux seuls ne sont pas susceptibles d'expliquer ce phénomène à grande échelle (McNutt 1998) : une origine profonde, liée à la convection mantellique, semble probable, mais demande encore à être expliquée.

2.2.2 Géochimie et bilan de chaleur : le manteau 'en boîtes'.

Les géochimistes analysent les laves émises à la surface de la Terre et utilisent les éléments radioactifs de celles-ci comme traceurs pour remonter à la composition initiale de leurs sources dans le manteau. Ils distinguent essentiellement deux types de laves (voir par exemple la revue récente de Hofmann 1997) :

– les laves émises au niveau des dorsales océaniques appelées MORB (Mid Ocean Rift Basalt) proviennent d'un réservoir dégazé et bien mélangé, occupant la partie supérieure du manteau : leur composition demeure relativement constante sur l'ensemble de la planète. Ce réservoir a été appauvri en éléments incompatibles par l'extraction de la croûte continentale, et occupe entre 25% (Jacobsen & Wasserburg 1979) et 90% (Hofmann 1997) du manteau global.

– les laves des points chauds appelées OIB (Oceanic Island Basalt) présentent quant à elles des compositions très variables, mais systématiquement plus riches en éléments radiogéniques et en gaz : elles proviennent d'un ou de plusieurs réservoirs situés en profondeur.

La géochimie démontre donc l'existence d'hétérogénéités importantes dans le manteau, qu'elle image comme un ensemble de 'boîtes' de compositions différentes. Ce résultat est par ailleurs confirmé par le bilan de chaleur de la Terre : de manière à expliquer le flux

actuel qui s'échappe à la surface tout en maintenant une température interne raisonnable dans le passé, un réservoir caché, enrichi en éléments radioactifs, doit exister en profondeur (McKenzie & Richter 1981; Honda 1995; Kellog, Hager & Van der Hilst 1999).

De telles hétérogénéités à grande échelle se maintenant sur toute l'histoire de la Terre ne sauraient être purement passives : compte tenu de l'efficacité du mélange dans le manteau (Hofmann & McKenzie 1985; Christensen 1989; Van Keken & Zhong 1999; Ferrachat & Ricard 2001), une stratification en densité et/ou un contraste important de viscosité sont en effet indispensables (voir par exemple la revue récente de Van Keken, Hauri & Ballentine 2002). Toutefois, les données actuelles ne permettent de contraindre ni la morphologie, ni la profondeur, ni les caractéristiques physiques de ces réservoirs. Leur origine demeure également sujette à controverse : leur formation pourrait être due

- à la présence en profondeur d'un changement de phase (Yeganeh-Haeri, Weidner & Ito 1989; Nataf & Houard 1993),

- à la remontée de matériel lourd en provenance du noyau (Hansen & Yuen 1988; Knittle & Jeanloz 1991), puisque ce dernier n'est pas encore en équilibre avec le manteau (Stevenson 1981),

- au stockage et au recyclage au-dessus de la limite noyau–manteau du matériel océanique subducté (Gurnis 1986; Christensen & Hofmann 1994; Albarède 1998; Coltice & Ricard 1999),

- à l'accumulation dans la partie inférieure du manteau de fer et d'éléments sidérophiles lors de la différenciation de la Terre (Solomatov & Stevenson 1993; Sidorin & Gurnis 1998),

- à l'extraction de la croûte continentale uniquement à partir d'une couche supérieure du manteau (DePaolo & Wasserburg 1976; Allègre, Othman, Polve & Richard 1979; O'Nions, Evensen & Hamilton 1979),

et bien sûr à la combinaison de plusieurs de ces éléments.

2.2.3   Les données sismiques : image actuelle et instantanée du manteau.

Les multiples réflexions des ondes sismiques en profondeur mettent en évidence les grandes discontinuités radiales de la Terre (figure 2.1) : leur étude a ainsi permis de détecter les limites de la graine, du noyau externe, et du manteau. À l'intérieur de ce dernier, deux discontinuités majeures ont été repérées : à 660 km de profondeur, correspondant à la transition de phase (Ito & Takahashi 1989), et 200 à 300 kilomètres au-dessus de la limite noyau-manteau, marquant le début de la couche D" (Lay 1989). Il est toutefois important de noter que cette méthode ne peut détecter que des discontinuités

- suffisamment fortes pour engendrer un signal réfléchi se propageant jusqu'à la surface.
- marquées par des interfaces relativement planes, sur lesquelles le signal n'est pas détruit par interférences.

Depuis une dizaine d'années, les images tomographiques permettent par ailleurs de réaliser un 'scanner' de l'intérieur de la Terre, en repérant en trois dimensions les variations des vitesses sismiques dans le manteau (Li & Romanowicz 1996; Masters, Johnson, Laske & Bolton 1996; Grand, Van der Hilst & Widiyantoro 1997; Su & Dziewonski 1997; Van der Hilst, Widiyantoro & Engdahl 1997; Bijwaard, Spakman & Engdahl 1998; Mégnin & Romanowicz 2000). Le problème actuel réside dans l'interprétation de ces images : les zones de vitesses sismiques rapides correspondent à des zones denses, donc au premier ordre à des zones froides. Cette vision simple néglige toutefois les variations de densité d'origine chimique (i.e. compositionnelle), qui peuvent pourtant jouer un rôle important. De plus, les modèles tomographiques demeurent encore relativement peu précis, et proposent des résultats très variables les uns des autres. Nous pouvons toutefois repérer deux constatations robustes particulièrement importantes dans le cadre de notre étude :

- tout d'abord, tous les modèles tomographiques démontrent que la transition de phase à 660 km n'arrête pas systématiquement la subduction des plaques
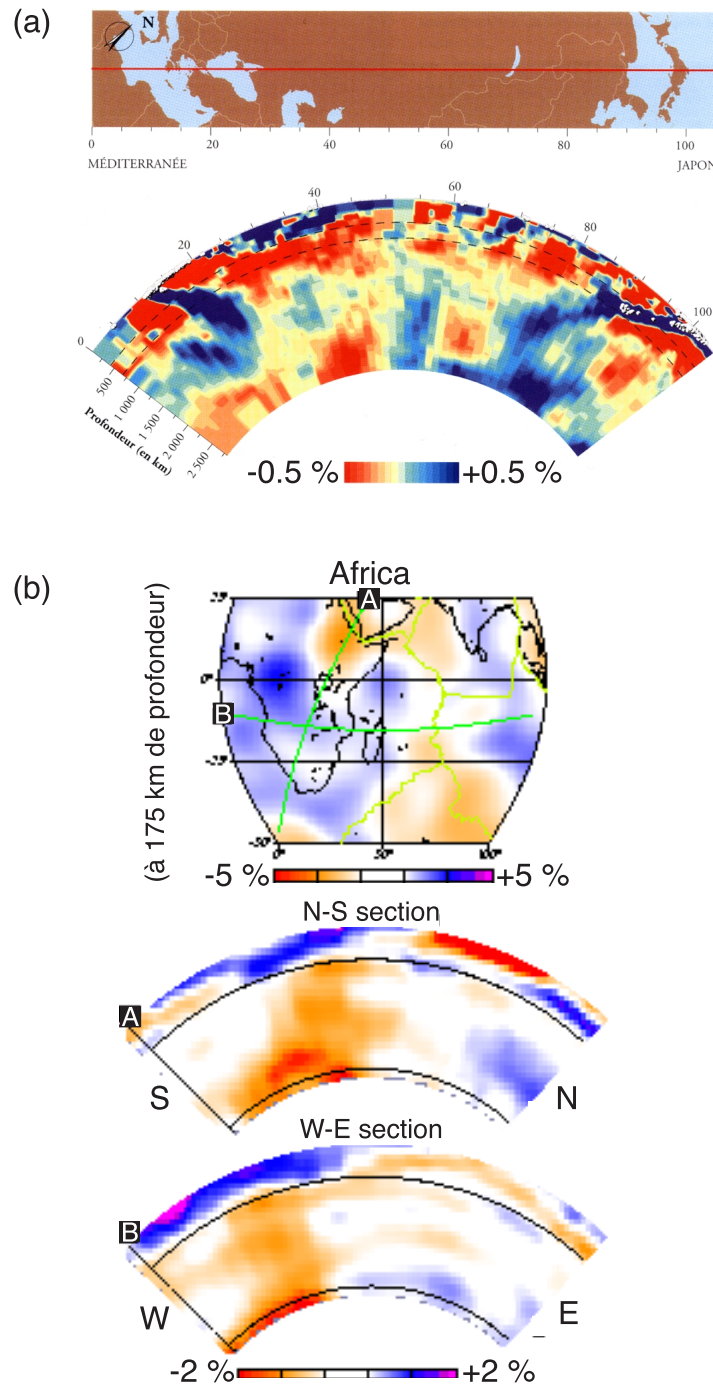
FIG. 2.3 – *Images tomographiques démontrant (a) la subduction des plaques océaniques au-delà de la transition de phase (Bijwaard, Spakman & Engdahl 1998) et (b) l'origine dynamique profonde du superswell Africain (Mégnin & Romanowicz 2000).*

océaniques (figure 2.3*a*) : certaines semblent au contraire plonger jusqu'à la li-
mite noyau-manteau, ou s'accumuler à environ 2000 km de profondeur (voir par
exemple la revue récente de Fukao, Widiyantoro & Obayashi 2001).

– par ailleurs, tous les modèles tomographiques imagent sous les deux superswells des
zones de vitesses sismiques lentes aux parois abruptes (< 50 km d'après Ni, Tan,
Gurnis & Helmberger 2002) et qui s'étendent jusqu'à la base du manteau (figure
2.3*b*), démontrant l'origine dynamique profonde de ces structures. Une anomalie
de température seule ne semble pas susceptible d'expliquer le signal observé : une
différence de composition chimique est également nécessaire (Yuen, Cadek, Chope-
las, & Matyska 1993 ; Masters, Johnson, Laske & Bolton 1996 ; Su & Dziewonski
1997 ; Ishii & Tromp 1999 ; Bréger, Romanowicz & Ng 2001).

2.3   Les modèles de convection mantellique.

Le problème principal des modèles de convection mantellique est de parvenir à
réconcilier l'image instantanée donnée par la sismologie, qui implique une dynamique
convective à l'échelle globale, avec la conservation sur des milliards d'années de plusieurs
réservoirs chimiques distincts. Ils doivent en outre expliquer comment générer simul-
tanément les différentes structures convectives à différentes échelles observées en surface.

2.3.1   Les modèles historiques.

Les géophysiciens se sont pendant plusieurs dizaines d'années divisés entre deux
modèles, qui apparaissent aujoud'hui inexacts, mais qui vont toutefois servir de point
de départ à notre étude :

– dans le modèle de convection à deux couches (figure 2.4*a*), la transition de phase
à 660 km de profondeur marque également la séparation entre les deux réservoirs
géochimiques du manteau : le manteau supérieur correspond au réservoir appauvri
source des MORB, et le manteau inférieur à un réservoir primitif (i.e. non appauvri,
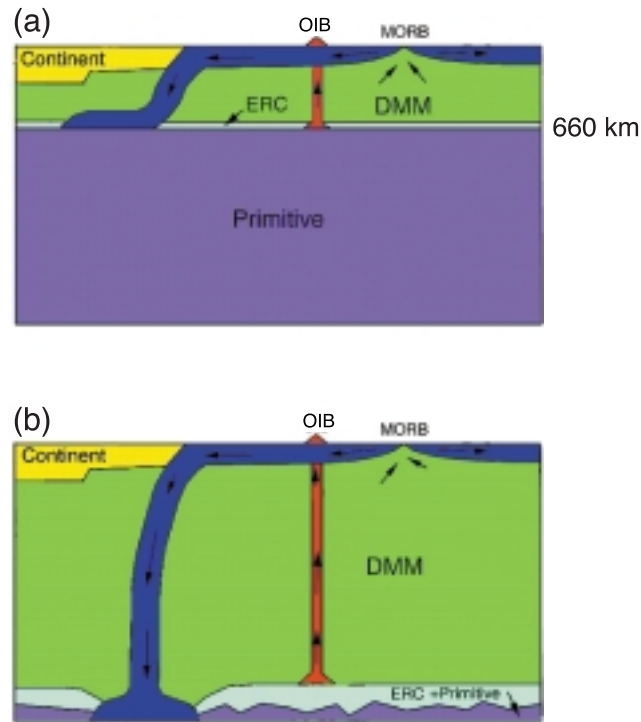
FIG. 2.4 – *Modèles de convection mantellique (d'après Tackley 2000a) : (a) modèle de convection à deux couches et (b) modèle de convection à une couche. ERC : croûte océanique recyclée. DMM : manteau source des MORB.*

non dégazé) source des OIB (DePaolo & Wasserburg 1976; Allègre, Othman, Polve & Richard 1979; O'Nions, Evensen & Hamilton 1979). Ces deux parties convectent séparément, sans échange de masse important. Ce modèle ne s'accorde cependant pas aux données sismiques, puisqu'il interdit le passage des plaques océaniques à travers la transition de phase.

– dans le modèle de convection à une couche (figure 2.4*b*), le manteau convecte dans son intégralité, et est donc entièrement mélangé. Ce modèle autorise la subduction des plaques océaniques jusqu'à la base du manteau, mais il ne dispose pas d'une couche primitive suffisamment importante pour expliquer les données géochimiques et équilibrer le bilan de chaleur.

Enfin, aucun de ces deux modèles ne parvient à expliquer la coexistence des différentes échelles convectives.

2.3.2   Modèles intermédiaires.

Ces deux modèles historiques correspondent, d'un point de vue dynamique, aux cas limites de convection dans un système à deux couches : les deux fluides se mélangent immédiatement (convection à une couche) ou demeurent totalement et indéfiniment isolés (convection à deux couches). Il existe cependant entre ces régimes stationnaires extrêmes une multitude de situations possibles (Olson & Kincaid 1991; Davaille 1999*b*) : les réservoirs géochimiques ne constituent pas obligatoirement des boîtes indéformables et immobiles, séparées par la transition de phase. Il est vrai qu'en dehors de la couche D", trop petite pour former à elle seule le réservoir primitif, la sismologie ne détecte pas d'autre discontinuité franche en profondeur. Il est toutefois possible de 'cacher' une seconde couche en imaginant par exemple une interface très chahutée, ou encore une situation isopycnique (i.e. dans laquelle les contrastes de densité d'origine chimique sont compensés par des effets thermiques). Un candidat sérieux à une telle discontinuité a été récemment proposé au sein du manteau inférieur (Van der Hilst & Kárason 1999).

Par ailleurs, ces modèles historiques supposent implicitement que le manteau est dans un régime stationnaire, ce qui n'est pas forcément le cas : une manière de réconcilier les observations est en effet de supposer que le manteau était initialement stratifié, de manière à conserver les réservoirs distincts, et qu'il évolue depuis quelques millions d'années seulement vers un régime à une couche (Davaille 1996; Allègre 1997; Davaille 1999*b*).

Ces différentes propositions demandent toutefois à être testées et quantifiées précisément, ce que nous avons essayé de réaliser à travers une série d'expériences analogiques. Partant de la seule constatation que le manteau terrestre est hétérogène, et qu'un contraste de densité - éventuellement lié à un contraste de viscosité - est nécessaire pour maintenir ces hétérogénéités sur des durées suffisantes, nous nous sommes placés dans le

cas le plus simple de convection hétérogène : un système à deux fluides stratifié chimique-ment. Et la première conclusion de nos expériences est que ce système très simple montre déjà une richesse et une variabilité de comportements complètement inattendues.

Chapitre 3

Modélisation analogique.

3.1 Dispositif expérimental.

Le dispositif expérimental est présenté sur la figure 3.1 : deux fluides de densités, de viscosités et d'épaisseurs différentes sont superposés dans une cuve, puis chauffés par le bas et refroidis par le haut. Les parois latérales des cuves utilisées au cours de ces expériences sont en plexiglas, ce qui permet une bonne visualisation des phénomènes, tout en minimisant les pertes latérales de chaleur (épaisseur de l'ordre de 3 cm). Les parois supérieures et inférieures quant à elles sont constituées de plaques de cuivre dont les températures sont régulées respectivement par un cryostat et un thermostat : le système est donc soumis à un flux de chaleur constant pendant les quelques minutes de mise en température des fluides, puis à un contraste de température constant pendant le reste de l'expérience. 5 cuves différentes ont été employées : la table 3.1 présente leurs dimensions. Ces variations de taille nous ont permis, en faisant varier le rapport d'aspect, de mieux contraindre l'importance des effets de bord. La cuve 5, peu large, nous a en outre permis de réaliser des expériences à deux dimensions pour une meilleure visualisation.

L'un des principaux problèmes de préparation auxquels nous nous sommes heurtés est celui du dépôt successif, et sans mélange, des deux couches de fluide : nous avons pour
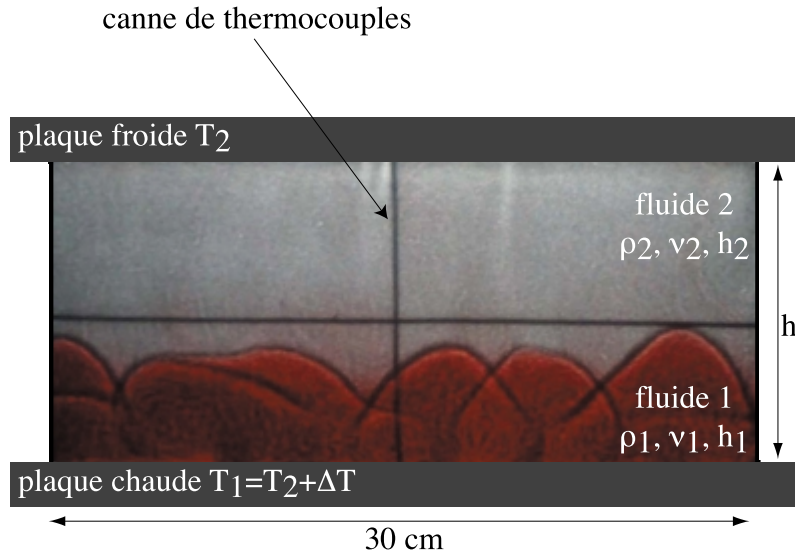
FIG. 3.1 – *Dispositif expérimental.*

cela utilisé une grille de nylon placée juste au-dessus du premier fluide pour briser le jet lors de la superposition du second, avant d'être retirée très lentement.

Nous avons également réalisé, avec le même dispositif expérimental, deux expériences illustratives à trois couches.

cuve	longueur (cm)	largeur (cm)	hauteur h (cm)	épaisseur des parois (cm)
1	30	30	6.1	3
2	30	30	8.0	3.1
3	30	30	14.8	3.1
4	30	30	20.0	3.1
5	30	10	16.4	2.8

TAB. 3.1 – *Dimensions des différentes cuves utilisées.*

dilatation thermique α (*)	diffusivité thermique κ	conductivité thermique k
$2 \times 10^{-4} K^{-1}$ à 20°C	$1.42 \times 10^{-7} m^2 s^{-1}$	$0.59 W m^{-1} K^{-1}$

TAB. 3.2 – *Propriétés des solutions de natrosol. (*) : mesurée au laboratoire.*

3.2 Les fluides utilisés.

3.2.1 Les solutions de natrosol.

Nous avons utilisé dans la plupart des expériences des mélanges d'eau, de natrosol et de sel (Tait & Jaupart 1989). Le natrosol est un polymère qui, mélangé en faible quantité avec de l'eau, modifie radicalement la viscosité de la solution sans en perturber d'une manière significative les autres propriétés (qui restent semblables à celles de l'eau). Ainsi, l'ajout de 0.2 à 1.5 % en masse de polymère engendre une viscosité η de 0.028 Pa.s à 110 Pa.s, c'est-à-dire 28 à 110000 fois la viscosité de l'eau, alors que la variation de densité reste limitée à 0.5% (figure 3.2) : l'ajout d'une faible quantité de sel à ce mélange permet alors d'en contrôler indépendamment la masse volumique. Toutes les mesures de densité et de viscosité ont été effectuées au laboratoire, à l'aide respectivement d'un densimètre Anton Paar DMA 5000 (précision de 3×10^{-4}%) et d'un rotoviscosimètre Haake RV20 (précision de 25%).

Les solutions de natrosol sont totalement miscibles (i.e. pas de tension de surface). Leur viscosité est newtonienne à faible taux de déformation (figure 3.3a) et ne dépend que faiblement de la température (figure 3.3b) : dans la plupart des expériences, ces variations d'origine thermique sont négligeables par rapport au saut de viscosité d'origine chimique prenant place à l'interface, ce qui facilite l'interprétation des résultats. La table 3.2 présente les valeurs caractéristiques des autres propriétés physiques. Le coefficient de dilatation thermique varie également avec la température (figure 3.4) : dans la suite, nous utiliserons donc sa valeur à la température moyenne de la cuve, sauf pour les phénomènes locaux où nous utiliserons la valeur locale.
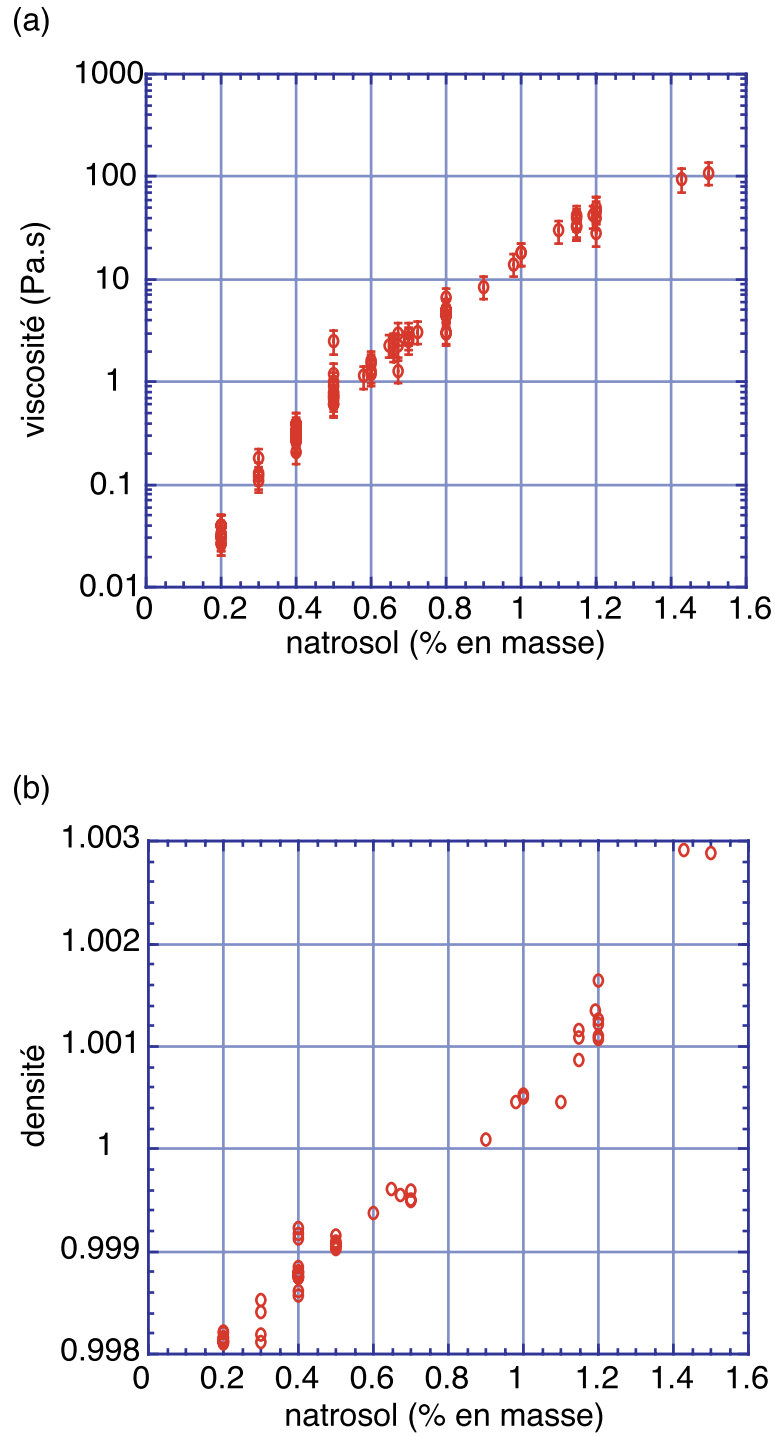
FIG. 3.2 – (a) Variation de la viscosité et (b) de la densité des solutions de natrosol en fonction de la quantité de natrosol ajoutée (valeurs mesurées au laboratoire).

a)

b)
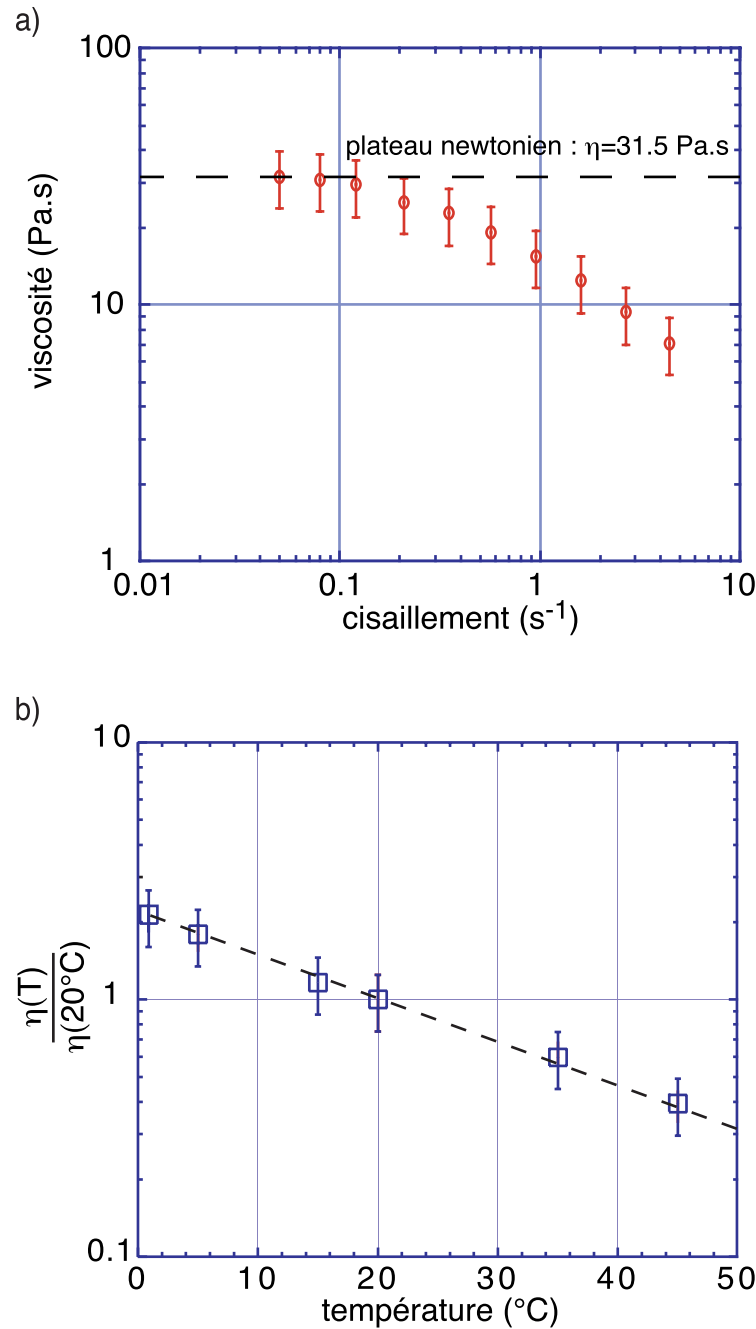
Fig. 3.3 – (a) Mesure de la viscosité d'une solution à 1.1% en masse de natrosol à l'aide d'un rotoviscosimètre Haake RV20. A faible déformation, nous retrouvons une viscosité constante, correspondant à un fluide newtonien. Dans nos cuves, les vitesses sont de l'ordre du centimètre par minute sur une distance typique de 10 cm, ce qui correspond à un gradient typique de $1.7 \times 10^{-3} \, s^{-1}$. (b) Variation de la viscosité des solutions de natrosol en fonction de la température : la droite en pointillés représente la loi expérimentale $\eta(T)/\eta(20^oC) = 2.2e^{-0.038T}$, où T désigne la température en ^oC.
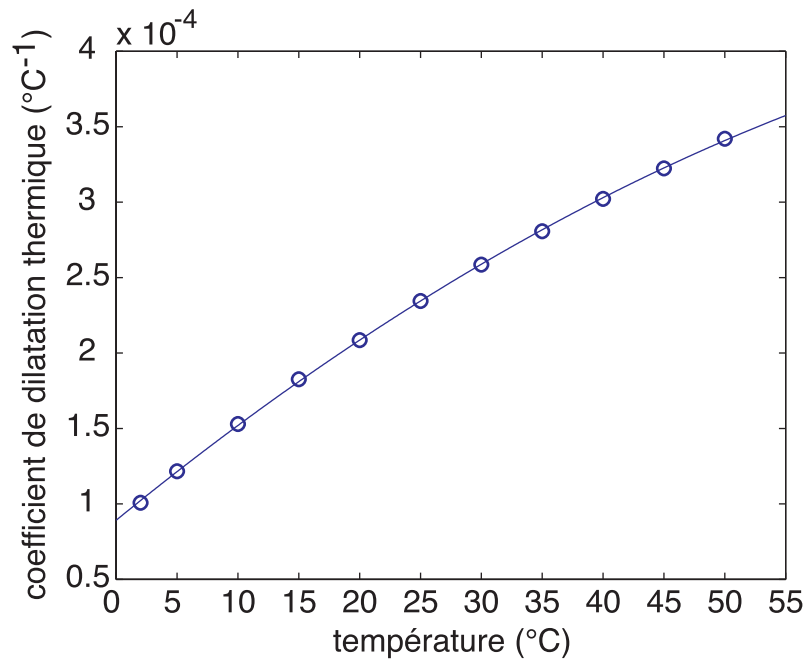
FIG. 3.4 – *Variation du coefficient de dilatation thermique des solutions de natrosol en fonction de la température. La courbe représente la loi expérimentale $\alpha(T) = -3.1 \times 10^{-8}T^2 + 6.6 \times 10^{-6}T + 8.9 \times 10^{-5}$, où T désigne la température en ^oC.*
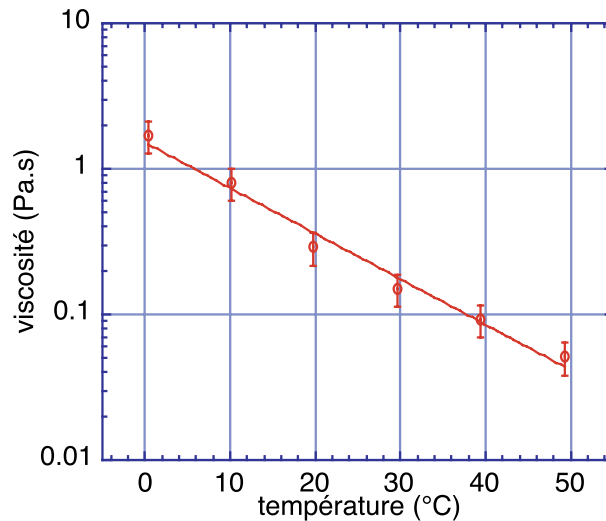
FIG. 3.5 – *Variation de la viscosité du sucre liquide haute pureté DDC 131 avec la température.*

3.2.2   Autres fluides : huiles silicones et sirops de sucre.

Nous avons utilisé pour certaines expériences des huiles silicones $47V5000$ et $45V500$, qui présentent deux avantages importants :

– leur viscosité est rigoureusement Newtonienne.

– leur coefficient de dilatation thermique ne varie pas avec la température.

Ces expériences nous ont donc permis de confirmer la validité de nos approximations pour les solutions de Natrosol, dont les paramètres physiques (viscosité et dilatation thermique) ont un comportement plus compliqué.

Nous avons également réalisé quelques expériences avec du sucre liquide haute pureté DDC 131 fourni par Béghin Say, pour étudier l'influence d'une viscosité fortement dépendante de la température (figure 3.5).

Toutefois, l'emploi de ces fluides s'avère beaucoup moins pratique que celui des solutions de natrosol : ils ne peuvent en effet être fabriqués à la demande au laboratoire, en choisissant indépendamment leurs viscosité et densité.

canne	position des thermocouples en cm par rapport à l'extrémité						
1	3.12	4.12	4.68	5.10	5.72	5.92	6.20
2	0.35	0.60	1.25	2.05	3.90	5.95	7.20
	8.20	9.25	10.25	12.70	13.70	14.30	14.70
3	5.00	7.00	8.00	9.05	9.60	10.15	10.65
	12.70	14.80	15.85	16.30	16.80	18.05	19.05

TAB. 3.3 – *Position des différents thermocouples dans les trois cannes utilisées (précision de 0.03 cm).*

3.3   Mesures.

3.3.1   Mesures de température.

Pour accéder aux températures à l'intérieur de la cuve, nous disposons de 30 thermocouples disposés sur trois cannes : leurs coordonnées précises sont reportées dans la table 3.3. Ces cannes sont suffisamment fines ($\sim 2mm$) pour ne pas perturber d'une manière significative la dynamique de notre système visqueux. Toutes les 30 secondes, un ordinateur interroge ces différents thermocouples qui lui renvoient par l'intermédiaire d'une interface IEEE une différence de potentiel directement proportionnelle à la température du site : par une calibration précise, cette dernière est alors connue au dixième de degré près.

Selon la disposition des différentes cannes, nous avons pu obtenir :
- des profils horizontaux de température (canne n^o3).
- des profils verticaux (cannes n^o1 et 2) et donc, par interpolation de la courbe, une estimation des flux de chaleur aux bornes.
- une image précise de l'évolution dans le temps des températures, et par transformée de Fourier, un spectre des fréquences les plus sollicitées par la dynamique.
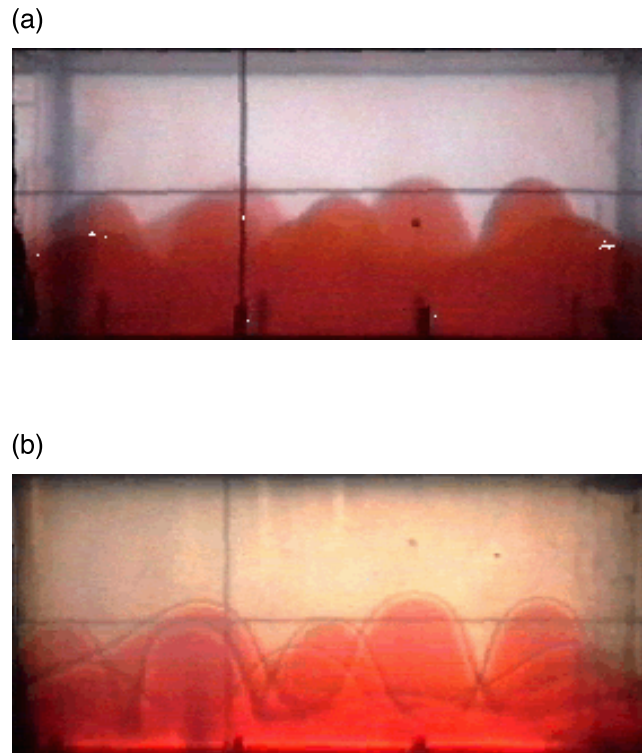
FIG. 3.6 – *Visualisation simple (expérience n°18) : (a) image directe et (b) au même instant à travers le verre dépoli.*

3.3.2 Visualisation simple.

De manière à suivre visuellement l'évolution du système, nous avons dans un premier temps coloré un des deux fluides avec du colorant alimentaire. Une caméra vidéo nous a alors permis d'enregistrer par un côté de la cuve, soit directement (figure 3.6*a*), soit à travers un verre dépoli (figure 3.6*b*), l'évolution des structures jusqu'à homogénéisation des couleurs : nous avons ainsi pu accéder aux structures les plus importantes, et quantifier leurs vitesses caractéristiques de développement, ainsi que leurs périodicités spatiales et temporelles. Il faut toutefois noter que cette technique nous donne accès à la projection sur un plan de l'ensemble des structures présentes sur toute la profondeur de la cuve : il est ensuite très difficile d'isoler les différents phénomènes.

3.3.3   Méthode de visualisation par plan laser.

La convection dans un système à deux couches se traduit expérimentalement par des phénomènes tridimensionnels très compliqués et par des effets à petite échelle, comme par exemple le mélange entre les deux fluides : il a donc été indispensable dans nos expériences d'accéder à des structures très fines, de taille millimétrique, ce qui est impossible par la méthode de visualisation simple.

Nous avons donc amélioré notre dispositif en implémentant une nouvelle technique de visualisation par plan laser (figure 3.7). Grâce à une lentille cylindrique, le faisceau émis par un laser est transformé en fin plan de lumière vertical ou horizontal, puis projeté à travers la cuve : il permet alors d'isoler une tranche à l'intérieur du système. L'ajout préalable de quelques milligrammes de fluorescéine à l'une des deux couches permet alors d'observer des structures très fines (figure 3.8a). Par ailleurs, il est également possible d'ajouter dans les fluides des cristaux liquides dont la transition de phase se fait à température fixée : dans un plan donné, tous les cristaux à la température de transition réfléchissent la lumière du laser, imageant ainsi précisément une isotherme (figure 3.8b). Cette méthode nous a permis d'améliorer considérablement notre visibilité du problème.

Ce projet a exigé énormément d'investissements, à la fois en moyens et en temps. Il a pu être réalisé grâce à la collaboration de Catherine Carbonne, Damien Jurine et Valérie Vidale. L'ensemble du bloc optique a été monté sur un banc Norcam ajustable latéralement et verticalement, permettant d'effectuer un balayage de l'intégralité de la cuve. A terme, en réalisant un balayage automatique couplé avec le système de prise de vues, cette technique permettra de reconstruire à trois dimensions et avec une précision millimétrique l'intégralité des structures dynamiques.

(a)

(b)
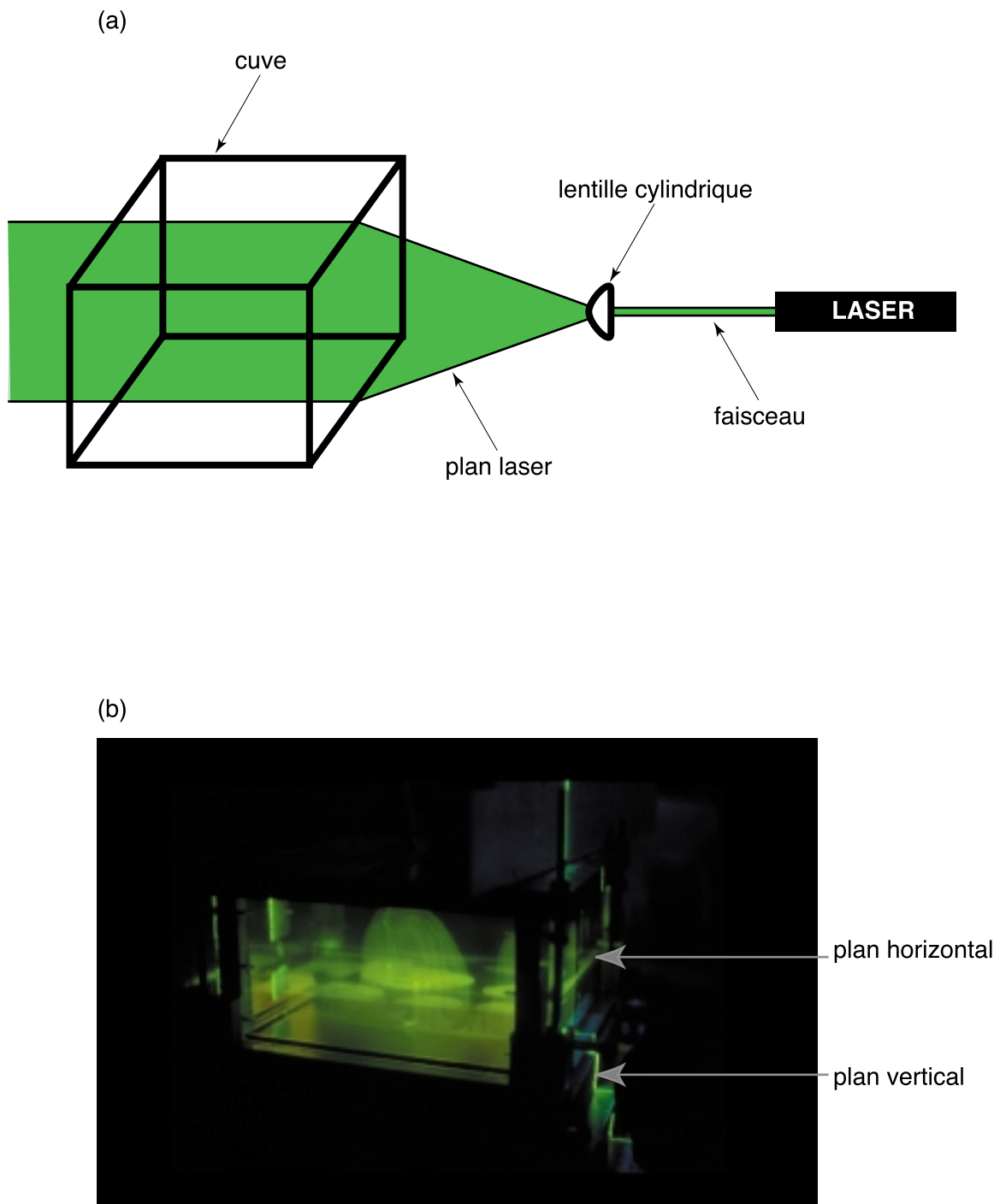
FIG. 3.7 – (a) Schéma théorique et (b) photographie de la visualisation par plan laser.
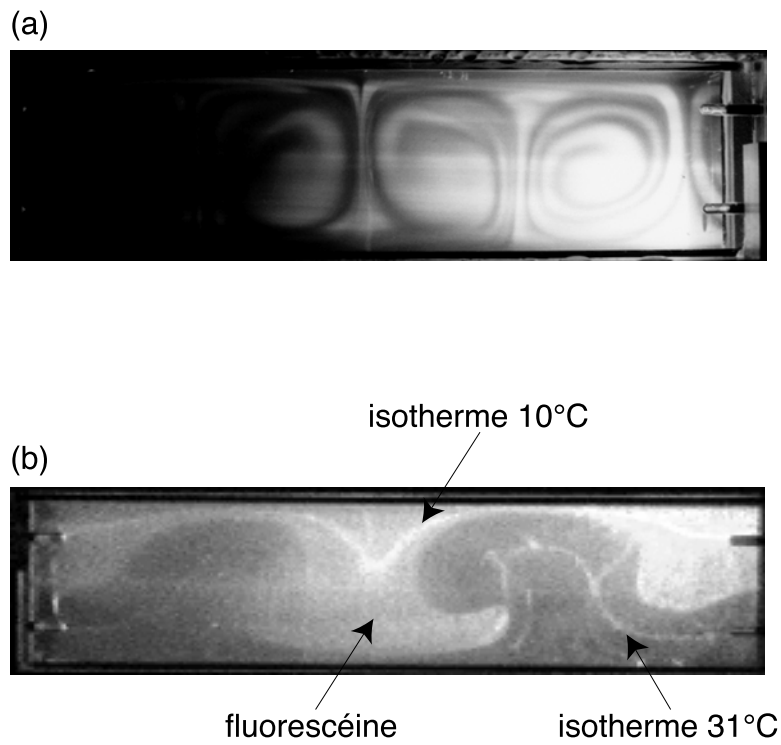
FIG. 3.8 – *(a) Visualisation du mélange grâce à la fluorescéine (expérience n°51) et (b) visualisation des isothermes (expérience n°56 : le fluide inférieur contient des cristaux liquides imageant l'isotherme 31°C, et le fluide supérieur de la fluorescéine ainsi que des cristaux liquides imageant l'isotherme 10°C).*

3.4 Avantages et inconvénients d'une modélisation analogique.

La plupart des études et modélisations actuelles du manteau se font d'un point de vue numérique (voir Tackley 2000a pour une revue récente) : les codes sont de plus en plus précis et intègrent de plus en plus de complications naturelles. Ainsi, il est aujourd'hui possible de prendre en compte, dans un modèle sphérique, la variation des paramètres physiques avec la pression et la température, les transitions de phase en profondeur, les effets d'un chauffage radioactif hétérogène, la présence des continents en surface... Le défi actuel consiste à modéliser la formation et le comportement naturel des plaques tecto-niques (Tackley 2000a). Pourtant, un système trop complexe, dans lequel les nombreux paramètres ne sont pas toujours bien contraints, ne permet plus de juger de l'influence et de l'importance des divers phénomènes physiques modélisés.

Tous ces effets sont bien sûr hors de portée de notre modèle simple ; notre approche est toutefois complémentaire. Notre objectif n'est pas de fabriquer un manteau miniature, mais de quantifier précisément les effets de deux paramètres qui nous semblent primor-diaux : les contrastes de densité et de viscosité entre les deux parties du manteau. Nous cherchons donc à comprendre 'l'ordre 1' du système mantellique, venant se superposer à 'l'ordre 0' constitué par la tectonique des plaques. L'approche expérimentale permet alors d'accéder - en trois dimensions - à l'intégralité de l'évolution temporelle des diverses échelles de convection.

Première partie

Convection thermique dans un système à deux couches : étude théorique et expérimentale.

Introduction.

Le premier chapitre de cette partie est consacré à l'étude de stabilité de la convection thermique dans un système relativement simple : deux fluides miscibles de densités et de viscosités différentes sont superposés dans une cuve, puis chauffés par le bas et refroidis par le haut. Initialement, le fluide le plus lourd est situé au-dessous du plus léger, mais cette configuration peut éventuellement être renversée par les effets thermiques.

La stabilité de ce système a déjà été étudiée dans le cas où les propriétés physiques des deux fluides (exceptée la densité) sont égales (Richter & Johnson 1974) ou très proches (Renardy & Joseph 1985). Rasenat, Busse & Rehberg (1989) se sont quant à eux focalisés sur les couplages thermiques et visqueux au niveau de l'interface supposée plane. Notre objectif, dans le cadre de l'étude du manteau, est d'étudier plus particulièrement l'influence des contrastes de viscosité et de densité sur la déstabilisation de l'interface.

Les équations caractéristiques du problème correspondent aux équations 'classiques' de la convection dans chacune des deux couches (voir §1.2 de l'introduction générale, p. 18), auxquelles il faut ajouter les conditions de continuité de la vitesse, des contraintes, de la température et du flux de chaleur à l'interface. Ces équations peuvent être adimensionnées en se focalisant sur le mouvement possible de l'interface, et font apparaître quatre nombres sans dimension (en plus du nombre de Prandtl, considéré comme infini) :

– le rapport de viscosité

$$\gamma = \frac{\nu_1}{\nu_2}, \tag{1}$$

où ν_i désigne la viscosité cinématique du fluide i.

– le rapport d'épaisseur

$$a = \frac{h_1}{H},$$ (2)

où h_1 désigne l'épaisseur du fluide 1 et $H = h_1 + h_2$.

– le nombre de Rayleigh du système global, mesurant l'intensité de la convection

$$Ra = \frac{\alpha g \Delta T H^3}{\kappa \nu_2},$$ (3)

où α désigne le coefficient de dilatation thermique à la température moyenne de la cuve, κ le coefficient de diffusivité thermique, g l'accélération de la pesanteur, et ΔT la différence totale de température.

– le nombre de flottabilité, rapport entre le contraste stabilisant de densité d'origine chimique et le contraste déstabilisant de densité d'origine thermique

$$B = \frac{\rho_{1_0} - \rho_{2_0}}{\alpha \rho_0 \Delta T},$$ (4)

où ρ_{i_0} désigne la densité du fluide i à la température T_0 et $\rho_0 = (\rho_{1_0} + \rho_{2_0})/2$.

La linéarisation des équations caractéristiques du problème permet ensuite d'étudier la stabilité de la convection : pour chaque triplet (γ, a, B), nous déterminons la valeur critique du nombre de Rayleigh Ra_c pour laquelle le premier mouvement apparaît. Deux types de démarrage sont alors possibles, comme le montre la figure 1 :

– lorsque $B > B_c(\gamma, a)$, où $B_c(\gamma, a)$ désigne le nombre de flottabilité critique fonction de γ et de a, le régime stratifié prend place : les effets thermiques ne sont pas suffisants pour renverser la stratification chimique initiale, et la convection se développe au-dessus et en-dessous d'une interface plane.

– lorsque $B < B_c(\gamma, a)$, le régime oscillatoire se développe : les effets thermiques peuvent renverser la stratification chimique initiale, et la convection se développe sur toute l'épaisseur de la cuve ; l'interface oscille autour de sa position d'équilibre. En augmentant progressivement le nombre de Rayleigh depuis sa valeur critique, la fréquence de ces oscillations décroît rapidement, et s'annule finalement pour
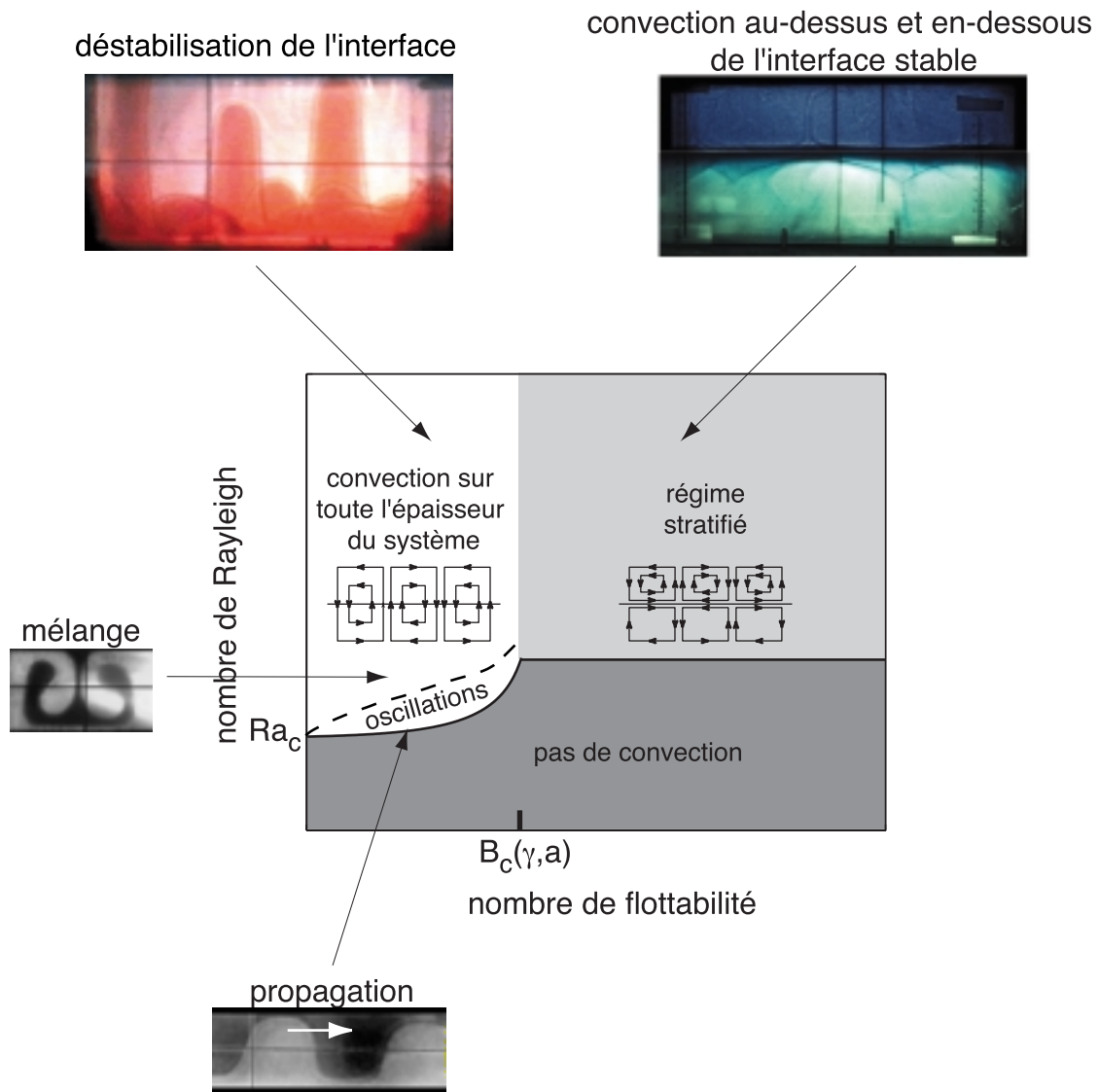
FIG. 1 – *Principaux résultats de l'étude de stabilité : les courbes théoriques sont reportées sur le graphique, et les photographies montrent les régimes correspondants observés expérimentalement.*

$Ra/Ra_c > 5$ typiquement : le régime oscillatoire se transforme en régime de convection sur toute l'épaisseur du système.

Nos expériences sont en bon accord avec ces résultats théoriques. À proximité de la stabilité marginale, les comportements et échelles caractéristiques du système réel sont exactement ceux donnés par l'étude linéaire. À plus haut Ra, les valeurs théoriques de $B_c(\gamma, a)$ demeurent correctes pour déterminer la stabilité initiale de l'interface ; toutefois, les caractéristiques et l'évolution du système sont complètemement modifiées par l'existence et l'interaction de multiples phénomènes non-linéaires, et constituent l'objet du troisième chapitre de cette partie.

À haut nombre de Rayleigh, plusieurs échelles de convection se superposent dans le système : en plus du régime thermochimique à grande échelle (stratifié ou sur toute la cuve) que nous venons de décrire, et qui met en jeu les deux fluides simultanément, une convection thermique à petite échelle se développe à l'intérieur de chacun, sous la forme de panaches provenant de la déstabilisation des couches limites externes. Ces différentes structures interagissent et donnent naissance à de multiples comportements que nous avons décrits et cartographiés en fonction des caractéristiques du système (figures 2 et 3) :

– tant que le nombre de flottabilité est grand ($B > 0.3 - 0.5$ typiquement), le régime thermochimique sélectionné est stratifié, en accord avec la stabilité marginale. Pour des couches suffisamment épaisses, la convection se développe au-dessus et en dessous de l'interface: les structures purement thermiques qui se mettent en place peuvent localement et partiellement déformer l'interface, avec une amplitude qui décroît lorsque le contraste de densité augmente. Nous appelons ce phénomène la topographie dynamique, pour le distinguer de la déstabilisation intégrale du système. Lorsque l'une des deux couches est plus fine que la couche limite thermique correspondante, des panaches se forment tout comme dans la convection classique à une couche ; toutefois, ceux-ci sont stabilisés par la présence de la couche stratifiée, dont ils entraînent un fin filament.

– lorsque B est plus petit ($B \leq 0.3$ typiquement), le système dans son intégralité se déstabilise, et de grandes structures thermochimiques se développent depuis la couche dont le nombre de Rayleigh est le plus faible : le fluide le plus visqueux envahit le second sous la forme de grands cylindres verticaux appelés 'diapirs', tandis que le matériel le moins visqueux développe des 'cavity plumes', grandes sphères alimentées par un fin conduit. La dynamique de ces deux types de structures est contrôlée essentiellement par le fluide le plus visqueux, qui limite les mouvements à l'échelle de la cuve toute entière. Lorsque le contraste de viscosité γ est faible ($1/5 < \gamma < 5$ typiquement), les deux fluides se mélangent immédiatement ; plusieurs pulsations successives sont néanmoins possibles pour un contraste de viscosité plus important, sous la forme de pulsations verticales à fort B et de vidanges successives des deux couches à faible B ou dans le cas d'une couche fine.

Ces mécanismes correspondent bien sûr à un état transitoire : la grande difficulté à haut nombre de Rayleigh est que le régime change au cours du temps en fonction de l'évolution thermique et de l'efficacité du mélange entre les deux couches. Le paramètre fondamental correspond donc au nombre de flottabilité effectif B_{eff}, basé sur le profil réel de température dans la cuve et sur la valeur réelle du contraste chimique à l'interface. B_{eff} diminue au cours du temps, et l'interface se déstabilise lorsque le fluide le plus visqueux convecte et $B_{eff} < 1$.

Dans tous les cas, le système évolue vers une convection 'classique' à une couche. Toutefois, nos expériences démontrent que la coexistence de deux fluides différenciés peut se maintenir très longtemps : en particulier, la durée précédant la déstabilisation de l'interface dépend exponentiellement du contraste de densité. Ce régime transitoire pourrait donc s'avérer très intéressant dans le cadre du manteau terrestre, comme nous allons le voir dans la seconde partie de cette thèse.

déformations de l'interface

pulsations verticales

convection au-dessus et en-dessous
de l'interface stable

vidange des réservoirs

panaches thermochimiques
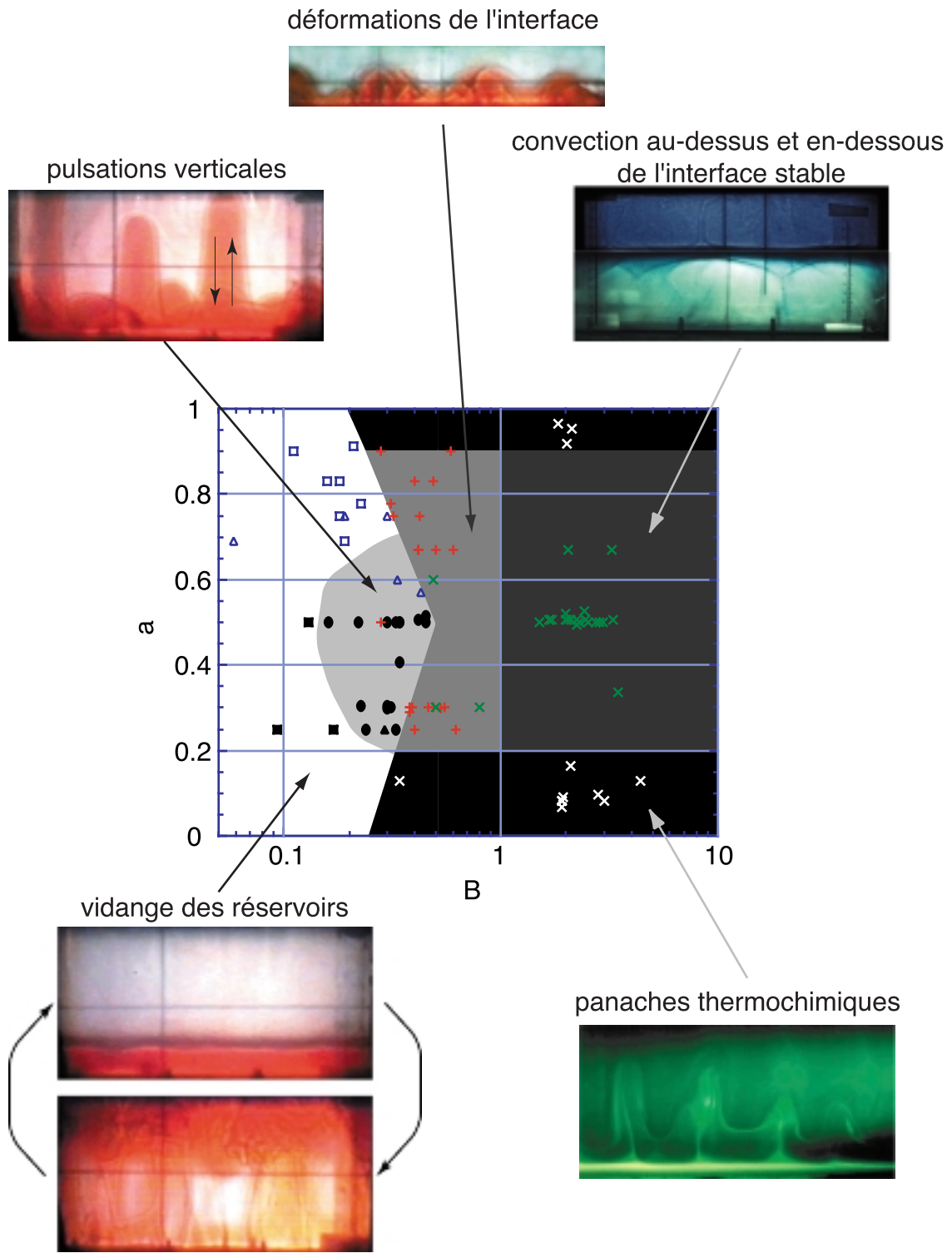
FIG. 2 – *Régimes de convection thermochimique observés à haut nombre de Rayleigh en fonction du nombre de flottabilité et du rapport de hauteur : les signes × correspondent à une interface plane, avec en blanc les expériences dans lesquelles une des deux couches est plus fine que la couche limite thermique correspondante ; les signes + indiquent les cas de topographie dynamique, les carrés les vidanges successives (plein: diapirs; vides: cavity plumes), les ronds les pulsations verticales et les triangles les cas de mélange immédiat des deux couches.*
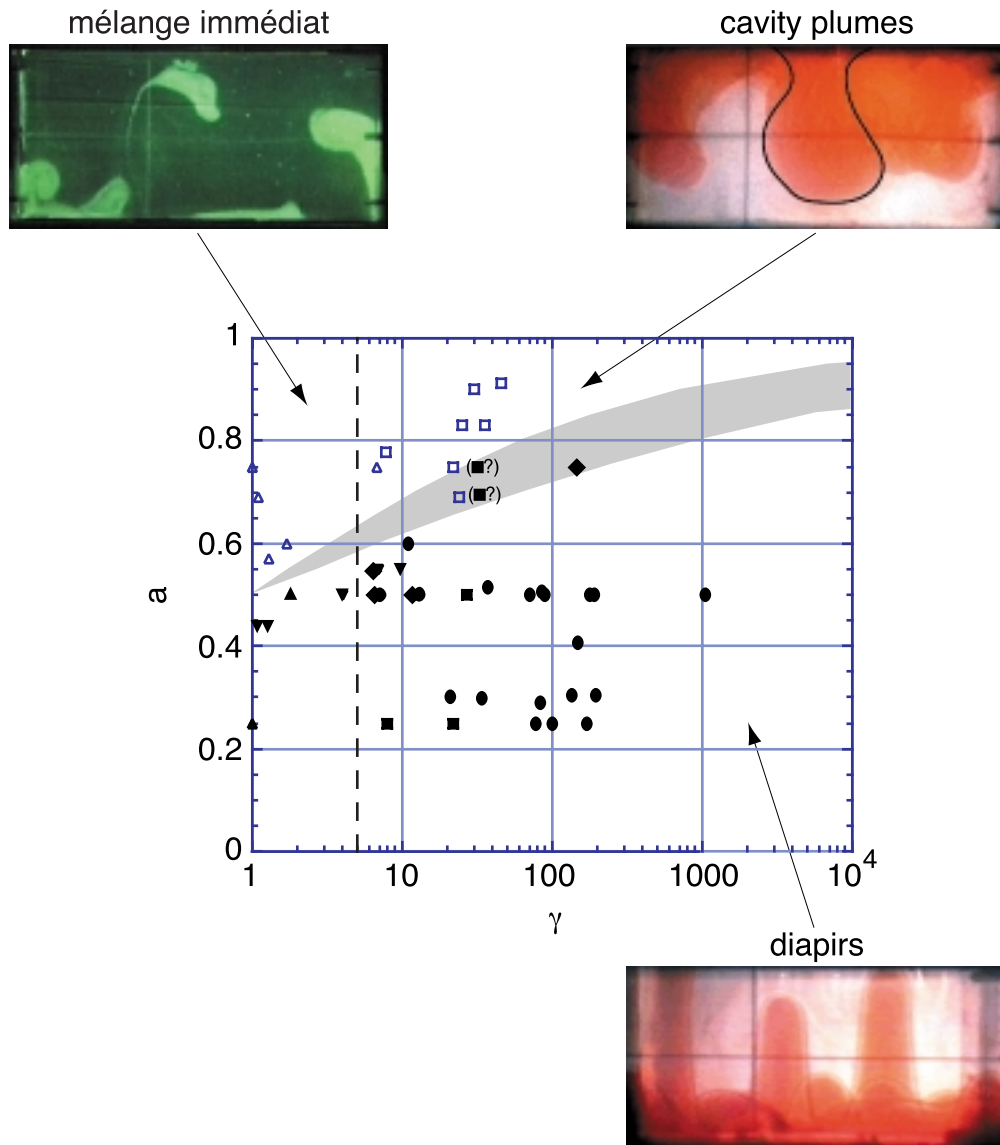
FIG. 3 – *Régimes de convection thermochimique observés à faible nombre de flottabilité en fonction des rapports de viscosité et de hauteur: les triangles correspondent à un mélange immédiat qui prend place typiquement pour $1 \leq \gamma < 5$, les losanges aux oscillations près de la stabilité marginale, les carrés aux vidanges successives, et les ronds aux pulsations verticales. Les symboles vides indiquent la formation de cavity plumes depuis la couche la moins visqueuse, les symboles pleins la formation de diapirs depuis la couche la plus visqueuse ; la région ombrée indique la zone de transition entre ces deux régimes.*

Chapitre 1

Stabilité de la convection thermique dans un système à deux fluides miscibles visqueux.

Stability of thermal convection in two superimposed miscible viscous fluids

By MICHAEL LE BARS AND ANNE DAVAILLE

Laboratoire de Dynamique des Systèmes Géologiques, Institut de Physique du Globe de Paris
CNRS, UMR 7579, 4 Place Jussieu, 75 252 Paris cedex 05, France

The stability of two-layer thermal convection in high-Prandtl-number fluids is investigated using laboratory experiments and marginal stability analysis. The two fluids have different densities and viscosities but there is no surface tension and chemical diffusion at the interface is so slow that it is negligible. The density stratification is stable. A wide range of viscosity and layer depth ratios is studied. The onset of convection can be either stationary or oscillatory depending on the buoyancy number B, the ratio of the stabilizing chemical density anomaly to the destabilizing thermal density anomaly: when B is lower than a critical value (a function of the viscosity and layer depth ratios), the oscillatory regime develops, with a deformed interface and convective patterns oscillating over the whole tank depth; when B is larger than this critical value, the stratified regime develops, with a flat interface and layers convecting separately. Experiments agree well with the marginal stability results. At low Rayleigh number, characteristic time and length scales are well-predicted by the linear theory. At higher Rayleigh number, the linear theory still determines which convective regime will start first, using local values of the Rayleigh and buoyancy numbers, and which regime will persist, using global values of these parameters.

1. Introduction

In contrast to the Rayleigh–Bénard problem for one fluid, instability in two chemically stratified fluid layers can be either steady or oscillatory (Richter & Johnson 1974), as for the closely related and well-documented case of double-diffusive convection (e.g. Veronis 1968; Turner 1979; Hansen & Yuen 1989). But the number of parameters involved in this problem is large and there exists no comprehensive picture of the domains in which a given regime prevails.

The steady case, where the interface remains flat and convection develops in two superimposed layers, has been extensively studied, because of its suggested occurrence in the Earth's mantle (Richter & McKenzie 1981; Busse 1981; Cserepes & Rabinowicz 1985; Ellsworth & Schubert 1988; Cserepes, Rabinowicz & Rosemberg-Borot 1988; Sotin & Parmentier 1989). Rasenat, Busse & Rehberg (1989) showed that an oscillatory two-layer regime could also develop, involving no deformation of the interface, with a convective pattern oscillating between viscous and thermal coupling: experimental studies of this configuration has been performed by Busse & Sommermann (1996) and Andereck, Colovas & Degen (1996). However, studies of the oscillatory regime where the interface deforms and convection develops over the whole depth of the tank have been limited to cases where the physical properties of the two fluids (viscosity, thermal diffusivity, thermal expansivity) are equal (Richter

& Johnson 1974; Schmeling 1988) or nearly equal (Renardy & Joseph 1985; Renardy & Renardy 1985).

One question that remains open is the fate of the oscillatory regime when the viscosity contrast between the two layers varies by several orders of magnitude. The answer to this question could provide valuable insight into the dynamics of the Earth's mantle where large viscosity variations are expected and the type of convection ('two-layered' or 'whole-mantle') is still controversial (Olson, Silver & Carlson 1990; Tackley 2000). Motivated by this geophysical interest, laboratory experiments have recently been performed to investigate the influence of the viscosity contrast on two-layer thermal convection at high Rayleigh and Prandtl numbers (Davaille 1999a, b; Le Bars & Davaille, in preparation). The two fluids were miscible in the sense that there was no surface tension at the interface. Depending on the buoyancy number B, the ratio of the stabilizing chemical density anomaly to the destabilizing thermal density anomaly, two regimes were observed: for $B > 1$, thermal convection develops in two superimposed layers, separated by a thermal boundary layer at a relatively undeformed interface, while for $B < 0.35 - 0.55$, the interface deforms in large domes which move up and down quasi-periodically.

Here, we use marginal stability analysis and laboratory experiments to investigate further the stability and occurrence of the two thermochemical regimes, as a function of the viscosity, depth and density ratios between the two fluids: our purpose is to determine for each case the onset of convection and the prevailing regime. Section 2 sets up the problem formally and presents the results of the marginal stability analysis. In §3, these results are first compared with experiments at low Rayleigh number, and then used to determine the stability of two-layer systems at higher Rayleigh number.

2. Marginal stability analysis

2.1. *Analytical formulation*

In the two-dimensional x, z space, we consider two superimposed layers of fluids, respectively of densities ρ_{1_0} and ρ_{2_0}, kinematic viscosities v_1 and v_2 (dynamic viscosities η_1 and η_2), and depth d_1 and d_2 (figure 1a). Only the case where the density stratification is stable is studied, so that the heavier fluid is at the bottom. All the physical properties of the two fluids are taken to be equal, except their densities and viscosities. There is neither surface tension nor chemical diffusion at the interface between the two fluids. The lower and upper planes are held at uniform temperatures T_1 and T_2 respectively. Each plane is assumed to be a perfect thermal conductor, and the kinematic condition on those boundaries is either traction-free, for comparison with previous work, or rigid (zero horizontal velocity) for comparison with the experiments. Unless specified, numerical values presented in this paper are for rigid boundaries.

To non-dimensionalize the problem, we use the length scale $d = d_1 + d_2$, the total thickness of fluid, and the temperature scale $\Delta T = T_1 - T_2$, the total temperature difference. In this study, we aim to determine the occurrence of the oscillatory regime, where the interface deforms in large domes (Davaille 1999b): we thus choose a velocity scale characteristic of this problem, namely the Stokes velocity of a dome developing from layer 1 into layer 2: $v = \alpha g \Delta T d^2 / v_2$, where α is the thermal expansivity and g the acceleration due to gravity. The time scale is given by $d/v = v_2 / \alpha g \Delta T d$, and the viscous pressure scale by $\eta_2 v / d = \alpha \rho_{2_0} g \Delta T d$. In the following, all the variables are non-dimensionalized using these scales.
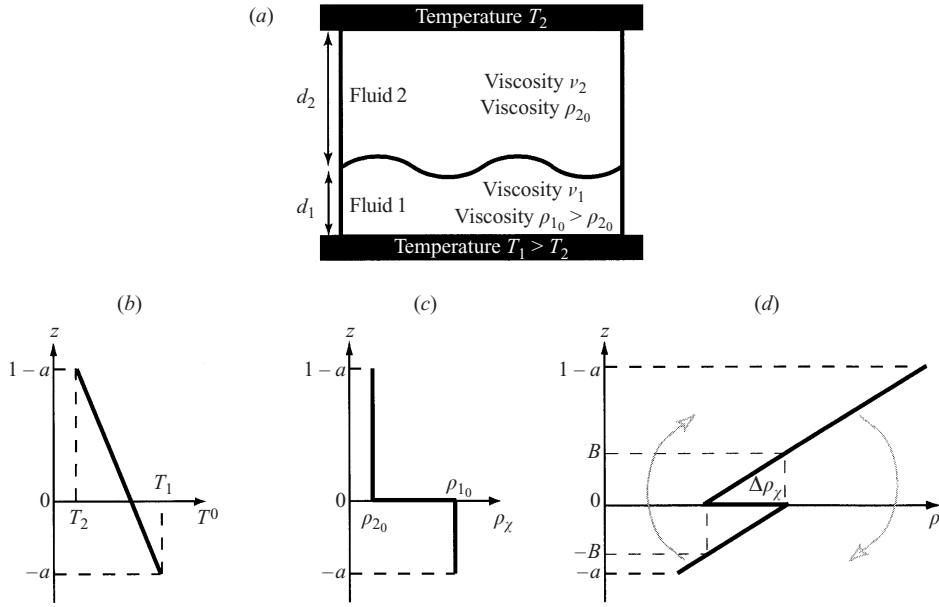
FIGURE 1. Configuration of the problem: (*a*) set-up, (*b*) linear temperature profile, (*c*) chemical density profile and (*d*) effective density profile, taking into account thermal and chemical effects.

We study the linear stability of the static solution, which exhibits a linear temperature profile (figure 1*b*):

$$T = \frac{T_1}{\Delta T} - (z + a), \tag{2.1}$$

where $a = d_1/d$. Let θ_i and p_i be the deviations of the temperature and pressure from their static distribution, and $\boldsymbol{u}_i$ be the velocity vector. Assuming that thermal effects and chemical density contrast are small, the fluids are considered incompressible, except for buoyancy terms (Boussinesq approximation). In a first-order approximation, the equation of state used within each layer i is thus

$$\rho_i(T) = \rho_{i_0} - \alpha \rho_0 (T \Delta T - T_0), \tag{2.2}$$

where $\rho_0 = (\rho_{1_0} + \rho_{2_0})/2$. We obtain for each layer i a dimensionless form of the equations governing the motion:

$$\nabla \cdot \boldsymbol{u}_i = 0, \tag{2.3}$$

$$\frac{Ra}{Pr} \left(\frac{\partial}{\partial t} + \boldsymbol{u}_i \cdot \nabla \right) \boldsymbol{u}_i = -\nabla p_i + \theta_i \boldsymbol{k} + \frac{v_i}{v_2} \nabla^2 \boldsymbol{u}_i, \tag{2.4}$$

$$Ra \left[\left(\frac{\partial}{\partial t} + \boldsymbol{u}_i \cdot \nabla \right) \theta_i - \boldsymbol{u}_i \cdot \boldsymbol{k} \right] = \nabla^2 \theta_i. \tag{2.5}$$

The vertical unit vector $\boldsymbol{k}$ is directed opposite to gravity. The Rayleigh and Prandtl numbers are defined by

$$Ra = \frac{\alpha g \Delta T d^3}{\kappa v_2} \quad \text{and} \quad Pr = \frac{v_2}{\kappa},$$

where κ is the thermal diffusivity. We also define the viscosity ratio between the two layers $\gamma = v_1/v_2$. Since we are interested in the onset of infinitesimal disturbances,

the nonlinear terms $(\boldsymbol{u}_i \cdot \nabla)\boldsymbol{u}_i$ and $(\boldsymbol{u}_i \cdot \nabla)\theta_i$ are negligible. Furthermore, we restrict our attention to the case of infinite Prandtl number, relevant to the Earth's mantle. Then, taking twice the curl of (2.4), and using (2.5) to eliminate the temperature, one obtains for the vertical velocity w_i:

$$\left(Ra\frac{\partial}{\partial t} - \nabla^2\right)\nabla^4 w_1 = -\frac{Ra}{\gamma}\frac{\partial^2 w_1}{\partial x^2}, \tag{2.6a}$$

$$\left(Ra\frac{\partial}{\partial t} - \nabla^2\right)\nabla^4 w_2 = -Ra\frac{\partial^2 w_2}{\partial x^2}. \tag{2.6b}$$

The outer boundary conditions are in each layer ($z = -a$ and $z = 1 - a$):

$$w = \frac{\partial w}{\partial z} = 0 \text{ for a rigid boundary,} \tag{2.7a}$$

$$w = \nabla^2 w = 0 \text{ for a free boundary,} \tag{2.7b}$$

and $\theta = 0$ which yields

$$\nabla^4 w = 0. \tag{2.8}$$

The equilibrium position of the interface between the fluids is assumed to be $z = 0$. Distortions of the interface from this position are described by the function $h(x,t)$. Assuming that those distortions are small, a Taylor expansion around $z = 0$ is used to obtain the linearized interfacial conditions (see Joseph & Renardy 1993 for the complete derivation):

The kinematic condition for the material interface yields

$$w_1 = \frac{\partial h}{\partial t}. \tag{2.9}$$

Continuity of velocity and incompressibility yield

$$w_1 = w_2, \tag{2.10}$$

$$\frac{\partial w_1}{\partial z} = \frac{\partial w_2}{\partial z}. \tag{2.11}$$

Continuity of shear stress yields

$$\gamma\frac{\partial^2 w_1}{\partial z^2} - \frac{\partial^2 w_2}{\partial z^2} = \gamma\frac{\partial^2 w_1}{\partial x^2} - \frac{\partial^2 w_2}{\partial x^2}. \tag{2.12}$$

Continuity of normal stress yields

$$p_1 - 2\gamma\frac{\partial w_1}{\partial z} = p_2 - 2\frac{\partial w_2}{\partial z} + Bh, \tag{2.13a}$$

where B is the buoyancy number, the ratio of the stabilizing chemical density anomaly to the destabilizing thermal density anomaly:

$$B = \frac{\rho_{1_0} - \rho_{2_0}}{\alpha\rho_0\Delta T}.$$

Taking $\partial^3/\partial t\partial x^2$ of (2.13a) and eliminating p_i with (2.4) and h with (2.9), we obtain

$$\nabla^2\frac{\partial^2}{\partial t\partial z}(\gamma w_1 - w_2) + 2\frac{\partial^4}{\partial t\partial z\partial x^2}(\gamma w_1 - w_2) = -B\frac{\partial^2 w_1}{\partial x^2}. \tag{2.13b}$$

Continuity of temperature yields

$$\theta_1 = \theta_2 \Rightarrow \gamma \nabla^4 w_1 = \nabla^4 w_2. \tag{2.14}$$

Continuity of heat flux yields

$$\frac{\partial \theta_1}{\partial z} = \frac{\partial \theta_2}{\partial z} \Rightarrow \gamma \nabla^4 \frac{\partial w_1}{\partial z} = \nabla^4 \frac{\partial w_2}{\partial z}. \tag{2.15}$$

Because we used a scaling characteristic of interface deformation, the buoyancy number B appears in (2.13). Other studies using the classical thermal diffusive scaling (Richter & Johnson 1974; Joseph & Renardy 1993) lead to the appearance of R_s, Rayleigh number based on the chemical density difference:

$$R_s = \frac{(\rho_{1_0} - \rho_{2_0})g d^3}{\kappa \eta_2}. \tag{2.16}$$

These two numbers are simply linked by the relation

$$R_s = Ra\, B. \tag{2.17}$$

Analysing the problem in terms of normal modes, the solution is sought in the form

$$w(x, z, t) = W(z) \exp(ikx + st) \text{ with } s = \sigma + i\omega. \tag{2.18}$$

Hence, $W(z)$ is solution of the following equations:
for $0 \geqslant z \geqslant -a$,

$$(sRa + k^2 - D^2)(D^2 - k^2)^2 W_1 = k^2 \frac{Ra}{\gamma} W_1, \tag{2.19a}$$

for $1 - a \geqslant z \geqslant 0$,

$$(sRa + k^2 - D^2)(D^2 - k^2)^2 W_2 = k^2 Ra\, W_2, \tag{2.19b}$$

where D stands for d/dx. The general solution of (2.19) is
for $0 \geqslant z \geqslant -a$,

$$W_1 = \sum_{1 \leqslant j \leqslant 3} A_{1j} \exp(q_{1j}(a + z)) + B_{1j} \exp(-q_{1j}(a + z)), \tag{2.20a}$$

for $1 - a \geqslant z \geqslant 0$,

$$W_2 = \sum_{1 \leqslant j \leqslant 3} A_{2j} \exp(q_{2j}(1 - a - z)) + B_{2j} \exp(-q_{2j}(1 - a - z)). \tag{2.20b}$$

The coefficients q_{ij} are solutions of the equations:
for $0 \geqslant z \geqslant -a$,

$$(sRa + k^2 - q_{1j}^2)(q_{1j}^2 - k^2)^2 = \frac{Ra}{\gamma} k^2, \tag{2.21a}$$

for $1 - a \geqslant z \geqslant 0$,

$$(sRa + k^2 - q_{2j}^2)(q_{2j}^2 - k^2)^2 = Ra k^2, \tag{2.21b}$$

and the twelve constants A_{ij} and B_{ij} are determined by the six matching conditions at the interface (2.10)–(2.15) and the six outer boundary conditions (2.7)–(2.8). Those conditions represent an homogeneous system of equations for A_{ij} and B_{ij}. Non-zero solutions exist if the determinant of the coefficient matrix (given in the Appendix) vanishes. The system thus represents a transcendental equation relating a, γ, B, Ra, k

and complex s, that must be solved numerically. Since the problem defined above is not self-adjoint, the determinant and the eigenvalues can be complex, and the onset of convection can be oscillatory as well as stationary. Moreover, the equations are identical on interchanging (γ, a) and $(1/\gamma, 1 - a)$. So only results for $\gamma \geqslant 1$ will be presented, which means that the lower layer will always be the more viscous. This is also the situation encountered in our laboratory experiments.

2.2. Results for marginal stability

Looking for the marginal stability, we assume that $\sigma = 0$ and thus s reduces to $i\omega$. For fixed values of the parameters a, γ and B, the roots of the determinant are sought in the (k, ω, Ra) space, using the Nelder–Mead simplex method (Nelder & Mead 1965). In each case, the critical Rayleigh number is the minimum value of Ra as the wavenumber k is varied.

2.2.1. Accuracy of the method

The convergence of the computer code was checked for the case $\gamma = 1$. For layers of equal properties, there are two situations identical to the classical Rayleigh–Bénard problem in one fluid. The eigenvalues for those cases are real, and given by Chandrasekhar (1961):

(a) when there is no density jump at the interface ($B = 0$), convection occurs throughout the whole layer with $Ra_c = 657.51$ and $k = 2.22$ for free boundaries and $Ra_c = 1707.76$ and $k = 3.12$ for rigid boundaries;

(b) when $a = 0.5$, the most unstable two-layer mode, which has zero vertical velocity at the interface, corresponds in each layer to Rayleigh–Bénard convection with a free boundary condition at the interface; it occurs, with our notation, at $Ra_c = 10520.16$ and $k = 4.43$ for free boundaries, and at $Ra_c = 17610.39$ and $k = 5.365$ for rigid boundaries (corresponding respectively to $Ra_c = 657.51$ and $Ra_c = 1100.65$ if the characteristic scales are taken to be those of one layer).

The more general case encountered throughout the (B, Ra) parameter space for $\gamma = 1$ and $a = 0.5$ has already been solved by Richter & Johnson (1974) for free boundaries. There, the eigenvalues are either real or complex, producing respectively either steady stratified convection or oscillatory instabilities. Our computer code reproduces exactly their numerical results.

2.2.2. Dependence on B

Figure 2 shows the stability diagram of the system for a given (γ, a) and figure 3 the corresponding interface velocity, horizontal wavelength ($\lambda = 2\pi/k$) and temporal frequency. Depending on B, instability sets in under two different regimes:

(a) Stratified regime: for B greater than a critical value $B_c(\gamma, a)$, the most unstable mode has a zero vertical velocity at the interface (figure 3a); convection develops above and below the interface with a wavelength comparable to one layer depth (figure 3b); motions are steady (figure 3c). The interface remains at its equilibrium position $h = 0$, and the stability of the stratified regime is independent of B (figure 2), as expected from (2.13a). The vertical velocity is maximum in the less viscous fluid, whereas in the other fluid motions are delayed and much slower: the less viscous layer is thus active, and the more viscous one passively driven by viscous coupling at the interface.

(b) Oscillatory regime: for B smaller than $B_c(\gamma, a)$, the vertical velocity is maximum at the interface (figure 3a) and the pulsation is non-zero (figure 3c); the interface deforms and oscillatory motions develop over the whole box depth (figure 3b). This
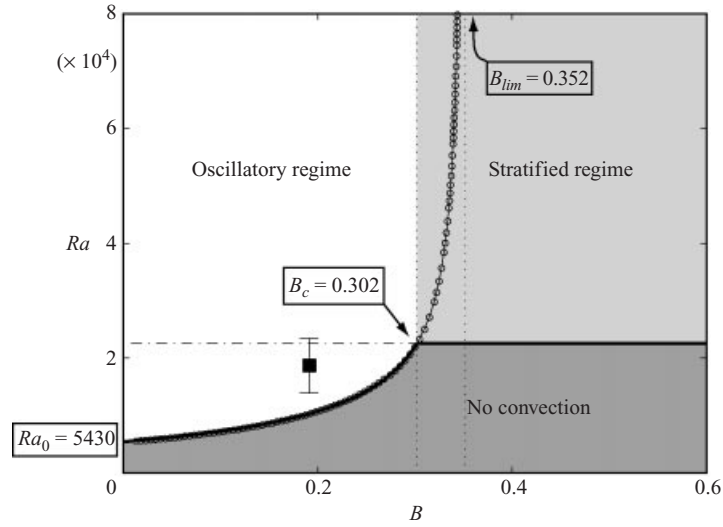
FIGURE 2. Neutral curves of marginal stability analysis in the case $\gamma = 6.7$, $a = 0.5$. Dash-dotted line corresponds to the stratified regime and circles to calculated points of the oscillatory regime (the solid line represents the fit according to 2.25b). The bold solid line follows the most unstable regime: in the dark grey domain, no convection develops, whereas in the white domain, the oscillatory regime is the most unstable and in the light grey domain, the stratified regime is the most unstable. The square shows the measured value of experiment 47.

oscillatory instability sets in since the density at the bottom of the lower layer is smaller than the density of the upper layer in spite of the stabilizing jump across the interface (and/or the density at the top of the upper layer is higher than the density of the lower layer). From (2.1) and (2.2),

$$\rho_i = \rho_{i_0} - \alpha \rho_0 \Delta T \left(\frac{T_1 - T_0}{\Delta T} - (z + a) \right). \qquad (2.22)$$

Thermal effects reverse the chemical density contrast when

$$\rho_1(z) = \rho_2(0) \Leftrightarrow z = -B \text{ (provided } B \leqslant a) \qquad (2.23a)$$

and

$$\rho_2(z) = \rho_1(0) \Leftrightarrow z = B \text{ (provided } B \leqslant 1 - a). \qquad (2.23b)$$

Thus a Rayleigh–Taylor-type overturning instability operates throughout part of the cycle (figure 1d), while dissipative effects (viscous forces and thermal diffusion) together with the stabilizing density contrast across the interface lead to a restoring force throughout the remainder of the cycle. These oscillatory motions can take the form of standing waves if the horizontal dimension of the cell is a multiple of the horizontal wavelength of the flow; otherwise, travelling waves develop. Their critical Rayleigh number increases with B, since the restoring force due to the stable density contrast becomes bigger (figure 2). For the closely related double-diffusive convection case where for example a layer of water with a stabilizing linear salt gradient is heated from below (Veronis 1968; Baines & Gill 1969), the critical Rayleigh number Ra_c scales as

$$Ra_c = Ra_0 + R_s, \qquad (2.24)$$

where R_s is the Rayleigh number based on the total chemical density contrast. The
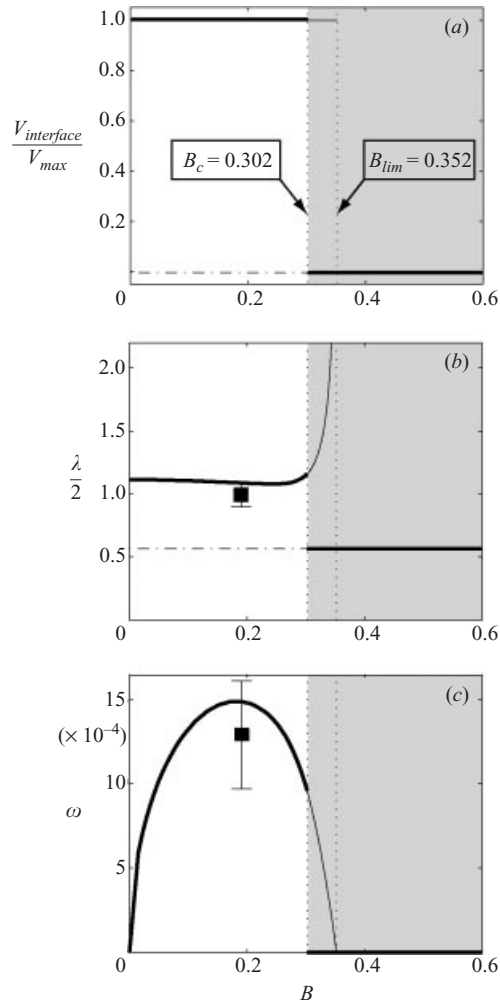
FIGURE 3. (a) Ratio of vertical interface velocity to maximum vertical velocity, (b) half horizontal wavelength ($\lambda/2 = \pi/k$) and (c) temporal frequency for the case $\gamma = 6.7$, $a = 0.5$. Dash-dotted line corresponds to the stratified regime, solid line to the oscillatory regime, and the bold solid line follows the most unstable regime. In the white domain, the oscillatory regime is the most unstable and in the light grey domain, the stratified regime is the most unstable. Squares show measured values of experiment 47.

system is destabilized when there is enough energy to overcome viscous and thermal diffusion effects as in classical Rayleigh–Bénard convection (Ra_0) and to reverse the stabilizing salt gradient (R_s). Although we have a chemical density jump at the interface instead of a linear salinity gradient, we find a similar dependence and the results are well-fitted by

$$Ra_c = Ra_0 + \beta R_s, \tag{2.25a}$$

where β is a constant. Using (2.17),

$$Ra_c = \frac{Ra_0}{1 - B/B_{lim}}, \tag{2.25b}$$

FIGURE 4. Active layer in the stratified regime. The solid line shows the effective transition and the dashed line corresponds to $Ra_1 = Ra_2$.
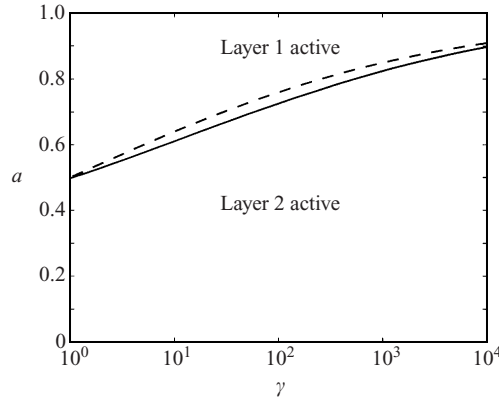
where $B_{lim} = 1/\beta$ (figure 2). The two constants entering (2.25b) are function of a and γ. $B_{lim}(\gamma, a)$ corresponds to the point where the chemical stratification becomes too important to be reversed by any thermal effect, and so the oscillatory regime disappears ($Ra_c \to \infty$). $Ra_0(\gamma, a)$ corresponds to the limit where B tends towards 0, and the oscillatory mode transforms itself into the classical steady ($\omega \to 0$) whole layer mode with a viscosity jump, since no chemical stratification acts against the thermal destabilization.

2.2.3. *Influence of a and γ*

(a) Stratified regime: the stratified regime is independent of the buoyancy ratio B. Therefore, the individual Rayleigh numbers of each layer are helpful to describe the dynamics:

$$Ra_1 = \frac{a^4}{\gamma} Ra \quad \text{and} \quad Ra_2 = (1-a)^4 Ra. \tag{2.26}$$

When the two layers have the same thickness ($a = 0.5$), the onset of convection is determined by the layer with the greater Rayleigh number, as already shown by Rasenat *et al.* (1989). When the depth ratio $a \neq 0.5$, the active layer (i.e. where the velocity is maximum) is not always the one with the higher Rayleigh number Ra_i, for it is easier for a viscous layer to entrain a less viscous layer than the reverse (figure 4).

In all cases, the convective motion wavelength is, at first order, proportional to the thickness of the active layer (figure 5b). Convection in the other layer is passive, being viscously driven only, and becomes more and more sluggish as the viscosity ratio increases. As γ becomes infinite (typically $\gamma > 100$), the more viscous layer behaves almost rigidly, and the critical Rayleigh number of the system increases towards an asymptotic value which corresponds to a layer of fluid below a slab of finite conductivity (Nield 1968) (figures 6a and 6c).

According to marginal stability analysis, the coupling between the two layers is always viscous, irrespective of the vertical temperature profile. For $\gamma = 1$ and $a = 0.5$, the temperature perturbation changes sign at the interface $z = 0$. As γ increases, the depth where the temperature perturbation θ changes sign moves into the most viscous layer, so that for $a = 0.5$ and $\gamma > 5$, the vertical temperature profile is correlated over the whole depth (a situation usually encountered when the two layers are 'thermally coupled') although the motions in the layers are still viscously coupled. To reconcile
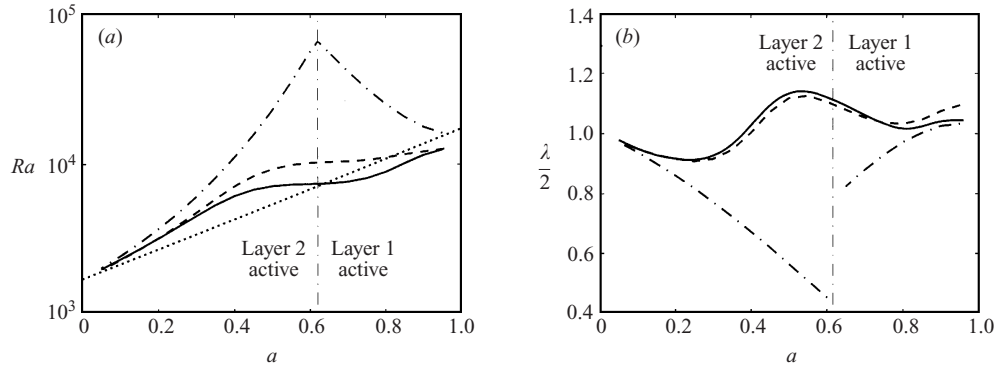
FIGURE 5. (a) Critical Rayleigh number and (b) half-wavelength as a function of the layer depth ratio for a fixed value of the viscosity ratio ($\gamma = 10$). Dash-dotted lines correspond to the stratified regime, dashed lines to the oscillatory regime when $B = 0.10$ and solid lines to the steady whole-layer regime ($B = 0$). The dotted line represents the fit according to (2.30a): in the case $\gamma = 10$, 'vertical' oscillations are predominant for almost all values of the layer depth ratio and the simple law (2.30a) reproduces numerical results within 30%.
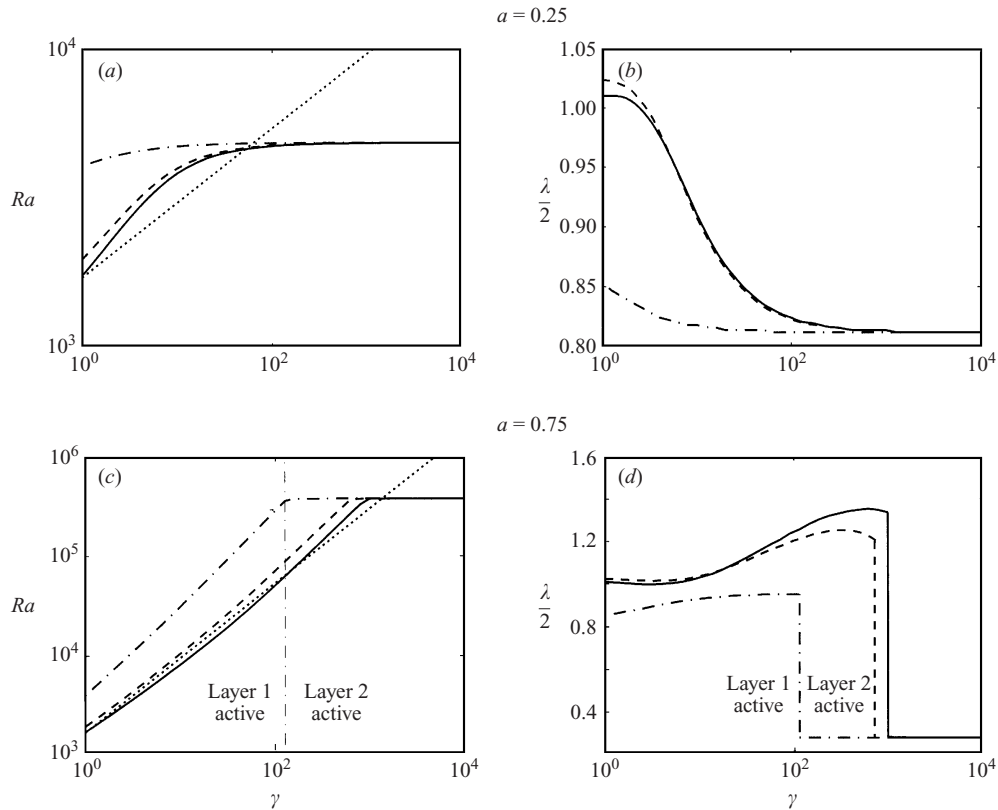
FIGURE 6. (a, c) Critical Rayleigh number and (b, d) half-wavelength as a function of the viscosity ratio for fixed values of the layer depth ratio. Dash-dotted lines correspond to the stratified regime, dashed lines to the oscillatory regime when $B = 0.10$ and solid lines to the steady whole-layer regime ($B = 0$). The dotted line represents the fit according to (2.30a): in the case $a = 0.75$, 'vertical' oscillations take place for $\gamma < 10^3$ and the simple law (2.30a) reproduces numerical results within 30%; on the other hand, for $a = 0.25$, 'horizontal' oscillations take place very rapidly and (2.30a) therefore is of no use for $\gamma > 10$.
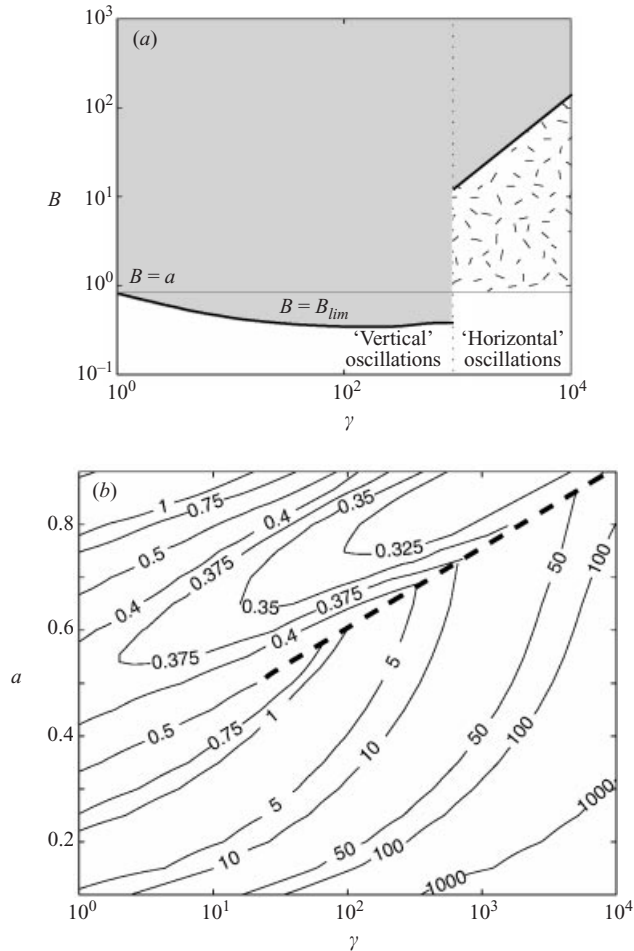
FIGURE 7. (a) B_{lim} as a function of the viscosity ratio for $a = 0.75$; the white domain corresponds to oscillations with an unstable whole-layer density profile ($B < a$ or $B < 1 - a$) and the hatched domain to oscillations with a stable whole-layer density profile ($B > a$ and $B > 1 - a$). In the grey domain, oscillations are impossible. (b) Contour plot of B_{lim}; the dashed line follows the discontinuity observed in (a).

the viscous coupling at the interface with the vertical thermal structure where the temperature perturbation does not change sign throughout the whole tank depth, a third roll sometimes appears in the passive layer. For finite-amplitude perturbations or well above criticality, it is thus expected that both temperature and motions will be thermally coupled for $\gamma > 5$. This has been seen experimentally by Rasenat *et al.* (1989) and in finite-amplitude calculations by Cserepes *et al.* (1988).

(b) Oscillatory regime: depending on the value of γ, two types of oscillations can appear, corresponding to two different mechanisms. When the viscosity contrast is not too high, oscillations are due to the opposite effects of chemical and thermal density anomalies, as previously described: the whole-layer density profile is unstable for all values of $B < B_{lim}$ (figure 7), and a Rayleigh–Taylor overturn takes place, leading to convection over the whole depth (figure 8a). As a result, the interface velocity is high (figure 9) and the horizontal wavelength comparable to the tank thickness (figures 5b, 6b and 6d). These whole depth convective oscillations will be referred to
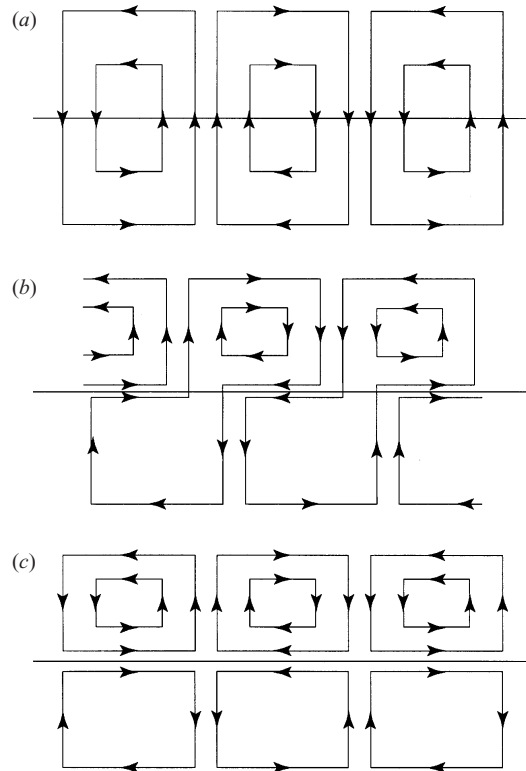
FIGURE 8. Sketch of streamlines in the case of (*a*) 'vertical' oscillations, (*b*) 'horizontal' oscillations and (*c*) stratified regime.

as 'vertical' oscillations. In this case, it is interesting to define an equivalent viscosity of the two-fluid system, for instance

$$v_{eq} \sim v_1^a \times v_2^{1-a} \tag{2.27}$$

and an equivalent Rayleigh number

$$Ra_{eq} = Ra\,\frac{v_2}{v_{eq}} \sim Ra \times \gamma^{-a}. \tag{2.28}$$

When chemical effects vanish ($B = 0$), convection in the two-layer system is identical to the classical convection in the one-fluid equivalent system: according to Chandrasekhar (1961), the onset is defined by

$$Ra_{eq} = 1707.76. \tag{2.29}$$

This means for the two-layer system

$$Ra_0 \sim 1707.76 \times \gamma^a \tag{2.30a}$$

and using (2.25*b*),

$$Ra_c \sim \frac{1707.76}{1 - B/B_{lim}} \times \gamma^a. \tag{2.30b}$$

Although the values of Ra_0 calculated from the complete resolution of (2.7)–(2.21) span over two orders of magnitude, (2.30*a*) predicts them within 30% (figures 5*a*
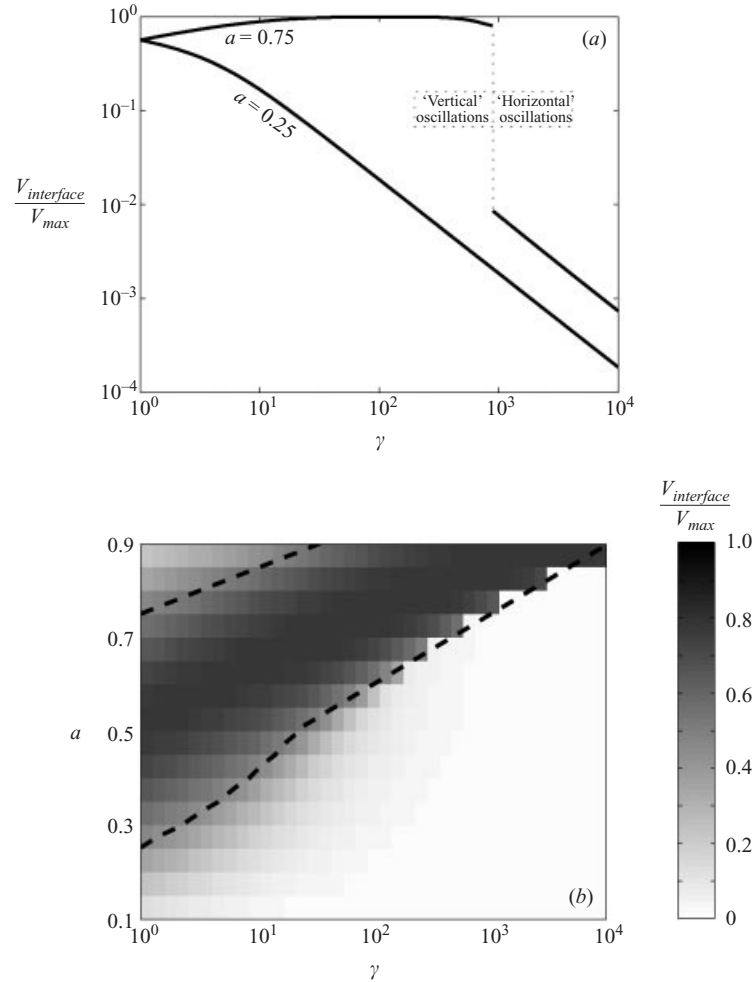
FIGURE 9. Ratio of vertical interface velocity to maximum vertical velocity (a) for two fixed values of layer depth ratio and (b) over the whole range of viscosity and layer depth ratios. The dashed line corresponds to $B_{lim} = \max(a, 1 - a)$: low interface velocities are systematically associated with stable whole-layer density profiles.

and 6c). The approximations (2.30a) and (2.30b) are valid when 'vertical' oscillations occur, i.e. in the domain of (γ, a) outlined on figure 9(b).

On the other hand, when the viscosity ratio increases, the interface acts like a barrier: vertical motions are deflected, and the streamlines become more and more concentrated in the less viscous layer (figure 8b). This behaviour is reminiscent of thermal convection in a fluid whose viscosity depends strongly on temperature, where convection occurs in a sublayer over which the viscosity ratio is less than 100 (Stengel, Olivier & Broker 1982; Richter, Nataf & Daly 1983; Davaille & Jaupart 1993). The wavelength of the convective pattern thus decreases from a value comparable to the full thickness of the tank to a value comparable to the thickness of layer 2 (figures 6b and 6d): convection does not develop over the whole depth but only in the less viscous layer, the more viscous one being slightly perturbed by thermal coupling at the interface. The system thus tends towards the previously described stratified regime where the less viscous fluid is the active layer: the critical Rayleigh number smoothly

increases towards the asymptotic value for the stratified regime (figures 6*a* and 6*c*), while the time frequency of the oscillations tends towards 0. Moreover, the maximum vertical velocity scales as the typical convective velocity in layer 2

$$V_{max} \sim \frac{\alpha g \Delta T_2 d_2^2}{\nu_2},\tag{2.31}$$

where ΔT_2 is the temperature difference across layer 2, whereas the interface velocity is limited by the penetration of this thermal instability in the viscous layer, thus scaling as

$$V_{interface} \sim \frac{\alpha g \Delta T_2 d_2^2}{\nu_1}.\tag{2.32}$$

As a result, the ratio $V_{interface}/V_{max}$ rapidly decreases as γ^{-1} (figure 9*a*). Simultaneously, B_{lim} significantly increases and becomes larger than a and $1-a$: oscillations are possible with a stable whole-layer density profile (figure 7). Oscillations still exist because of the opposite effects of thermal and viscous coupling that decorrelate horizontal motions around the interface. The mechanism of these 'horizontal' oscillations is thus comparable to the oscillatory coupling instabilities described by Rasenat *et al.* (1989) in the absence of interface deformation.

The transition between 'vertical' and 'horizontal' oscillations is continuous for $a \leqslant 0.5$ (figures 6*a* and 6*b*). In this case, motion in the less viscous thicker layer slightly precedes motion in the other one: it thus initiates oscillations, which are progressively confined as γ increases. For $a \geqslant 0.5$, the transition is sharp (figures 6*c* and 6*d*). 'Vertical' oscillations are first initiated by the viscous thicker layer, but as γ increases, this fluid becomes too rigid to move: 'horizontal' oscillations initiated by the other fluid then take place.

When a tends towards 0 or 1, the proximity of the outer boundary prevents the interface from oscillating, and the oscillatory mode transforms itself into the classical steady ($\omega \to 0$) one-layer mode. As shown in figure 5, the wavenumber tends towards 3.12, corresponding to $\lambda/2 \approx 1$, whereas Ra_c tends towards 1707.76 for $a \to 0$ and towards $1707.76 \times \gamma$ for $a \to 1$ (because our scaling uses the viscosity of layer 2).

2.3. *Development of the oscillatory regime*

Besides marginal stability, it is also interesting to determine the behaviour of the most unstable oscillatory mode for given γ, a, B, Ra. In this case, the roots of the determinant are now sought in the (σ, ω) space, the wavenumber k being fixed to the value determined by marginal stability. Starting from the neutral curve and increasing Ra, we observe that the growth rate σ progressively increases, whereas the frequency of the oscillations ω rapidly decreases and finally vanishes for $Ra > Ra_{lim}(B)$ (figure 10): thermal effects are then high enough permanently to reverse the chemical stratification, and the oscillatory regime is transformed into a steady whole-layer mode, as already noted when $B = 0$.

3. Laboratory experiments

3.1. *Experimental set-up*

We performed laboratory experiments in which two superimposed layers of viscous fluids, initially isothermal at T_0, are suddenly cooled from above and heated from below. The fluids are mixtures of water, salt for density control and cellulose for viscosity control. The density, viscosity and depth of each fluid as well as the boundary

γ	a	B	Ra
1 to 6×10^4 $\pm 50\%$	0.03 to 0.97 $\pm 5\%$	0.048 to 4.4 $\pm 1\%$	6.7×10^3 to 6.1×10^8 $\pm 25\%$

TABLE 1. Range and accuracy of experiments dimensionless numbers.
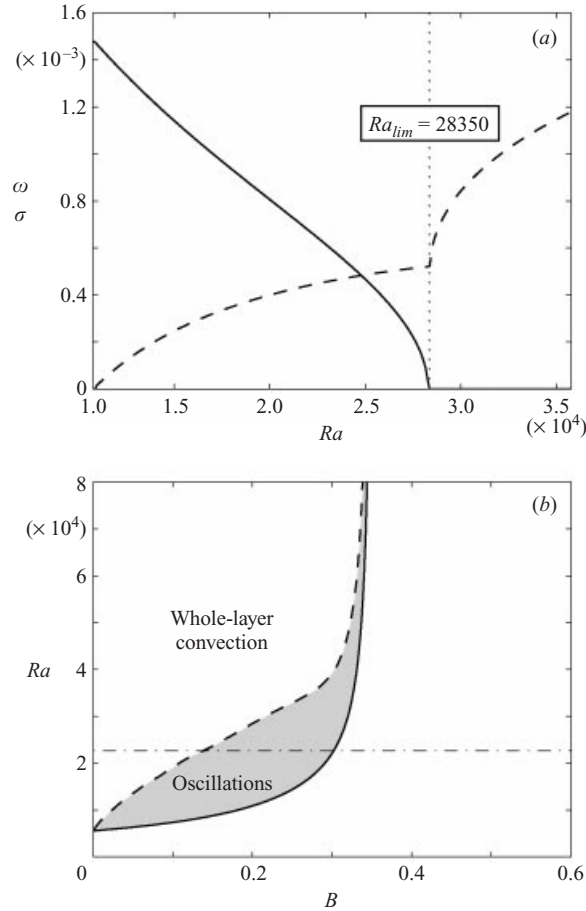
FIGURE 10. Development of the oscillatory regime in the case $\gamma = 6.7$, $a = 0.5$. (a) Evolution of the temporal periodicity ω (solid line) and the growth rate σ (dashed line) when Ra is progressively increased from the marginal stability value at $B = 0.20$. (b) Boundary between oscillatory and whole-layer regimes: the solid line corresponds to the neutral curve of the oscillatory regime and the dashed line to $Ra = Ra_{lim}(B)$. The neutral curve of the stratified regime is also reported (dash-dotted line).

temperatures are measured for each experiment, in order to determine the characteristic dimensionless numbers. Variation ranges and accuracy are listed in table 1. The only major uncertainty comes from the viscosity measurements (accuracy of 25%). However, as demonstrated by the linear study, changes in γ over the error range have a minor influence on the dynamics. Prandtl numbers in each layer are always greater than 100 to ensure that inertial effects are non-existent (Krishnamurti 1970). The liquids are miscible in all proportions and the temperature-dependence of the

Exp. number	γ	a	B	B_c	Ra	$Ra_c(B)$	$Ra_{lim}(B)$	Behaviour
2	12.5	0.5	0.26	0.28	2.2×10^4	2.1×10^4	3.3×10^4	osc.
3	12	0.5	0.18	0.28	5.2×10^4	1.4×10^4	3.0×10^4	whole layer
7	149	0.75	0.24	0.25	4.2×10^5	2.9×10^5	4.3×10^5	osc.
45	1.3	0.44	0.10	0.32	6.8×10^3	2.7×10^3	6.6×10^3	whole layer
46	1.1	0.44	0.048	0.32	6.7×10^3	2.0×10^3	4.0×10^3	whole layer
47	6.7	0.5	0.20	0.30	1.8×10^4	1.1×10^4	2.8×10^4	osc.

TABLE 2. Dimensionless parameters and behaviour of the experiments close to marginal stability. B_c and $Ra_c(B)$ are the theoretical values of critical buoyancy and Rayleigh numbers; $Ra_{lim}(B)$ is the calculated value where oscillations are replaced by steady whole-layer convection (see §2.3).

viscosity is negligible compared to its composition-dependence. The high viscosities render diffusion of salt across the interface extremely slow compared to the characteristic time scale of the instabilities (Davaille 1999a). Moreover, to be able to compare the experimental results with the linear stability analysis, we consider here only the experiments where the initial density stratification is sharp. Heat and mass transfer are monitored over time by measuring temperature profiles and the densities of both layers. More details can be found in Davaille (1999a).

Since the fluids are miscible in all proportions, slow mixing by mechanical entrainment occurs through the interface and the characteristics of convection (thermal structure, regime, etc.) evolve through time, from two-layer to classical Rayleigh–Bénard convection. However, typical mixing times are at least one order of magnitude greater than thermochemical time scales. We focus hereafter on the early stages of the experiments.

3.2. *Close to marginal stability*

Six of our experiments were close to marginal stability (see table 2). Since the stratified case is well-documented (Richter & McKenzie 1981; Busse 1981; Cserepes & Rabinowicz 1985; Ellsworth & Schubert 1988; Cserepes *et al.* 1988; Sotin & Parmentire 1989), we concentrated on the oscillatory regime. The onset of all experiments is always the same. First a linear temperature profile progressively sets in the tank by heat diffusion: the thermal structure at onset is thus exactly the same as our theoretical study. Provided $Ra > Ra_c(B)$, convection then begins and the interface deforms in large domes with a horizontal wavelength comparable to twice the tank depth (figure 11a), as predicted by the marginal stability analysis (figure 3b and table 3). These domes progressively rise, and finally reach the cold plate where they begin to cool down and become heavier. Two behaviours can then occur:

(i) When domes do not spread under the cold plate, no large-scale stirring operates: the two fluids remain separate, and oscillations begin (figure 11b). Large temperature variations are recorded. Their periodicities are in good agreement with the theory (figure 3c and table 3). Only travelling waves are observed, because the horizontal dimension of our tank is not a multiple of the horizontal wavelength of the flow (tank 30 cm wide for typical periodicities of 12 cm or 16 cm).

(ii) When domes spread under the cold plate, stirring operates from the first oscillation: fluid 1 sinks back while entraining part of the other fluid, leading to a spiral pattern (figure 11c). Steady convection thus takes place over the whole depth of the tank. However, we observed in oscillatory experiments that the temperature

(a)

Cold plate

8 cm

Fluid 2
Probe
Fluid 1

Hot plate

Travelling

(b)

First oscillation
period = 200 min

Linear T^0
profile

(c)

Half oscillation
period = 2×100 min

Linear T^0
profile
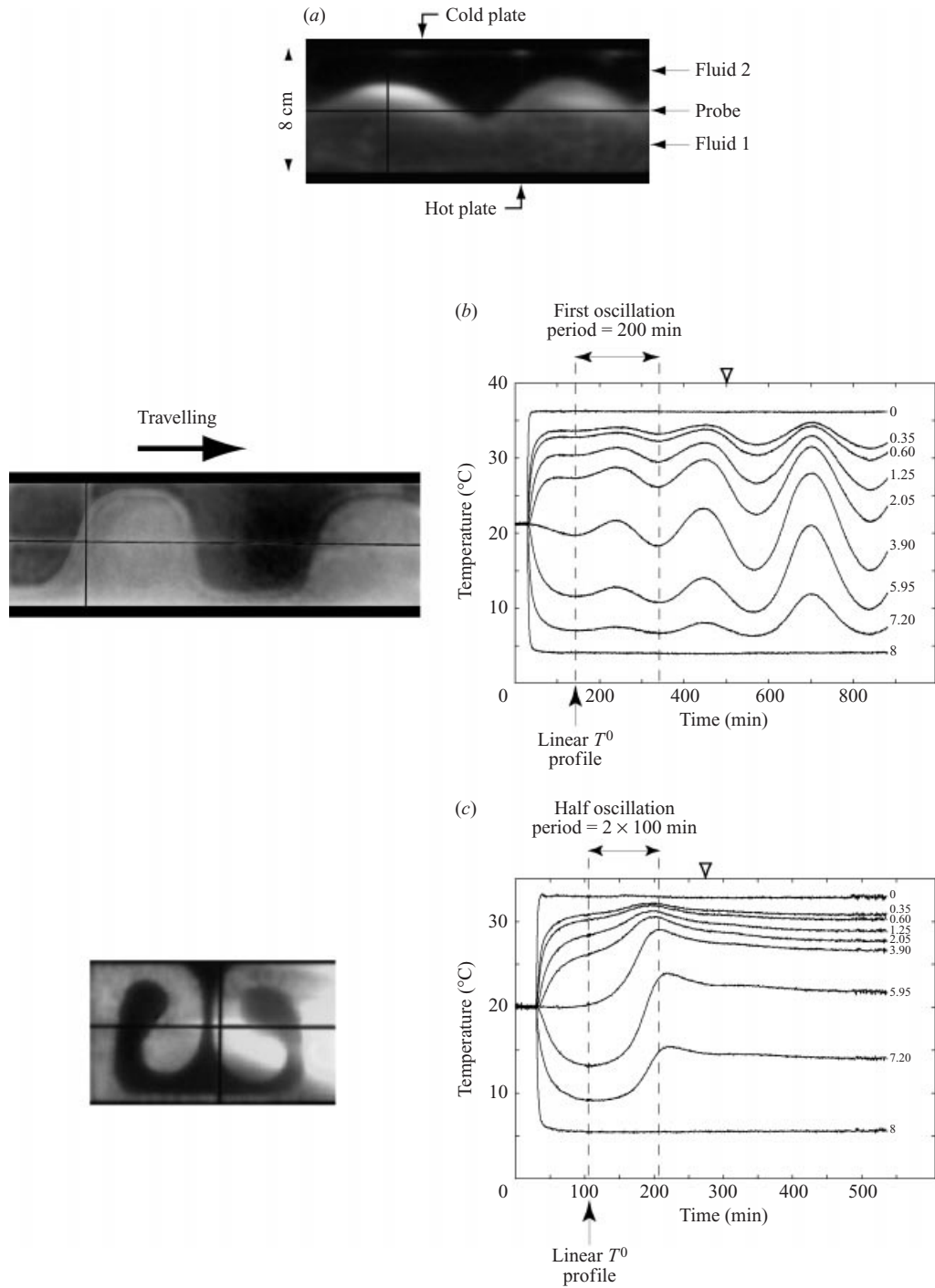
FIGURE 11. (a) Onset of convection, characteristic of all experiments close to marginal stability. (b) Picture and vertical temperature signal of experiment 47, where travelling waves were observed during more than 24 hours and (c) the same for experiment 46, where whole-layer convection took place. Positions of the vertical thermocouples (in cm) are reported in the right of the temperature signals and triangles show the time when photos were taken.

Exp. number	$\lambda_e/2$	$\lambda_{ms}/2$	ω_e	ω_{ms}
2	1.1	1.1	8.5×10^{-4}	7.8×10^{-4}
3	1.1	1.1	9.0×10^{-4}	9.3×10^{-4}
7	1.0	0.98	8.4×10^{-5}	7.6×10^{-5}
45	0.91	1.0	3.4×10^{-3}	3.6×10^{-3}
46	0.93	1.0	3.3×10^{-3}	3.1×10^{-3}
47	1.0	1.1	1.3×10^{-3}	1.5×10^{-3}

TABLE 3. Horizontal wavelengths and temporal frequencies of the experiments close to marginal stability. Subscript e stands for experimental values, and ms for marginal stability. Temporal frequencies are determined using the temperature signal in the tank; for spiral patterns, a virtual period is deduced from the first half of the oscillation (accuracy $\pm 25\%$). Horizontal wavelengths are determined using an horizontal temperature profile at the beginning of interface deformation (accuracy $\pm 10\%$).

signal is symmetrical (figure 11b): the time for domes to rise is equal to half a period. So one can deduce from the temperature signal of steady whole-layer experiments an extrapolated temporal periodicity, which also shows good agreement with the theoretical value (table 3).

Which behaviour will actually prevail depends on the relative values of thermal and chemical density anomalies, as already described in §2.3: when thermal effects are strong compared to chemical stratification (high Ra or small B), whole-layer convection takes place instead of oscillations.

Care is required to extrapolate the linear study results to experiments, in particular because of the theoretical assumption that the interface deformation remains small. But it is noticeable that the mode excited in these experiments is exactly the one determined by the marginal stability analysis. Moreover, the further development of the selected mode is also predicted: the calculated values of Ra_{lim} separating whole-layer convection from oscillations are in good agreement with observations (table 2). This was also observed by Schmeling (1988) in numerical simulations for $\gamma = 1$, $a = 0.5$ (figure 12).

3.3. Stability of two-layer convection

When the Rayleigh number is high compared to the critical value, finite-amplitude effects are so important that typical scales of convection can no longer be derived from the marginal stability analysis. However, the two convective regimes are still observed (Olson & Kincaid 1991; Davaille 1999b): we can thus use the linear theory to solve two problems for each experiment, namely which regime develops first and which regime remains once the temperature gradient is established.

3.3.1. Onset of instability

The thermal structure at $t = 0$ in our tank is different from the initial linear temperature profile of the marginal stability: in the experiments, the two fluids are initially at the same temperature T_0, and then suddenly heated from below and cooled from above. Thermal boundary layers subsequently grow symmetrically from the hot and cold plates, until the first convective feature appears. We observed two types of onset:

(a) the deformation of the interface over a large scale (several centimetres), corresponding to the oscillatory regime;

(b) the appearance of small (less than one centimetre) short-lived plumes coming
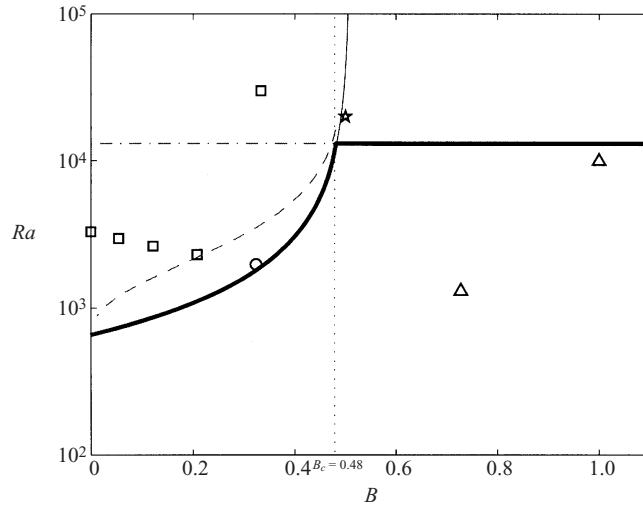
FIGURE 12. Numerical simulations by Schmeling (1988) for $\gamma = 1$, $a = 0.5$: squares correspond to whole-layer convection, the star to the stratified regime, the circle to oscillations and triangles to no convection. Results of the linear study are also reported: the dash-dotted line corresponds to the stratified regime, the solid line to the oscillatory regime. The bold solid line follows the most unstable regime and the dashed line $Ra = Ra_{lim}(B)$.

from the destabilization of one of the outer thermal boundary layers (Olson 1984; Davaille 1999*a*). Those plumes correspond to thermal convection in a sublayer, and thus to the stratified regime.

In order to follow the evolution of the experiment during the setting of the temperature gradient, we can calculate an effective Rayleigh number based on the typical length scale of thermal effects

$$Ra_{eff} = \frac{\alpha g \Delta T (2\delta)^3}{\kappa \nu_2} = Ra \left(\frac{2\delta}{d} \right)^3, \tag{3.1}$$

where δ is the theoretical size of a thermal boundary layer growing by conduction. Since the chemical stratification is already established over the whole tank depth (fixed R_s), the corresponding effective buoyancy number is

$$B_{eff} = \frac{R_s}{Ra_{eff}} = B \left(\frac{d}{2\delta} \right)^3. \tag{3.2}$$

In the (B, Ra) space, the experiment thus follows the curve

$$Ra_{eff} = Ra \frac{B}{B_{eff}}, \tag{3.3}$$

and the onset of convection is determined by the first intersection of this curve with the curve of marginal stability (figure 13). The oscillatory regime can be triggered when $Ra \geqslant Ra_c(B)$, and the intersection corresponds to

$$Ra_{eff} = Ra_c(B_{eff}). \tag{3.4}$$

This means, using (2.25*b*),

$$Ra_{eff} = Ra_0 + \frac{B}{B_{lim}} Ra \Leftrightarrow \delta_{osc} = \frac{d}{2} \left(\frac{Ra_0}{Ra} + \frac{B}{B_{lim}} \right)^{1/3}. \tag{3.5}$$
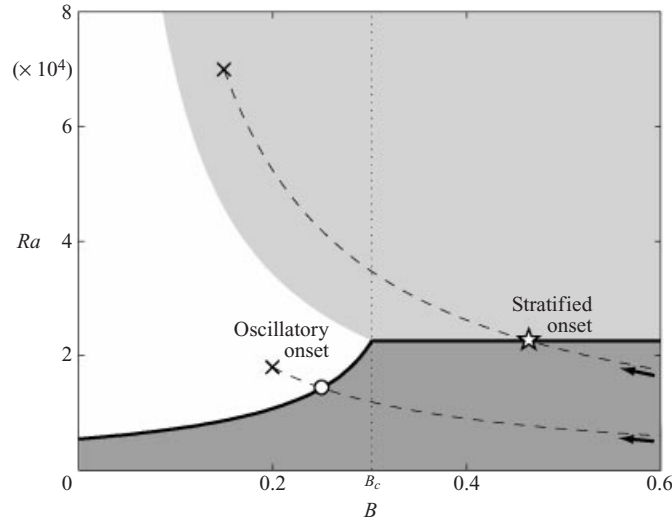
FIGURE 13. Onset of convection in the (B, Ra) space for $\gamma = 6.7$, $a = 0.5$. In the dark grey domain no convection develops, whereas in the white domain the oscillatory regime sets in first and in the light grey domain the stratified regime sets in first. The dashed lines represent the time evolution of two possible experiments during the setting of the temperature gradient: the onset of convection corresponds to their first intersection with the neutral curve of marginal stability (bold solid line).

The stratified regime can be triggered when $Ra \geqslant Ra_{strat}$, and the intersection corresponds to

$$Ra_{eff} = Ra_{strat} \Leftrightarrow \delta_{strat} = \frac{d}{2}\left(\frac{Ra_{strat}}{Ra}\right)^{1/3}. \tag{3.6}$$

We can however notice that for very large values of layer Rayleigh number ($Ra_i > 10^5$ typically), the corresponding thermal boundary layer will be destabilized before 'seeing' the interface and the second fluid, following Howard's mechanism for purely thermal plumes (Howard 1964): the onset will thus be given by

$$\delta_{strat} = d_i \left(\frac{1100.67}{Ra_i}\right)^{1/3}. \tag{3.7}$$

Since the thermal boundary layer initially grows by conduction, the first convective motion corresponds to the smallest δ. Depending on the relative value of B and Ra, this defines three different domains (figure 13):

no convection when $Ra < Ra_{strat}$ and $Ra < Ra_c(B)$;
oscillatory regime sets in first when $\delta_{osc} < \delta_{strat}$;
stratified regime sets in first when $\delta_{osc} > \delta_{strat}$.

All experiments agree well with this model, independently of the relative value of B and B_c (figure 14). The convective history of each experiment must thus be divided into two independent steps: first, the temperature gradient is progressively established over the tank depth, and effective values (B_{eff}, Ra_{eff}) determine which regime starts first; but as soon as this convective motion appears, (B_{eff}, Ra_{eff}) are meaningless, and global values (B, Ra) must be used.
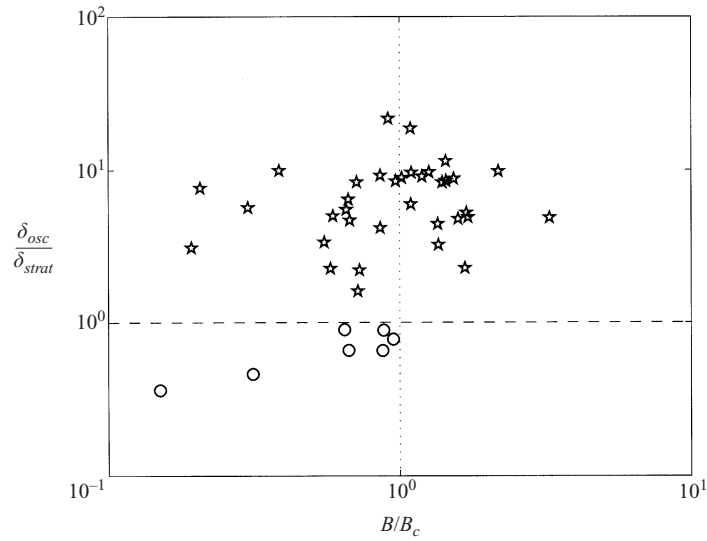
FIGURE 14. Observed onset for all experiments as a function of the ratio $\delta_{osc}/\delta_{strat}$. Stars correspond to experiments where small plumes start first (stratified regime), and circles to experiments where large domes start first (oscillatory regime).
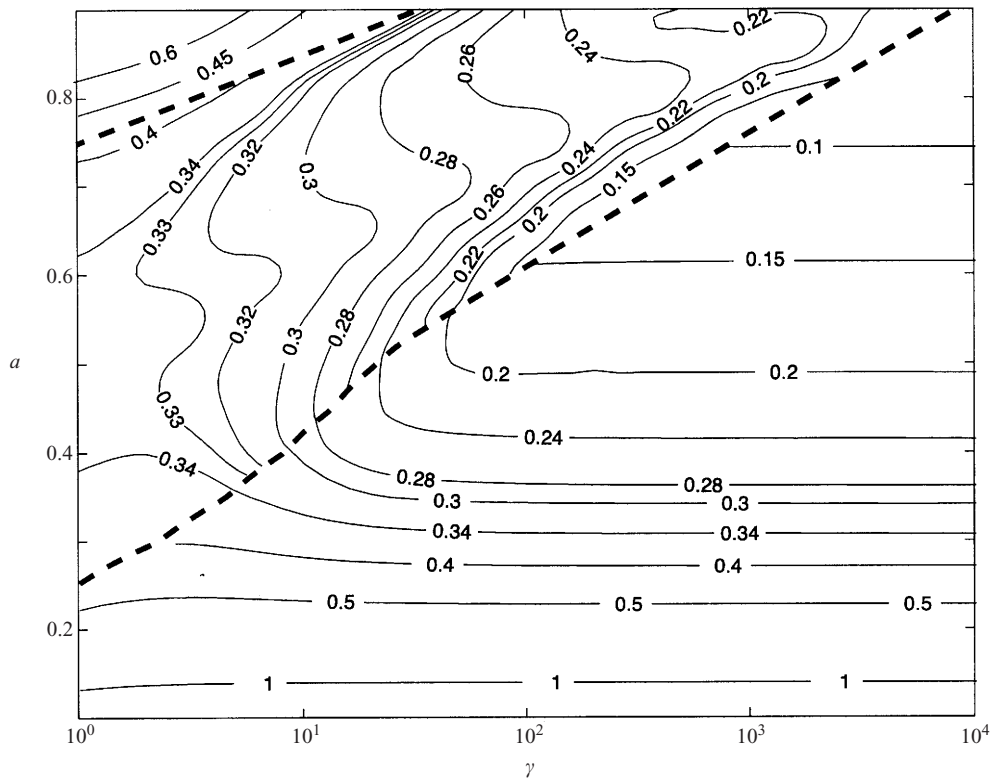

FIGURE 15. Calculated $B_c(\gamma, a)$ over the whole parameter space. The dashed line corresponds to $B_{lim} = \max(a, 1 - a)$, thus to the limit between 'vertical' and 'horizontal' oscillations (see § 2.2.3).
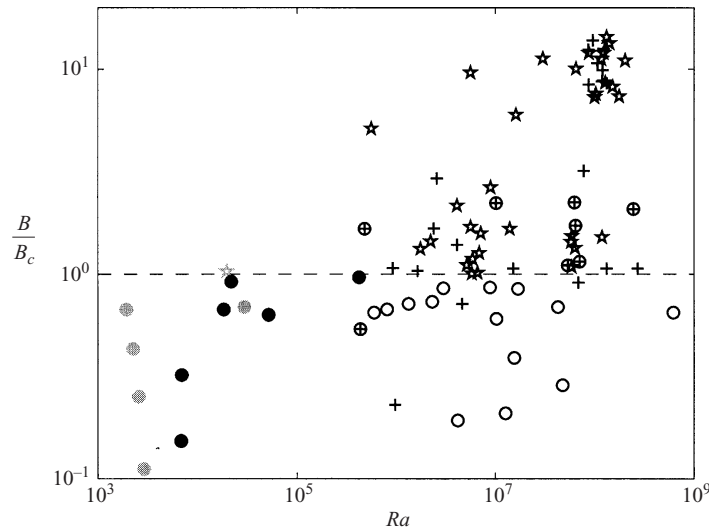
FIGURE 16. Observed persistent regime as a function of the ratio B/B_c. Experiments corresponding in marginal stability to 'vertical' oscillations are shown by stars when the interface remains stable and circles when the interface deforms in large domes (open circles denote experiments where domes appear after a stratified onset). Experiments corresponding in marginal stability to 'horizontal' oscillations are shown by crosses when the interface remains stable and cross-circles when the interface deforms in large domes. Numerical simulations by Schmeling (1988) are also reported in grey.

3.3.2. Oscillatory whole-layer versus steady stratified regimes

According to the linear stability analysis, which thermochemical regime is the most unstable depends on the relative value of the buoyancy number B and the critical buoyancy number $B_c(\gamma, a)$ (figure 2). In the experiments, once the convection has begun, we can thus try to determine whether the interface will be deformed or not by comparing the values of the experimental B and the theoretical $B_c(\gamma, a)$ (figure 15). Figure 16 shows for all experiments the nature of the observed regime depending on the ratio $B/B_c(\gamma, a)$. The agreement between theory and observations is quite good, except for some points corresponding in marginal stability to 'horizontal' oscillations (see §2.2.3): this is due to the difficulty in extrapolating linear theory results to experiments. We can reasonably suppose that 'vertical' oscillations characterized in the linear study by high interface velocities and whole-layer instable density profiles will effectively lead to the formation of large domes over the whole tank depth: indeed, all corresponding experiments agree well with the theory. However, in the case of 'horizontal' oscillations, which are due to opposite effects of viscous and thermal coupling, the linear theory predicts low interface velocities as well as stable whole-layer density profiles: a finite-amplitude study would thus be necessary to know whether the predicted interface oscillations will give rise to an effective large-scale deformation, but this is beyond the scope of this paper.

We can however notice that the theoretical B_c for 'vertical' oscillations varies in the limited range 0.2–0.4 over the whole parameter space (figure 15). These typical values also seem to be relevant for the experiments with large viscosity contrast and/or a thin layer, where 'vertical' oscillations are observed experimentally for B between 0.093 and 0.33, whereas the interface remains stable for B larger than 0.32.

4. Conclusion

The influence of a contrast in viscosity on the linear stability of two-layer thermal convection in the presence of stable density stratification has been investigated. Depending on the buoyancy number, the ratio of the stabilizing chemical density anomaly to the destabilizing thermal density anomaly, two regimes are found: (i) for $B < B_c(\gamma, a)$, an oscillatory regime where vertical motion exists at the interface; and (ii) for $B > B_c(\gamma, a)$, a steady two-layer regime where there is no vertical motion at the interface. Laboratory experiments agree well with this simple rule, even at high Rayleigh number. In the experiments however, the initial convective regime can be different from the final state, since the temperature gradient responsible for the thermal density contrast is progressively imposed on initially isothermal fluids, whereas the chemical density contrast is already present. During this transient state, local values of the parameters must be used.

This study has focused on the early stages of the experiments, but since the fluids are miscible, the characteristics of convection evolve through time. The description of the stratified regime can be found in Davaille (1999a); the next problem is thus fully to describe the behaviour of oscillatory domes as well as the mixing between the two layers. It is however already apparent that even density contrasts smaller than 1% can radically change the dynamics of convection, particularly if it is coupled with a viscosity contrast.

Appendix. Determinant for rigid boundaries

A homogeneous system of twelve equations in twelve unknowns is obtained by substituting the expansions (2.20) into the boundary conditions (2.7)–(2.8) and (2.10)–(2.15). The coefficient matrix is

$$
\left|
\begin{array}{cc}
1 & 0 \\
\pm q_{1j} & 0 \\
(q_{1j}^2 - k^2)^2 & 0 \\
0 & 1 \\
0 & \pm q_{2j} \\
0 & (q_{2j}^2 - k^2)^2 \\
e^{\pm q_{1j}a} & -e^{\pm q_{2j}(1-a)} \\
\pm q_{1j}\,e^{\pm q_{1j}a} & \pm q_{2j}\,e^{\pm q_{2j}(1-a)} \\
\gamma(q_{1j}^2 + k^2)\,e^{\pm q_{1j}a} & -(q_{2j}^2 + k^2)\,e^{\pm q_{2j}(1-a)} \\
\pm q_{1j}s\gamma(q_{1j}^2 - 3k^2)\,e^{\pm q_{1j}a} & (\pm q_{2j}s(q_{2j}^2 - 3k^2) - k^2 B)\,e^{\pm q_{2j}(1-a)} \\
\gamma(q_{1j}^2 - k^2)^2\,e^{\pm q_{1j}a} & -(q_{2j}^2 - k^2)^2\,e^{\pm q_{2j}(1-a)} \\
\pm q_{1j}\gamma(q_{1j}^2 - k^2)^2\,e^{\pm q_{1j}a} & \pm q_{2j}(q_{2j}^2 - k^2)^2\,e^{\pm q_{2j}(1-a)}
\end{array}
\right.
$$

Each column in this matrix actually corresponds to six columns: the coefficients of the first column with the '+' sign correspond to unknowns $A_{1j}, 1 \leqslant j \leqslant 3$, and with the '−' sign to $B_{1j}, 1 \leqslant j \leqslant 3$; the coefficients of the second column with the '+' sign correspond to $A_{2j}, 1 \leqslant j \leqslant 3$, and with the '−' sign to $B_{2j}, 1 \leqslant j \leqslant 3$.

REFERENCES

ANDERECK, C. D., COLOVAS, P. W. & DEGEN, M. M. 1996 Observations of time-dependent behavior in the two-layer Rayleigh–Bénard system. In *Advances in Multi-Fluid Flows* (ed. Y. Y. Renardy, A. V. Coward, D. Papageorgiou & S. M. Sun). SIAM.

BAINES, P. G. & GILL, A. E. 1969 On thermohaline convection with linear gradients. *J. Fluid Mech.* **37**, 289–306.

BUSSE, F. H. 1981 On the aspect ratio of two-layer mantle convection. *Phys. Earth Planet. Inter.* **24**, 320–324.

BUSSE, F. H. & SOMMERMANN, G. 1996 Double-layer convection: a brief review and some recent experimental results. In *Advances in Multi-Fluid Flows* (ed. Y. Y. Renardy, A. V. Coward, D. Papageorgiou & S. M. Sun). SIAM.

CHANDRASEKHAR, S. 1961 *Hydrodynamic and Hydromagnetic Stability*. Dover.

CSEREPES, L. & RABINOWICZ, M. 1985 Gravity and convection in a two-layered mantle. *Earth Planet. Sci. Lett.* **76**, 193–207.

CSEREPES, L., RABINOWICZ, M. & ROSEMBERG-BOROT, C. 1988 Three-dimensional infinite Prandtl number convection in one and two layers with implications for the Earth's gravity field. *J. Geophys. Res.* **93**, 12009–12025.

DAVAILLE, A. 1999a Two-layer thermal convection in miscible fluids. *J. Fluid Mech.* **379**, 223–253.

DAVAILLE, A. 1999b Simultaneous generation of hotspots and superswells by convection in a heterogeneous planetary mantle. *Nature* **402**, 756–760.

DAVAILLE, A. & JAUPART, C. 1993 Transient high-Rayleigh number thermal convection with large viscosity variations. *J. Fluid Mech.* **253**, 141–166.

ELLSWORTH, K. & SCHUBERT, G. 1988 Numerical models of thermally and mechanically coupled two-layer convection of highly viscous fluids. *Geophys. J.* **93**, 347–363.

HANSEN, U. & YUEN, D. A. 1989 Subcritical double-diffusive convection at infinite Prandtl number. *Geophys. Astroph. Fluid Dyn.* **47**, 199–224.

HOWARD, L. N. 1964 Convection at high Rayleigh number. In *Proc. 11th Intl Congr. Appl. Mech.* (ed. H. Görtler), pp. 1109–1115. Springer.

JOSEPH, D. D. & RENARDY, M. 1993 *Fundamentals of Two-Fluids Dynamics*. Springer.

KRISHNAMURTI, R. 1970 On the transition to turbulent convection. *J. Fluid Mech.* **42**, 295–320.

NELDER, J. A. & MEAD, R. 1965 A simplex method for function minimization. *Computer J.* **7**, 308–313.

NIELD, D. A. 1968 The Rayleigh–Jeffreys problem with boundary slab of finite conductivity. *J. Fluid Mech.* **32**, 393–398.

OLSON, P. 1984 An experimental approach to thermal convection in a two-layered mantle. *J. Geophys. Res.* **89**, 11293–11301.

OLSON, P. & KINCAID, C. 1991 Experiments on the interaction of thermal convection and compositional layering at the base of the mantle. *J. Geophys. Res.* **96**, 4347–4354.

OLSON, P., SILVER, P. G. & CARLSON, R. W. 1990 The large scale structure of convection in the Earth's mantle. *Nature* **344**, 209–215.

RASENAT, S., BUSSE, F. H. & REHBERG, I. 1989 A theoretical and experimental study of double-layer convection. *J. Fluid Mech.* **199**, 519–540.

RENARDY, M. & RENARDY, Y. 1985 Perturbation analysis of steady and oscillatory onset in a Bénard problem with two similar liquids. *Phys. Fluids* **28**, 2699–2708.

RENARDY, Y. & JOSEPH, D. D. 1985 Oscillatory instability in a Bénard problem of two fluids. *Phys. Fluids* **28**, 788–793.

RICHTER, F. M. & JOHNSON, C. E. 1974 Stability of a chemically layered mantle. *J. Geophys. Res.* **79**, 1635–1639.

RICHTER, F. M. & MCKENZIE, D. P. 1981 On some consequences and possible causes of layered convection. *J. Geophys. Res.* **86**, 6133–6142.

RICHTER, F. M., NATAF, H. C. & DALY, S. F. 1983 Heat transfer and horizontally-averaged temperature of convection with large viscosity variations. *J. Fluid Mech.* **129**, 173–192.

SCHMELING, H. 1988 Numerical models of Rayleigh–Taylor instabilities superimposed upon convection. *Bull. Geol. Inst. Univ. Uppsala* **14**, 95–109.

SOTIN, C. & PARMENTIER, E. M. 1989 On the stability of a fluid layer containing a univariant phase transition: application to planetary interiors. *Phys. Earth Planet. Inter.* **55**, 10–25.

STENGEL, K. C., OLIVIER, D. S. & BROKER, J. R. 1982 Onset of convection in a variable-viscosity fluid. *J. Fluid Mech.* **120**, 411–431.

TACKLEY, P. J. 2000 Mantle convection and plate tectonics: toward an integrated physical and chemical theory. *Science* **288**, 2002–2007.

TURNER, J. S. 1979 *Buoyancy Effects in Fluids.* Cambridge University Press.

VERONIS, G. 1968 Effect of a stabilizing gradient of solute on thermal convection. *J. Fluid Mech.* **34**, 315–336.

Chapitre 2

Compléments à l'étude de stabilité marginale.

2.1 Influence of the variations of thermal expansion coefficient.

In addition to the marginal stability study presented in chapter 1, we can study the case where thermal expansion coefficients of layers 1 and 2 are different (respectively α_1 and α_2). The density profile corresponding to the linear temperature profile writes

$$\rho_i = \rho_{i_0} - \alpha_i \rho_0 ((T_1 - T_0) - (z + a)\Delta T), \tag{2.1}$$

where z is the height adimensionalized by H. The effective density contrast at the interface $(z = 0)$, taking into account both thermal and chemical effects, is then equal to

$$\Delta \rho_{interface} = \Delta \rho_\chi + (\alpha_2 - \alpha_1)\rho_0 ((T_1 - T_0) - a\Delta T). \tag{2.2}$$

In particular, one can notice that

$$\Delta \rho_{interface} < 0 \iff B < (\frac{T_1 - T_0}{\Delta T} - a) \times (\frac{\alpha_1}{\alpha_2} - 1), \tag{2.3}$$

where

$$B = \frac{\rho_{1_0} - \rho_{2_0}}{\alpha_2 \rho_0 \Delta T}. \tag{2.4}$$

The density profile is then unstable independently of convective effects, and the critical Rayleigh number is equal to 0 (figure 2.1a).

The main control parameter in a two-layer system is the buoyancy number B that appears in the continuity of normal stress (see equation (2.13) on page 67). In the present configuration, B is replaced by

$$\widetilde{B} = B + (\frac{T_1 - T_0}{\Delta T} - a) \times (1 - \frac{\alpha_1}{\alpha_2}). \tag{2.5}$$

As a first approximation, we can forget changes in α and use results from the previous chapter in remplacing B with $\widetilde{B}$ (figure 2.1a). Then,
  - a chemically unstable density profile, given by $B < 0$ when α is constant, now corresponds to $\widetilde{B} < 0$: this condition is similar to (2.3).
  - the critical value $\widetilde{B}_c$ separating stratified and whole-layer regimes depends on γ and a, but is almost independent on α_1/α_2. We then deduce from (2.5) that

$$\widetilde{B}_c = B_c(\frac{\alpha_1}{\alpha_2} = 1) \tag{2.6}$$

so

$$B_c(\frac{\alpha_1}{\alpha_2}) = B_c(\frac{\alpha_1}{\alpha_2} = 1) + (\frac{T_1 - T_0}{\Delta T} - a) \times (\frac{\alpha_1}{\alpha_2} - 1), \tag{2.7}$$

in good agreement with numerical results (figure 2.1b).

This simple linear study thus indicates that the physics of the problem is independent of the explicit variations in $\alpha(T)$: in our experiments, its mean value is used.
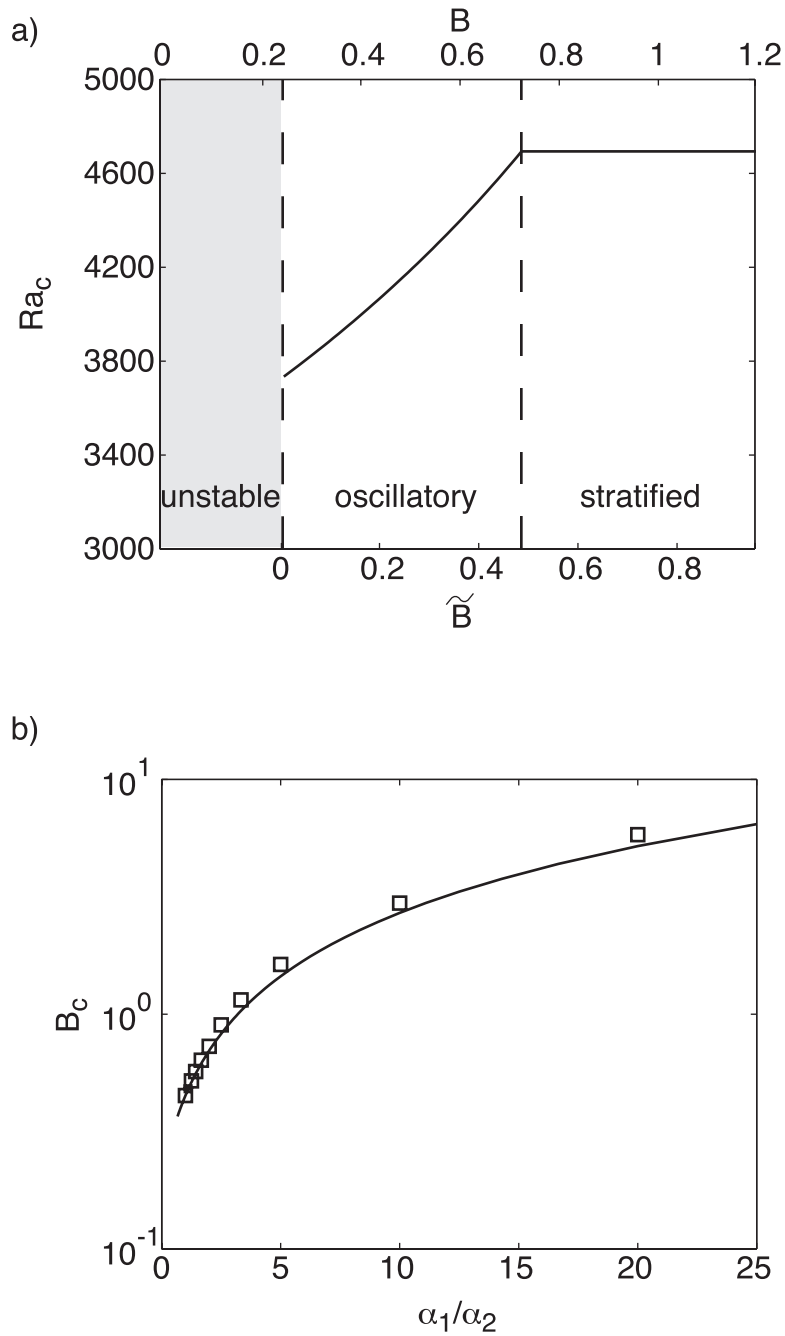
FIG. 2.1 – *a) Neutral curves of marginal stability analysis as a function de B and $\widetilde{B}$ in the case $\alpha_1/\alpha_2 = 2$, $\gamma = 10$, $a = 0.25$. b) B_c as a function of α_1/α_2 for $\gamma = 10$, $a = 0.25$: squares stand for calculated points and the solid line indicates the fit according to the law (2.7).*
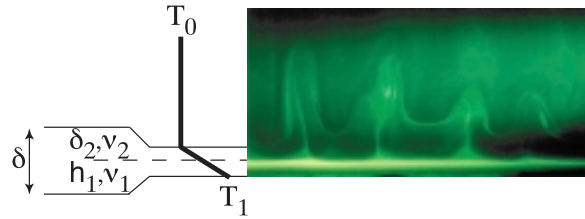
FIG. 2.2 – *Destabilization of a thin stratified lower layer: picture of the thermochemical plumes and sketch of the linear temperature profile in the thermal boundary layer.*

2.2   Application of the marginal stability analysis to the destabilization of a thin stratified layer.

Experiments of Anne Davaille & Fabien Girard focusing on the influence of a thin stratified layer (i.e. thinner than the thermal boundary layer) on the dynamics of plumes provide an excellent test for the marginal stability analysis (Davaille, Girard & Le Bars 2002). Starting from isothermal fluids, a thermal boundary layer progressively grows by conduction and becomes thicker than the stratified layer. The configuration is then locally similar to the one in the linear study presented above: two layers of fluid with different densities and viscosities are subjected to a linear temperature profile (figure 2.2); the only difference comes from the outer boundary conditions, which are rigid-free in the present case.

It is then possible to extend the phenomenological model of Howard (1964) to this two-layer system: we therefore define a local Rayleigh number

$$Ra_{local} = \frac{\alpha g (T_1 - T_0) \delta^3}{\kappa \nu_2} \qquad (2.8)$$

and suppose that plumes are generated as soon as Ra_{local} reaches a critical value Ra_c. The marginal stability analysis (modified for rigid-free boundary conditions) then indicates the values of Ra_c, which depend on the fixed viscosity contrast γ and on the time-decreasing local layer depth ratio $a_{local} = h_1/\delta$ (see for instance figure 2.3). As shown in table 2.1, measured and predicted values of δ are in good agreement.
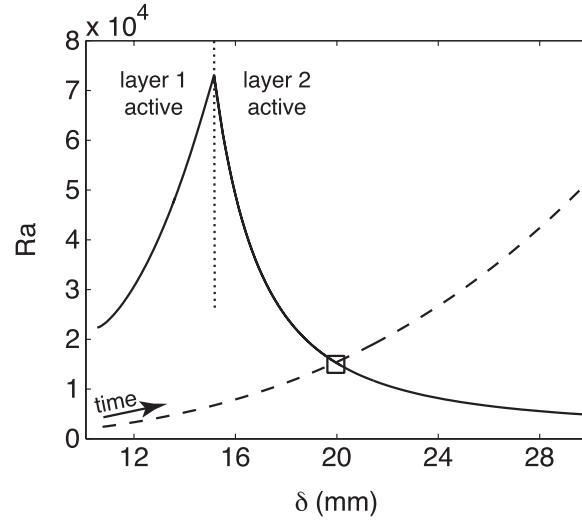
FIG. 2.3 – *Critical Rayleigh number (solid line) and local Rayleigh number (dashed line) as a function of the growing thermal boundary layer thickness δ for experiment $TL10$. The onset is shown by a square.*

n^o	Ra	a	γ	B	δ_{meas} (mm)	δ_{cal} (mm)
$TL10$	4.6×10^5	0.16	15	2.70	20 ± 4	19.7
$TL20$	7.0×10^5	0.090	24	2.47	17 ± 2	13.6
$TL30$	1.5×10^6	0.082	51	4.46	14.9	11.0
$TL40$	9.2×10^5	0.13	38	0.35	15.3	15.8
$TL60$	1.1×10^6	0.097	59	2.59	16.6	12.7
$TL100$	1.2×10^7	0.92	10.5	1.63	14.5	14.2
$TL200$	1.3×10^8	0.95	10.5	1.90	18.6	18.6
$TL300$	1.3×10^7	0.068	30	2.10	20.3	18.3
$TL310$	9.2×10^7	0.10	263	2.67	15.6	14.7
$TL320$	1.4×10^7	0.92	0.447	1.63	20.7	17.7

TAB. 2.1 – *Dimensionless numbers (using the same definitions as in chapter 1), measured values of the thermal boundary layer thickness and calculated values at onset as shown in figure 2.3.*

Chapitre 3

Régimes de déformation de l'interface.

3.1 Introduction.

The interest in two-layer thermal convection has been largely inspired by natural problems, in particular the dynamics of the Earth's mantle (see Tackley 2000a for a recent review); besides, it has also been a theoretical challenge, because of the possibility of Hopf bifurcation and time-dependence at marginal stability (Richter & Johnson 1974). This problem has thus been extensively studied in the past 30 years. However, the simple fact of adding a second layer considerably complicates the problem of thermal convection and opens up a very large parameter space that has not yet been fully explored.

Stability analysis (Richter & Johnson 1974; Renardy & Joseph 1985; Renardy & Renardy 1985; chapter 1 of this work) has pointed out the possible occurence of two different regimes depending on the buoyancy number B, the ratio of the stabilizing chemical density anomaly to the destabilizing thermal density anomaly: i) when B is larger than a critical value B_c depending both on viscosity and layer depth ratios, a stratified regime

takes place, with convecting patterns developing above and below a stable interface; ii) when B is lower than the critical value, a whole-layer regime takes place, with a deformed interface and convecting patterns developing over the whole depth of the system.

Finite-amplitude studies have then mostly addressed the stratified case because of its suggested occurence in the Earth's mantle (Richter & McKenzie 1981; Busse 1981; Olson 1984; Cserepes & Rabinowicz 1985; Ellsworth & Schubert 1988; Cserepes, Rabinowicz & Rosemberg-Borot 1988; Sotin & Parmentier 1989; Cardin, Nataf & Dewost 1991; Olson & Kincaid 1991; Davaille 1999*a*). Other studies have also been performed to characterize the respective influence of thermal and mechanical coupling between layers, restricting the interface to remain flat (Rasenat, Busse & Rehberg 1989; Busse & Sommermann 1996; Andereck, Colovas & Degen 1996; Degen, Colovas & Andereck 1998). In particular, they described a time-dependent behaviour, involving no deformation of the interface, with a convective pattern oscillating between viscous and thermal coupling.

Recently, the whole-layer regime has been reported experimentally by Davaille (1999*b*): focusing on the interaction of thermal convection with a sharp discontinuity in density and viscosity in the parameter range likely to be relevant to the Earth's mantle, she observed large periodic interface deformations developing over the whole depth of the system. Using the same experimental set-up (figure 3.1), Le Bars & Davaille (2002) showed that close to marginal stability, the early scales of the whole-layer regime are well predicted by the linear analysis. At large Rayleigh number Ra, the situation is complicated by the superimposition of various types of convective features: only looking at one of the two fluids, the destabilization of its outer thermal boundary layer possibly leads to the formation of small-scale plumes as in classical Rayleigh-Bénard convection (Howard 1964), thus referred as 'purely thermal'; but purely thermal features from hot and cold plates also interact at the interface, where they induce a large-scale thermochemical regime, either with a stable interface (even if partly deformed), thus corresponding to the stratified regime, or with a fully destabilized interface, thus corresponding to the whole-layer regime. As shown in figure 3.2, the critical value $B_c(\gamma, a)$ determined by marginal
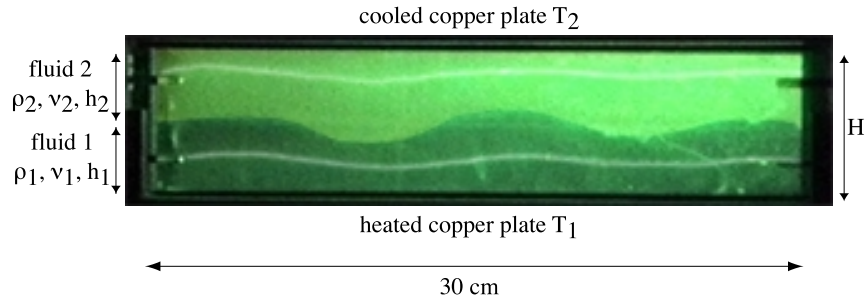
FIG. 3.1 – *Experimental set-up and onset of whole-layer regime in experiment n°56 (close to marginal stability). The lower layer 1 is dyed with fluorescein. White lines in the lower and upper layers correspond respectively to isotherms 31°C and 10°C (Davaille, Vidal, Le Bars, Jurine & Carbonne 2002). The initial wavelength of interface deformation is equal to twice the tank depth, as predicted by the linear study (chapter 1, Le Bars & Davaille 2002).*

stability - typically ranging between 0.2 and 0.5 - is still relevant for the early stages of experiments (a few overturn times), but the system then evolves through time.

In the present study, we focus on cases where the interface deforms: our purpose is to complete the first conclusions presented above in precisely describing the onset, patterns and evolution of the various convective features. Experimental conditions are summarized in section 3.2 and possible behaviours of the whole-layer regime close to marginal stability are presented in section 3.3. We then address large Ra dynamics: section 3.4 focuses on the small-scale purely thermal regime, and section 3.5 on the large-scale whole-layer thermochemical mode. Section 3.6 finally characterizes the time-evolution and the progressive stirring between the two fluids.

3.2   Experimental conditions.

The experimental set-up is similar to Davaille (1999a) (figure 3.1): two fluids with different kinematic viscosities (ν_1 and ν_2), densities (ρ_{1_0} and ρ_{2_0} at temperature T_0) and
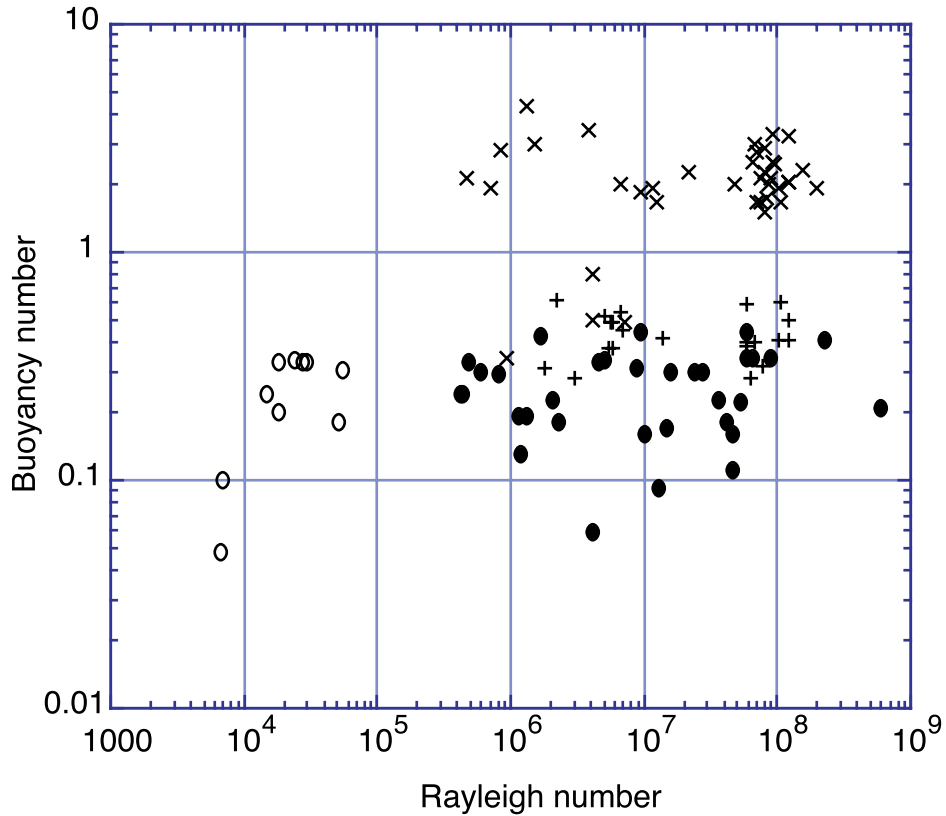
FIG. 3.2 – *Observed initial large-scale thermochemical regime as a function of Rayleigh and buoyancy numbers: circles, '×' and '+' represent experiments where the initial large-scale regime is respectively the whole-layer regime, the stratified regime (including points from Davaille 1999a) and the stratified regime with partly deformed interface. Open circles denote experiments close to marginal stability, where only one scale of convection is excited.*

depths (h_1 and h_2), initially at ambiant temperature, are superimposed in a tank and suddenly cooled from above at temperature T_2 and heated from below at temperature T_1.

The initial density distribution is stable, and because of experimental constraints, the heaviest fluid 1 is also always the most viscous. The Prandtl number in each layer is always greater than 100 to ensure that inertial effects are non-existent (Krishnamurti 1970). The high viscosities render diffusion of salt across the interface extremely slow compared to the characteristic time-scale of the instabilities. Heat transfers are monitored through time by measuring a vertical and an horizontal temperature profiles. Physical properties of both layers are measured for each experiment: the only important uncertainty comes from the viscosity measurements (accuracy of 25%). Moreover, the viscosities and the coefficient of thermal expansion α are temperature-dependent (see §3.2 of the general introduction, pp. 41). In the following, we use their values at the initial mean temperature of the tank (20^oC), which is relevant for global processes (see §2.1, pp. 89); for local processes however, as for instance thermal boundary layer instabilities, values at the local temperature are used. The temperature-dependence of viscosity is smaller than its composition-dependence for most of the experiments.

Apart from the Prandtl number, four dimensionless numbers are necessary to fully describe the two-layer system:

– the viscosity ratio

$$\gamma = \frac{\nu_1}{\nu_2}. \tag{3.1}$$

– the layer depth ratio

$$a = \frac{h_1}{H}, \tag{3.2}$$

where $H = h_1 + h_2$.

– the Rayleigh number

$$Ra = \frac{\alpha g \Delta T H^3}{\kappa \nu_2}, \tag{3.3}$$

where κ is the thermal diffusivity coefficient and $\Delta T = T_1 - T_2$. It is sometimes more convenient to use the Rayleigh numbers of each layer taken separately

$$Ra_i = \frac{\alpha_i g \Delta T_i h_i^3}{\kappa \nu_i}, \tag{3.4}$$

where ΔT_i is the temperature contrast through layer i and α_i the thermal expansion coefficient at the mean temperature of layer i.

– the buoyancy number, ratio of stabilizing chemical density anomaly to destabilizing thermal density anomaly

$$B = \frac{\Delta \rho_\chi}{\alpha \rho_0 \Delta T}, \tag{3.5}$$

where $\Delta \rho_\chi = \rho_{1_0} - \rho_{2_0}$ is the chemical stratification and $\rho_0 = (\rho_{1_0} + \rho_{2_0})/2$.

γ and a characterize the differences between the two layers, Rayleigh numbers measure the strength of convection, and B determines the stability of the whole system and the ability of the interface to deform. Values of the parameters for the 59 experiments are listed in table 3.1. This set of experiments allows us to separate several behaviours from the simple trend presented in figure 3.2: all regimes indexed in table 3.1 are schematically presented in figure 3.3 and will be precisely described in the following.

TAB. 3.1 – *Values of experiments dimensionless numbers (γ, a, B, Ra) and observed thermochemical regime: TD=dynamic topography, STR=stratified, WL=whole-layer; close to marginal stability, osc=oscillations, comp=composite overturn/oscillations; at large Ra, vo=vertical oscillations, icr=initial configuration reversals, 1=most viscous layer invading, 2=less viscous layer invading. Experiments n^o1 to 7 are performed in a $(30 \times 30 \times 6.1\ cm)$ tank (i.e. widths $= 30\ cm$, height $= 6.1\ cm$), experiments n^o45 to 51 in a $(30 \times 30 \times 8\ cm)$ tank, 2D experiment n^o24 in a $(30 \times 10 \times 16.4\ cm)$ tank and all the others in a $(30 \times 30 \times 14.8\ cm)$ tank. Working fluids are mixture of water, cellulose and salt (see §3.2 of the general introduction, pp. 41), except for experiment n^o13 where silicone oils $47V5000$ and $45V500$ are used.*

| experiment n°	γ	a	B	Ra	behaviour
1	27	0.5	0.13	1.2E+06	WL1icr
2	12	0.5	0.24	1.5E+04	WLosc->comp
3	12	0.5	0.18	5.2E+04	WLcomp
5	190	0.5	0.33	4.8E+05	WL1vo
6	170	0.25	0.24	4.3E+05	TD->WL1vo
7	150	0.75	0.24	4.2E+05	WLcomp
8	13	0.5	0.16	1.0E+07	WL1vo
9	22	0.25	0.17	1.5E+07	WL1icr
10	100	0.25	0.33	4.6E+06	TD->WL1vo
13	8	0.25	0.093	1.3E+07	WL1icr
16	1	0.25	0.29	8.0E+05	TD->WL1overturn
17	1	0.75	0.3	5.9E+05	WL2overturn
18	21	0.3	0.31	8.8E+06	WL1vo
19	17	0.3	0.55	6.6E+06	TD
20	15	0.3	0.8	4.1E+06	STR/small TD
21	9	0.3	0.49	5.8E+06	TD
22	12	0.3	0.38	5.9E+06	TD
23	100	0.3	0.5	4.1E+06	STR
24	16	0.3	0.46	6.8E+06	TD
25	37	0.3	0.39	5.9E+07	TD
26	590	0.9	0.28	6.3E+07	TD
27	30	0.9	0.11	4.7E+07	WL2icr
28	11	0.6	0.49	7.1E+06	STR->WL1
29	30	0.83	0.4	5.9E+07	TD
30	20	0.83	0.49	5.6E+06	TD
31	25	0.83	0.18	4.2E+07	WL2icr
32	1.7	0.6	0.34	5.1E+06	strat->WL2overturn
33	1.3	0.57	0.43	1.7E+06	strat->WL2overturn
35	77	0.25	0.4	6.8E+07	TD->WL1vo
36	23	0.9	0.59	5.8E+07	TD
37	1.8	0.5	0.28	3.0E+06	TD->WL1overturn
38	70	0.5	0.22	5.4E+07	WL1vo
39	1	0.25	0.62	2.2E+06	strat->TD
40	23	0.75	0.42	1.4E+07	TD
41	1400	0.75	0.32	7.7E+07	TD
42	22	0.75	0.18	2.3E+06	WL2 or 1 icr
43	24	0.69	0.19	1.3E+06	WL2 or 1 icr
44	2	0.69	0.059	4.1E+06	WL2overturn
45	1.3	0.44	0.1	6.8E+03	WLoverturn
46	1.1	0.44	0.048	6.7E+03	WLoverturn
47	6.7	0.5	0.2	1.8E+04	WLosc
48	6.5	0.55	0.34	2.4E+04	WLcomp
49	7	0.55	0.33	2.9E+04	Wloverturn
50	10	0.55	0.3	5.5E+04	Wloverturn
51	4.1	0.5	0.33	1.8E+04	WLoverturn
52	140	0.3	0.3	2.4E+07	WL1vo
53	180	0.5	0.3	2.7E+07	WL1vo
54	190	0.3	0.23	3.6E+07	WL1vo
56	6.8	0.5	0.33	2.8E+04	WLcomp
57	83	0.29	0.38	5.5E+06	TD->WL1vo
58	10	0.75	0.19	1.2E+06	WL2overturn
60	14	0.3	0.53	5.1E+06	TD
61	6.8	0.78	0.31	1.8E+06	TD
62	7.7	0.78	0.23	2.1E+06	WL2icr
63	36	0.83	0.16	4.6E+07	WL2icr
5overs98	150	0.41	0.34	9.0E+07	WL1
6overs98	46	0.91	0.21	5.9E+08	WL2
7overs98	34	0.3	0.3	1.6E+07	WL1
A800	4000	0.51	0.41	2.3E+08	WL1
uncertainty	50%	5%	10%	40%	

(c)

(b)

(d)

(a)

B

a

(e)
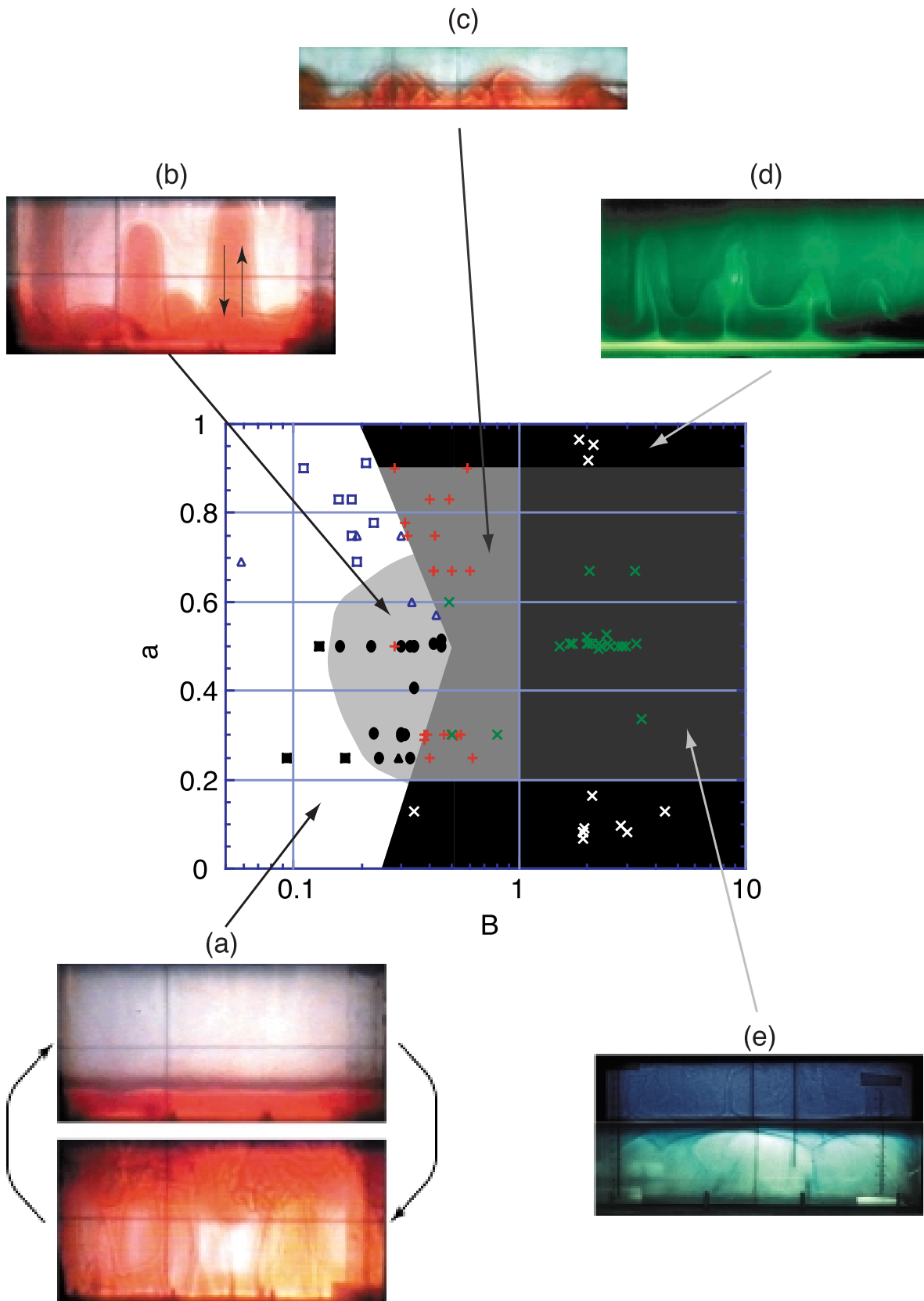
FIG. 3.3 – *Regimes diagram as a function of the buoyancy number B and the layer depth ratio a: triangles correspond to immediate mixing, squares to initial configuration reversals illustrated in pictures (a) and circles to vertical oscillations illustrated in picture (b); empty symbols correspond to domes from the upper less viscous fluid 2, and filled symbols to domes from the lower most viscous fluid 1. As in figure 3.2, '+' represent stratified experiments with interface deformations as in picture (c), which possibly evolve towards destabilization, and '×' stratified regime with a flat interface (including points from Davaille 1999a): thermochemical plumes shown in picture (d) take place when one layer is thinner than the corresponding thermal boudary layer (see §2.2 pp. 92 and Davaille, Girard & Le Bars 2002); when both layer are large enough, convection develops above and below the interface as in picture (e).*

3.3   Whole-layer regime at low Rayleigh number.

Ten experiments were performed close to marginal stability. In our experiments, the two fluids are initially at the same temperature T_0, and then heated from below and cooled from above. Outer thermal boundary layers subsequently grow from hot and cold plates (phase (i) on figure 3.4b) until a linear temperature profile is established through the whole tank. Then, provided the critical Rayleigh number is reached, convection starts under the form of large domes with a wavelength comparable to twice the tank depth (figure 3.1), which grow in both direction until they reach the opposite boundary (phase (ii) on figure 3.4b). The wavelength and time-scale of those convective features are well predicted by marginal stability analysis (see chapter 1). Their subsequent behaviour ranges between two limit cases.

3.3.1   Overturning.

In some experiments, as for instance experiment n^o46 presented in figure 3.4, the domes spread under the boundary plates, cool down (respectively heat up) and finally
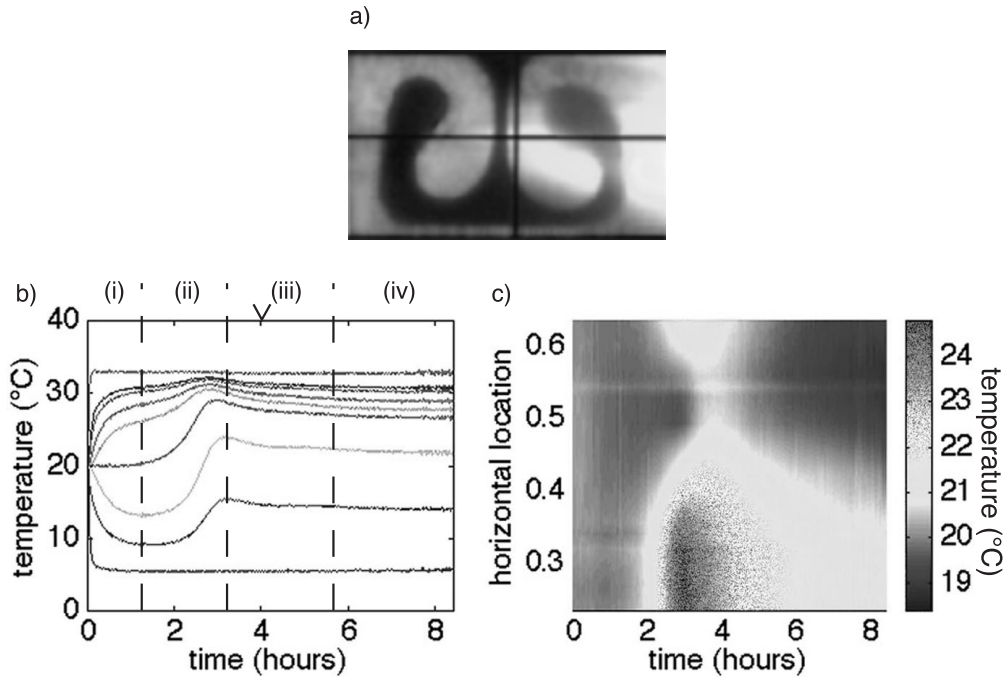
FIG. 3.4 – a) Picture, b) vertical temperature signal and c) horizontal temperature signal for experiment n°46, where overturning operates. On b) the triangle shows the time when the picture was taken; successive curves at decreasing temperatures correspond to thermocouples located at 0, 0.35 cm, 0.60 cm, 1.25 cm, 2.05 cm, 3.90 cm, 5.95 cm, 7.20 cm and 8 cm from the hot lower plate. Phase (i) corresponds to the establishment of a linear temperature gradient by conduction from the copper plates, phase (ii) to a rising hot dome, phase (iii) to the cooling of this dome and phase (iv) to the steady state.

sink (respectively rise) back while encapsulating part of the other fluid. This corresponds to phase (iii) on figure 3.4b. The temperature structure then remains fixed throughout the rest of the experiment (phase (iv) on figure 3.4b): the convective motions are steady and the initial heterogeneities are stirred and stretched by the flow. When their size becomes small enough, they are finally completely erased by chemical diffusion.
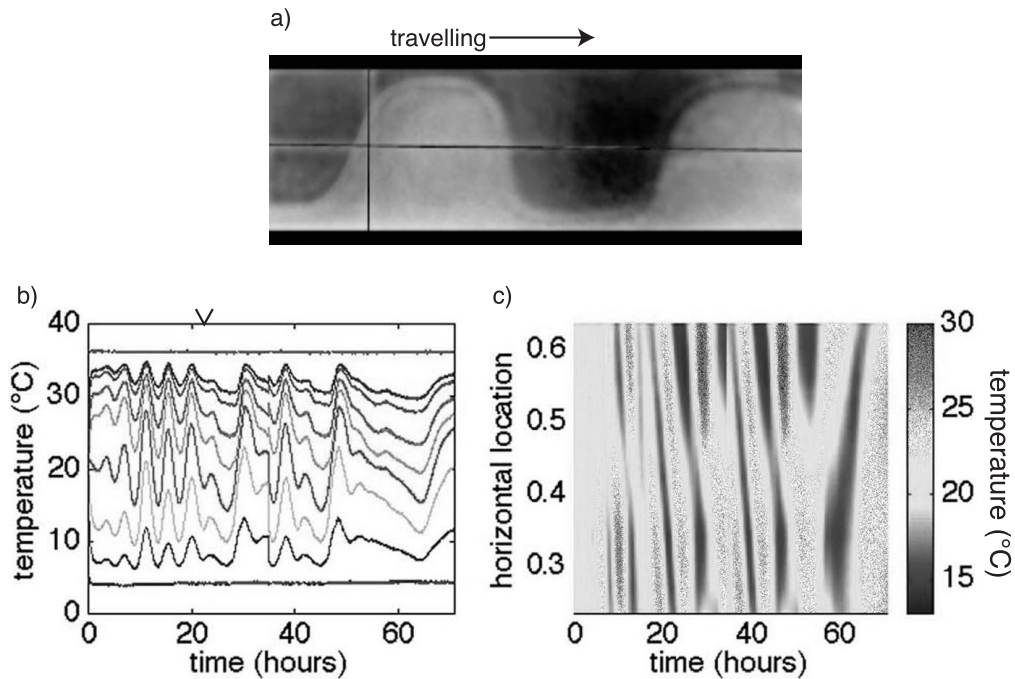
FIG. 3.5 – *The same for experiment n°47, where travelling waves are recorded during several days.*

3.3.2 Oscillations.

Very close to Ra_c, thermal effects just compensate chemical stratification, thermal diffusion and viscous dissipation. Then hot domes still develop but they do not spread under the cold plate before cooling down (figure 3.5a) and no large scale stirring operates. Although the interface is highly deformed, the two fluids remain separate and travelling waves with a period comparable to predictions from marginal stability analysis can be observed during several days (figure 3.5b,c). This behaviour is most easily observed when the viscosity contrast is relatively large ($\gamma > 5$ or $\gamma < 1/5$) and/or when the buoyancy ratio is close to critical, in agreement with theoretical linear study (see chapter 1).

However, oscillations during several days are quite difficult to obtain experimentally because they occur in a very narrow (Ra,B) window (Richter & Johnson 1974; see also chapter 1) and are very sensitive to small perturbations in the thermal boundary
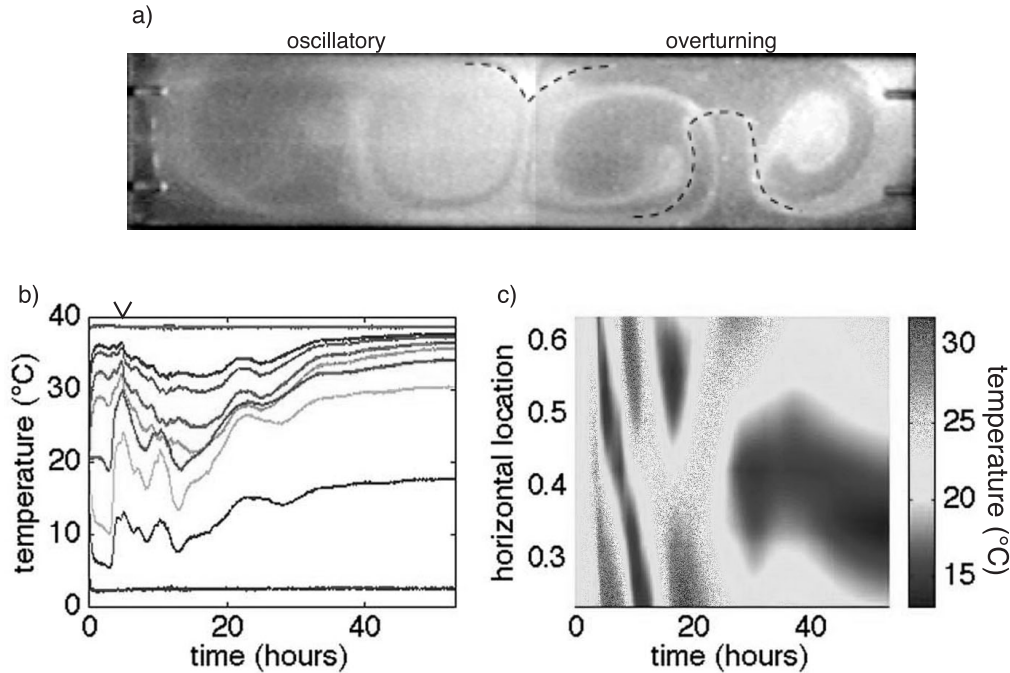
FIG. 3.6 – *The same for experiment n°56, where 3 oscillations are recorded before over-turning (dashed lines show isotherms 31°C and 10°C, Davaille, Vidal, Le Bars, Jurine & Carbonne 2002).*

conditions. Therefore, in most experiments, both modes combine and some pulsations are observed before complete mixing. For example, the experiment presented in figure 3.6 is carried in the adequate (Ra,B) range, but exhibits an asymmetric encapsulating structure:

- on the right half of the tank, overturning patterns comparable to those presented in figure 3.4 take place.
- on the left half of the tank, two zones constituted mostly of fluid 1 and fluid 2 respectively are observed. These zones act as the domes seen in figure 3.5*a*, and travel as well; but stirring is sufficiently efficient to lead to one-layer convection after three pulsations (figure 3.6*b*, *c*).

In the following, we will now focus on large Ra dynamics. Then, two types of convec-
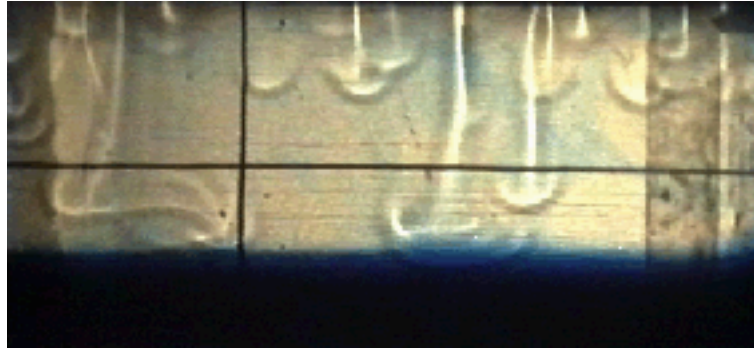
FIG. 3.7 – *Purely thermal plumes in layer 2 coming from the destabilization of the cold thermal boundary layer (experiment nº13).*

tive features are superimposed on two different lengthscales: in each fluid, purely thermal features as shown in figure 3.7 appear from the destabilization of the outer thermal boundary layers, whereas the large-scale thermochemical mode takes place at the interface from the interaction between the two fluids.

3.4 Large Rayleigh number dynamics: characteristics of the small-scale purely thermal mode.

3.4.1 Onset of purely thermal convection.

At high Rayleigh numbers, the onset of convection corresponds to the appearance of purely thermal features, coming out of the growing thermal boundary layers either in layer 1 above the hot plate or in layer 2 below the cold plate. The behaviour of each fluid taken separately is comparable to the classical one-fluid Rayleigh-Bénard convection: when the layer Rayleigh number Ra_i is supercritical, the thermal features inside fluid i take the form either of cells with a typical size comparable to the layer depth or of plumes coming from the destabilization of the corresponding outer thermal boundary layer (figure 3.7).
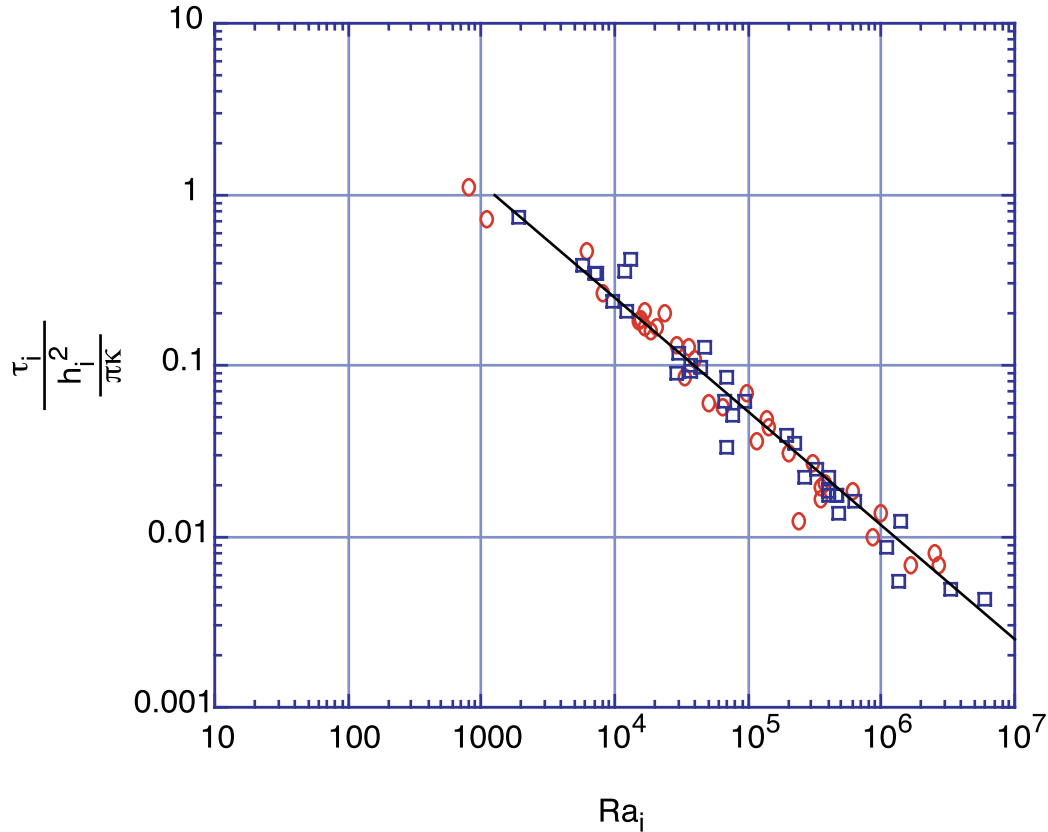
FIG. 3.8 – *Thermal onset times in layer 1 (circles) and layer 2 (squares) depending on the layer Rayleigh number. The line corresponds to the best fit according to (3.6): the experimental critical value is $Ra_c = 1300 \pm 500$.*

For $Ra_i > 10^4$ typically, the onset time scales as (Howard 1964)

$$\tau_i = \frac{h_i^2}{\pi \kappa} \left(\frac{Ra_c}{Ra_i} \right)^{2/3}. \tag{3.6}$$

Our measurements follow well this model (figure 3.8), and the experimental critical value $Ra_c = 1300 \pm 500$ agrees with the theoretical value 1100.65 for rigid-free boundaries conditions (Chandrasekhar 1961).

3.4.2 Interaction with the interface: dynamic topography.

When thermal plumes reach the interface, they are impinged both by density and viscosity contrasts. For large buoyancy ratio ($B > 1$ typically), the chemical stratification acts like a barrier and prevents penetration. However, when $B \leq 1$, thermal features coming from one of the outer boundary can partly and locally destabilize the interface. We call it 'dynamic topography', because it is essentially due to motions in each of the layers taken separately.

3.4.2.1 Thermal plumes coming from the most viscous layer.

This is the most favourable case to generate topography at the interface, since the only barrier to interface deformation is the density stratification. Then, once convection has started in the most viscous layer, fluid 1 can locally penetrate fluid 2. It does so under the form of cylinders with an almost constant diameter comparable to the thermal boundary layer thickness δ_1 (figure 3.9), whereas the whole system remains stable. Those instabilities stop before reaching the opposite boundary.

Looking at the equations of motions, this behaviour can simply be modelled by adding a stratification term (due to the chemical density contrast) to the classical equations for Rayleigh-Bénard convection (see §1.3 of the general introduction, pp. 22). In our experiments, inertial effects are negligible: motions are thus controlled by the equilibrium between buoyancy effects and viscous dragging forces. Let θ and w be the typical temperature excess and the typical convective velocity. When a thermal plume from layer 1 rises into fluid 2, its buoyancy is reduced because of the chemical stratification $\Delta\rho_\chi$, while viscous dragging forces remain dominated by motions in the most viscous fluid 1 (Whitehead & Luther 1975). Hence, at first order, the equation of motion becomes

$$\eta_1 \frac{w}{\delta_1^2} \sim (\alpha\rho\theta - \Delta\rho_\chi)g. \tag{3.7}$$

Because of heat diffusion, the temperature excess evolves through time: the scaling linear
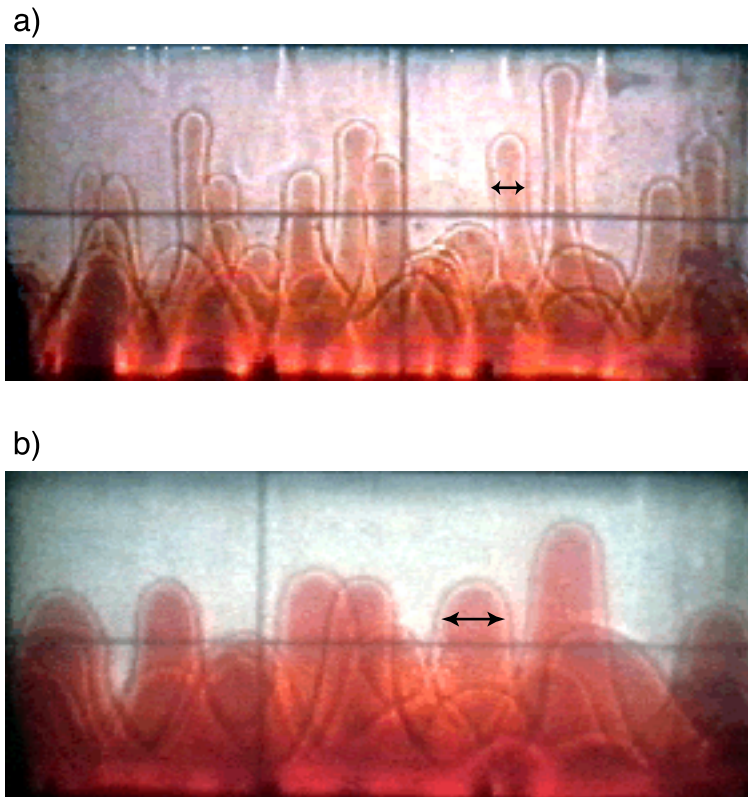
a)

b)

FIG. 3.9 – *Pictures of dynamic topography due to the most viscous layer 1. a) Experiment n°25: the arrow shows the measured typical diameter (1.4 $\pm$ 0.1 cm), close to the thermal boundary layer thickness $\delta_1 = 1.5 \pm 0.1$ cm measured by the vertical thermocouples probe. b) Experiment n°22: the arrow shows the measured typical diameter (2.5 $\pm$ 0.2 cm), close to the thermal boundary layer thickness $\delta_1 = 2.3 \pm 0.1$ cm measured by the vertical thermocouples probe.*

analysis gives

$$\frac{\partial \theta}{\partial t} \sim -\kappa \frac{\theta}{\delta_1^2}, \tag{3.8}$$

thus

$$\theta \sim \Delta T exp(-t/\tau), \tag{3.9}$$

where $\tau = \delta_1^2/\kappa$ is the typical time of diffusion through a plume. The motion of a diapir of fluid 1 into fluid 2 therefore is given by

$$\eta_1 \frac{w}{\delta_1^2} \sim (\alpha \rho \Delta T exp(-t/\tau) - \Delta \rho_\chi)g. \tag{3.10}$$

According to this equation, dynamic topography is possible only if $\alpha \rho \Delta T > \Delta \rho_\chi$, which means $B < 1$: the velocity then vanishes at time

$$t_{max} \sim -\tau ln(B), \tag{3.11}$$

which also gives the maximum elevation.

Let $p(t)$ be the penetration of fluid 1 above the interface: as a first order, we can write

$$\frac{dp}{dt} \sim w, \tag{3.12}$$

Integration in time of (3.12) using (3.10) leads to

$$p(t) \sim \frac{\alpha \rho g \Delta T \delta_1^4}{\kappa \eta_1}(1 - exp(-t/\tau)) - \frac{\Delta \rho_\chi g \delta_1^4}{\kappa \eta_1}\frac{t}{\tau}, \tag{3.13}$$

taking $p(0) = 0$. This can also be written

$$p(t) = C_1 \frac{\alpha \rho g \Delta T \delta_1^4}{\kappa \eta_1}(1 - exp(-t/\tau) - B\frac{t}{\tau}), \tag{3.14}$$

where C_1 is a scaling factor which will be determined experimentally. We see that the interface initially rises because of thermal buoyancy, but it finally sinks because of combined effects of thermal diffusion and chemical stratification. The maximum height is given by

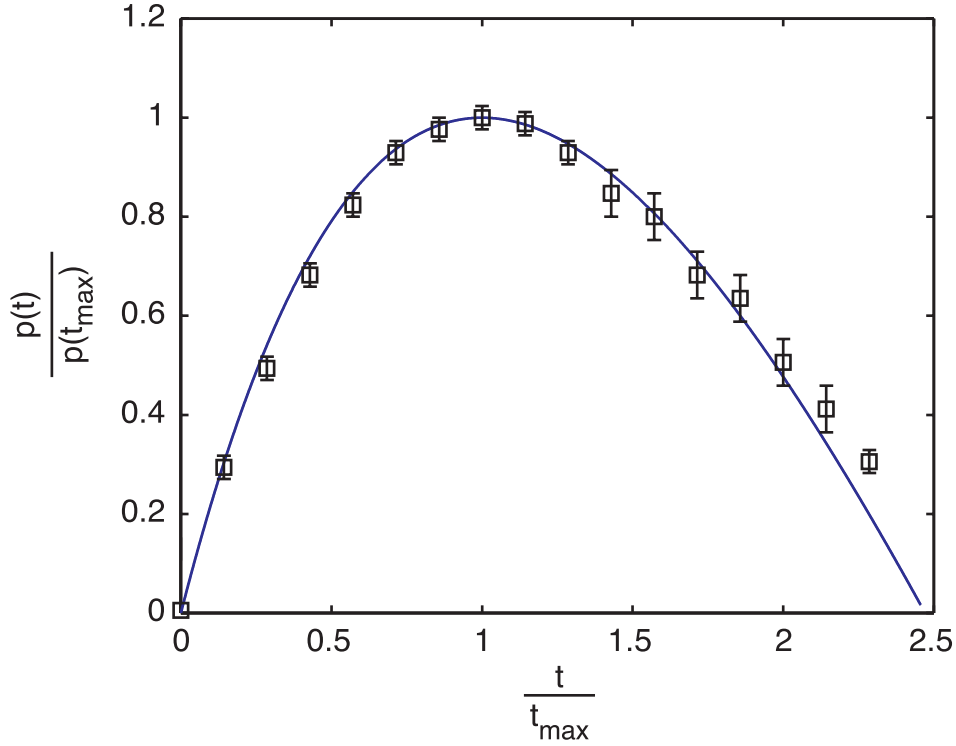$$p(t_{max}) = C_1 \frac{\alpha \rho g \Delta T \delta_1^4}{\kappa \eta_1}(1 - B + B \times ln(B)), \tag{3.15}$$

FIG. 3.10 – *Evolution of the penetration as a function of time for experiment n° 22: squares show measured values, and the line represents the fit according to (3.14) and (3.15). Because of entrainment, the final position of the interface is slightly higher than its initial position; after reconstruction of the outer thermal boundary layer, a new topography can develop.*

provided $p(t_{max})$ remains lower than the layer 2 depth. Scaling laws (3.14) and (3.15) explain well the data (figures 3.10 and 3.11), provided that the experimental constant is $C_1 = 0.0031 \pm 0.0011$. Besides, the time for maximum elevation in figure 3.10 is

$$t_{max} = -(0.058 \pm 0.006) \times \tau ln(B), \qquad (3.16)$$

introducing a scaling factor $C_2 = 0.058 \pm 0.006$ in (3.11). Numerical values of C_1 and C_2 are both consistent with choosing a characteristic lengthscale $\widetilde{\delta_1} = (0.24 \pm 0.08) \times \delta_1$ instead of δ_1: this may be linked to the cylindrical morphology of the studied structures.
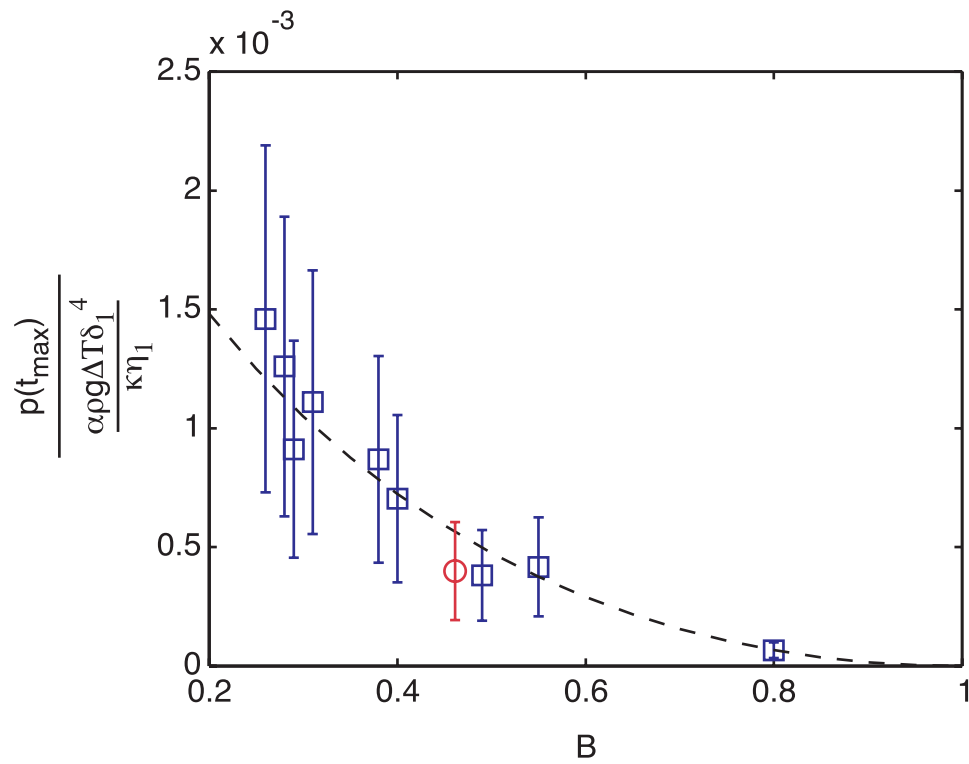
FIG. 3.11 – *Evolution of the maximum penetration of the dynamic topography for experiments n°16, 18, 19, 20, 21, 22, 25, 35, 37 (squares) and 2D experiment n°24 (circle). The dashed line represents the best fit according to (3.15): the experiments give a scaling factor $C_1 = 0.0031 \pm 0.0011$.*
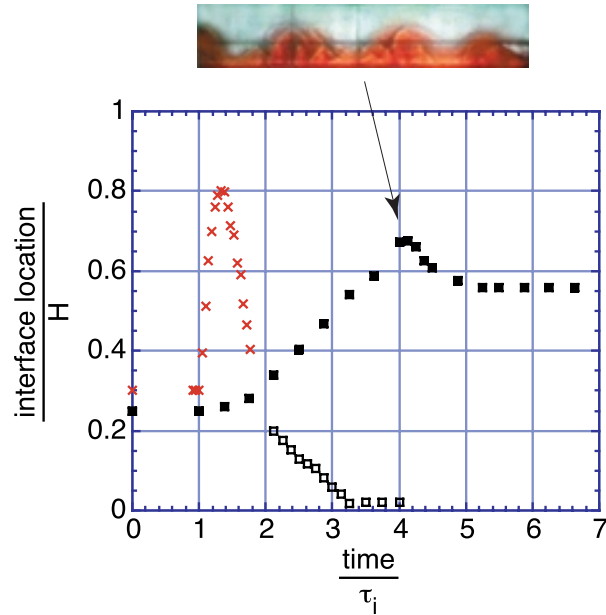
FIG. 3.12 – *Dynamic topography in experiment n°6: layer 1 is stagnant and progressively deformed by convection in layer 2. Filled and empty squares respectively represent the evolution of the maximum and the minimum interface elevation as a function of time (normalised by the period of thermal plumes in layer 2). At time $t = 4 \times \tau_2$, when the picture was taken, layer 1 depth reaches a sufficient value for the local Rayleigh number to be critical. The evolution of dynamic topography driven by the most viscous layer in experiment n°22 is also reported with '×'; time is then normalised by the period of thermal plumes in layer 1.*

3.4.2.2   Thermal plumes coming from the less viscous layer.

This configuration is less favourable to partial invasion since a thermal plume coming from the less viscous layer 2 encounters a viscosity increase as well as a density stratification at the interface. Therefore, it will deform the interface only if the most viscous layer is stagnant: interface topography is then sculpted progressively by several successive thermal plumes on a much longer time-scale than in the previous case (figure 3.12).

3.5   Large Rayleigh number dynamics: characteristics of the large-scale thermochemical whole-layer regime.

3.5.1   Different types of whole-layer convection.

The whole-layer regime corresponds to the full destabilization of the system: it involves both layers, no matter what their thermal history and their convective state are. It is thus to be distinguished from the dynamic topography addressed in §3.4. Close to marginal stability, two behaviours are possible as described in §3.3: oscillations take place at relatively large B and/or low Ra and/or large viscosity ratio γ, and overturning takes place otherwise. The same observation is still relevant at large Ra, as shown in figure 3.13.

3.5.1.1   Overturning.

When $1 \leq \gamma < 5$ typically (figure 3.13), the whole-layer regime takes the form of large convective features developing through the whole depth of the tank. The interface is distorted in all directions, and the two-layer initial system is never reconstructed: overturning and immediate stirring operates (see also Olson & Kincaid 1991).

3.5.1.2   Pulsations.

When $\gamma > 5$ typically, the whole-layer regime gives rise to large-scale oscillations: the two fluids conserve their own identity, and the initial two-layer system is periodically reconstructed. The number of observed pulsations rapidly increases with γ (figure 3.13). Two mechanisms of initial system reconstruction are possible, namely vertical oscillations and initial configuration reversals:

– the typical evolution of vertical oscillations is presented in figure 3.14. Starting from an isothermal stratified system, the lower fluid is progressively heated and
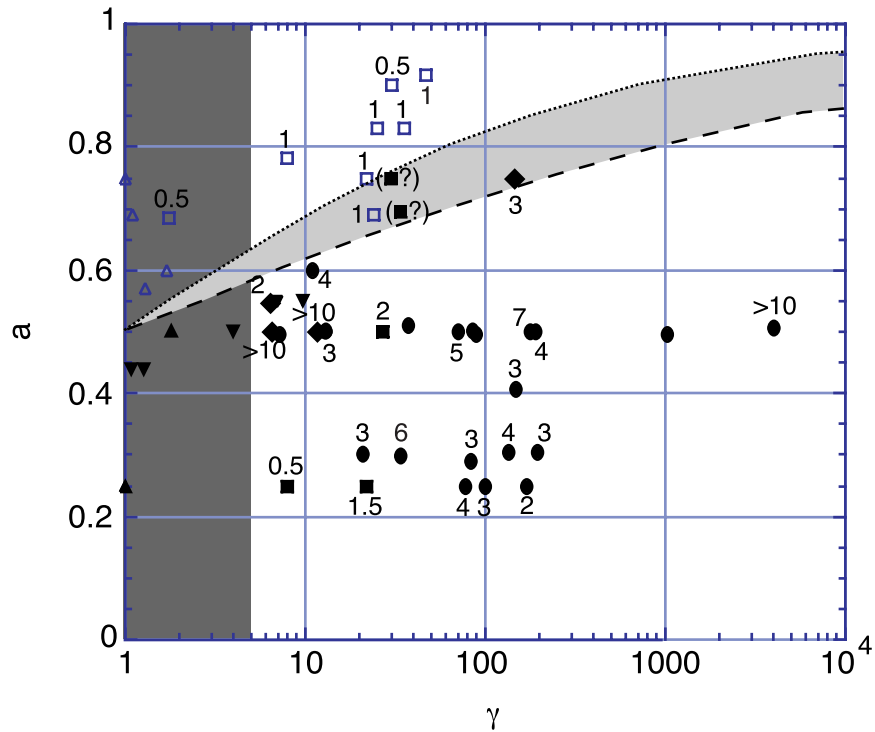
FIG. 3.13 – *Observed behaviours of whole-tank convection as a function of layer depth and viscosity ratios: triangles stand for overturning and immediate stirring, diamonds for oscillations close to marginal stability, circles for 'vertical oscillations' and squares for 'initial configuration reversals'; the numbers near the symbols indicate the number of pulsations, from 0 to > 10. The spouting direction as defined in §3.5.3 is also reported here: empty points correspond to cavity plumes and filled points to diapiric plumes; the dotted line represents the theoretical law (3.30) $a = 1/(1 + \gamma^{-0.2})$ and the dashed line the theoretical law (3.32) $a = 1/(1 + \gamma^{-1/3})$.*

becomes lighter, whereas the upper fluid is cooled and becomes heavier (either by conduction or thermal convection in each layer). Once the chemical density anomaly is cancelled by thermal effects, the interface deforms in large domes that rapidly propagate until they reach the opposite boundary: fluid 1 near the cold plate becomes heavier whereas fluid 2 near the hot plate becomes lighter. The initial stratification finally reappears and the system goes back to its initial configuration. A new oscillation can begin. Entrainment between the two layers of course slowly works by advection, but more than 10 successive pulsations have been observed (3 pulsations in experiment n^o18, figure 3.16a).

– initial configuration reversals are presented in figure 3.15. They correspond to the behaviour predicted by Herrick & Parmentier (1994): the whole invading layer is progressively emptied, until the initial configuration is totally reversed, with fluid 1 lying above fluid 2. Then, fluid 1 cools down, fluid 2 heats up, and the system finally goes back to initial state. In this case, stirring also works by advection, but several successive reversals can be observed (3 in experiment n^o9 for instance, figure 3.16b).

Vertical oscillations take place when domes cool down (respectively heat up) faster than they spread out in the vincinity of the cold plate (respectively hot plate), and rapidly collapse into initial state: it thus happens when the restoring force due to chemical stratification is predominant compared to the thermal buoyancy, that is when the buoyancy number is large ($B > 0.2 - 0.3$ typically, see figure 3.3) and/or the Rayleigh number relatively small. On the contrary, initial configuration reversals take place when the chemical stratification is low compared to the thermal buoyancy ($B < 0.2$ typically and/or large Ra), but also when the invading layer is small and thus rapidly emptied ($a < 0.3$ or $a > 0.7$, see figure 3.3).
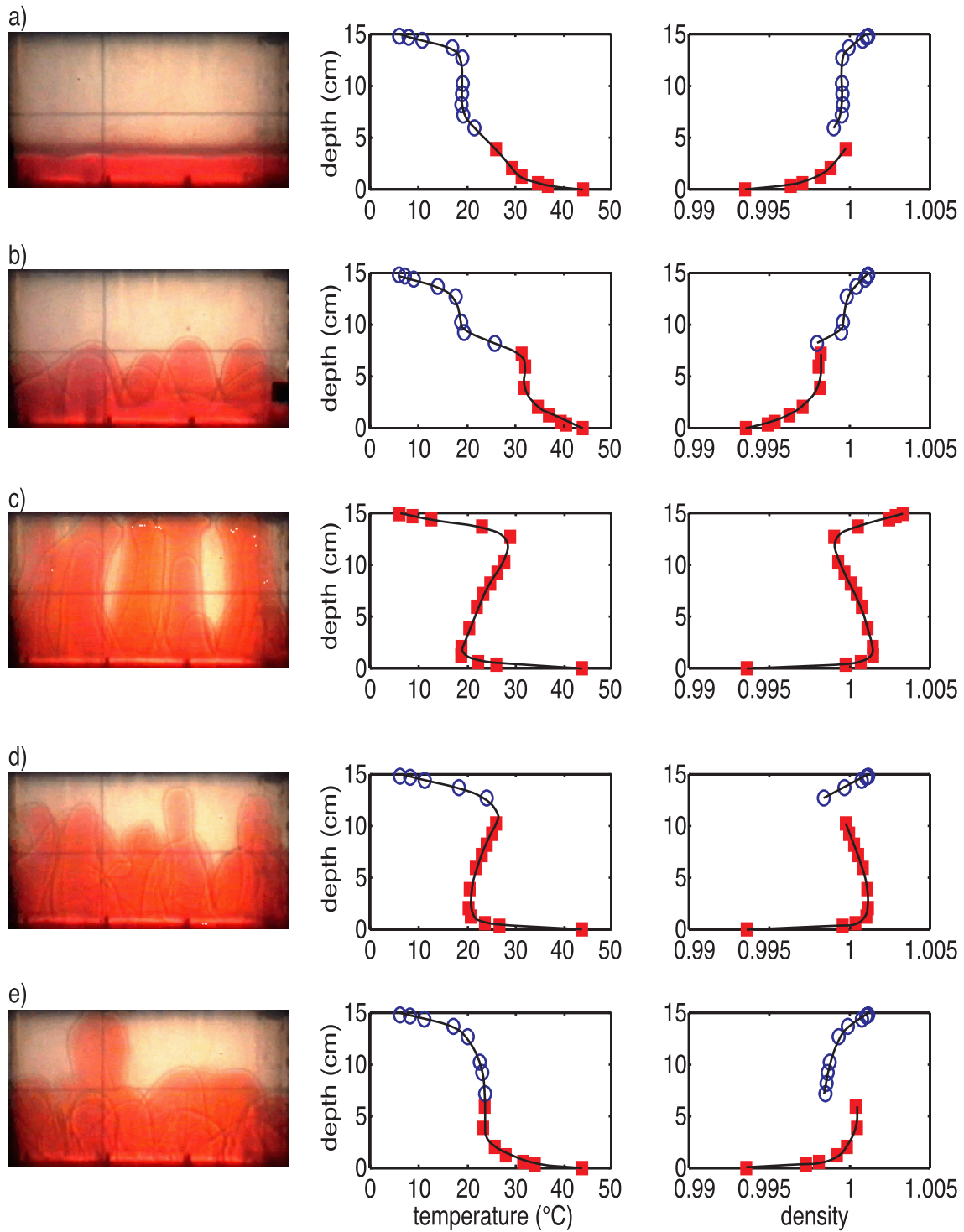
F$_{IG}$. 3.14 – *Whole-layer dynamics of experiment n°18 under the form of vertical oscillations: pictures, measured vertical temperature profiles and deduced density profiles according to the equation of state $\rho_i(T) = \rho_{i0}(1 - \alpha(T)(T - T_0))$. Filled squares stand for thermocouples located in fluid 1, and empty circles in fluid 2. a) Initial configuration, just before destabilization ($t = 13.5$ min): the two layers are stratified. Convection characterized by a vertical temperature profile has developed in layer 2, whereas conduction takes place in layer 1. b) Fluid 1 is now lighter than fluid 2, leading to a rising dome ($t = 16$ min). c) The dome reaches the cold plate, where it progressively cools down and becomes heavier than the surrounding fluid 2 ($t = 20$ min). d) It thus sinks ($t = 23$ min) and e) finally goes back to its initial state ($t = 27.5$ min); an another dome has risen in the background.*
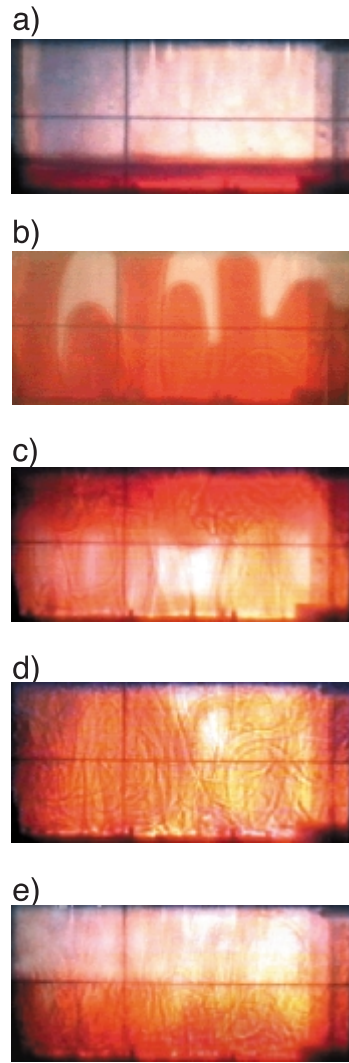
FIG. 3.15 – *Whole-layer dynamics of experiment nº9 under the form of initial configuration reversals: a) chemically stratified state, just before destabilization (t = 9 min). b) Fluid 1 is now lighter than fluid 2, leading to rising domes (t = 12 min). c) The layer 1 reforms under the cold plate, where it progressively cools down and becomes heavier; fluid 2 now corresponds to the lower layer and is progressively heated (t = 14.5 min). d) The initial stratification finally reappears: both fluids go back to initial position (t = 17 min) and e) the chemically stratified system is reformed (t = 20.5 min).*
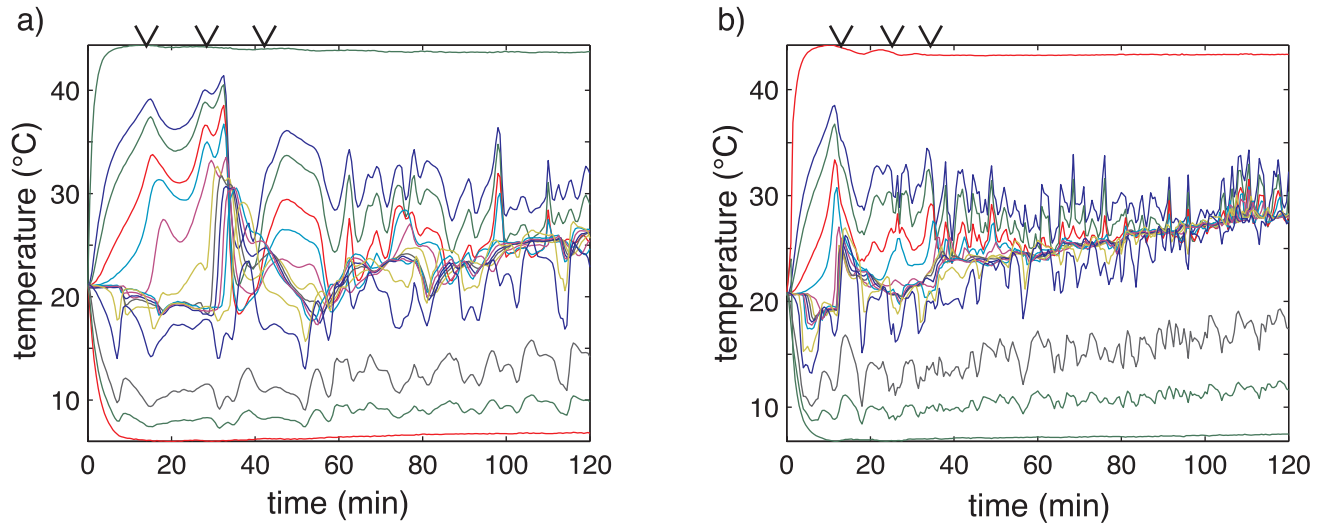
F IG. 3.16 – *Temperature signals registrered by the vertical thermocouples for a) experiment nº18 (vertical oscillations) and b) experiment nº9 (initial configuration reversals). Arrows indicate observed onset of whole-layer pulsations.*

3.5.2   Onset of whole-layer regime.

The whole-layer regime is excited when the thermal buoyancy is large enough to induce motions over the whole depth of the tank in spite of thermal diffusion, viscous dragging and chemical stratification. The details of its onset depend on the initial conditions in the system.

3.5.2.1   Initial buoyancy ratio lower than critical.

When the buoyancy number is lower than the critical value determined by marginal stability, the whole-layer regime is the most unstable thermochemical mode (see chapter 1): starting from isothermal fluids, it is thus excited as soon as heat is transferred through the whole depth of the tank, either by conduction or thermal convection inside each fluid. Its onset time is therefore equal to the longest onset time of purely thermal mode in layers 1 and 2, as defined by (3.6) (figure 3.17).
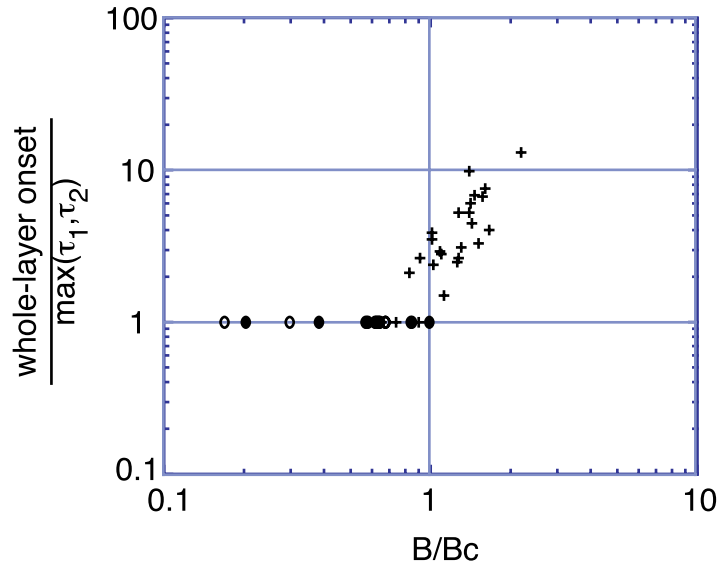
FIG. 3.17 – *Onset time for whole-layer convection divided by the maximum purely thermal convective time in the two layers, as a function of the buoyancy number normalized by the critical buoyancy number determined with marginal stability analysis. Circles stands for 'marginally unstable' experiments, and '+' for 'marginally stable' experiments that are finally destabilized; empty points correspond to experiments where the less viscous layer invades the most viscous one.*
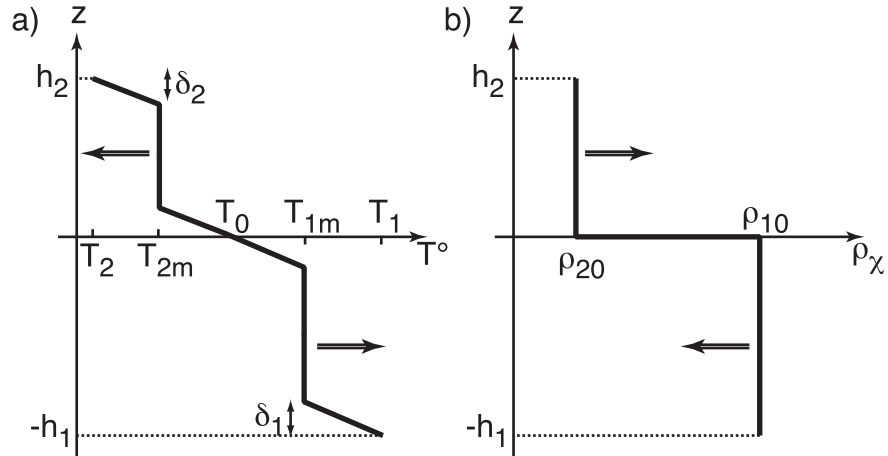
FIG. 3.18 – *Sketches of a) the temperature profile and b) the chemical density profile at large Rayleigh numbers; arrows indicate the temporal evolution.*

3.5.2.2   Initial buoyancy ratio greater than critical.

When $B > B_c(\gamma, a)$, the configuration is 'marginally stable': the linear study predicts a stratified regime with a stable interface. It is indeed observed experimentally, at least during a few overturns. However, thermal and chemical evolutions of the system at high Rayleigh numbers progressively encourage destabilization through time: as sketched in figure 3.18,

- the temperature is almost constant through the core of each convecting layer, and a thermal boundary layer develops around the interface with a temperature jump that gradually increases (Herrick & Parmentier 1994).
- thermal convection in each layer induces entrainment across the interface by viscous coupling (Davaille 1999 *a*), which continuously decreases the chemical stratification.

In this context, a first order approach consists in forgetting the effective thermal and chemical variations and only considering a constant mean density in each layer with a sharp change at the interface:

$$\overline{\rho_i} = \rho_{i0} - \overline{\alpha\rho_0(T - T_0)_i}, \tag{3.17}$$

where $\overline{\alpha\rho_0(T - T_0)}_i$ is the mean value of thermal buoyancy $\alpha\rho_0(T - T_0)$ over the layer i. Such a system is then comparable to Rayleigh-Taylor configurations (see for instance Whitehead & Luther 1975) and becomes unstable provided

$$\overline{\rho_1} < \overline{\rho_2}. \tag{3.18}$$

In terms of buoyancy number, (3.18) means that the effective buoyancy number based on real chemical and thermal contrasts

$$B_{eff}(t) = \frac{\Delta\rho_\chi(t)}{\overline{\alpha\rho_0(T - T_0)}_1 - \overline{\alpha\rho_0(T - T_0)}_2} \tag{3.19}$$

becomes strictly lower than 1.

In the experiments, B_{eff} can be measured using the vertical thermocouples probe. As shown in figure 3.19, destabilization indeed takes place for B_{eff} slightly smaller than 1: the mean experimental value at onset is

$$B_{eff} = 0.98 \pm 0.12 \tag{3.20}$$

for $0.51 < a < 0.83$, $1.3 < \gamma < 25$ and $1.7 \times 10^6 < Ra < 7.5 \times 10^7$.

This simplified model focuses on the influence of the chemical stratification on the destabilization: for the whole-layer regime to be excited, thermal effects has to reverse the initial density contrast. It is indeed the predominant effect at large Ra–large B. However, it implicitly neglects thermal and viscous diffusions during motions over the whole depth of the tank. A more complete analytical model can be proposed following Herrick & Parmentier (1994): the buoyancy effectively available for motions over the whole depth of the tank is given by

$$\Delta\rho_{eff} = \overline{\rho_2} - \overline{\rho_1} = [\overline{\alpha\rho_0(T - T_0)}_1 - \overline{\alpha\rho_0(T - T_0)}_2] - \Delta\rho_\chi(t). \tag{3.21}$$

Whole-layer motions are mainly governed by the most viscous fluid: therefore, we define the Rayleigh number characteristic of interface destabilization as

$$Ra_{eff} = \frac{\Delta\rho_{eff}gH^3}{\kappa\eta_1}. \tag{3.22}$$
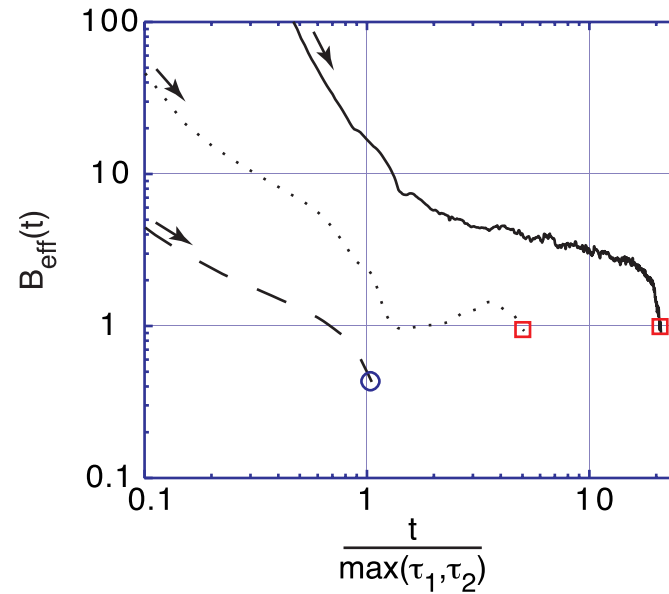
FIG. 3.19 – *Time evolution of the effective buoyancy number until interface destabilization for experiments nº8 (marginally unstable: dashed line), nº28 (marginally stable, but destabilized after 1 hour, once temperature contrast at the interface has reached a sufficient value: dotted line) and nº910 from Davaille (1999a) (marginally stable, but destabilized after 8.5 hours because of thermal evolution and mixing at the interface: solid line).*

Whole-layer motions are excited when Ra_{eff} reaches the critical value of one-layer convection with rigid boundaries $Ra_c = 1707.76$ (Chandrasekhar 1961), which means that $\Delta\rho_{eff}$ reaches the critical value

$$\Delta\rho_c = \frac{Ra_c}{Ra}\alpha\rho_0\Delta T \times \gamma. \qquad (3.23)$$

The chemical evolution of the system can be modeled using the scaling laws defined by Davaille (1999a): it takes place on a much longer time-scale that the thermal evolution, as observed in the experiments (see figure 3.19 for instance). One can thus separate two trends, namely

- a middle term thermal evolution: the chemical density anomaly can then be taken as a constant and (3.23) means that the effective buoyancy number has to reach a critical value

$$B_c = \frac{1}{1 + \frac{\gamma}{B} \times \frac{Ra_c}{Ra}}. \qquad (3.24)$$

- a long term chemical evolution: one can then consider that the thermal evolution of the system has reached a steady state. For instance, the heat balance for the idealized situation sketched in figure 3.18 implies:

$$\frac{T_1 - T_{1m}}{\delta_1} = \frac{T_{1m} - T_{2m}}{\delta_1 + \delta_2} = \frac{T_{2m} - T_2}{\delta_2}, \qquad (3.25)$$

where T_{im} is the mean interior temperature of layer i and δ_i is the thermal boundary layer thickness, so

$$T_{1m} - T_{2m} = \frac{\Delta T}{2}. \qquad (3.26)$$

At long term, we can thus write

$$\overline{\alpha\rho_0(T - T_0)}_1 - \overline{\alpha\rho_0(T - T_0)}_2 = \epsilon \times \alpha\rho_0\Delta T \qquad (3.27)$$

where ϵ is a constant that depends on the variations of $\alpha(T)$ ($\epsilon = 1/2$ if α is constant). (3.23) then means in terms of effective buoyancy number

$$B_c = 1 - \epsilon \times \gamma \times \frac{Ra_c}{Ra}. \qquad (3.28)$$

(3.24) and (3.28) thus complete the condition $B_{eff} < 1$ given previously in introducing thermal diffusion and mechanical dissipation in the condition for destabilization. However, both conditions tend quite quickly towards 1, and the error bars on our measured B_{eff} do not allow us to recover experimentally the expected dependence.

From a general point of view, we conclude that the onset of whole-layer convection at high Rayleigh number occurs whenever the more viscous layer convects and $B_{eff} < 1$.

3.5.3   A Rayleigh-Taylor type destabilization: shapes and direction of spouting.

As observed in the closely-related case of Rayleigh-Taylor instabilities (Whitehead & Luther 1975), the pattern of destabilization depends on the direction of doming: in most experiments, we observe domes developing from the most viscous fluid into the less viscous one in the form of large cylinders called 'diapiric plumes' separated by cusps (figure 3.20 a). In some cases however, those cusps transform into active sinking features, under the form of large blobs followed by a thinner tail, comparable to cavity plumes (figure 3.20 b).

In Rayleigh-Taylor instabilities, the direction of spouting (i.e. superexponential growth of interfacial extrema) is determined by the relative value of two parameters, characterizing the 'penetrability' of each layer (Ribe 1998):

- the viscosity ratio, since it is easier to penetrate a less viscous layer.
- the layer depth ratio, since it is easier to invade a deeper layer, where boundary conditions don't limit motions.

For 'rigid' boundary conditions, the spout changes when

$$\frac{h_1}{h_2} = (\frac{\nu_1}{\nu_2})^{0.2}$$
(3.29)

(Ribe 1998, private communication), which means with our notations

$$a = \frac{1}{1 + \gamma^{-0.2}}.$$
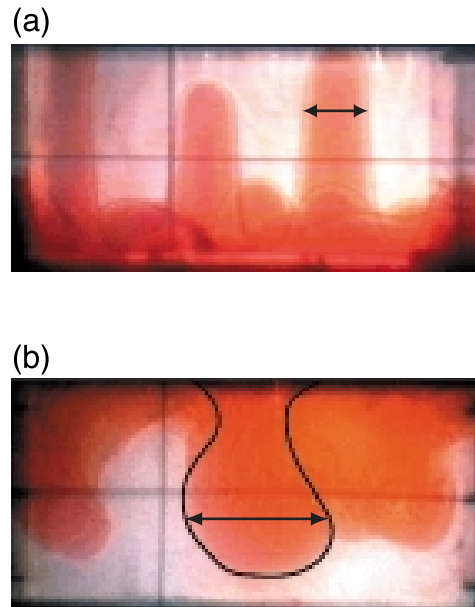(3.30)

(a)

(b)

FIG. 3.20 – *Typical forms of the Rayleigh-Taylor type destabilization: a) experiment nº9, where the invading layer is the most viscous (diapiric plume); the arrow shows the measured diameter 4.2 ± 0.2 cm for a theoretical value given by (3.34) of 4.3 ± 0.9 cm; b) experiment nº31, where the invading layer is the less viscous (cavity plume): the arrow shows the measured diameter 9.3 ± 1.0 cm for a theoretical value given by (3.35) of 10.3 ± 2.1 cm.*

In our configuration, the destabilization is due to thermal transfers, which must therefore be taken into account. Consider a buoyant particle located at the interface: its ability to reach the i boundary is measured by Ra_i, ratio of buoyancy to thermal and viscous diffusive effects through the fluid i (see for instance Turner 1979, pp. 208-209). Once the interface is unstable, its deformation will tend to develop through the layer were motions are easier, thus through the layer with the highest Ra_i. The doming direction then changes when

$$Ra_1 = Ra_2, \tag{3.31}$$

which means at first order

$$\frac{h_1}{h_2} = \left(\frac{\nu_1}{\nu_2}\right)^{1/3} \Leftrightarrow a = \frac{1}{1 + \gamma^{-1/3}}. \tag{3.32}$$

As described by Ribe (1998), the higher exponent in (3.32) than in (3.30) corresponds to an increased influence of the viscosity ratio: in the Rayleigh-Taylor calculations, the configuration is unstable by its own and viscosities only act on the 'penetrability'. In our proposed first order approach, viscosities have a twofold influence: they influence the 'penetrability', but also control heat transfers, which are responsible for the interface destabilization.

Experimental observations reported in figure 3.13 indicate a dependence on a and γ in agreement with (3.30) and (3.32), but do not allow to choose between the two proposed coefficients.

3.5.4   Characteristic wavelength and diameter.

The selected wavelength in our configuration is totally different from Rayleigh-Taylor instabilities (figure 3.21a). Actually, initial perturbations of the interface are due to thermal transfers from hot and cold plates. Since largest temperature fluctuations come from the most viscous fluid, it also control the wavelength of doming: figure 3.21b then exhibits
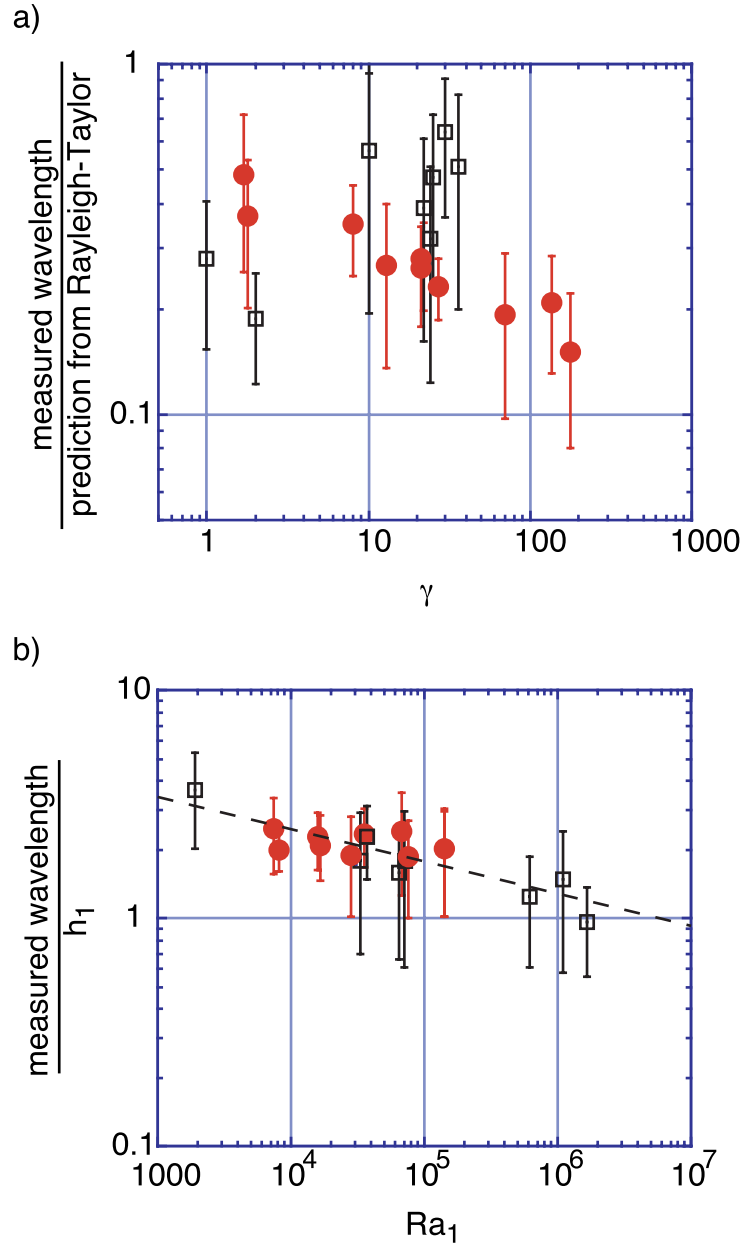
FIG. 3.21 – *a) Wavelength of diapiric plumes (filled circles) and cavity plumes (squares) normalized by the predictions for Rayleigh-Taylor instabilities ($\lambda = 4\pi h_1(\gamma/180)^{1/5}$ in the case of $a << 1$ and $\gamma >> 1$ and $\lambda = 2\pi h_2(\gamma/3)^{1/3}$ in the case of a close to 1 and $\gamma >> 1$, Ribe 1998): theoretical values for Rayleigh-Taylor instabilities do not indicate the relevant parameter dependence. b) Wavelength of diapiric plumes (filled circles) and cavity plumes (squares) normalized by the depth of the most viscous layer as a function of the most viscous layer Rayleigh number: heat transfers in fluid 1 control the initial perturbations at the interface, thus the selected wavelength.*
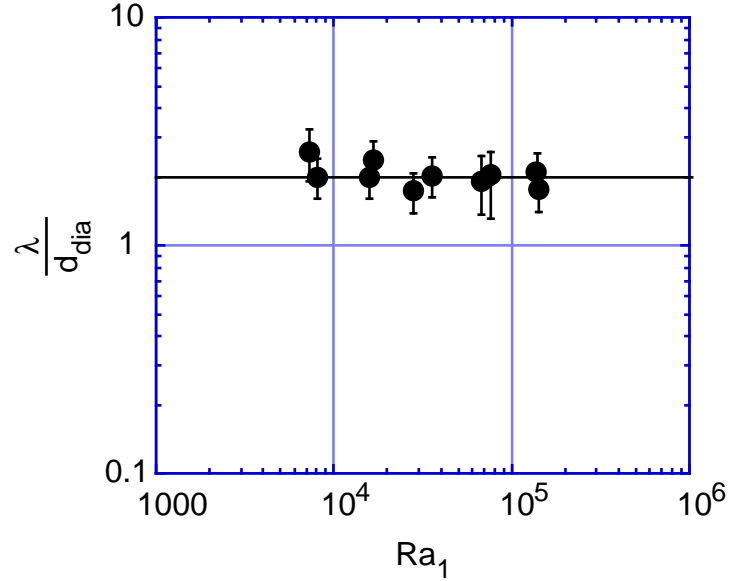
FIG. 3.22 – *Ratio of wavelength to diameter of diapiric plumes as a function of the most viscous layer Rayleigh number: the line shows the mean value* 2.0 ± 0.3.

a slight dependence on Ra_1 corresponding to the experimental law

$$\frac{\lambda}{h_1} = 9.1 \times Ra_1^{-0.14}, \tag{3.33}$$

accurate for both directions of doming with a typical precision of 20%.

As observed in figures 3.20a and 3.22, the diameter of diapiric plumes then scales as

$$\frac{\lambda}{d_{dia}} = 2.0 \pm 0.3. \tag{3.34}$$

Measurements for cavity plumes are more difficult since our tank is not large enough to observe more than 2 or 3 successive structures and not long enough for the expected spherical shape with a fixed diameter d_{cav} to fully develop before reaching the opposite plate. A simple volume conservation of fluid 2 however gives

$$4/3\pi(d_{cav}/2)^3 \sim \lambda^2 \times h_2 \tag{3.35}$$

that seems to indicate the relevant order of magnitude (see figure 3.20b for instance).

In both cases, we must notice that when purely thermal plumes exist in the layer before doming, each dome collects several small-scale instabilities.

3.5.5   Typical velocities.

Since inertial effects are negligible, convective motions are controlled by the equilibrium between buoyancy effects and viscous dragging forces. When both layers are involved, dragging forces are dominated by the most viscous fluid (Whitehead & Luther 1975): the scaling analysis then gives a typical domes velocity

$$w \sim \frac{\Delta\rho_{eff}gd^2}{\eta_1}, \tag{3.36}$$

where d is a typical size of the dome and $\Delta\rho_{eff}$ the density contrast available for motion over the whole depth as given by (3.21), taking into account both thermal and chemical effects.

Figure 3.23 present measurements for two examples. Cavity plumes exhibit a constant velocity (figure 3.23a), which can be compared to (3.36) using measured $\Delta\rho_{eff}$ and $d = d_{cav}$: results are presented in figure 3.24. In the case of diapiric plumes, the development can be divided in two steps (figure 3.23b):

   – during an 'initiation' stage, the diameter of the interface deformation progressively increases with the height and the velocity is mostly constant. The theoretical value (3.36) can then be calculated taking measured $\Delta\rho_{eff}$ and $d = d_{dia}$ (see figure 3.24).

   – once the interface deformation reaches a value comparable to d_{dia}, a 'maturation' stage starts: the deformation takes the form of a cylinder with a nearly constant diameter. The characteristic length that must be used in (3.36) is intermediate between the height of the plume h and d_{dia}, and the rising speed rapidly increases with h. This behaviour is reminiscent of the ascent of diapirs created by injection of a buoyant viscous fluid through a small orifice, presented by Olson & Singer (1985): a coefficient $ln(h/d_{dia})$ was then introduced in (3.36) to take into account the cylindrical morphology. In our experiments however, the relatively small depth
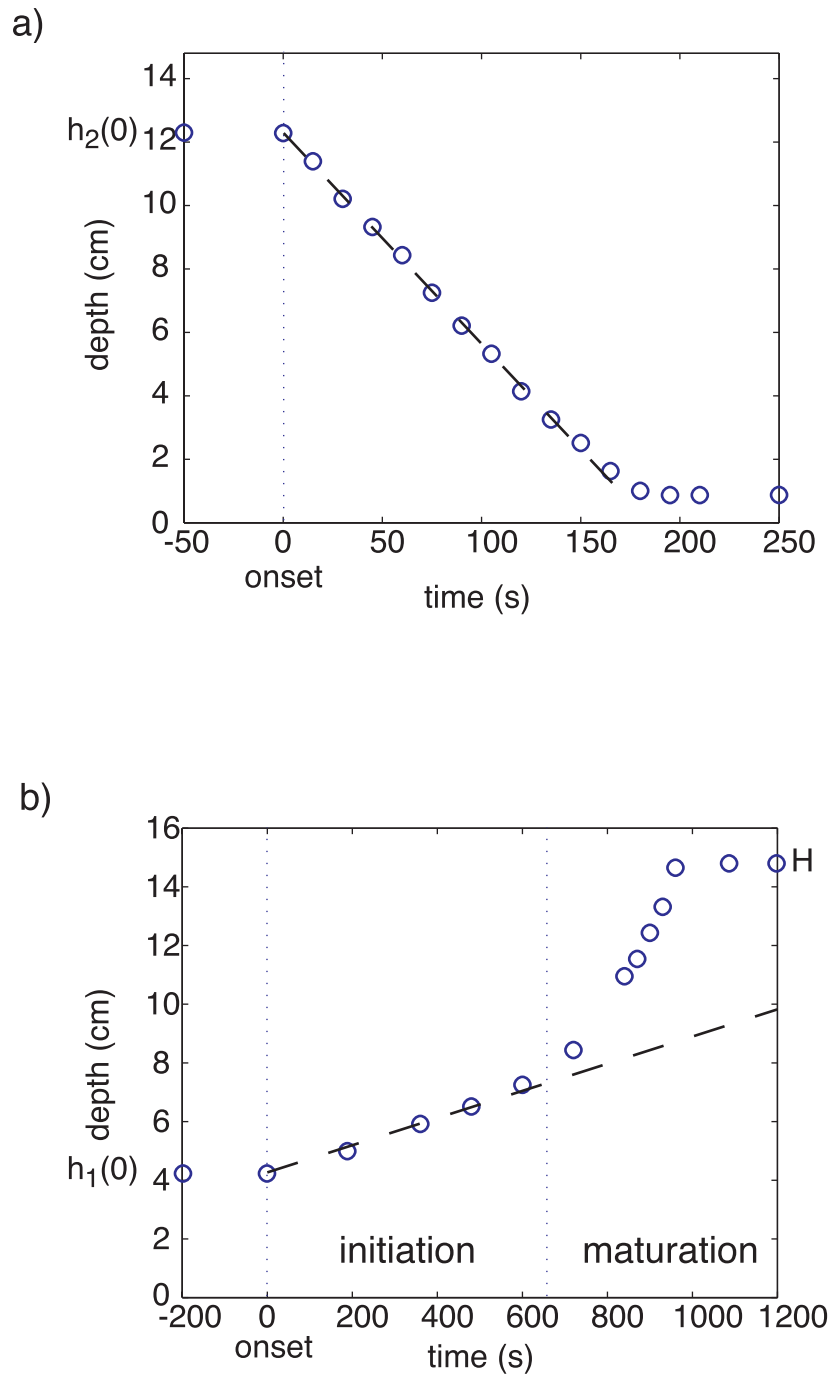
a)

b)

FIG. 3.23 – *Position of the interface as a function of time for a) a cavity plume in experiment n°27 (measured velocity $w = -4.0$ cm min^{-1}, dashed line) and b) a diapiric plume in experiment n°10 (measured initial velocity $w_{init} = 0.33$ cm min^{-1}, dashed line).*
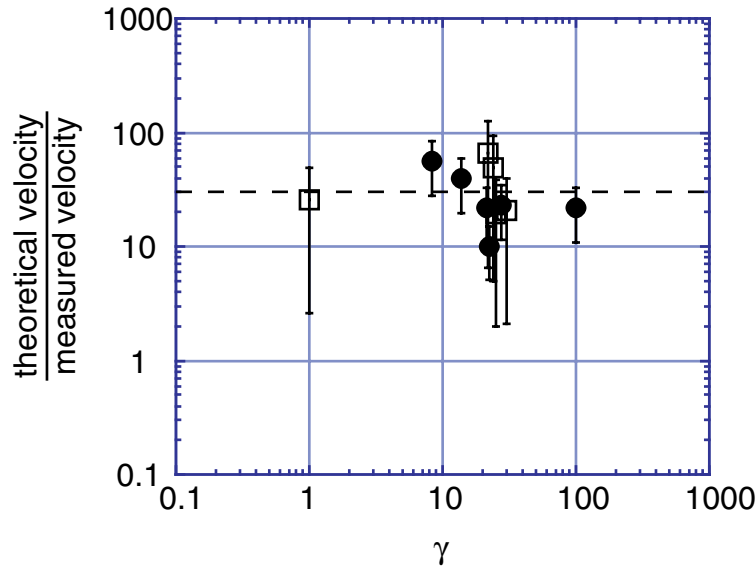
FIG. 3.24 – *Ratio of the theoretical velocity given by (3.36) to the measured velocity of diapiric plumes (filled circles) and cavity plumes (squares): the dashed line corresponds to a scaling factor $C_3 = 1/(32 \pm 18)$.*

of the tank as well as the large error bars on the theoretical speed do not allow to recover such a dependence.

As shown in figure 3.24, both initial velocities of diapiric plumes and constant velocities of cavity plumes are consistent with a scaling factor

$$C_3 = \frac{1}{32 \pm 18}. \tag{3.37}$$

The large scattering is mainly due to the difficulties in measuring $\Delta\rho_{eff}$ and d_{cav} (see §3.5.2 and §3.5.4).

3.5.6   Pulsation periods at large viscosity ratio.

As described in §3.5.2, the interface is destabilized when thermal effects are large enough to induce whole-tank motions in spite of thermal and mechanical diffusion as well as chemical stratification: for the initial destabilization, this means that the thermal

density contrast between the two fluids has to increase from 0 (initially isothermal fluids) to the critical value $\Delta\rho_\chi \, + \, \Delta\rho_c$, where $\Delta\rho_c$ depends on viscous and thermal diffusions (see §3.5.2). Then, the chemical signal $\Delta\rho_\chi$ remains stable, and the further rising and sinking motions only correspond to the gain and loss of the 'dynamic' part of the density difference $\Delta\rho_c$ (Herrick & Parmentier 1994): this is mostly controlled by the fluid with greater viscosity, which slows down the whole process. We can thus scale the observed pulsation periods at large viscosity ratio with the characteristics of layer 1. It turns out that the dependence is similar to the case of purely thermal convection:

$$t_{pulsation} = \frac{h_1^2}{\pi\kappa}(\frac{Ra_c}{Ra_1})^{2/3}, \tag{3.38}$$

where the experimental determination of Ra_c gives $Ra_c = 880 \pm 170$ (figure 3.25). Thermal plumes in layer 1 and thermochemical features have close periodicities. However, the critical Rayleigh number for whole-layer motions is smaller, in agreement with marginal stability analysis that predicts whole-layer regime to be the most unstable (see chapter 1). Moreover, these two convective features act on totally different lengthscales, since several small-scale thermal plumes are collected inside each large-scale thermochemical structure (see §3.5.4).

3.6   Time evolution: from whole-layer to one-layer convection.

Once the two-layer system is destroyed, thermochemical heterogeneities are dispersed over the whole volume of the tank: the mixture can then be considered as a single equivalent fluid, characterized by

  – a complicate viscosity, strongly spatially variable.
  – an 'internal' temperature field due to the thermal compensation of the chemical stratification between fluids 1 and 2.
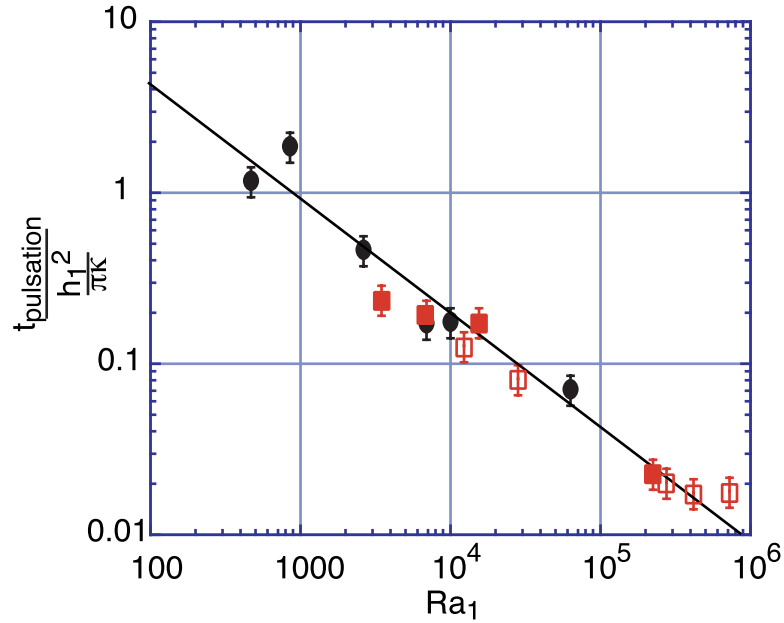
FIG. 3.25 – *Observed periods of initial system reconstruction depending on the Rayleigh number of the layer with greater viscosity. Circles stand for 'vertical oscillations' and squares for 'initial configuration reversals'; empty points correspond to cavity plumes and filled points to diapiric plumes. The line shows the best fit according to (3.38): $Ra_c = 880 \pm 170$.*

Looking at the destabilization of the outer thermal boundary layers, we must notice that the local viscosity of the equivalent fluid ν_{local} depends on the local proportion of fluids 1 and 2, and can thus range between ν_1 (fluid 1 alone) and ν_2 (fluid 2 alone). Since the excited period depends on $\nu_{local}^{2/3}$ (Howard 1964), a noisy wavelet analysis is recorded (figure 3.26c). Morover, as described in §3.5.6, the 'chemical' signal $\Delta\rho_\chi$, corresponding to the temperature variation

$$\frac{\Delta\rho_\chi}{\alpha\rho} = B \times \Delta T, \tag{3.39}$$

is stable, and does not act on convective motions that are controlled by additional fluctuations: the passage of a particle of fluid 1 anywhere in the tank thus differs from the passage of a particle of fluid 2 by $B \times \Delta T$, explaining the presence of large temperature variations over the whole depth (figure 3.26b).

Local stirring and ultimately chemical diffusion progressively annihilates the chemical difference between the two fluids, thus the associated temperature difference: the usual configuration finally comes back, characterized by

- fluctuations limited to the thermal boundary layers (figure 3.26b).
- two excited periods only, corresponding to plumes from hot and cold plates. Their periods scale as (Howard 1964)

$$\tau_i = \frac{1}{\pi\kappa}\left(Ra_c\frac{\kappa\nu_{mixed}}{\alpha g\Delta T_i}\right)^{2/3}, \tag{3.40}$$

where ν_{mixed} corresponds to the viscosity of the 'mixed' solution. The critical Rayleigh number determined experimentally $Ra_c = 1100 \pm 420$ (figure 3.27) is in close agreement with the theoretical value for 'free-rigid' boundary conditions 1100.65 (Chandrasekhar 1961) and with the value determined in §3.4.1 for the onset of thermal convection inside each layer.

The overall duration of thermochemical heterogeneities is very difficult to determine, since all dimensionless numbers directly influence it: the buoyancy number actually controls the 'chemical' resistance to stirring, the viscosity ratio controls the 'mechanical'
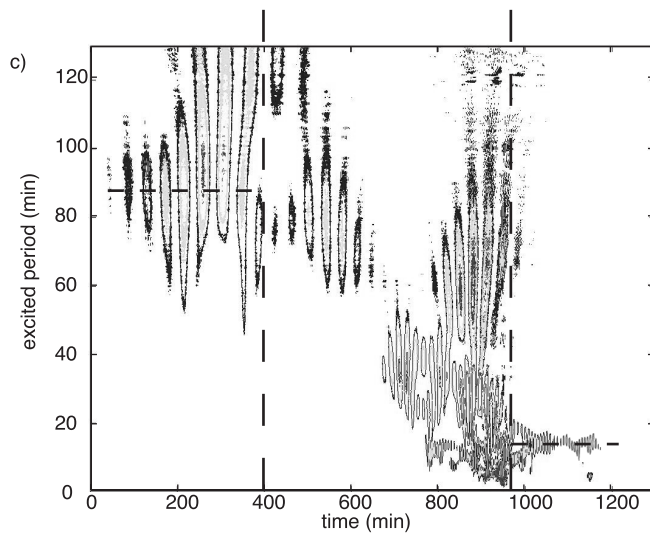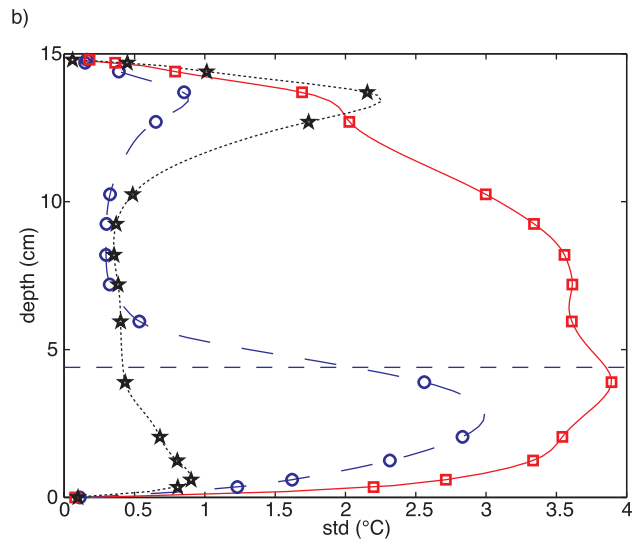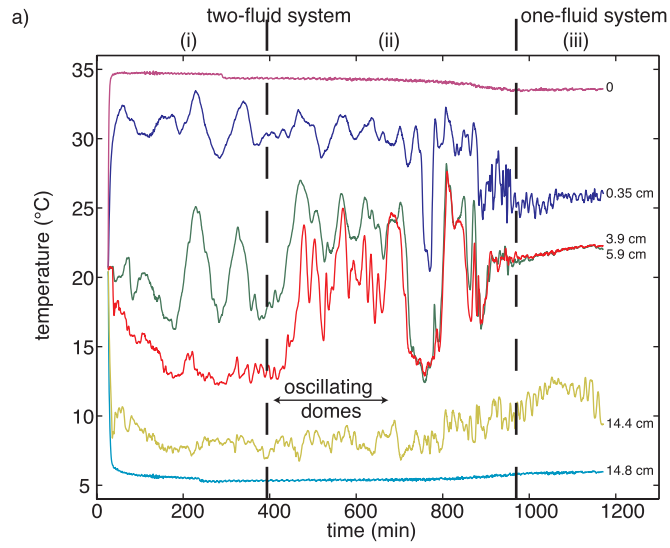
FIG. 3.26 – *Time evolution of experiment n°20. a) Temperature signals recorded by 6 thermocouples located on the vertical probe: their location is reported on the right (initial interface position: 4.4 cm). The time history can be divided in three parts: (i) the stratified phase, where purely thermal convection develops above and below a stable interface; (ii) the whole-layer phase, where the interface is destabilized and whole-tank convection takes place; (iii) the final one-layer phase, where the interior of the tank is well mixed (classical Rayleigh-Bénard convection). b) Standard deviation of the temperature signal (measured by the vertical probe) as a function of depth: circles correspond to the stratified phase (weak convection in layer 1, strong convection in layer 2), squares to the whole-layer phase and stars to the final one-layer phase. c) Wavelet analysis of the temperature signal in the hot thermal boundary layer (thermocouple located at 0.35 cm of the hot plate): contours follow most excited periods.*
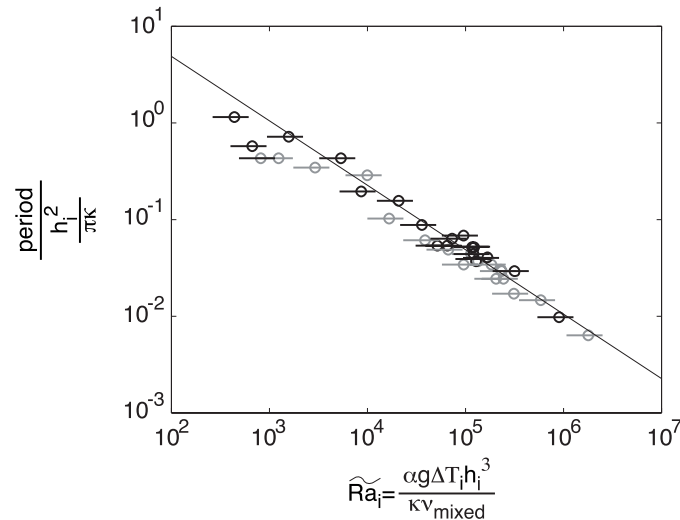

FIG. 3.27 – *Plumes periods measured after mixing in the vicinity of the cold plate (black) and of the hot plate (grey) depending on the local Rayleigh number. The line corresponds to the best fit according to (3.40) with a critical value $Ra_c = 1100 \pm 420$.*
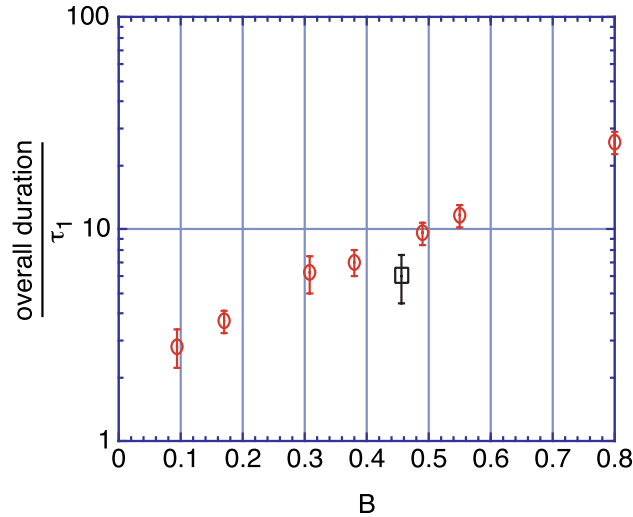
FIG. 3.28 – *Overall duration of chemical heterogeneities normalized by the typical convective time in layer 1 as a function of B for experiments n°9, 13, 18, 19, 20, 21, 22 (circles) and 2D experiment n°24 (square): in these experiments, only the buoyancy number significantly changes ($\gamma = 8 - 22$, $a = 0.25 - 0.30$, $Ra = 4.1 \times 10^6 - 1.5 \times 10^7$).*

resistance to stirring, the layer depth ratio controls the relative volume of heterogeneities and the Rayleigh number controls the convective stirring power. Studying the variation of the overall duration with all dimensionless numbers is beyond the scope of this paper. Moreover, with our experimental setting, only the buoyancy number can be changed independently of all other parameters: as shown in figure 3.28, the overall duration then exhibits a strong exponential dependence on B. The chemical heterogeneities can thus persist for very long time compared to the characteristics of thermal convection.

3.7   Conclusion.

At large Rayleigh number, motions in a two-fluid system are due to three distinct phenomena: purely thermal convection inside layer 1, purely thermal convection inside layer 2, and large-scale thermochemical convection, where both layers are involved.

Experiments reported in this paper have supplemented the study of the two-layer Bénard problem in the particular case where the interface between the two fluids largely deforms. Two different mechanisms have been described:

- dynamic topography appears from the local and partial intrusion into one fluid of purely thermal features coming from the other one.
- a Rayleigh-Taylor type overturn takes place at the interface when the system is unstable according to marginal stability ($B \leq B_c(\gamma, a)$, see chapter 1), or when the most viscous layer convects and the effective buoyancy number based on the real chemical and temperature profiles becomes lower than 1.

Both regimes are transient and systematically evolve towards one-layer Rayleigh-Bénard convection. Heterogeneities are however registered during very long times compared to typical time-scales of thermal convection. Further experiments are now necessary to understand and quantify the influence of viscosity and density contrasts on mixing processes of such active heterogeneities.

Deuxième partie

Applications aux systèmes planétaires.

Introduction.

Les données géochimiques couplées avec les études de l'efficacité du mélange dans la Terre démontrent la présence d'hétérogénéités actives à grande échelle, mais n'en précisent ni l'origine, ni la taille, ni la localisation, ni les caractéristiques (voir par exemple la revue récente de Van Keken, Hauri & Ballentine 2002). Notre étude expérimentale permet de décrire et quantifier les différents régimes possibles dans l'espace des paramètres approprié à la Terre. Elle propose en outre une explication dynamique simple à divers modèles de convection mantellique proposés jusqu'à présent : lors de l'évolution typique d'une expérience à deux couches (voir figure 1), le régime stratifié apparaît tout d'abord, dans lequel la convection s'organise au-dessus et en-dessous de l'interface plane (modèle 'historique' à deux couches : DePaolo & Wasserburg 1976 ; Allègre, Othman, Polve & Richard 1979 ; O'Nions, Evensen & Hamilton 1979) ; de la topographie dynamique se développe ensuite, formant dans un premier temps de petites ondulations en profondeur (modèles de Kellog, Hager & van der Hilst 1999 et de Samuel & Farnetani 2002) ; ces déformations légères grandissent progressivement, donnent naissance à de larges 'piles' dans les zones chaudes montantes (modèles de Tackley 1998 et de Hansen & Yuen 2000), et se déstabilisent finalement sous la forme de grands dômes oscillant sur toute l'épaisseur du système (modèle de Davaille 1999b) ; enfin le mélange prend place, créant des 'blobs' actifs encapsulés dans le système convectif (Manga 1996 ; Becker, Kellogg & O'Connell 1999 ; Merveilleux du Vignaux & Fleitout 2001), dont la taille diminue progressivement jusqu'à obtenir un système homogène.
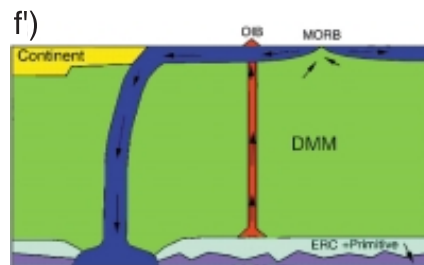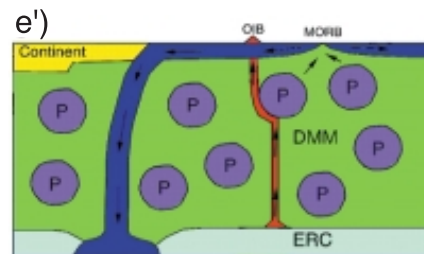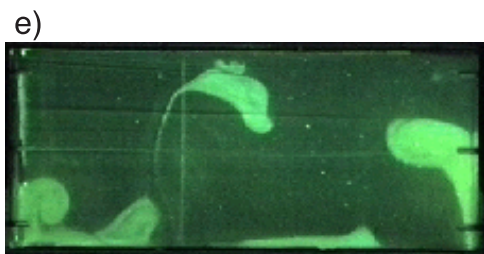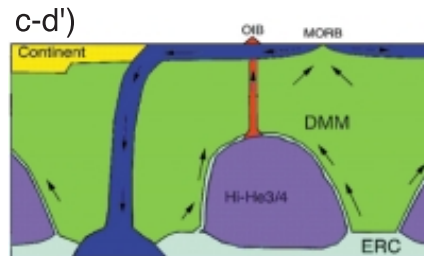
a) plaque froide T$_2$

fluide 2 (ρ_2, ν_2, h$_2$)

fluide 1 (ρ_1, ν_1, h$_1$)

plaque chaude T$_1$

b) cannes de thermocouples

c)

d)

e)

f)

a')

b')

c-d')

e')

f')
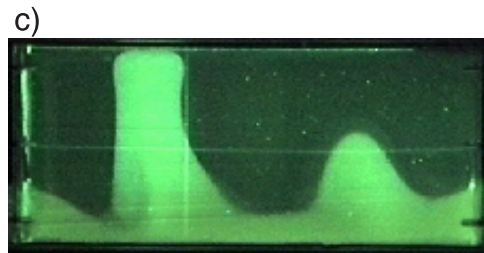
F$_{IG}$. 1 – *Évolution dans le temps de l'expérience n°52 et comparaison avec les modèles de dynamique du manteau proposés jusqu'à présent (schémas de Tackley 2000a : ERC=croûte océanique recyclée ; DMM=manteau source des MORB) : a) $t = 0$ min ; b) $t = 15$ min ; c) $t = 20$ min ; d) $t = 30$ min ; e) $t = 120$ min ; f) $t = 240$ min ; a') manteau stratifié à 660 km (DePaolo & Wasserburg 1976 ; Allègre, Othman, Polve & Richard 1979 ; O'Nions, Evensen & Hamilton 1979) ; b') couche primitive profonde (Kellog, Hager & van der Hilst 1999 ; Samuel & Farnetani 2002) ; c-d') 'piles' primitives sous les zones chaudes montantes (Tackley 1998 ; Hansen & Yuen 2000) et/ou dômes oscillants (Davaille 1999b) ; e') 'blobs' visqueux (Manga 1996 ; Becker, Kellogg & O'Connell 1999 ; Merveilleux du Vignaux & Fleitout 2001) ; f') convection à une couche.*

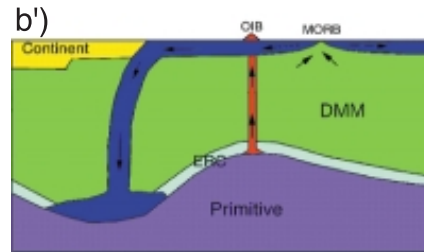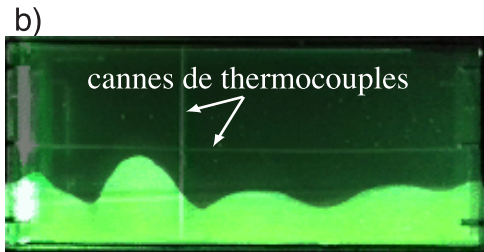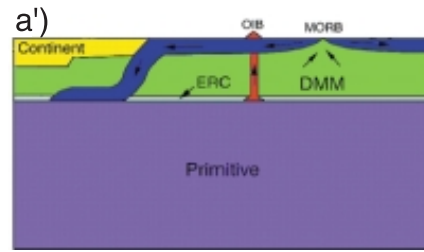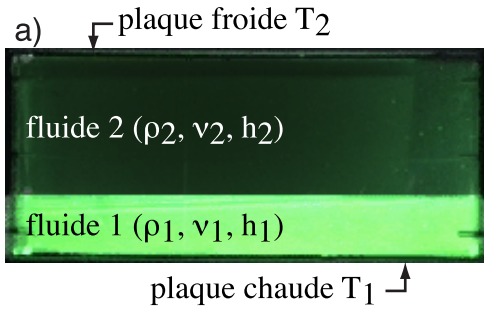Un tel modèle met donc tout particulièrement l'accent sur l'évolution dans le temps du régime convectif. Quantitativement, nous démontrerons dans le premier chapitre qu'il pourrait s'accorder avec l'entraînement progressif puis la déstabilisation d'une couche inférieure 'primitive' sur toute l'histoire de la Terre (Davaille, Le Bars & Carbonne 2002), mais également avec une succession de cycles formation/déstabilisation d'une couche profonde créée à la base du manteau par la subduction (Christensen & Hofmann 1994).

Le régime de pulsations (figure 1c, d) semble spécialement convenir à la configuration actuelle de notre planète, comme nous le verrons dans le second chapitre : ainsi, d'après nos lois d'échelle, les superswells Pacifique et Africain peuvent s'expliquer dynamiquement par la montée de dômes dix fois moins visqueux que le manteau environnant. Le signal sismique lié à de telles structures thermochimiques correspond quantitativement aux modèles tomographiques (voir par exemple figure 2).

Plus généralement, les pulsations thermochimiques offrent un cadre théorique nouveau à l'interprétation des grands cycles géologiques enregistrés sur les planètes de type terrestre à l'échelle de plusieurs centaines de millions d'années : ce sera l'objet du troisième chapitre. Une estimation du flux de chaleur lié aux dômes démontre que ces derniers induisent des variations du même ordre de grandeur que le flux moyen : en surface, les
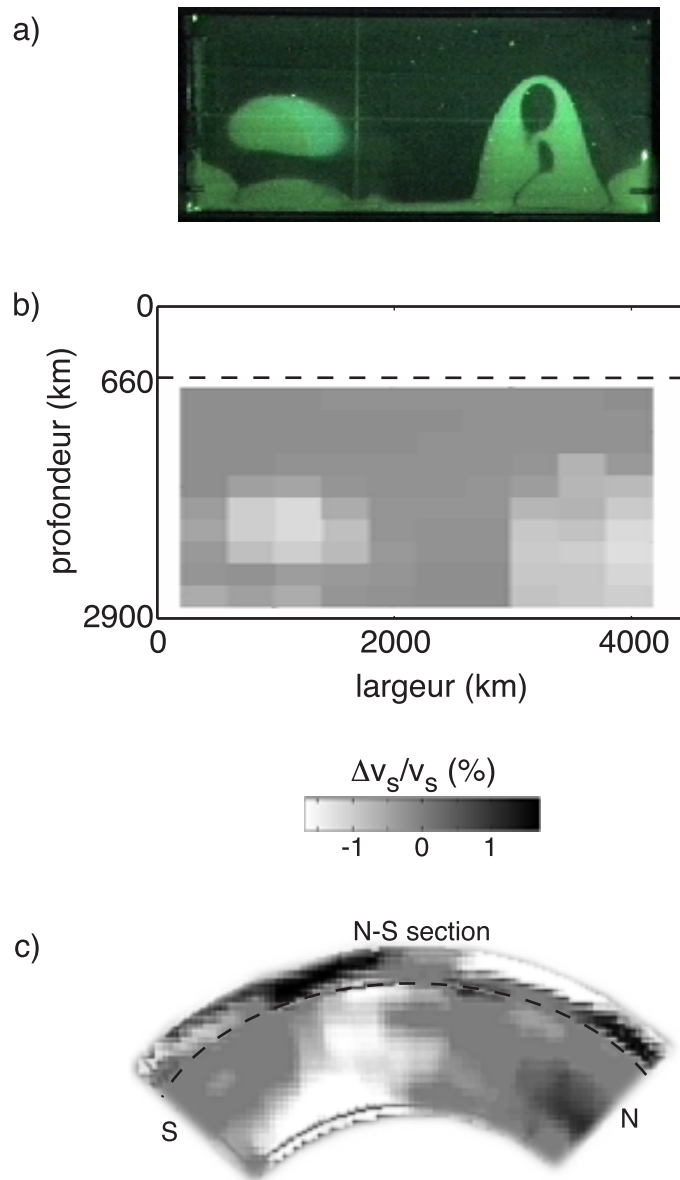
FIG. 2 – *a) Photographie du régime de pulsations dans l'expérience nº52 ; b) signal tomo-graphique en ondes S associé à a), mis à l'échelle du manteau inférieur ; c) coupe tomo-grapique nord-sud sous le superswell Africain (d'après le modèle SAW24B16 en ondes S de Mégnin & Romanowicz 2000).*

pulsations pourraient donc se traduire par des périodes de très forte activité volcanique, conduisant par exemple au renouvellement intégral de la surface de Vénus il y a 500 millions d'années (Strom, Schaber & Dawson 1994) ; à la base du manteau terrestre, les modifications importantes des conditions aux limites thermiques pourraient modifier la dynamique du noyau et expliquer ainsi la présence de longues périodes sans inversion du champ magnétique (Courtillot & Besse 1987 ; Larson & Olson 1991).

Notre modèle analogique semble donc prometteur, à la fois qualitativement et quantitativement. Il est toutefois impossible d'intégrer dans notre cuve expérimentale l'ensemble des complications naturelles existantes. La plupart d'entre elles (par exemple la présence des continents en surface, la chauffage interne, la transition de phase à 660 km, les variations des propriétés physiques avec la température et la profondeur, que nous étudierons au chapitre 4) ne modifient pas fondamentalement la physique du système à deux couches. En revanche, la tectonique des plaques, qui constitue 'l'ordre 0' de la convection mantellique, demande maintenant à être prise en compte (Tackley 2000a).

Chapitre 1

Évolution des figures de convection dans le manteau terrestre.

1.1 Introduction.

Plate tectonics is the major convective feature observed at the Earth's surface: hot mantle rocks rise at the mid-ocean ridges, and cold plates sink at the subduction zones, thus imaging large convective cells comparable to the ones observed in classical Rayleigh-Bénard convection (Bénard 1901; Rayleigh 1916). However, the complete process is not that simple: a realistic model of mantle convection must reconcile conflicting geochemical evidences demonstrating the persistence of separated reservoirs and geophysical evidences suggesting whole-mantle motions.

The systematic differences in isotopic composition of magma erupted in mid-ocean riges (MORB) and intra-plate volcanoes (OIB) actually require the existence of large-scale heterogeneities for billions of years (see for instance reviews by Zindler & Hart 1986 and Hofmann 1997). Mass balance based on the bulk silicate Earth composition (Allègre, Hamelin, Provost & Duprè 1987; O'Nions & Tolstikhin 1994) as well as heat budgets (McKenzie & Richter 1981; Kellog, Hager & Van der Hilst 1999) also suggest

the presence of an hidden reservoir radiogenically enriched. Its origin, size, form and location are however not constrained. Initially, the interface between the two layers has been located at the major seismic discontinuity detected at 660 km depth, which is now known to correspond to a phase transition (Ito & Takahashi 1989). In this '660-layered' model (DePaolo & Wasserburg 1976; Allègre, Othman, Polve & Richard 1979; O'Nions, Evensen & Hamilton 1979), the upper mantle has been depleted by the extraction of the continental crust and is the source of MORB; it convects separately from the lower primitive mantle producing OIB. The absence of important mass transfers between the two layers is however contradicted by recent tomographic models that exhibit subducting plates all the way down to the core-mantle boundary (Grand, Van der Hilst & Widiyantoro 1997; Van der Hilst, Widiyantoro & Engdahl 1997; Bijwaard, Spakman & Engdahl 1998; but see also Fukao, Widiyantoro & Obayashi 2001). Such motions over the whole mantle depth are expected to mix large-scale passive heterogeneities well within the lifetime of the Earth (Hofmann & McKenzie 1985; Christensen 1989; Van Keken & Zhong 1999; Ferrachat & Ricard 2001), and thus imply a 'one-layer' model.

None of these historical models is capable of taking into account all observations, but each introduces fundamental aspects of the problem. Various configurations have then been imagined. Some studies have focused on the effects of the 660 km phase transition, proposing a recent change in the style of convection (Davaille 1996; Allègre 1997; Davaille 1999b) or an intermittent one-layer/660-layered model, where catastrophic flushing events periodically take place through it (Machetel & Weber 1991; Tackley, Stevenson, Glatzmaier & Schubert 1993; Weinstein 1993; Stein & Hofmann 1994; Condie 1998). Other have described the importance of subduction, which continuously reintroduces heterogeneities forming a new layer at the base of the mantle (Gurnis 1986; Christensen & Hofmann 1994; Albarède 1998; Coltice & Ricard 1999). Numerous works have also proposed the existence of a second reservoir with various geometries, independently of the 660 km boundary: it could take the form of an ondulating deep layer (Kellog, Hager & Van der Hilst 1999; Samuel & Farnetani 2002), of two giant piles under Africa and French Polynesia respec-

tively (Tackley 1998; Hansen & Yuen 2000), of pulsating domes moving up and down quasi-periodically (Davaille 1999b), or of viscous blobs encapsulated in the whole convecting mantle (Manga 1996; Becker, Kellogg & O'Connell 1999; Merveilleux du Vignaux & Fleitout 2001).

The key feature for reconciling the data in a dynamic feasible model is to consider the time evolution of the system: geochemical evidences actually result from processes taking place over millions of years, whereas tomographic images correspond to an instantaneous 'scanner' of the Earth's interior.

In our study, we address the problem of mantle convection from a 'fluid dynamics' point of view through laboratory experiments. Since we know that the Earth's mantle is non-homogeneous, we focus on a simple case of heterogeneous thermal convection: two layers of fluid with different densities and viscosities are superimposed and subjected to a destabilizing temperature contrast. The characteristics of heterogeneities in the Earth's mantle are unknown. In the context of our experimental study, it means that all values of dimensionless numbers B, Ra_i, γ and a are possible, and any behaviours described in the previous chapter, as well as those described by Richter & McKenzie (1981), Olson & Kincaid (1991), Davaille (1999a and b) and in numerical simulations by Tackley (1998 and 2002), Kellog, Hager & van der Hilst (1999), Montague & Kellog (2000), Hansen & Yuen (2000), Samuel & Farnetani (2002), can be excited: the only constraint is that the global Rayleigh number is large, at least 10^5.

1.2 Stratified versus whole-layer large-scale regimes.

When the buoyancy number is large ($B > 0.3 - 0.5$, see figure 1.1), the system is stable (at least temporarily) and convection develops above and below the interface, as described in layered mantle models (figure 1.2a, a'). Besides, small-scale purely thermal convection can also develop inside layer i, provided the layer Rayleigh number is large enough ($Ra_i > 10^3$). Provided $B \leq 1$, convective features then partially deform the
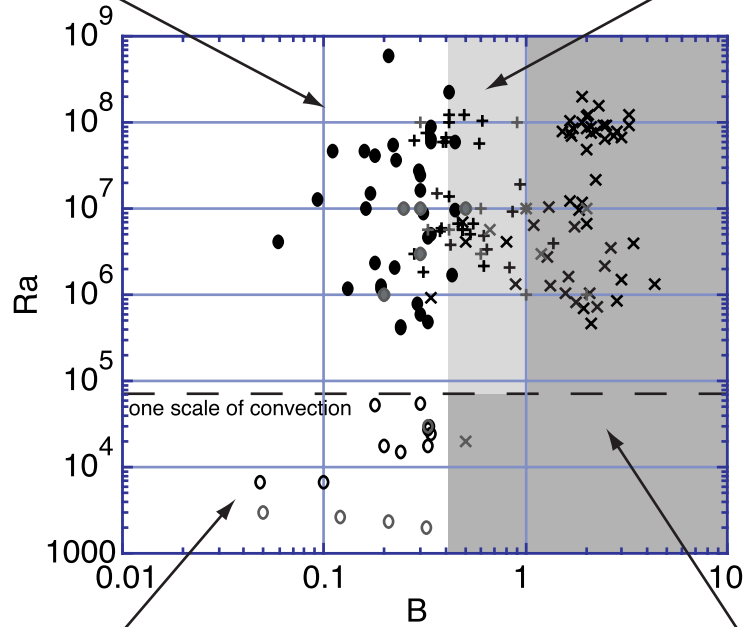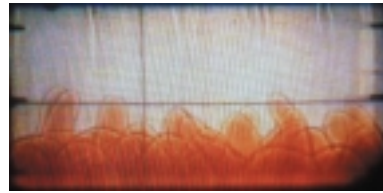
small-scale thermal plumes

+
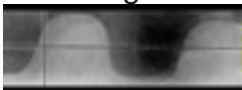large-scale
thermochemical dome

interface deformations

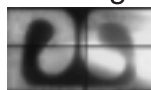

oscillatory onset

then
travelling waves   mixing

   and/or

convection above/below
the flat interface

FIG. 1.1 – *Observed regime as a function of Rayleigh and buoyancy numbers: circles re-present whole-layer convection (empty circles for experiments close to marginal stability, where only one scale of convection takes place), '+' signs stratified convection with inter-face deformations, which eventually becomes unstable (light shaded area), and '×' signs stratified convection throughout the whole duration of the experiment (dark shaded area). In black, experiments by Richter & McKenzie (1981), Davaille (1999a and b) and from this work; in gray, numerical calculations by Schmeling (1988), Tackley (1998 and 2002), Kellog, Hager & van der Hilst (1999), Montague & Kellog (2000), Hansen & Yuen (2000) and Samuel & Farnetani (2002). As far as the Earth is concerned, B is unknown and Ra ranges between 10^5 and 10^8 typically.*

interface with an amplitude that rapidly decreases when B increases, a mechanism that we call 'dynamic topography': in the context of Earth's models, small deformations would correspond to the deep ondulations described by Kellog, Hager & van der Hilst (1999) and Samuel & Farnetani (2002) (figure 1.2b, b'); piles of Tackley (1998) could possibly correspond to larger deformations (figure 1.2c-d').

When the buoyancy number is small ($B \leq 0.3 - 0.5$, see figure 1.1), the system is fully unstable and convection develops over the whole depth of the tank. The influence of the viscosity ratio γ is then fundamental: when $1/5 < \gamma < 5$ typically, overturning and immediate stirring operate, corresponding to the one-layer model. However, several pulsations are observed for $\gamma > 5$ or $\gamma < 1/5$ typically, as described in the doming model of Davaille (1999b) (figure 1.2c, d, c-d'): the piles observed at present (Tackley 1998; Hansen & Yuen 2000) could then correspond to an instantaneous picture of these oscillating domes. Moreover, even when the two-layer system is destroyed, chemical heterogeneities still exist inside the tank, corresponding to the 'primitive blobs' shown in figure 1.2e, e' (Manga 1996; Becker, Kellogg & O'Connell 1999; Merveilleux du Vignaux & Fleitout 2001). For large viscosity ratios, one-layer convection (figure 1.2f, f') is only the final state of whole-layer convection.
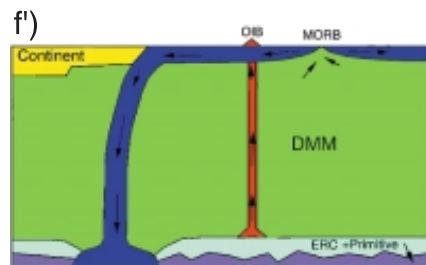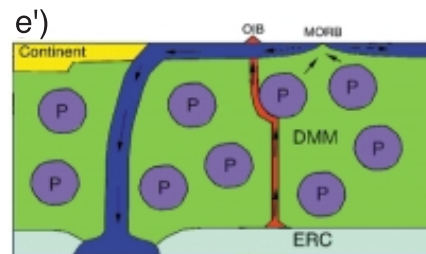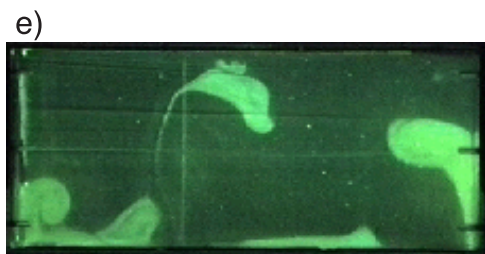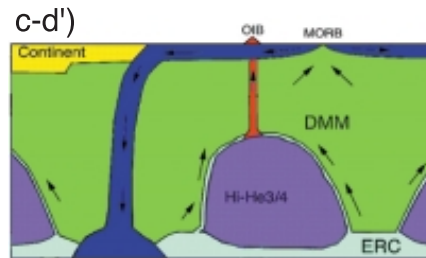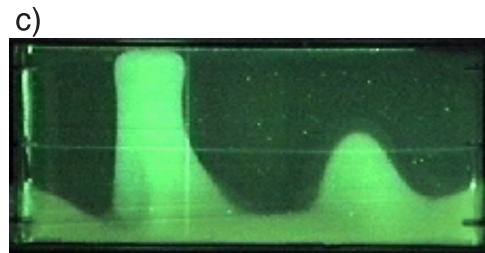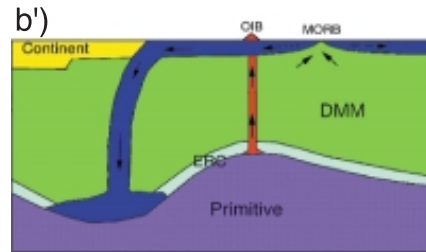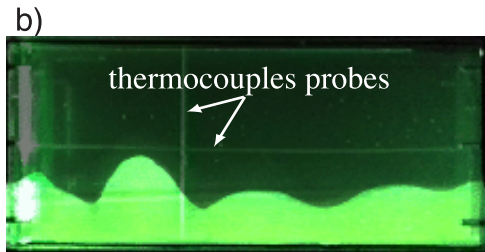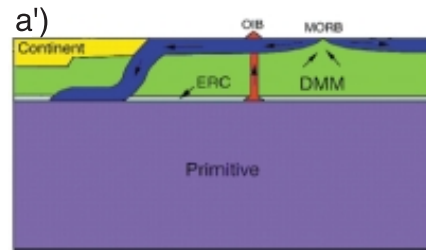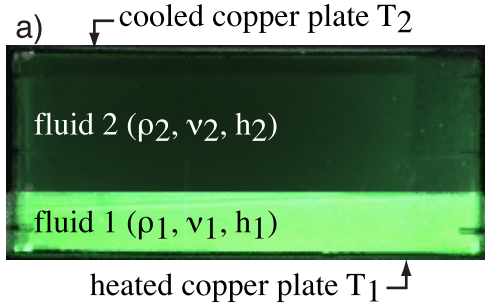
FIG. 1.2 – *Time evolution of experiment nº52 and comparison with various proposed mantle models (sketches from Tackley 2000a: DMM = depleted MORB mantle; ERC = enriched recycled crust): a) t = 0 min; b) t = 15 min; c) t = 20 min; d) t = 30 min; e) t = 120 min; f) t = 240 min; a') 660-layered mantle (DePaolo & Wasserburg 1976; Allègre, Othman, Polve & Richard 1979; O'Nions, Evensen & Hamilton 1979); b') ondulating deep layer (Kellog, Hager & van der Hilst 1999; Samuel & Farnetani 2002); c-d') primitive piles (Tackley 1998; Hansen & Yuen 2000) and oscillating doming (Davaille 1999b); e') primitive blobs (Manga 1996; Becker, Kellogg & O'Connell 1999; Merveilleux du Vignaux & Fleitout 2001); f') one-layer model.*

1.3 Hotspots formation.

Hotspots (i.e. intra-plate volcanoes) are often explained by the presence of small plumes rising from a thermal boundary layer somewhere in the deep Earth (Morgan 1972). A simple model locating this boundary at the base of the mantle is however incapable of explaining the chemical diversity of the magmas erupted at the surface (Hofmann 1997) and the physical characteristics of all natural situations (some structures are too cold or too weak, Albers & Christensen 1996).

In our two-layer experiments, we observe various small-scale rising features that could account for the numerous natural structures (Davaille, Girard & Le Bars 2002; Courtillot, Davaille, Besse & Stock 2002). In the stratified regime, two situations could generate very stable and long-lived hotspots as for instance Louisville (120 My) and Hawaii (75 My):

– when both layers convect, entrainment patterns take place at the interface under the form of two-dimensional sheets in the most viscous layer and steady tubular plumes in the less viscous one (figure 1.3a, Davaille 1999a).

– when one layer is thinner than the corresponding thermal boundary layer, plumes appear coming from the destabilization of the thermal boundary layer as in classical Rayleigh-Bénard convection (see part I §2.2, pp. 92); however, as shown in figure
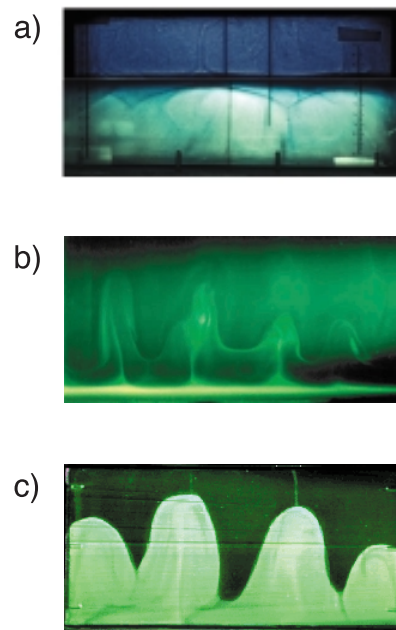
FIG. 1.3 – *Various types of hotspots observed in two-layer experiments: a) entrainment patterns at the interface of a stratified system (Davaille 1999a); b) thin stratified layer; c) small plume on the top of an oscillating dome.*

1.3*b*, they locally deform the interface into cusps and entrain a thin film of the stratified layer by viscous coupling: both effects act to anchor the plumes (Namiki & Kurita 1999; Davaille, Girard & Le Bars 2002), which persist until the whole stratified layer is eroded.

In the pulsatory regime, plumes form on the top of oscillating domes (figure 1.3*c*): their duration is limitated by the pulsatory behaviour of the large-scale structure, and they could give rise to short-tracks hotspots as observed in the Pacific (McNutt 1998).

In all cases, those rising plumes sample mainly the bottom thermal boundary layer on the upper reservoir and entrain a small portion (at most 10%) of the material located below: any interface inside the mantle could thus give rise to hospots with different intensity, duration and geochemical composition.

1.4 Temporal evolution of a two-layer mantle.

The most striking feature is that all proposed Earth's mechanisms described above can successively take place during a typical experiment: as shown in figure 1.2, the thermal and/or chemical temporal evolutions of the system give rise to a fully stratified regime, then to small interface ondulations, then to large piles, then to whole-tank pulsations, then to isolated blobs and finally to one-layer convection. Such an evolution was also partly observed in numerical simulations by Hansen & Yuen (2000), starting from an linear chemical profile. The Earth's regime is not in a steady state, but has evolved through time.

In addition to this qualitative result, we can also demonstrate that such a process is quantitatively plausible in the Earth: to do so, we will now study two situations, respectively with a lower 'primitive' reservoir (i.e. created in the early Earth's history) and with a reservoir progressively growing through oceanic crust subduction. Precise parameters in both cases are totally unknown; our purpose is not to describe the 'real' story, but to illustrate the feasibility of such an evolutive dynamics in the parameter range likely to be

relevant to the Earth.

1.4.1   Evolution of a primitive layer.

As observed in the experiments, an initially stratified two-layer system progressively evolves towards the whole-layer regime because of entrainment through the interface: each layer continuously incorporates thin tendrils of the other, and no purely 'primitive' reservoir can persist. Scaling laws defined by Davaille (1999a) demonstrates that the typical duration of the stratified case depends on B, γ, Ra_i, and initial conditions, which are all unknown for the Earth. In all cases however, the mantle is capable of erasing a minimum of 2% chemical stratification through its history (Davaille, Le Bars & Carbonne 2002).

Figure 1.4 shows a simple example of a possible Earth's evolution, taking an initial interface location at 660 km depth, an initial upper mantle viscosity of 10^{20} Pa s, an initial lower mantle viscosity of 100×10^{20} Pa s, corresponding to initial Rayleigh numbers $Ra_1 \sim 7.2 \times 10^6$ and $Ra_2 \sim 4.5 \times 10^6$, and an initial stratification of 3%. In this case, the mantle erases the whole 3% in 5400 My; we can also notice that the depth of the interface progressively sinks towards the core. However, before it reaches it, the density contrast becomes small enough for the whole-system regime to be excited ($B_{eff} < 1$): at onset, $6 < \gamma < 24$ and several pulsations are then possible. The lower layer then forms large encapsulated blobs that will persist during millions of years (Manga 1996; Becker, Kellogg & O'Connell 1999; Merveilleux du Vignaux & Fleitout 2001), until they are finally erased by advection and chemical diffusion. Our simple model thus demonstrates that thermo-chemical features of pristine origin but not primitive composition may survive over the entire history of the Earth.
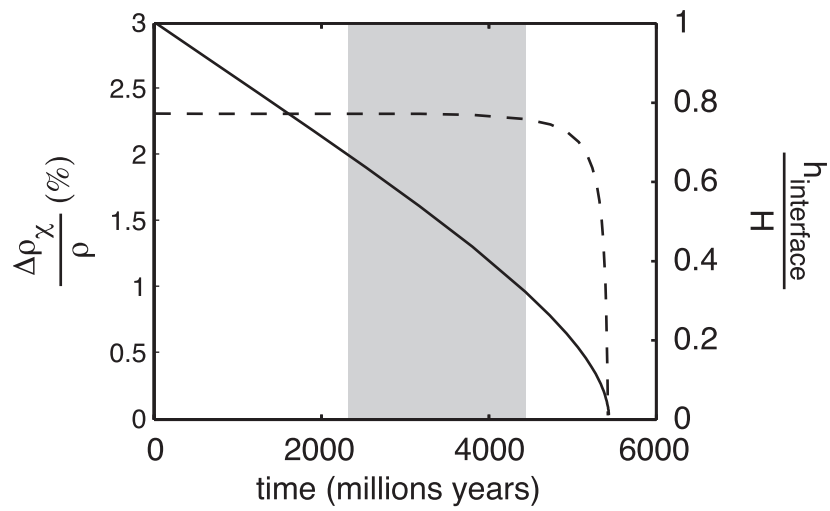
FIG. 1.4 – *Typical evolution of the density contrast between the two layers (solid line, left scale) and the interfacial depth (dashed line, right scale), obtained with the scaling laws of Davaille (1999a). The interface was originally located at the transition zone, the initial density contrast was 3% and the initial viscosity contrast 100. The shaded area represents the domain of possible onset of the whole-system regime.*

1.4.2   Destabilization of a layer formed by subduction.

Subducted oceanic crust is colder and chemically denser than the surrounding mantle: it may therefore segregate at the bottom of the convecting mantle and progressively build a new reservoir (Gurnis 1986; Christensen & Hofmann 1994; Albarède 1998; Coltice & Ricard 1999). At the same time however, heat flux from the core progressively warms up this layer, possibly leading to its destabilization. Such a mechanism can be quantified, using results from our experiments to determine the thermochemical regime of this two-layer system.

Let ϕ be the volumic rate of subduction, $\Delta\rho_\chi$ the chemical stratification, T_0 the plate temperature at the base of the mantle (to be compared with the surrounding temperature T_{mantle}) and Q the heat flux from the core. The growing layer thickness $h(t)$ increases through time because of the material brought by subduction:

$$S\frac{dh}{dt} = \phi, \tag{1.1}$$

where S is the surface over which the layer forms. Its mean temperature $T(t)$ also evolves because of heating from the core and cooling from the added subducted material. A simple balance per unit surface indicates that the heat accumulated at time $t + dt$ over the thickness $h + dh$ is equal to the heat accumulated at time t over the thickness h plus the heat from the subducted plate added during dt (thickness dh, temperature T_0) plus the heat coming from the core:

$$\rho C_p (T + dT) \times (h + dh) = \rho C_p T \times h + \rho C_p T_0 \times dh + Qdt, \tag{1.2}$$

where C_p is the specific heat per unit mass, so

$$h\frac{dT}{dt} = \frac{Q}{\rho C_p} + (T_0 - T)\frac{dh}{dt}. \tag{1.3}$$

We do not know the time variations of the various parameters ϕ, Q and T_0. A simplified model can be proposed taking them constant. Then supposing $h(t = 0) = 0$, (1.1)

implies

$$h(t) = \frac{\phi}{S}t, \tag{1.4}$$

and from (1.3),

$$t\frac{dT}{dt} = \frac{QS}{\rho C_p \phi} + T_0 - T. \tag{1.5}$$

This model is too simple to follow the entire evolution of the growing layer. However, the differential equation (1.5) indicates that starting from T_0, the mean temperature increases towards the maximum value

$$T_{max} = \frac{QS}{\rho C_p \phi} + T_0. \tag{1.6}$$

We can then propose a necessary condition for the layer destabilization: as described previously, a chemically stratified layer becomes unstable provided its effective buoyancy number reaches a critical value B_c. In the present case, it means that the mean temperature of the growing layer reaches a critical value T_c given by

$$\frac{\Delta \rho_\chi}{\alpha \rho (T_c - T_{mantle})} = B_c, \tag{1.7}$$

so

$$T_c = \frac{\Delta \rho_\chi}{\alpha \rho B_c} + T_{mantle}. \tag{1.8}$$

According to (1.6) and (1.8), the destabilization of the growing layer is possible provided

$$T_{max} > T_c. \tag{1.9}$$

The heat flux from the core has thus to be larger than a critical value, which increases with the chemical stratification $\Delta \rho_\chi$, the thermal anomaly of plates at the base of the mantle $T_{mantle} - T_0$ and the flux of subducted material ϕ:

$$Q > Q_c = (\frac{\Delta \rho_\chi}{\alpha \rho B_c} + T_{mantle} - T_0)\rho C_p \frac{\phi}{S}. \tag{1.10}$$

For the present state of subduction, Christensen and Hofmann (1994) indicate $\Delta\rho_\chi/\rho \sim 3\%$ and $\phi \sim 1/6 \times 20 \ \mathrm{km}^3 \ \mathrm{y}^{-1}$. The thermal anomaly of plates at the base of the mantle can be estimated from tomographic models (Li & Romanowicz 1996; Masters, Johnson, Laske & Bolton 1996; Grand, Van der Hilst & Widiyantoro 1997; Su & Dziewonski 1997; Van der Hilst, Widiyantoro & Engdahl 1997; Bijwaard, Spakman & Engdahl 1998; Mégnin & Romanowicz 2000), which exhibit typical velocity anomalies of $+1\%$ corresponding to a temperature contrast $T_{mantle} - T_0 \sim 100$ K. Taking $\rho \sim 4000 \ \mathrm{kg} \, \mathrm{m}^{-3}$, $C_p \sim 1000 \ \mathrm{J} \, \mathrm{kg}^{-1} \, \mathrm{K}^{-1}$, $\alpha \sim 10^{-5} \ \mathrm{K}^{-1}$ at the base of the mantle (Poirier 1991), $S \sim 1.5 \times 10^8 \ \mathrm{km}^2$ (the present surface of the Earth's core) and $B_c \sim 1$ (which is actually an upper bound based on convection in the growing layer, see part I §3.5.2, pp. 121), (1.10) gives a critical flux for a possible destabilization

$$Q_c \sim 10^{-2} \ \mathrm{W} \, \mathrm{m}^{-2}, \tag{1.11}$$

of the same order of magnitude than the present estimations of the core flux ($Q \sim 2 \times 10^{-2} \ \mathrm{W} \, \mathrm{m}^{-2}$, Poirier 1991). According to this oversimplified illustrating model, a destabilization is thus possible (see also figure 1.5). Then, the whole-layer dynamics takes place as previously described, consisting in several pulsations followed by overturning and stirring; simultaneously, the subduction process goes on and a new layer grows.

All the values taken in this illustration are present-day estimations, and may have been totally different in the past (see for instance Davies 1985): various scenarios can thus be imagined through the Earth's history.
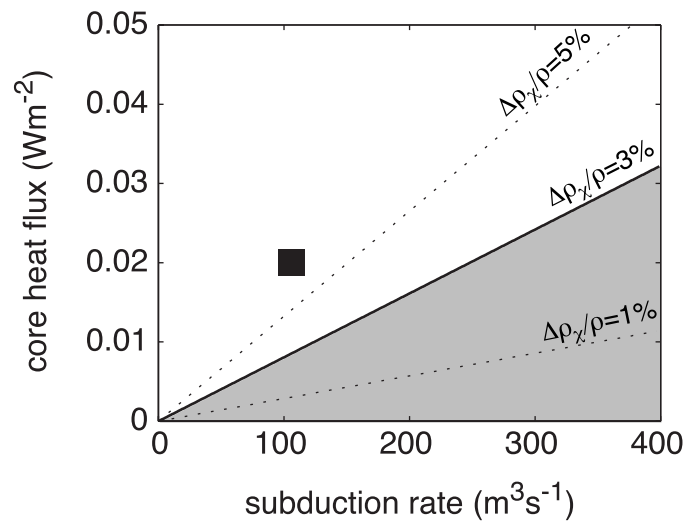
FIG. 1.5 – *Critical value of the core heat flux for layer destabilization as a function of the subduction rate for a chemical density contrast of* 3% *(curves for* $\Delta\rho_\chi/\rho = 1\%$ *and* 5% *are also reported in dotted lines): in the white area, the destabilization of the growing layer is possible; in the shaded area, the growing layer is stable. The black square shows present estimated values.*

Chapitre 2

Origine dynamique des superswells sur Terre.

2.1 The case study of the last Pacific pulsation.

The mantle beneath the Pacific plate seems to be confined in a simple natural tank: during the last 150 millions years, it has been isolated from the rest of the mantle by its subduction belt (Richards & Entgebretson 1992), and no continent has perturbed its upper thermal boundary. It is thus the best place for us to apply the scaling laws defined in the first part.

The 'Pacific superswell' (McNutt & Fisher 1987) is a huge zone about 5000 km large located in the south-central Pacific (figure 2.1) and characterized by a concentration of intra-plate volcanism and by an elevated topography, as much as 1 km higher than usual sea-floor of the same age (McNutt 1998). The mantle located below it exhibits anomalous slow velocities all the way down to the core-mantle boundary (Dziewonski & Woodhouse 1987; Li & Romanowicz 1996; Grand, Van der Hilst & Widiyantoro 1997; Van der Hilst, Widiyantoro & Engdahl 1997): it has thus been suggested that the Pacific superswell is due to the dynamic upwelling of a large body called 'superplume' (Larson
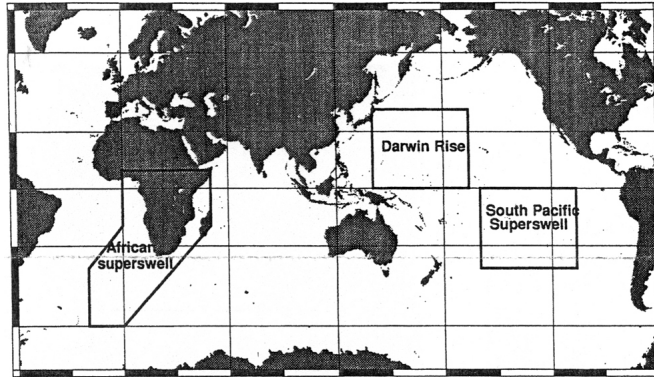
FIG. 2.1 – *Location of the Pacific superswell, of the Darwin Rise and of the African superswell (McNutt 1998).*

1991; Cazenave & Thoraval 1994), which may be stopped by the 660 km phase transition (Vinnik, Chevrot & Montagner 1997). Modelling based on tomography and geoid (Ishii & Tromp 1999) or tomography and mineralogy (Yuen, Cadek, Chopelas, & Matyska 1993) further demonstrate that thermal effects alone can not explain the entire geophysical evidences: they must be coupled with a chemical stratification. Another region now located on the west, the 'Darwin Rise' (figure 2.1), registered similar characteristics $110 - 90$ millions years ago (Ménard 1964; Winterer, Ntland, Van Waasbergen, Duncan, McNutt, Wolfe, Premoli Silva, Sager & Sliter 1993). Plate reconstruction demonstrates that it was then passing above the present-day superswell. The 'Pacific tank' has thus registered during the last 100 millions years a complete pulsation of the mantle (Larson 1991). Taking into account all these features, Davaille (1999b) suggested that superplumes originate from the pulsatory behaviour of thermochemical convection. Using the experimental results from the previous part, we are now able to quantify this statement, taking as a working hypothesis that the lower mantle contains two chemically distinct reservoirs (lower layer 1 and upper layer 2) initially separated by a flat interface, but presently in the pulsating regime. Typical parameters are listed in table 2.1: in all the following applications, one or two free parameters are systematically changed in their respective range, whereas the

fixed parameters	value	
H	2200 km	
ρ_2	4100 $\mathrm{kg\,m^{-3}}$	
ΔT	2000 K	
α	$3 \times 10^{-5}\ \mathrm{K^{-1}}$	
κ	$10^{-6}\ \mathrm{m^2\,s^{-1}}$	
free parameters	total range	preferred value
η_2	$10^{18} - 10^{23}$ Pa s	2×10^{21} Pa s
$\Delta\rho_\chi/\rho$	$0 - 4\%$	1%
$\gamma = \eta_1/\eta_2$	$10^{-3} - 10^{3}$	10^{-1}
$a = h_1/H$	$0 - 1$	0.3
Ra	$2.6 \times 10^5 - 2.6 \times 10^{10}$	1.3×10^7
B	$0 - 0.67$	0.17

TAB. 2.1 – *Typical values for the Earth's lower mantle.*

others are taken at the 'preferred' value.

2.1.1 Constraints on viscosity and layer depth ratios.

From our experimental study, three different evidences constrain the viscosity and layer depth ratios:

- for the thermochemical domes to rise from the lower layer towards the surface, the layer 1 Rayleigh number has to be smaller than the layer 2 Rayleigh number (see part I §3.5.3, pp. 127). Taking as a first order approximation

$$Ra_1 = Ra \times \frac{a^3}{\gamma} \times \frac{\Delta T_1}{\Delta T}, \tag{2.1a}$$

$$Ra_2 = Ra \times (1-a)^3 \times \frac{\Delta T_2}{\Delta T}, \tag{2.1b}$$

$$\Delta T_i \sim \Delta T/2, \tag{2.1c}$$

it means that

$$\gamma < \left(\frac{a}{1-a}\right)^3. \tag{2.2}$$

Two types of thermochemical structures are then possible: diapiric plumes will rise from a more viscous lower layer ($\gamma > 1$) and cavity plumes will form from a less viscous lower layer ($\gamma < 1$) (figure 2.2a).

– period and diameter of the thermochemical structures can be calculated using scaling laws defined in §3.5.4 and §3.5.6 of part I (pp. 129–134):

   • in the case of cavity plumes ($\gamma < 1$), fluid 2 is the most viscous and

$$\tau = \frac{h_2^2}{\pi\kappa}\left(\frac{880}{Ra_2}\right)^{2/3} \tag{2.3a}$$

$$d = 5.4 \times (h_1 h_2^2 \times Ra_2^{-0.28})^{1/3} \tag{2.3b}$$

   • in the case of diapiric plumes ($\gamma > 1$), fluid 1 is the most viscous and

$$\tau = \frac{h_1^2}{\pi\kappa}\left(\frac{880}{Ra_1}\right)^{2/3} \tag{2.4a}$$

$$d = 4.55 \times h_1 \times Ra_1^{-0.14}. \tag{2.4b}$$

Figures 2.2b et 2.2c show the results for $0 < a < 1$ and $10^{-3} < \gamma < 10^3$, and figure 2.3 exhibits their variations with the viscosity of the upper reservoir η_2.

Taking into account the uncertainty on Earth's data, errors on scaling laws, and also the extreme simplicity of our analogical model, we expect to predict the relevant orders of magnitude (period $\tau = 50 - 200$ My and diameter $d = 1000 - 3000$ km): then, lots of couples (γ, a) seem to be relevant for the mantle (figure 2.2). An additional constraint is given by the occurence of at least two successive pulsations in the Pacific: according to our experimental study, a viscosity contrast of at least one order of magnitude is therefore necessary.
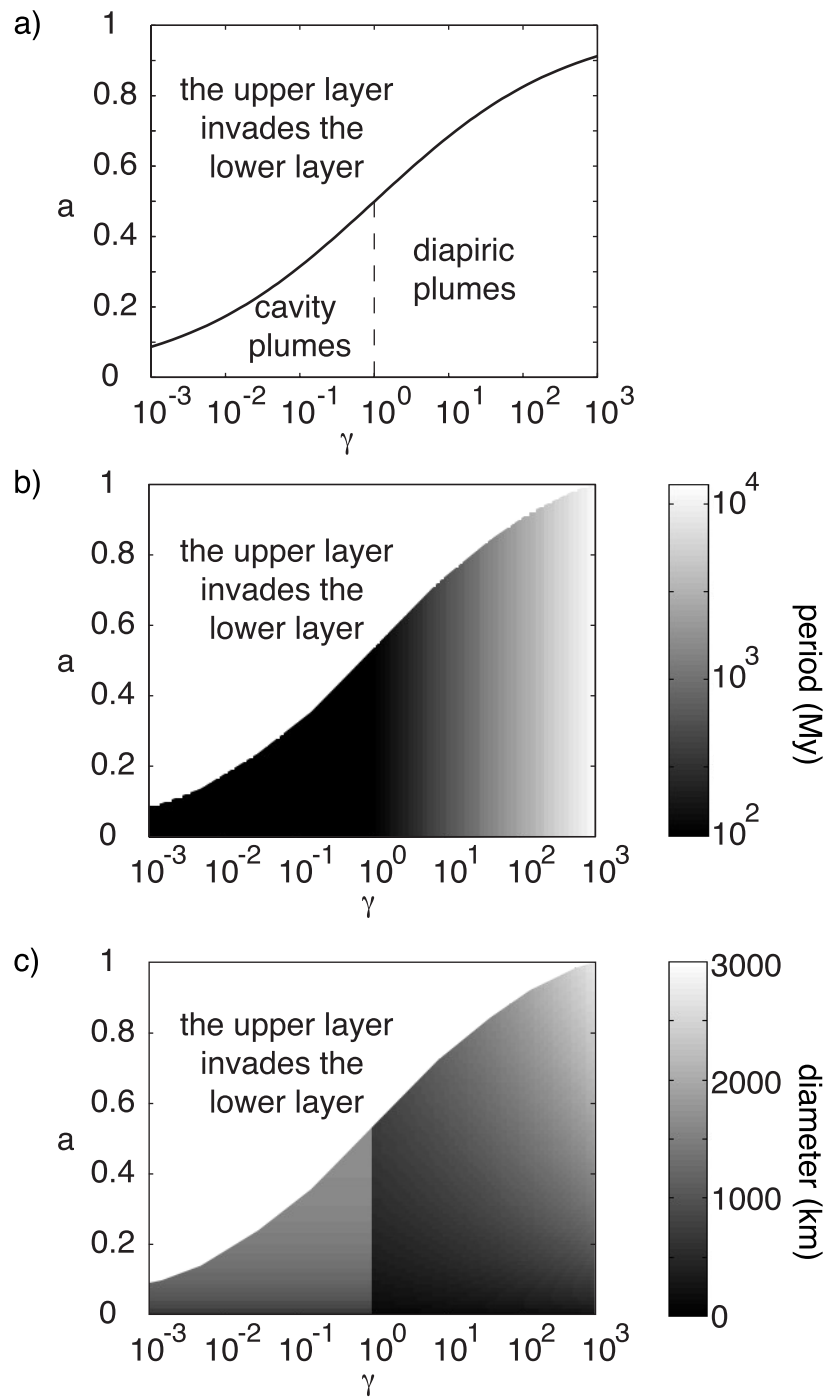
FIG. 2.2 – a) Spouting direction, b) period in millions years and c) diameter in km of thermochemical structures in the lower mantle as a function of γ and a.
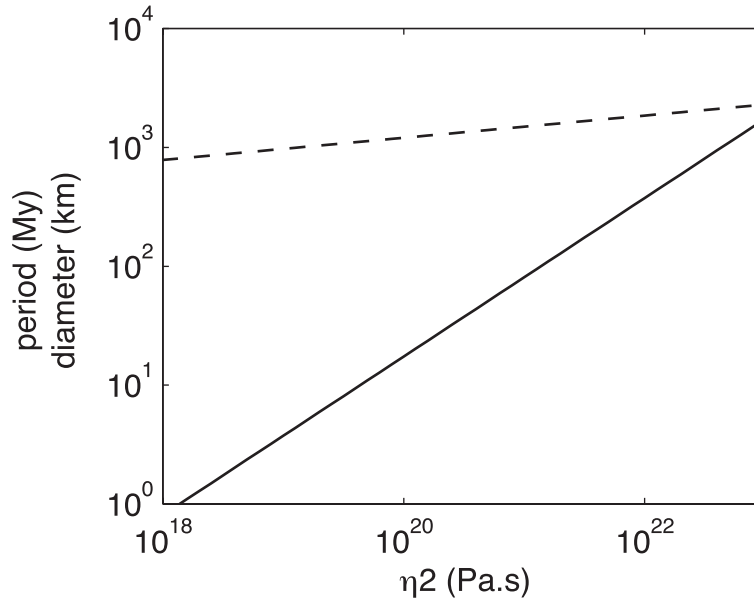
FIG. 2.3 – *Variation of the period of thermochemical domes (solid line) and of their diameter (dashed line) with the viscosity of the upper reservoir.*

The formation of a cavity plume then seems to be the most probable, with

$$10^{-2} < \gamma < 10^{-1}. \tag{2.5a}$$

$$0.2 < a < 0.33. \tag{2.5b}$$

The variations of viscosity inside the mantle are poorly known: in addition to the strong dependence on pressure and temperature (Karato & Wu 1993), one must take into account possible variations of structural origin, which are not constrained. Current models propose radial mean vertical profiles (Forte & Mitrovica 2001), but these results are not usable within the framework of strong lateral variations expected in our study (figure 2.4). The dependence on pressure is not reproducible in the laboratory, but it probably has a weak influence on thermochemical structures since the relevant parameter for domes dynamics corresponds to the viscosity contrast at the interface between the two fluids, therefore at a given pressure. The dependence on temperature can be mimicked by sugar solutions: one experiment with liquid sugar 'DDC 131' from Béghin Say (experiment
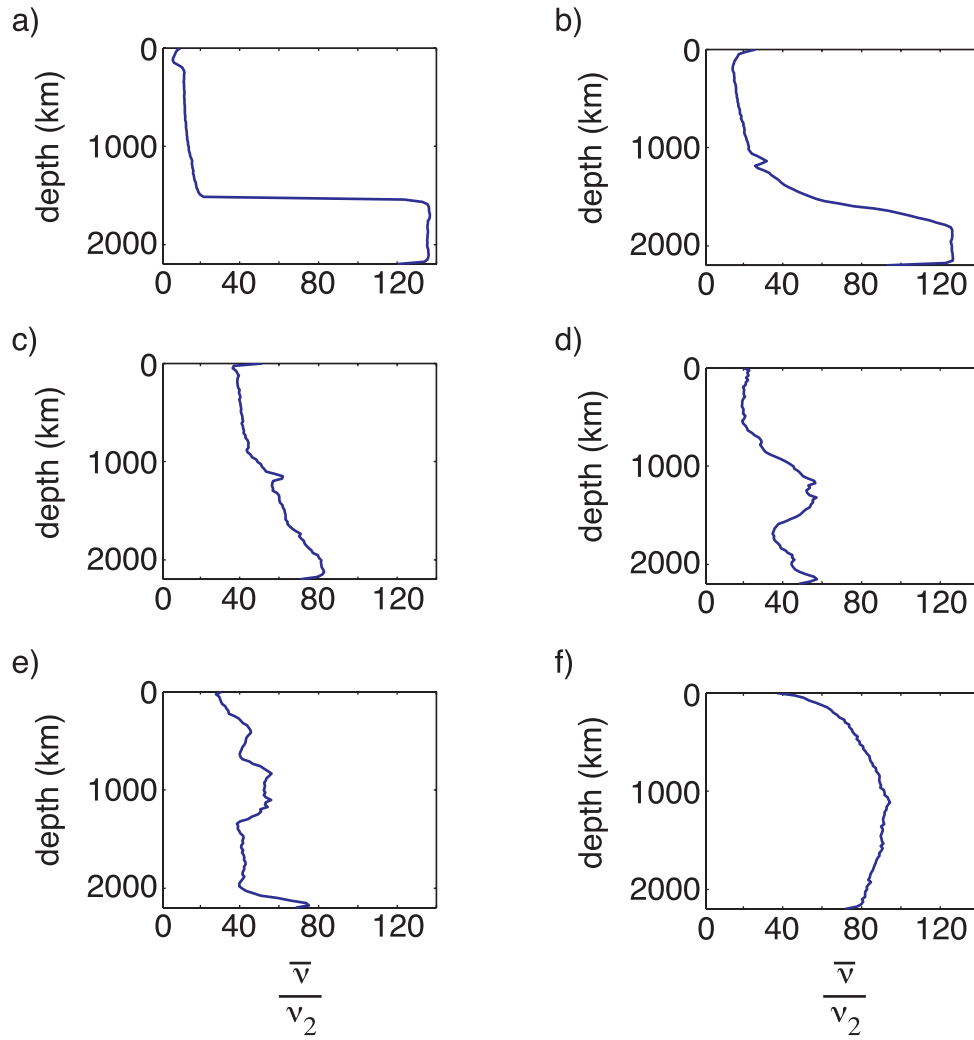
FIG. 2.4 – *Vertical viscosity profiles corresponding to the radial average of figure 1.2 pictures. Viscosity structures can not be deduced from the mean values. In the Earth, the presence of very viscous subducting plates even complicates the situation.*

LS01) has thus been performed (figure 2.5). It exhibits results qualitatively and quantitatively similar to the other experiments, taking for γ the viscosity contrast at the interface. In the Earth, the lower reservoir is chemically denser and possibly radiogenically enriched (Staudigel, Park, Pringle, Rubenstone, Smith & Zindler 1991): at a given depth, it is thus hotter than the upper layer. Independently of any structural effects, the viscosity ratio is expected to be smaller than 1, in agreement with (2.5a).

Results from (2.5b) correspond to an initial lower reservoir thickness (i.e. before destabilization) ranging between 440 km and 730 km. These values are in the lower bound of the predicted size of the geochemical 'undepleted' reservoir, which occupies between 10% (Hofmann 1997) and 75% (Jacobsen & Wasserburg 1979) of the whole mantle, corresponding to a thickness between 516 km and 2420 km. However, our predicted value only corresponds to the last pulsation of the Pacific: as illustrated in §1.4.1 and §1.4.2, the size of the reservoir (as well as the viscosity ratio) may have been larger in the past. Such variations have to be taken into account in geochemical studies to allow better comparisons.

2.1.2   Constraints on chemical density contrast.

Preferred values of the viscosity and layer depth ratios determined in the previous paragraph (see table 2.1) imply

$$Ra_1 \sim 1.8 \times 10^6 \text{ and } Ra_2 \sim 2.2 \times 10^6. \tag{2.6}$$

Both layers are thus strongly convecting: according to our experimental study (see part I §3.5.2, pp. 121), the effective buoyancy number in the pulsating regime is equal to the critical value

$$B_c = 0.98 \tag{2.7}$$
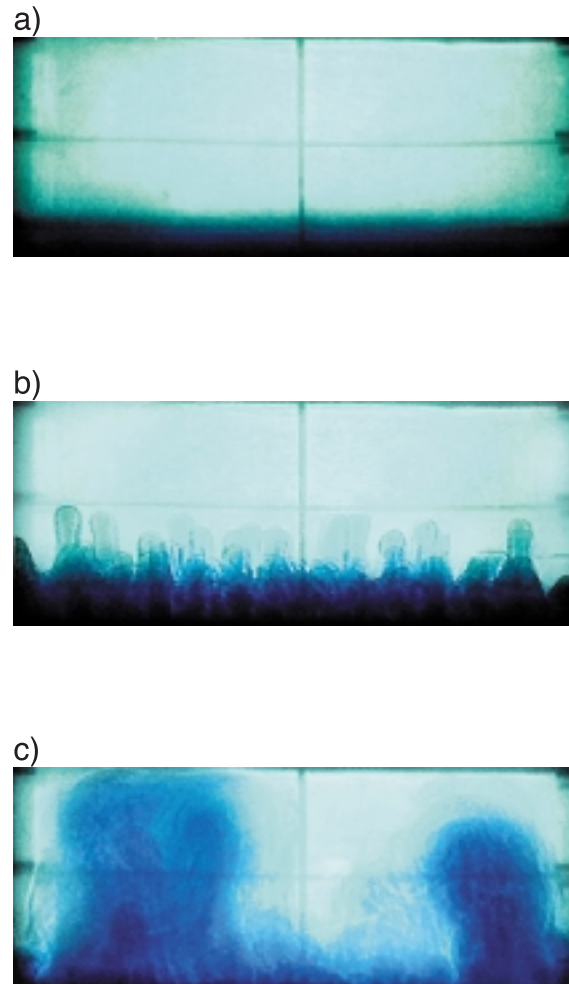
FIG. 2.5 – *Time evolution of experiment LS01 (no structural viscosity contrast, but strong dependence on temperature). a) t = 0 min : initial configuration. b) t = 2 min : purely thermal convection in the lower layer that partially penetrates the upper layer. c) t = 4 min : destabilization of the lower layer under the form of large cavity plumes.*

From equation (3.19) of part I (pp. 124), this corresponds to a typical temperature contrast between the two reservoirs

$$\theta = \frac{\Delta\rho_\chi}{B_c\alpha\rho}. \tag{2.8}$$

As shown in figure 2.6, θ can be very large, typically hundreds of degrees, and could possibly lead to local melting (Zerr, Diegeler & Boehler 1998). However, if we now look at the net density anomaly taking into account both thermal and chemical effects

$$\Delta\rho_{eff} = \alpha\rho\theta - \Delta\rho_\chi, \tag{2.9}$$

it corresponds to an 'apparent' thermal anomaly

$$\theta_{app} = \frac{\Delta\rho_{eff}}{\alpha\rho} \tag{2.10}$$

ranging between 0 and 30 K only (figure 2.6): this estimation is in good agreement with the deep temperature excess needed by McNutt & Judge (1990) to explain topography and geoid data in the Pacific. Besides, such a small anomaly coupled with a highly distorted interface could explain why Vidale, Schubert & Earle (2001) did not locate any thermochemical boundary despite a precise search.

2.2   The African uplift.

A second superswell is located in Africa and south Atlantic ocean (Nyblade & Robinson 1994, see figure 2.1). As for the Pacific superswell, it has been explained by the dynamical upwelling of a hot and very large structure (Lithgow-Bertelloni & Silver 1998), and high resolution tomographic inversions have imaged the presence of a superplume about 1200 km across with very sharp interfaces (Ritsema, Ni, Helmberger & Crotwell 1998; Ni, Tan, Gurnis & Helmberger 2002).

Gurnis, Mitrovica, Ritsema & Van Heijst (2000) have recently developed a dynamical model relating a superplume type motion to the surface residual topography (i.e. after
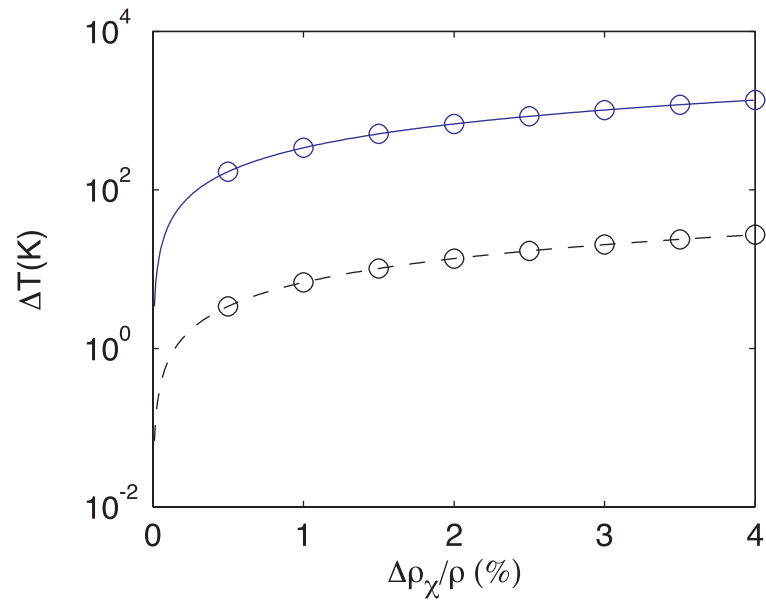
F<small>IG</small>. 2.6 – *Effective temperature contrast (solid line with circles) and apparent temperature contrast (dashed line with circles) as a function of the chemical density contrast for a pulsating dome.*

shallow sources of density have been removed) and to the average uplift rate registered in southern Africa. They concluded that

- a small (global) negative density contrast is needed to explain the present elevation of $300 - 600$m.
- a low viscosity inside the hot structure, which could be explained by the temperature-dependence of the viscosity (Karato & Wu 1993), is needed to account for the measured uplift rate of $5 - 30 \text{ m My}^{-1}$.

Their results are thus qualitatively similar to ours. Quantitatively, they were able to satisfy Earth's constraints with $\Delta\rho_{eff}/\rho \sim -0.2\%$ and $\eta_1 \sim 10^{21} - 10^{22} \text{ Pa s}$, whereas our preferred values determined in the Pacific (see table 2.1) imply $\Delta\rho_{eff}/\rho \sim -0.02\%$ and $\eta_1 \sim 10^{20} \text{ Pa s}$. However, according to their study, a 10-fold decrease in the density anomaly leads to a 10-fold decrease in topography and a 100-fold decrease in uplift rate, and a 10 to 100-fold decrease in the lower mantle viscosity leads to a 3 to 10-fold increase in topography and a 10 to 100-fold increase in uplift rate: both effects thus compensate and our preferred values could also fit the African case well.

Present-day convective pattern of the mantle thus appears to be dominated by a degree 2, with antipodal hot and chemically dense superplumes under Africa and Pacific respectively. Such a structure could account for the dominant degree 2 observed in the geoid (Cazenave, Souriau & Dominh 1989), and also for the anomalous flattening of the CMB inferred from geodetic estimates of the Earth's free core nutation (Forte, Mitrovica & Woodward 1995).

2.3   Seismic velocity anomalies.

In order to compare our results with Earth's data, it is possible to convert the chemical and thermal signals associated with an oscillating dome into shear waves, compressional

	perovskite	magnesiowüstite
K_0(GPa)	258.1	161.0
$\frac{\partial K}{\partial T}$(GPa)	-0.031	-0.028
$\frac{\partial K}{\partial P}$	4.1×10^{-9}	4.1×10^{-9}
$\frac{\partial K}{\partial x_{Fe}}$(GPa)	0	7.5
μ_0(GPa)	176.8	131.0
$\frac{\partial \mu}{\partial T}$(GPa)	-0.019	-0.024
$\frac{\partial \mu}{\partial P}$	1.4×10^{-9}	2.4×10^{-9}
$\frac{\partial \mu}{\partial x_{Fe}}$(GPa)	small (taken 0)	77.0
ρ_0(kg m^{-3})	4108	3583
$\frac{\partial \rho}{\partial x_{Fe}}$(kg m^{-3})	1070	2280

TAB. 2.2 – *Derivatives of bulk modulus, shear modulus and density for pure perovskite and pure magnesiowüstite as proposed by Samuel & Farnetani (2001) (temperature and pressure dependences from Matsui (2000) and Matsui, Paker & Leslie (2000); iron dependences from Wang & Weidner (1996) and references therein). Subscript 0 means surface temperature, surface pressure and $x_{Fe} = 0$. For the calculations of velocity anomalies, we use the hydrostatic pressure and the adiabatic temperature gradient.*

waves and bulk sound velocities, respectively given by

$$V_s = \sqrt{\frac{\mu}{\rho}}, \tag{2.11a}$$

$$V_p = \sqrt{\frac{K + (4/3)\mu}{\rho}}, \tag{2.11b}$$

$$V_\phi = \sqrt{\frac{K}{\rho}}, \tag{2.11c}$$

where K and μ are the bulk and the shear modulus.

Following Forte & Mitrovica (2001) and Samuel & Farnetani (2001), we only take into account two phases in the lower mantle: perovskite $(Mg,Fe)SiO_3$ and magnesiowüstite $(Mg,Fe)O$. Chemical density variations between the two reservoirs are due to changes in iron molar ratio $x_{Fe} = Fe/(Fe + Mg)$ and/or in volumic proportion of perovskite (Φ) and magnesiowüstite $(1 - \Phi)$. We suppose the upper reservoir to have a pyrolitic composition, corresponding to reference coefficients $x_{Fe} = 0.11$ and $\Phi = 0.68$ (Guyot, Madon, Peyronneau & Poirier 1988). The chemical density excess of the lower layer $\Delta\rho_\chi$ is then converted either in change in iron molar ratio for a fixed volumic proportion of perovskite or in change in volumic proportion of perovskite for a fixed iron molar ratio. In the whole-system regime, this stratification is compensated by a mean temperature excess θ given by (2.8), which we first suppose to apply to the whole lower reservoir. Bulk modulus and shear modulus are then calculated inside each layer for pure perovskite and pure magnesiowüstite using the derivative coefficients from Samuel & Farnetani (2001) (table 2.2), and seismic velocities are finally estimated inside each reservoir using a Voigt-Reuss-Hill average.

Results for three different models are presented in figure 2.7. We can first notice that all of them give relevant orders of magnitude as far as velocity anomalies are concerned, with typical amplitude between -6% and 3%. However, only variations of the volumic proportion of perovskite as shown in figures 2.7a and 2.7c are capable of reproducing two striking features observed by recent seismic studies of the deep lower mantle, namely (i) a large ratio of shear to compressional waves velocity anomalies (Roberston & Woodhouse 1996) and (ii) an anti-correlation between shear waves and bulk sound velocity anomalies (Su & Dziewonski 1997; Ishii & Tromp 1999). Changes in iron molar ratio alone do not give such characteristics (figure 2.7b).

Figure 2.8 shows the tomographic signal obtained with our method from picture d of figure 1.2 scaled to the mantle. Results can be filtered to take into account the resolution of Earth's tomography, typically 400 km in the horizontal direction and 200 km in the vertical direction: the complex pattern of thermochemical structures is then partially
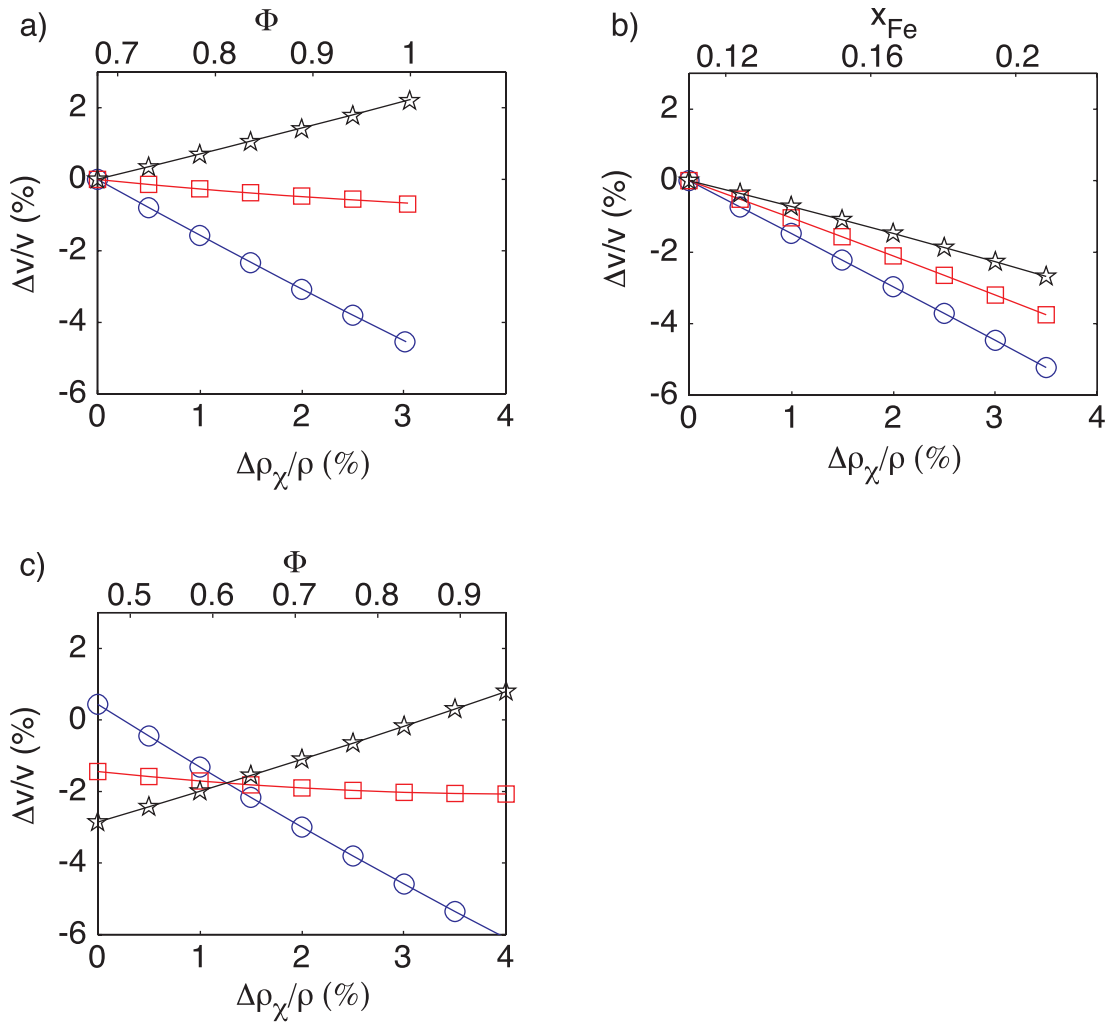
FIG. 2.7 – *Variations of the velocity anomalies at the mid-mantle depth as a function of the chemical density contrast for a pulsating dome (circles: shear waves; squares: compressional waves; stars: bulk sound). a) The iron molar fraction x_{Fe} is 0.11 in both reservoirs and the chemical density contrast comes from variations in the volumic proportion of perovskite Φ (top scale). b) $\Phi = 0.68$ in both reservoirs and the chemical density contrast comes from variations in x_{Fe} (top scale). c) $x_{Fe} = 0.11$ in the upper reservoir, $x_{Fe} = 0.16$ in the lower reservoir, and the variation in chemical density contrast comes from additional variations in Φ (top scale).*

erased and only the two major upwellings persist, representing for instance the Pacific and African superswells. Those results correspond to an 'average' point of view, supposing all points in the lower layer have the same temperature excess given by (2.8). However, (2.8) only indicates a mean value over the whole system at the time of destabilization: locally, the real temperature contrast can be larger, as for instance in the upper part of the rising dome, or smaller, as for instance in its lower part (see figure 3.14 of part I, pp. 119). Figure 2.9 then shows the relative variations of the predicted seismic anomaly: in the African superswell, this could explain the simultaneous detection of a stratified root (Ishii & Tromp 1999) and a buoyant head (Ritsema, Ni, Helmberger & Crotwell 1998). One must also notice that part of the thermochemical structures can be hidden from seismic detection by the local compensation of thermal and chemical effects: tomographic inversions may underestimate the real extension of superplumes.
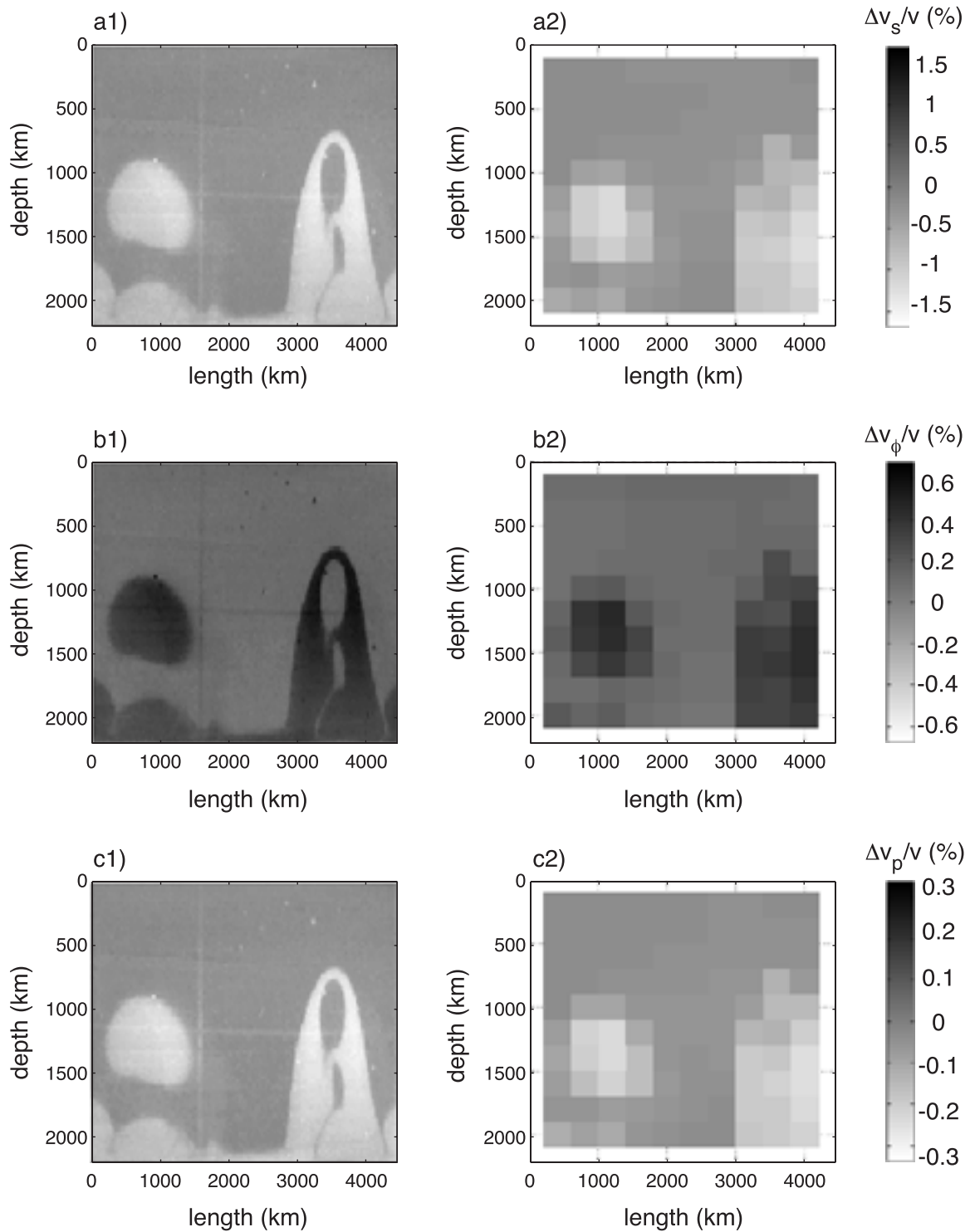
FIG. 2.8 – *Tomography of picture d) of figure 1.2, taking $x_{Fe} = 0.11$ and a variable Φ: a) shear waves, b) bulk sound and c) compressional waves. Pictures labelled '1' show direct results and pictures labelled '2' averaged signal through 400×200 km cells, comparable to typical Earth's models resolution.*
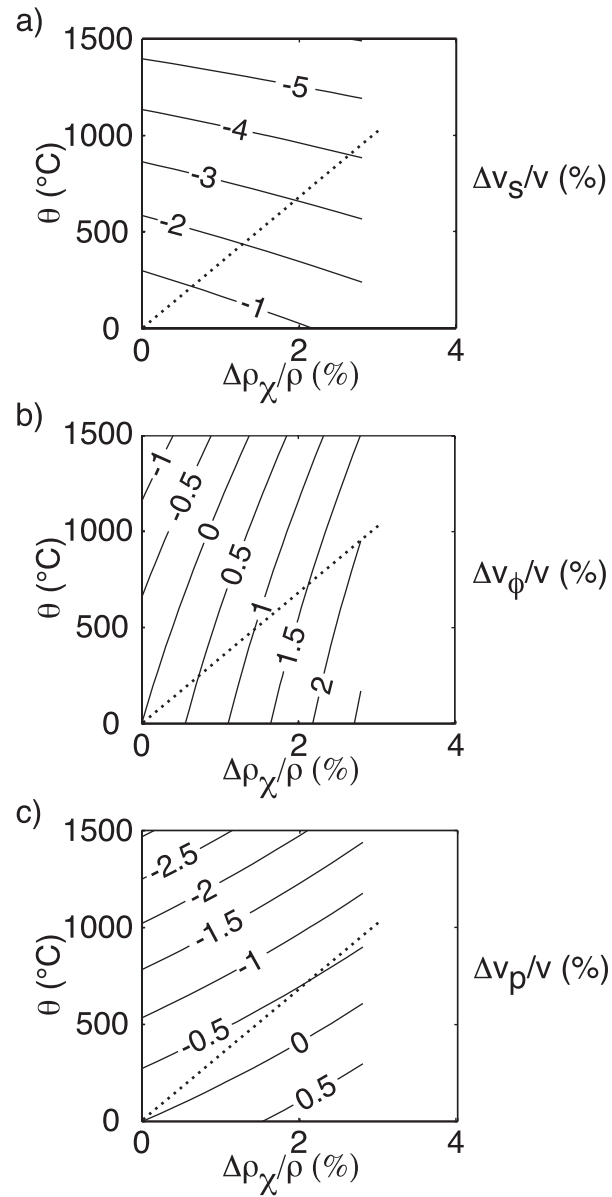
FIG. 2.9 – *Predicted seismic anomaly depending on the local temperature excess and the chemical density contrast, taking $x_{Fe} = 0.11$ and a variable Φ: a) shear waves, b) bulk sound and c) compressional waves. Dotted lines show the 'equilibrium' position, where thermal effects compensate for chemical stratification as given by the onset mean equation (2.8).*

Chapitre 3

Épisodicité dans les planètes de type terrestre.

3.1 Introduction.

Since its formation, the Earth has undergone gradual cooling, but this global decline has been interrupted by periods of enhanced convective vigor and surface heat flow (see for instance the recent review by Schubert, Turcotte & Olson 2001, pp. 626–627). Several mechanisms have already been identified that could create such episodicity. First, convection at high Rayleigh number is by essence episodic, generating thermal plumes: the arrival of such features at the surface could then account for the creation of major flood basalt events (Richards, Duncan & Courtillot 1989; White & McKenzie 1989). On a larger scale, Wilson cycles (1966) corresponding to the periodic fragmentation and reformation of supercontinents could be link to the temporal variability in plate tectonics. Numerous studies have also pointed out the effect of the 660 km endothermic phase transition on convection: it could actually generate the periodic occurence of abrupt changes in convective mode (660-layered/whole-mantle), consecutive with the sudden flushing of oceanic plates previously accumulated above the transition zone (Machetel & Weber 1991;

Tackley, Stevenson, Glatzmaier & Schubert 1993; Weinstein 1993). Such events have the potential to influence the mantle on a global scale (Weinstein 1993; Brunet & Machetel 1998): the arrival of cold avalanche material at the CMB would actually significantly modify core heat flux, whereas in order to conserve mass, hot material from the lower mantle would rapidly be injected into the upper mantle with attendant thermal consequences at the surface.

Pulsations in our analogical experiments now provide a new simple 'fluid-dynamics' explanation for episodicity at a global scale. As a matter of fact, the heat flux perturbations associated with a dome have the same order of magnitude than the average value in thermal boundary layers (figure 3.1a), and an important part of thermal transfers is thus attached to the pulsations of thermochemical structures. In the Earth, the heat flux related to a rising dome can be evaluated by

$$Q = \rho C_p \theta \times \pi (d/2)^2 \times v, \tag{3.1}$$

where C_p is the specific heat per unit mass, θ the thermal excess and v the rising velocity given by equation (3.36) of part I (pp. 132). Typical variations of v and Q with the chemical stratification are presented in figure 3.1b: a 1% density contrast implies

- a velocity of $8 \, \mathrm{cm \, y^{-1}}$, in good agreement with typical velocities given by plate tectonics.
- a heat flux of 3×10^{13} W, comparable to the total heat flux escaping from the Earth ($Q_{surface} \sim 4 \times 10^{13}$ W, Poirier 1991), and even larger than the estimated flux at the base of the mantle ($Q_{core} \sim 4 \times 10^{12}$ W, Poirier 1991).

The Earth's thermal history may have been punctuated by great variations corresponding to thermochemical pulsations, and current estimations of evacuated heat may largely underestimate the reality (see also Romanowicz & Gung 2002). We will now see the various possible consequences of such pulsations, particularly intense volcanism and modifications of magnetic field.
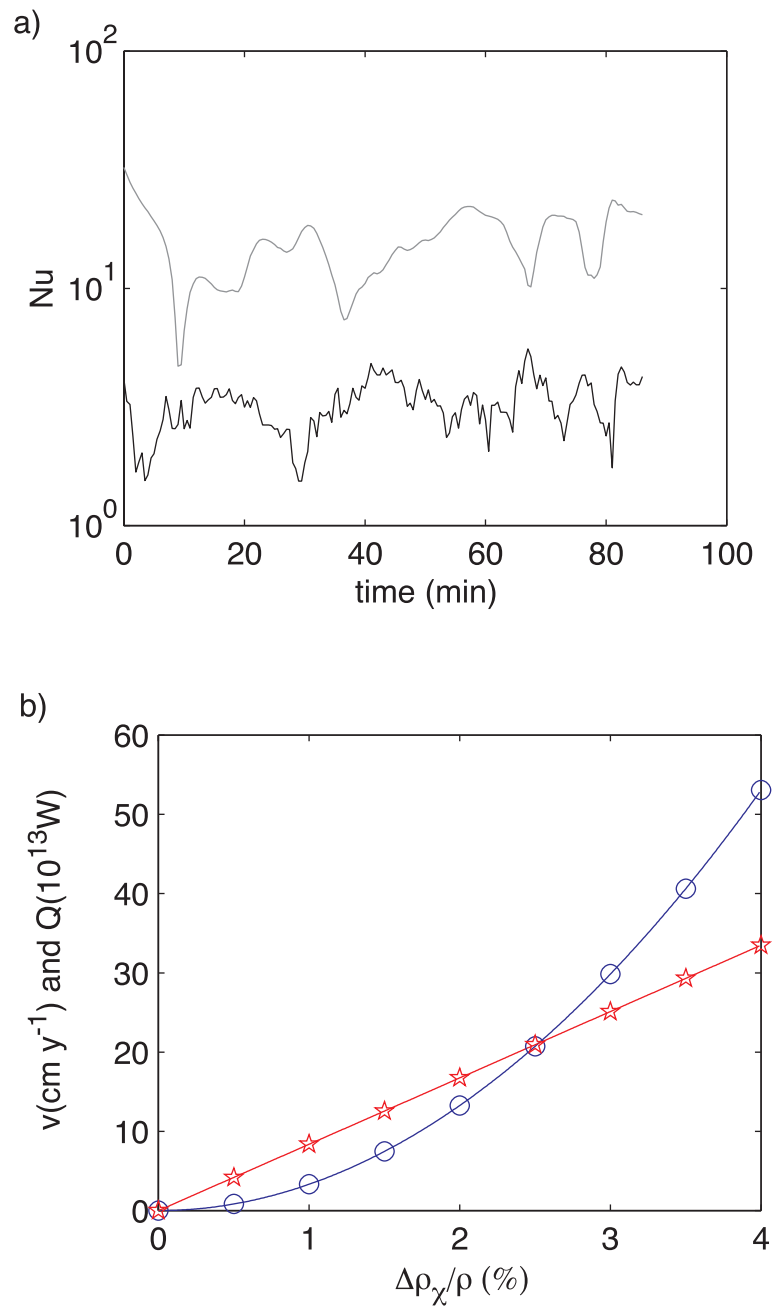
FIG. 3.1 – *a) Nusselt number (adimensional heat flux) in the hot (gray line) and cold (black line) thermal boundary layers during the pulsatory dynamics of experiment n°38. b) Typical rising velocity of a dome (stars) and associated heat flux (circles) as a function of the chemical stratification.*

3.2   Pulses of surface volcanism.

The heat transported by a dome is typically 80 times larger than the estimated value for Hawaii, the current most powerful hotspot ($Q_{Hawaii} \sim 3.6 \times 10^{11}$ W, Schubert, Turcotte & Olson 2001). We can thus expect each pulsation to have produced an intense volcanic activity at the surface. Such periods may be linked to various inter-related geological consequences through the Earth's history, such as (figure 3.2):

- episodic formation of significant quantities of hydrocarbons and coal (Larson 1991), as well as the emission of important volumes of CO_2 (Caldeira & Rampino 1991).

- significant climatic modifications, with anoxic conditions and temperature variations (Larson 1991; Caldeira & Rampino 1991; Garzanti 1993; Isley & Abbott 1999; Ray & Pande 1999).

- mass extinctions (Courtillot & Besse 1987; Courtillot, Jaeger, Yang, Feraud & Hofmann 1996; Ray & Pande 1999).

- pulses of oceanic and continental crust production (Larson 1991; Stein & Hofmann 1994; Condie 1998).

- rising of oceans level (Sheridan 1983; Larson 1991).

- initiation of major tectonic cycles, corresponding to the fragmentation and reformation of supercontinents (Sheridan 1983; Courtillot & Besse 1987; Condie 1998).

The best documented event took place in the Cretaceous, between 124 My and 83 My (Larson 1991): it can thus be related to the formation of the Darwin Rise. Many other episodes are proposed, but do not receive general agreement, because lots of proofs are gradually erased from geological registers. For instance, Condie (2002) proposes pulsations at 280 My, 480 My, 1900 My and 2700 My. Utsunomiya, Suzuki & Maruyama (2002) suggest that the Pacific superswell was created during fragmentation of supercontinent Rodinia 750 My ago, and then performed four pulsations ($550 - 500$ My, $300 - 250$ My, $124 - 83$ My and today); they also connect the first appearance of the African superswell with the fragmentation of Pangea 250 My ago. Isley & Abbott (1999) propose a series of
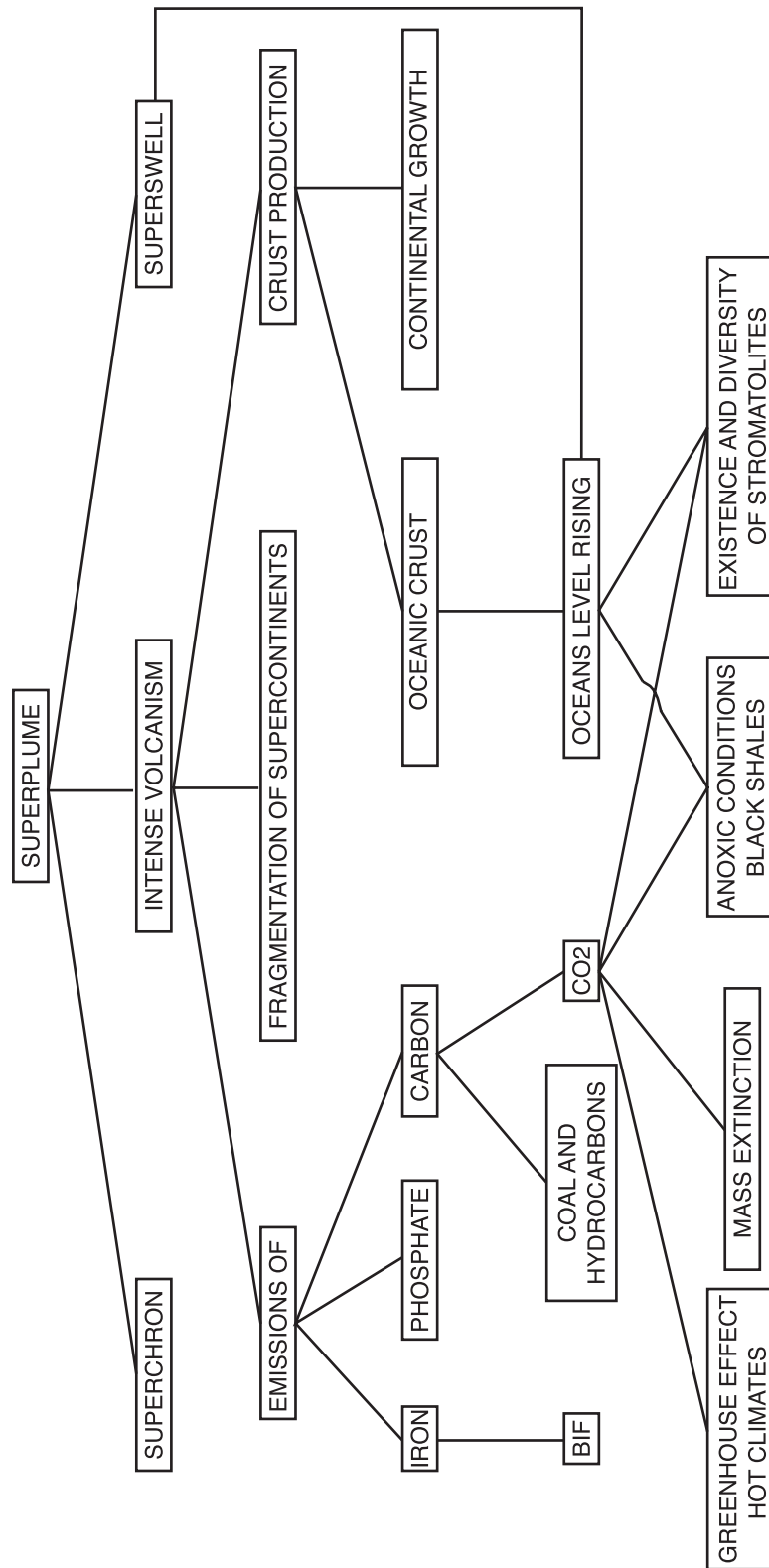
Fɪɢ. 3.2 – *Geological consequences of thermochemical domes.*

four pulses between 3800 My and 1600 My, at regular intervals of $200 - 300$ My.

3.3   Influence of the departure of a dome on the dynamo.

The terrestrial magnetic field is due mainly to rapid convective motions in the liquid external core. Its polarity has reversed on average every 0.22 My in the last millions of years (Larson & Olson 1991). However, some periods without magnetic inversion during several tens of million years are observed in the Earth's history. Such superchrons (Cox 1982) are too long to be accepted as part of the usual reversal process controlled by core dynamics: a lower mantle influence is thus expected (Merrill & McFadden 1995). The apparent correlation between superchrons and periods of strong volcanism described above (Sheridan 1983; Courtillot & Besse 1987; Larson 1991) then reinforces a superplume model: the rising of such a giant thermochemical feature would cause a large temperature decrease at the core-mantle boundary, thus a strong increase in the heat gradient; the larger heat flux would then affect motions in the core, possibly stabilizing the dynamo (Larson & Olson 1991). The estimated heat flux from our dynamical model quantitatively agrees with these proposals.

In addition to these temporal variations, the present-day antipodal Pacific and African superswells induce heterogeneous heat flow boundary conditions at the CMB that could account for the observed lateral variations of the geomagnetic field characteristics and for the asymmetric structure of the inner core (Sumita & Olson 1999). They could also be linked to the suggested occurrence of preferred pole paths near 90°W and 90°E longitudes during polarity reversals (see recent review by Gubbins 1994, but also Merrill & McFadden 1999).

These various phenomena are still controversial: rapid improvements in dynamo models will soon help to precisely test them. Besides, we don't claim that the rising of hot

thermochemical domes is the only explanation for the various long-term and large-scale magnetic evidences: the sinking of cold structures, as for instance subducted plates in the alternative 'flushing event' explanation presented above, could actually induce similar effects (Gallet & Hulot 1997; Labrosse 2002).

3.4   Pulsations on Venus and Mars.

The mantle of some terrestrial planets could also follow a pulsatory dynamics (Herrick & Parmentier 1994). As far as Venus is concerned, the observation of meteorites impacts shows that the surface of this planet was entirely renewed $300 - 500$ My ago in a very fast process ($< 10 - 50$ My) (Strom, Schaber & Dawson 1994); since then, its volcanic and tectonic activities have been considerably reduced. The explanation for these observations thus demands a fast, intense and large-scale phenomenon: presuming a two-layer mantle, it could correspond to an abrupt draining of the lower reservoir, such as we observed in experiments with small B (figure 3.3f, g, h). The absence of rigid tectonic plates could explain the integral renewal of the surface, in contrast to the Earth's superswells (figure 3.3c, d, e). Quantitative estimations of pulsations period are proposed in figure 3.4 taking $\alpha \sim 2 \times 10^{-5}$ K^{-1}, $\rho \sim 5250$ kg m^{-3}, $g \sim 8.6$ m s^{-2}, $\Delta T \sim 2000$ K, $H \sim 3000$ km, $\kappa \sim 10^{-6}$ m^2 s^{-1} and $\eta_2 \sim 10^{22}$ Pa s (Schubert, Turcotte & Olson 2001): for a less viscous lower reservoir ($\gamma < 1$), the period is controlled by the most viscous upper layer and the minimum period of resurfacing is obtained (i.e. 420 My); it can however become much longer for a most viscous lower reservoir. In the case of Venus, the spouting is not fixed as opposed to the Earth (see part I §2.1.1, pp. 169), since the resurfacing can also come from the destabilization of the upper cold lid invading the lower hot reservoir.

The early evolution of Mars has been marked by episodes of violent and fast release of enormous quantities of water stored on the surface (Kargel & Strom 1992), and right below the surface (Tanaka & Chapman 1992). These events could have been triggered by sudden increases in volcanic activity over large areas (Baker, Strom, Gulick, Kargel,
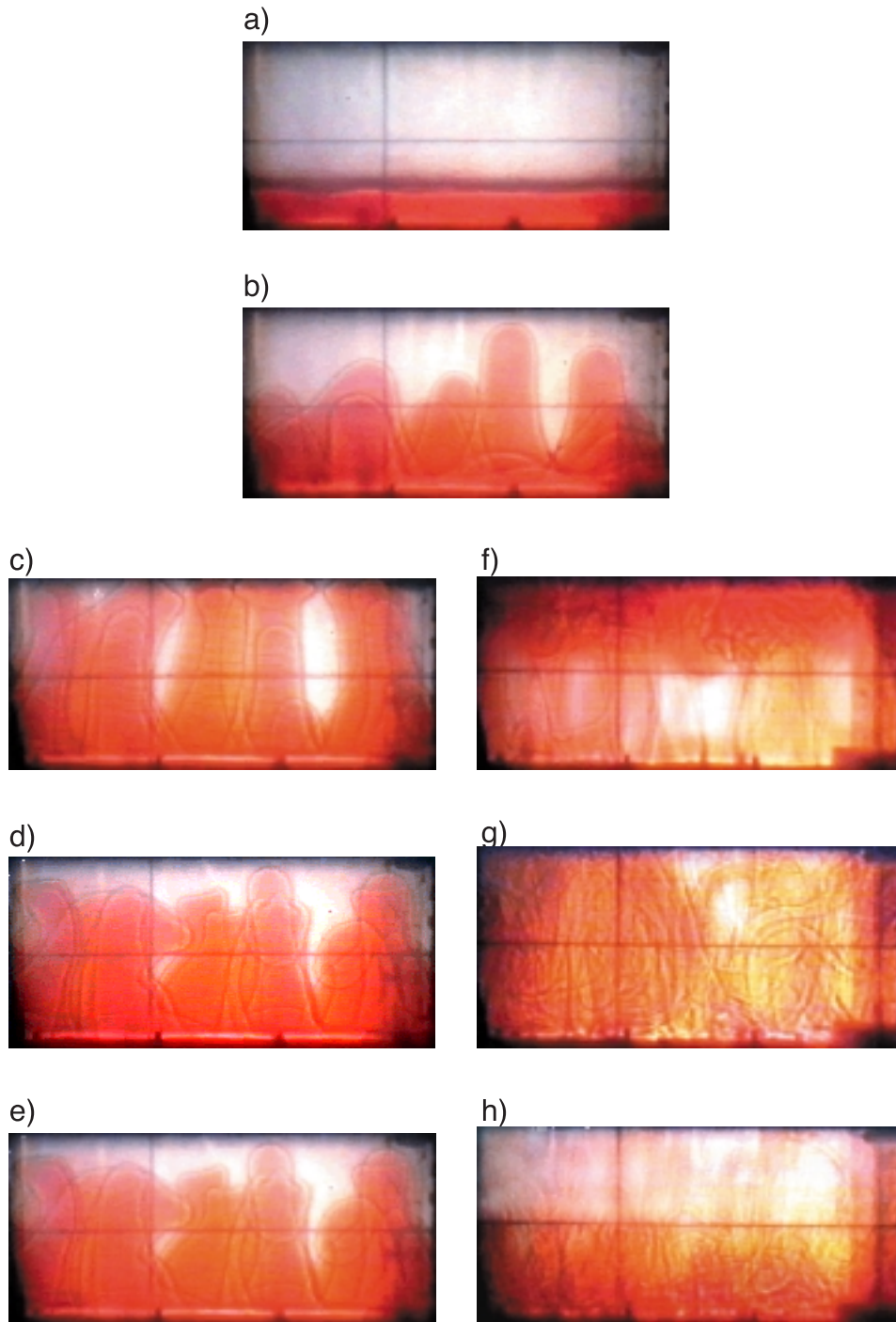
FIG. 3.3 – *Vertical pulsation in experiment n°18 (c, d, e) illustrating the formation of superswells in the Earth, and layer 1 emptying in experiment n°9 (f, g, h) illustrating Venus resurfacing. The onset is the same for both cases (a, b).*
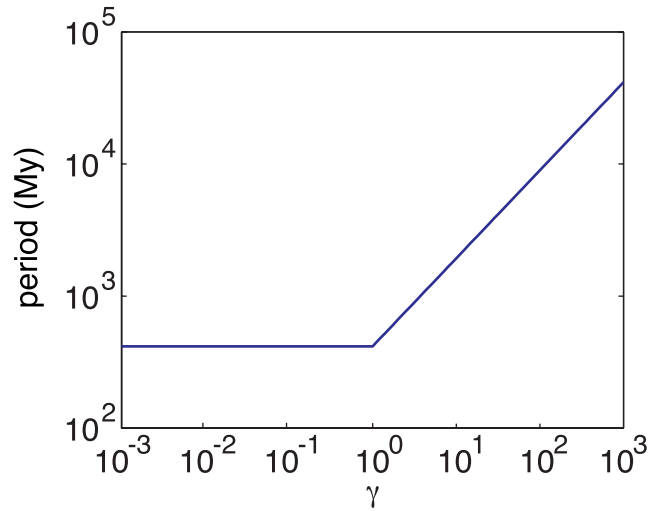
FIG. 3.4 – *Theoretical period of pulsations (in millions years) in the case of Venus as a function of γ.*

Komatsu & Kale 1991), which could be consecutive to thermochemical pulsations; the progressive stirring between the two reservoirs would then explain why these oscillations and the related volcanism have finally stopped one billion years ago (Greeley & Schneid 1991).

3.5   Conclusion.

All the implications presented in this chapter are mainly speculative, and do not allow to choose between the 'superplume' and the 'flushing event' explanations. However, they point out that (i) the evolution of various planets exhibits major cycles of convective activity that can not be explained in the framework of classical Rayleigh-Bénard convection, and (ii) the simple assumption of a second reservoir can explain these various phenomena, while insisting on the evolutionary character of the convective regime.

Chapitre 4

Limitations du modèle analogique.

Our experimental model precisely quantifies the effects of density and viscosity contrasts on the two-layer convection: it thus explains from a 'fluid-dynamics' point of view some key mechanisms taking place in the Earth. It is however impossible to build an experimental miniature mantle, taking into account all natural complications: we will thus try to estimate their respective influence.

4.1   Presence of the continents.

The continents at the surface of the Earth modify the upper thermal boundary conditions: within the framework of classical Rayleigh-Bénard convection, their presence results in focusing rising hot structures (Guillou & Jaupart 1995). One can thus imagine that this conclusion will remain essentially unchanged in the case of thermochemical structures. In particular, the presence of a 'supercontinent' will encourage the formation of a great dome, whose energy will be sufficient to split it up, thus initiating a new tectonic cycle (Sheridan 1983; Courtillot & Besse 1987; Condie 1998).

4.2   Internal heating.

Mantle rocks are radiogenic, creating internal heat sources for convection. Besides, heat budgets require the lower reservoir to be radiogenically enriched. Such a differentiated heating is not reproducible in our experiments. We can however estimate that it will have a twofold effect in the mantle. Inside one reservoir independently, the presence of internal heating will reduce the intensity of small-scale purely thermal regime: the effective Rayleigh number actually scales as (McKenzie, Roberts & Weiss 1974)

$$Ra_{eff} = Ra(1 - r/2), \qquad (4.1)$$

where Ra is the Rayleigh number for purely bottom heating and r the ratio of the internal heat flux over the total heat flux. But additional heat sources in the lower reservoir will increase its average temperature and thus the temperature difference between the two layers, which will tend to encourage destabilization.

4.3   Variations of the thermal expansion coefficient.

As seen in part I §2.1 (pp. 89), the effective variations of the thermal expansion coefficient do not really influence the large-scale thermochemical regime, since only the average buoyancy force between layers is important. For instance, Hansen & Yuen (2000) claim that a buoyancy number of 0.5 is sufficient to stabilize the deep layer over the Earth's history in their calculations. This value is calculated however with surface properties: taking into account the decrease of α by a factor 3 within the mantle, it corresponds to a mean value $B_{mean} = 1$, in agreement with our findings (see figure 1.1) and with previous numerical simulations (Tackley 1998; Montague & Kellog 2000).

The variation of α with depth is however of fundamental importance, since the regime of a given two-layer system will change with the location of the interface (Davaille 1999b): a typical heterogeneity of 1% associated with a temperature contrast of 340 K will actually be characterized by

- $B_{eff} = 0.98$ in the middle mantle ($\alpha = 3 \times 10^{-5}$ K^{-1}, Poirier 1991), therefore a whole-layer mode.

- $B_{eff} = 2.8$ at the base of the mantle ($\alpha = 1 \times 10^{-5}$ K^{-1}, Poirier 1991), therefore a stratified regime.

This mechanism could explain the simultaneous generation of hotspots and superswells from a single geochemical reservoir (Davaille 1999b); the D" layer, a region of seismic anomalies interpreted as a chemically distinct dense layer at the base of the mantle (Davies & Gurnis 1986; Hansen & Yuen 1988; Lay, Williams & Garnero 1998), would then correspond to the lower stratified part of this reservoir.

4.4   660 km phase transition.

The major seismic discontinuity in the mantle takes place around 660 km depth over a very narrow interval. It is due to an endothermic phase transition (Ito & Takahashi 1989), possibly coupled with a change in bulk composition (Schubert, Turcotte & Olson 2001, pp. 88).

As observed by Schubert, Yuen & Turcotte (1975), an endothermic phase change has a twofold effect on hot rising plumes: on the one hand, the temperature excess induces an upward deflection of the transition depth, thus creating a negative buoyancy force compared to the surrounding mantle; on the other hand, the latent heat release from the phase change induces an extra heating of the convective feature, thus a positive buoyancy force. The overall effect is to delay the passage of the structure, all the more when it is less viscous. When the negative Clapeyron slope is too strong, heat diffusion cancels the plume thermal buoyancy before it penetrates the upper mantle (Nakakuki, Sato & Fujimoto 1994; Schubert, Anderson & Goldman 1995).

One can expect the same mechanism to act on our large-scale thermochemical structures. The passage of a dome will be even more difficult because of its chemical stratification, as demonstrated by the following mechanistic model. Let θ be the typical tem-

perature excess of the rising structure and d its typical size: the overall buoyancy of the plume writes

$$\Delta \rho_{eff} \sim \alpha \rho \theta - \Delta \rho_\chi. \tag{4.2}$$

θ decreases through time because of heat diffusion: in a simple scaling linear analysis,

$$\frac{\partial \theta}{\partial t} \sim -\kappa \frac{\theta}{d^2}, \tag{4.3}$$

and

$$\theta \sim \theta_0 exp(-\frac{t}{d^2/\kappa}). \tag{4.4}$$

The dome begins to sink when $\Delta \rho_{eff}(t) = 0$, so at time

$$t_{down} \sim -\frac{d^2}{\kappa} ln(\frac{\Delta \rho_\chi}{\alpha \rho \theta_0}). \tag{4.5}$$

θ_0 corresponds to the temperature excess at the onset of destabilization, thus according to equation (2.8) (pp. 176),

$$t_{down} \sim -\frac{d^2}{\kappa} ln(B_c). \tag{4.6}$$

Penetration in the upper mantle is possible when the delay induced by the phase change is smaller than t_{down}.

In the case of purely thermal plumes, the same type of study gives

$$t_{down,plume} \sim \frac{d^2}{\kappa}. \tag{4.7}$$

Since B_c is smaller but very close to 1, $t_{down} << t_{down,plume}$: the penetration of a thermo-chemical structure is more difficult than the penetration of a thermal feature of the same size. However, domes are also larger than plumes, which counterbalances the previous effect (larger d implies larger t_{down} thus easier penetration, as observed in the numerical model by Tackley 1995).

Impeded structures have however important effects on the upper mantle: as shown by Steinbach & Yuen (1997), they spread laterally under the transition zone, and create (i) a low-viscosity zone separating upper and lower mantles and (ii) a source of secondary plumes in the upper mantle. Since we can not realise a phase transition in our tank, this effect has been illustrated by a three-layer experiment, where the density contrast between the lower layer 1 and the central layer 2 allows a whole-layer regime, whereas the density contrast between the central layer 2 and the upper layer 3 corresponds to a stable stratification. As shown in figure 4.1, domes then rise from the first interface, until they are trapped by the second one; a thermal boundary layer then grows between fluids 1 and 3, and gives rise to thermochemical plumes in the upper layer. Such a situation seems to take place in the Pacific superswell (Vinnik, Chevrot & Montagner 1997); the 'secondary plumes' (Davaille 1999*b*; Courtillot, Davaille, Besse & Stock 2002) created at the 660 km interface then generate the multiple weak hotspots observed at the surface (McNutt 1998).

To finish with, one must notice that the penetrability of the 660 km transition depends on the vigor of convection (Christensen & Yuen 1985; Zhao, Yuen & Honda 1992; Yuen, Reuteler, Balachandar, Steinbach, Malevsky, & Smedsmo 1994), and has thus evolved through time. In thermochemical convection, this will be even more complicated by the simultaneous influence of B and Ra, which both change through Earth's history. A complete study is necessary to complete the first order conclusions proposed here.

4.5 Influence of plate tectonics.

As a first approximation, tectonic plates correspond to rigid structures superimposed on the fluid mantle and following the large circulation cells induced by convection. One can then notice that tectonic plates isolate two great areas inside the mantle, corresponding to two natural tanks: one under the Pacific ocean (see also §2.1) and the other one under the Atlantic ocean. A superswell then develops inside each of these independent tanks
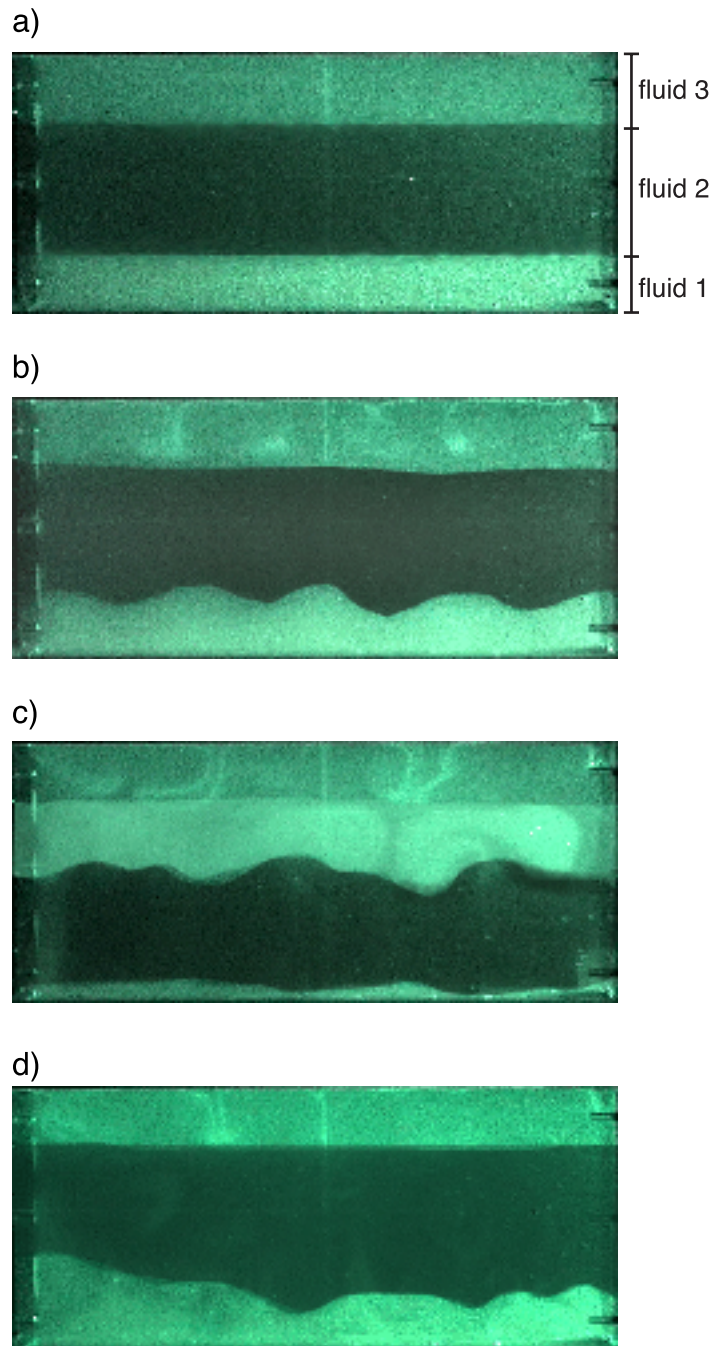
Fɪɢ. 4.1 – *Experiment with 3 layers* ($h_1 = 3.0$ *cm*, $h_2 = 7.8$ *cm*, $h_3 = 4.0$ *cm*, $\gamma_{1-2} = 56$, $\gamma_{2-3} = 3.6$, $B_{1-2} = 0.24$, $B_{2-3} = 1.46$, $Ra = 4.4 \times 10^7$): *a)* $t = 0\,\text{min}$, *b)* $t = 12\,\text{min}$, *c)* $t = 17\,\text{min}$ *and d)* $t = 24\,\text{min}$.

and can be studied by our analogical model. According to (2.9), a typical 1% chemical stratification will actually result in an effective destabilizing density contrast (taking into account both thermal and chemical effects)

$$\frac{\Delta \rho_{eff}}{\rho} = 0.02\%. \tag{4.8}$$

This effective jump is so small that it can not form a barrier to subduction: on the contrary, sinking plates deform the interface all the way down to the core-mantle boundary. Subduction therefore permanently reintroduce chemical heterogeneities at the base of the mantle, where they either build new reservoirs or replenish pre-existing ones (see §1.4.2, pp. 162): their sampling by rising thermochemical plumes then explains the geochemical 'oceanic' signature observed in some OIB (Hofmann & White 1982).

One must however remember that mantle and tectonic plates actually correspond to a single system (Tackley 2000a): the previous remarks are only first order approximations. The realistic processing of subduction will require a much more complex approach, well beyond the scope of this work (see for example Tackley 2000b).

4.6   Conclusion.

It is impossible of build a miniature Earth taking into account all natural complications. However, the study of a simple configuration where two fluids with different densities and viscosities are subjected to a temperature gradient proposes significant conclusions: starting from the assumption that the mantle has several distinct reservoirs, it demonstrates that (i) various behaviours are possible in the parameters range of the Earth; (ii) the convective regime is not stationary, but has evolved through time; (iii) each interface between geochemical reservoirs corresponds a thermal boundary layer and can give rise to hotspots of various size, amplitude, duration and composition; (iv) a pulsatory mechanism between two reservoirs explains most current available evidences both qualitatively and quantitatively.

Such gravitationaly stabilized reservoirs could for instance come from

– the presence of a phase transition (Yeganeh-Haeri, Weidner & Ito 1989; Nataf & Houard 1993),

– the rising of heavy material from the core (Hansen & Yuen 1988; Knittle & Jeanloz 1991), since it is not yet in equilibrium with the mantle (Stevenson 1981),

– the storage and recycling above the core-mantle boundary of the subducted recycled material (Gurnis 1986; Christensen & Hofmann 1994; Albarède 1998; Coltice & Ricard 1999)),

– the accumulation in the lower part of the mantle of iron and siderophiles elements during the early differenciation of the Earth (Solomatov & Stevenson 1993; Sidorin & Gurnis 1998),

– the extraction of the continental crust only from an upper part of the mantle (DePaolo & Wasserburg 1976; Allègre, Othman, Polve & Richard 1979; O'Nions, Evensen & Hamilton 1979),

– ...

and also from the combination of several of these propositions.

Our analogical model adresses the problem of mantle convection from a 'fluid dynamics' point of view, starting from existing reservoirs. Its further improvement demands to take into account the continuing processes of creation and destruction of chemical heterogeneities: in particular, it is now necessary (i) to establish geochemical budgets with evolving size and composition of the various reservoirs and (ii) to introduce the effects of plate tectonics, which corresponds to the order zero of mantle convection. Far from the simplified estimations proposed here, the complexity of these problems requires the collaboration between specialists from many subdisciplines of Earth science.

Conclusion générale.

Le manteau terrestre est hétérogène : il est constitué d'un ou de plusieurs réservoirs de densité et de viscosité différentes qui survivent sur des temps très longs, tout en autorisant des mouvements à l'échelle du système entier. Pour étudier sa dynamique, nous nous sommes donc placés dans le cas le plus simple de convection hétérogène : deux fluides de densités, de viscosités et d'épaisseurs différentes sont superposés dans une cuve, puis chauffés par le bas et refroidis par le haut. Notre objectif n'est pas de fabriquer un manteau miniature : les complications naturelles sont trop nombreuses pour être toutes intégrées dans un seul modèle (même numérique) et les caractéristiques précises du manteau ne sont encore que partiellement connues. Mais nous avons tenté (i) de quantifier précisément l'influence des contrastes de densité et de viscosité sur la dynamique du système à deux couches et (ii) de cartographier l'intégralité des régimes pouvant s'appliquer au manteau.

L'étude de stabilité marginale - théorique et expérimentale - a tout d'abord démontré l'existence de deux régimes thermochimiques différents en fonction du nombre de flottabilité B : (i) pour B plus grand qu'une valeur critique B_c, la convection se développe au-dessus et en-dessous de l'interface demeurant plane ; (ii) pour $B \leq B_c$, les mouvements convectifs se propagent sur toute l'épaisseur du système.

À haut nombre de Rayleigh, les expériences sont initialement en bon accord avec ces résultats : au premier ordre, le système reste globalement stable pour $B > 0.2 - 0.5$, tandis que l'interface se déstabilise pour $B \leq 0.2 - 0.5$; plusieurs pulsations successives peuvent alors prendre place lorsque le contraste de viscosité est d'un ordre de grandeur au moins. De multiples effets viennent cependant perturber ce schéma simple. Tout d'abord, des mouvements convectifs à petite échelle peuvent se développer à l'intérieur de chaque couche considérée séparément : la déstabilisation des couches limites externes engendre en effet la formation de panaches purement thermiques, qui peuvent localement et partiellement déformer l'interface. Par ailleurs, les deux fluides se mélangent progressivement, et le régime convectif évolue au cours du temps : un système initialement stratifié peut se déstabiliser, effectuer quelques oscillations puis se mélanger.

Sur Terre, un contraste de densité aussi faible que 2% peut avoir des répercussions

sur toute l'histoire du manteau. Nos diverses observations expérimentales permettent alors de proposer des conclusions importantes. Tout d'abord, toute une zoologie de comportements est possible entre les deux modèles extrêmes de convection 'à une couche' et 'à deux couches'. Le régime convectif du manteau a même pu changer au cours du temps : la plupart des modèles proposés schématiquement sur Terre prennent ainsi place successivement au cours de l'évolution d'une de nos expériences. Le régime pulsatif est alors particulièrement intéressant, puisqu'il offre une explication physique simple, à la fois qualitativement et quantitativement, aux grandes crises géologiques observées sur Terre et sur d'autres planètes. Enfin, à plus petite échelle, chaque interface entre deux réservoirs correspond à une couche limite thermique d'où peuvent se former de nouveaux panaches de taille, amplitude, durée et composition différentes, expliquant la grande variété des points chauds observés en surface.

Deux aspects de notre modèle analogique demandent maintenant des études plus poussées. Au niveau dynamique tout d'abord, le problème majeur consiste à caractériser plus précisément le mélange des hétérogénéités actives en fonction des contrastes de densité et de viscosité : cette étude est dorénavant possible grâce à la visualisation par plan laser, permettant d'accéder à des structures de taille millimétrique sur un plan vertical. D'un point de vue géophysique par ailleurs, il est maintenant indispensable de prendre en compte la tectonique des plaques (par exemple par des méthodes numériques), qui constitue la marque la plus visible de la convection mantellique.

En conclusion, nous pouvons noter que ce travail offre un cadre théorique nouveau à l'interprétation des données et des observations recueillies en surface. L'intégration de notre modèle dynamique de dôme montant dans un modèle réaliste de Terre devrait permettre d'estimer les valeurs typiques du bombement en surface, de la vitesse de soulèvement et de l'anomalie du géoïde, de manière à les comparer avec les données recueillies sur les superswells Africain et Pacifique. Enfin, en complément des premières pistes présentées ici, il serait dorénavant envisageable d'établir des bilans géochimiques précis, tenant compte du caractère évolutif des réservoirs et du style de convection, et

de réexaminer les données tomographiques en séparant - grâce à nos lois d'échelle - les variations de densité d'origine chimique et thermique.

Références

ALBARÈDE, F. 1998 Time-dependent models of U-Th-He and K-Ar evolution and the layering of mantle convection. *Chem. Geol.* **145**, 413–429.

ALBERS, M. & CHRISTENSEN, U. 1996 The excess temperature of plumes rising from the core mantle boundary. *Geophys. Res. Lett.* **23**, 3567–3570.

ALLÈGRE, C.J. 1997 Limitation on the mass exchange between the upper and lower mantle: the evolving convection regime of the Earth. *Earth Planet Sci. Lett.* **150**, 1–6.

ALLÈGRE, C.J., HAMELIN, B., PROVOST, A. & DUPRÈ, B. 1987 Topology in isotopic multispace and the origin of mantle chemical heterogeneities. *Phys. Earth Planet. Inter.* **19**, 293–306.

ALLÈGRE, C.J., OTHMAN, D.B., POLVE, M. & RICHARD, P. 1979 The Nd-Sr isotopic correlation in mantle materials and geodynamic consequences. *Earth Planet. Sci. Lett.* **81**, 319–337.

ALLÈGRE, C.J., STAUDACHER, T., SARDA, P. & KURZ, M. 1983 Constraints on evolution of Earth's mantle from rare gas systematics. *Nature* **303**, 762–766.

ANDERECK, C.D., COLOVAS, P.W. & DEGEN, M.M. 1996 Observations of time-dependent behaviour in the two-layer Rayleigh-Bénard system. In *Advances in Multi-Fluid Flows*. Renardy, Y.Y., Coward, A.V., Papageorgiou, D. & Sun, S.M. eds. SIAM Proceedings.

BAINES, P.G. & GILL, A.E. 1969 On thermohaline convection with linear gradients. *J. Fluid Mech.* **37**, 289–306.

BAKER, V.R., STROM, R.G., GULICK, V.C., KARGEL, J.S., KOMATSU, G. & KALE, V.S. 1991 Ancient oceans, ice sheets and the hydrological cycle on Mars. *Nature* **352**, 589–594.

BÉNARD, H. 1901 Les tourbillons cellulaires dans une nappe liquide transportant de la chaleur par convection en régime permanent. *Ann. Chim. Phys.* (7) **23**, 62–144.

BECKER, T.W., KELLOGG, J.B. & O'CONNELL, R.J. 1999 Thermal constraints on the survival of primitive blobs in the lower mantle. *Earth Planet Sci. Lett.* **171**, 351–365.

BIJWAARD, H., SPAKMAN, W. & ENGDAHL, E.R. 1998 Closing the gap between regional and global travel time tomography. *J. Geophys. Res.* **103**, 30055–30078.

BINA, C.R. 1998 Lower mantle mineralogy and the geophysical perspective. in *Ultrahigh pressure mineralogy.* Reviews in Mineralogy **37**, R.J. Hemley, Ed.

BOUSSINESQ, J. 1903 *Théorie analytique de la chaleur.* vol. 2. Paris: Gathier-Villars.

BRÉGER, L., ROMANOWICZ, B. & NG, C. 2001 The Pacific plume as seen by S, ScS and SKS. *Geophys. Res. Lett.* **28**, 1859–1862.

BRUNET, D. & MACHETEL, P. 1998 Large-scale tectonic features induced by mantle avalanches with phase, temperature, and pressure lateral variations of viscosity. *J. Geophys. Res.* **103**, 4929–4946.

BUSSE, F.H. 1981 On the aspect ratio of two-layer mantle convection. *Phys. Earth Planet. Inter.* **24**, 320–324.

BUSSE, F.H. & SOMMERMANN, G. 1996 Double-layer convection: a brief review and some recent experimental results. In *Advances in Multi-Fluid Flows.* Renardy, Y.Y., Coward, A.V., Papageorgiou, D. & Sun, S.M. eds. SIAM Proceedings.

CALDEIRA, K. & RAMPINO, M.R. 1991 The mid-cretaceous superplume, carbon dioxide, and global warming. *Geophys. Res. Lett.* **18**, 987–990.

CARDIN, PH., NATAF, H-C. & DEWOST, PH. 1991 Thermal coupling in layered convection: evidence for an interface viscosity control, from mechanical experiments and marginal stability analysis. *J. Phys. II* **1**, 599–622.

CAZENAVE, A., SOURIAU, A. & DOMINH, K. 1989 Global coupling of Earth surface topography with hotspots, geoid and mantle heterogeneities. *Nature* **340**, 54–57.

CAZENAVE, A. & THORAVAL, C. 1994 Mantle dynamics constrained by degree 6 surface topography, seismic tomography and geoid: inference on the origin of the south Pacific superswell. *Earth Planet Sci. Lett.* **122**, 207–219.

CHANDRASEKHAR, S. 1961 *Hydrodynamic and Hydromagnetic Stability.* Dover, New York, 652 pp.

CHRISTENSEN, U.R. 1989 Mixing by time-dependent convection. *Earth Planet. Sci. Lett.* **95**, 382–394.

CHRISTENSEN, U.R. & HOFMANN, A.W. 1994 Segregation of subducted oceanic crust in the convecting mantle. *J. Geophys. Res.* **99**, 19867–19884.

CHRISTENSEN, U.R. & YUEN, D.A. 1985 Layered convection induced by phase transitions. *J. Geophys. Res.* **90**, 10291–10300.

COLTICE, N. & RICARD, Y. 1999 Geochemical observations and one layer mantle convection. *Earth Planet Sci. Lett.* **174**, 125–137.

CONDIE, K.C. 1998 Episodic continental growth and supercontinents: a mantle avalanche connection? *Earth Planet. Sci. Lett.* **163**, 97–108.

CONDIE, K.C. 2002 Superplume events in Earth history. *Superplume Workshop Tokyo 2002*, at Tokyo Institute of Technology.

COURTILLOT, V. & BESSE, J. 1987 Magnetic-field reversals, polar wander and core-mantle coupling. *Science.* **237**, 1140–1147.

COURTILLOT, V., DAVAILLE, A., BESSE, J. & STOCK, J. 2002 Three distinct types of hotspots in the Earth's mantle. submitted to *Science*.

COURTILLOT, V., JAEGER, J.J., YANG, Z., FERAUD, G. & HOFMANN, C. 1996 in *Proc. Conf. on New Developments Regarding the KT Event and Other Catastrophes in Earth History*, edited by G. Ryder, D. Fastovsky & S. Gartner, Geol. Soc. Am. Spe. Pap. 307, Boulder, Colorado.

COX, A. 1982 Magnetostratigraphic time scale. In *A geologic time scale*, edited by W.B. Harland et al., Cambridge University Press, UK, 63–84.

CSEREPES, L. & RABINOWICZ, M. 1985 Gravity and convection in a two-layered mantle. *Earth Planet. Sci. Lett.* **76**, 193–207.

CSEREPES, L., RABINOWICZ, M. & ROSEMBERG-BOROT, C. 1988 Three-dimensional infinite Prandtl number convection in one and two layers with implications for the Earth's gravity field. *J. Geophys. Res.* **93**, 12009–12025.

DAVAILLE, A. 1996 Stratification and Mixing in the Mantle. *Eos Trans. AGU*, Fall Meet. Suppl., Abstract T42A-03.

DAVAILLE, A. 1999*a* Two-layer thermal convection in miscible fluids. *J. Fluid Mech.* **379**, 223–253.

DAVAILLE, A. 1999*b* Simultaneous generation of hotspots and superswells by convection in a heterogeneous planetary mantle. *Nature* **402**, 756–760.

DAVAILLE, A., GIRARD, F. & LE BARS, M. 2002 How to anchor hot spots in a convecting mantle? *Earth Planet. Sci. Lett.* **203**, 621–634.

DAVAILLE, A. & JAUPART, C. 1993 Transient high-Rayleigh number thermal convection with large viscosity variations. *J. Fluid Mech.* **253**, 141–166.

DAVAILLE, A., LE BARS, M. & CARBONNE, C. 2002 Thermal convection in an heterogeneous mantle. *Compte Rendus de l' Académie des Sciences*, Paris, in press.

DAVAILLE, A., VIDAL, V., LE BARS, M., JURINE, D. & CARBONNE, C. 2002 Imaging isotherms in viscous fluids. *Exp. Fluids.* in preparation.

DAVIES, G.F. 1985 Punctuated tectonic evolution of the Earth. *Earth Planet. Sci. Lett.* **136**, 363–379.

DAVIES, G.F. & GURNIS, M. 1986 Interaction of mantle dregs with convection: lateral heterogeneity at the core-mantle boundary. *Geophys. Res. Lett.* **13**, 1517–1520.

DEGEN, M.M., COLOVAS, P.W. & ANDERECK, C.D. 1998 Time-dependent patterns in the two-layer Rayleigh-Bénard system. *Phys. Rev. E* **57**, 6647–6659.

DEPAOLO, D. & WASSERBURG, G.J. 1976 Inferences about magma sources and mantle structure from variations of 143Nd/144Nd. *Geophys. Res. Lett.* **3**, 743–746.

DZIEWONSKI, A.M. & WOODHOUSE, J.H. 1987 Global images of the Earth's interior. *Science* **236**, 37–48.

ELLSWORTH, K. & SCHUBERT, G. 1988 Numerical models of thermally and mechanically coupled two-layer convection of highly viscous fluids. *Geophys. J.* **93**, 347–363.

FERRACHAT, S. & RICARD, Y. 2001 2001 Mixing properties in the Earths mantle: effects of the viscosity stratification and of oceanic crust segregation. *Geochem. Geophys. Geosys.* **2**.

FORTE, A.M., MITROVICA, J.X. & WOODWARD, R.L. 1995 Seismic-geodynamic determination of the origin of excess ellipticity of the core-mantle boundary. *Geophys. Res. Lett.* **22**, 1013–1016 .

FORTE, A.M. & MITROVICA, J.X. 2001 Deep-mantle high-viscosity flow and thermochemical structure inferred from seismic and geodynamic data. *Nature* **410**, 1049–1056 .

FUKAO, Y., WIDIYANTORO, S. & OBAYASHI, M. 2001 Stagnant slabs in the upper and lower mantle transition region. *Rev. Geophys.* **39**, 291–324.

GALLET, Y. & HULOT, G. 1997 Stationary ad nonstationary behaviour within the geomagnetic polarity time scale. *Geophys. Res. Lett.* **24**, 1875–1878.

GARZANTI, E. 1993 Himalayan ironstones, 'superplumes', and the breakup of Gondwana. *Geology* **21**, 105–108.

GRAND, S.P., VAN DER HILST, R.D. & WIDIYANTORO, S. 1997 High resolution

global tomography: a snapshot of convection in the Earth. *Geol. Soc. Am. Today* **7**, 1–7.

GREELEY, R. & SCHNEID, B.D. 1991 Magma generation on Mars: amounts, rates and comparisons with Earth, Moon and Venus. *Science* **254**, 996–998.

GUBBINS, D. 1994 Geomagnetic polarity reversals: a connection with secular variation and core-mantle interaction?. *Rev. Geophys.* **32**, 61–83.

GUILLOU, L. & JAUPART, C. 1995 On the effect of continents on mantle convection. *J. Geophys. Res.* **100**, 24217–24238.

GURNIS, M. 1986 The effects of chemical density differences on convective mixing in the Earth's mantle. *J. Geophys. Res.* **91**, 11407–11419.

GURNIS, M., MITROVICA, J.X., RITSEMA, J. & VAN HEIJST, H-J. 2000 Constraining mantle density structure using geological evidence of surface uplift rates: the case of the African superplume. *Geochemistry, Geophysics, Geosystems* **1**.

GUYOT, F., MADON, M., PEYRONNEAU, J. & POIRIER, J.-P. 1988 X-ray microanalysis of high-pressure/high-temperature phases synthesized from natural olivine in a diamond-anvill cell. *Earth Planet. Sci. Lett.* **90**, 52–64.

HANSEN, U. & YUEN, D.A. 1988 Numerical simulations of thermal-chemical instabilities at the core-mantle boundary. *Nature* **334**, 237–240.

HANSEN, U. & YUEN, D.A. 1989 Subcritical double-diffusive convection at infinite Prandtl number. *Geophys. Astroph. Fluid Dyn.* **47**, 199–224.

HANSEN, U. & YUEN, D.A. 2000 Extended-Boussinesq thermal-chemical convection with moving heat sources and variable viscosity. *Earth Planet. Sci. Lett.* **176**, 401–411.

HERRICK, D.L. & PARMENTIER, E.M. 1994 Episodic large-scale overturn of two-layer mantles in terrestrial planets. *J. Geophys. Res.* **99**, 2053–2062.

HOFMANN, A.W. 1997 Mantle geochemistry: the message from oceanic volcanism. *Nature* **385**, 219–229.

HOFMANN, A.W. & MCKENZIE, D.P. 1985 The destruction of geochemical heterogeneities by differential fluid motions during mantle convection. *Geophys. J. R. astr. Soc.* **82**, 163–206.

HOFMANN, A.W. & WHITE, W.M. 1982 Mantle plumes from ancient oceanic crust. *Earth Planet Sci. Lett.* **57**, 421–436.

HONDA, S. 1995 A simple parameterized model of Earth's thermal history with the transition from layered to whole mantle convection. *Earth Planet Sci. Lett.* **131**, 357–369.

HOWARD, L.N. 1964 Convection at high Rayleigh number. In *Proc. 11. Int. Congr. Appl. Mech.* (ed. H. Görtler), pp. 1109–1115. Springer.

ISHII, M. & TROMP, J. 1999 Normal-mode and free-air gravity constraints on lateral variations in velocity and density of Earth's mantle. *Science* **285**, 1231–1236.

ISLEY, A.E. & ABBOTT, D.H. 1999 Plume-related mafic volcanism and the deposition of banded iron formation. *J. Geophys. Res.* **104**, 15461–15477.

ITO, E. & TAKAHASHI, E. 1989 Post-spinel transformations in the system Mg2Si04-Fe2Si04 and some geophysical implications. *J. Geophys. Res.* **94**, 10637–10646.

JACOBSEN, S.B. & WASSERBURG, G.J. 1979 The mean age of mantle and crustal reservoirs. *J. Geophys. Res.* **84**, 7411–7428.

JOSEPH, D.D. & RENARDY, M. 1993 *Fundamentals of two-fluids dynamics.* Springer, New York, 443 pp.

KARATO, S. & WU, P. 1993 Rheology of the upper mantle: a synthesis. *Science* **260**, 771–778.

KARGEL, J.S. & STROM, R.G. 1992 Ancient glaciation on Mars. *Geology* **62**, 310–316.

KELLOG, L.H., HAGER, B.H. & VAN DER HILST, R.D. 1999 Compositional stratification in the deep mantle. *Science* **283**, 1881–1884.

KNITTLE, E. & JEANLOZ, R. 1991 Earths core-mantle boundary: results of experiments at high pressures and temperatures. *Science* **251**, 1438–1443.

KRISHNAMURTI, R. 1970 On the transition to turbulent convection. *J. Fluid Mech.* **42**, 295–320.

LABROSSE, S. 2002 Hotspots, mantle plumes and core heat loss. *Earth Planet. Sci. Lett.* **199**, 147–156.

LARSON, R.L. 1991 Geological consequences of superplumes. *Geology* **19**, 963–966.

LARSON, R.L. & OLSON, P. 1991 Mantle plumes control magnetic reversal frequency. *Earth Planet. Sci. Lett.* **107**, 437–447.

LAY, T. 1989 Structure of the core-mantle transition zone: a chemical and thermal boundary layer. *EOS Trans. AGU* **70**, 49–59.

LAY, T., WILLIAMS, Q. & GARNERO, E.J. 1998 The core-mantle boundary layer and deep Earth dynamics. *Nature* **392**, 461–467.

LE BARS, M. & DAVAILLE, A. 2002 Stability of thermal convection in two superimposed miscible viscous fluids. *J. Fluid Mech.* **471**, 339–363.

LI, X-D. & ROMANOWICZ, B. 1996 Global mantle shear velocity model developed using nonlinear asymptotic coupling theory. *J. Geophys. Res.* **101**, 22245–22272.

LITHGOW-BERTELLONI, C. & SILVER, P.G. 1998 Dynamic topography, plate driving forces and the African superswell. *Nature* **395**, 269–272.

MACHETEL, P. & WEBER, P. 1991 Intermittent layered convection in a model mantle with an endothermic phase change at 670km. *Nature* **350**, 55–57.

MANGA, M. 1996 Mixing of heterogeneities in the mantle: effects of viscosity differences. *Geophys. Res. Lett.* **23**, 403–406.

MASTERS, G., JOHNSON, S., LASKE, G. & BOLTON, H. 1996 A shear-velocity modl of the mantle. *Phil. Trans. R. Soc. Lond.* **354**, 1385–1410.

MATSUI, M. 2000 Molecular dynamics simulation of $MgSiO_3$ perovskite and the 660 km seismic discontinuity. *Phys. Earth Planet. Interiors* **121**, 77–84.

MATSUI, M., PARKER, S.C. & LESLIE, M. 2000 The MD simulation of the equation of state of MgO: application as a pressure calibration standard at high temperature and high pressure. *American Mineralogist* **85**, 312–316.

MCKENZIE, D. & RICHTER, F.M. 1981 Parameterized convection in a layered region and the thermal history of the Earth. *J. Geophys. Res.* **86**, 11667–11680.

MCKENZIE, D. ROBERTS, J. & WEISS, N. 1974 Convection in the Earth's mantle: towards a numerical simulation. *J. Fluid Mech.* **62**, 465–538.

MCNUTT, M.K. & FISHER, K.M. 1987 The south Pacific superswell. In *Seamounts, Islands and Atolls* Keating, B.H. & al., S.M. eds. Geophys. Monogr. Ser.**43** A.G.U., Washington DC, 25–34.

MCNUTT, M.K. & JUDGE, A.V. 1990 The superswell and mantle dynamics beneath the south Pacific. *Science* **248**, 969–975.

MCNUTT, M.K. 1998 Superswells. *Rev. Geophys.* **36**, 211–244.

MÉGNIN, C. & ROMANOWICZ, B. 2000 The shear velocity structure of the mantle from the inversion of body, surface and higher modes waveforms. *Geophys. J. Int.* **143**, 709–728.

MÉNARD, H.W. 1964 *Marine geology of the Pacific.* McGraw-Hill, New York, 138–146.

MERRILL, R.T. & MCFADDEN, P.L. 1995 Dynamo theory and paleomagnetism. *J. Geophys. Res.* **100**, 317–326.

MERRILL, R.T. & MCFADDEN, P.L. 1999 Geomagnetic polarity transitions. *Rev. Geophys.* **37**, 201–226.

MERVEILLEUX DU VIGNAUX, N. & FLEITOUT, L. 2001 Streching and mixing of viscous blobs in Earth's mantle. *J. Geophys. Res.* **106**, 30893–30908.

MONTAGUE, N.L. & KELLOG, L.H. 2000 Numerical models of a dense layer at the base of the mantle and implications for the geodynamics of D". *J. Geophys. Res.* **105**, 11101–11114.

MORGAN, W.J. 1972 Plate motions and deep convection. *Geol. Soc. Amer. Mem.* **132**, 7–22.

NAKAKUKI, T., SATO, H. & FUJIMOTO, H. 1994 Interaction of the upwelling plume with the phase and chemical boundary at the 670 km discontinuity–effects of temperature-dependent viscosity. *Earth Planet. Sci. Lett.* **121**, 369–384.

NAMIKI, A. & KURITA, K. 1999 The influence of boundary heterogeneity in experimental models of mantle convection. *Geophys. Res. Lett.* **26**, 1929–1932.

NATAF, H-C. & HOUARD, S. 1993 Seismic discontinuity at the top of D”: a world-wide feature ? *Geophys. Res. Lett.* **20**, 2371–2374.

NELDER, J.A. & MEAD, R. 1965 A simplex method for function minimization. *Computer J.* **7**, 308–313.

NI, S., TAN, E., GURNIS, M. & HELMBERGER, D. 2002 Sharp sides to the African superplume. *Science* **296**, 1850–1852.

NIELD, D.A. 1968 The Rayleigh-Jeffreys problem with boundary slab of finite conductivity. *J. Fluid Mech.* **32**, 393–398.

NYBLADE, A.A. & ROBINSON, S.W. 1994 The African superswell. *Geophys. Res. Lett.* **21**, 765–768.

OLSON, P. 1984 An experimental approach to thermal convection in a two-layered mantle. *J. Geophys. Res.* **89**, 11293–11301.

OLSON, P. & KINCAID, C. 1991 Experiments on the interaction of thermal convection and compositional layering at the base of the mantle. *J. Geophys. Res.* **96**, 4347–4354.

OLSON, P., SILVER, P.G. & CARLSON, R.W. 1990 The large scale structure of convection in the Earth's mantle. *Nature* **344**, 209–215.

OLSON, P. & SINGER, H. 1985 Creeping plumes. *J. Fluid Mech.* **158**, 511–531.

O'Nions, R.K., Evensen, N.M. & Hamilton, P.J. 1979 Variations in 143Nd/144Nd and 87Sr/86Sr ratios in oceanic basalts. *Earth Planet. Sci. Lett.* **34**, 13–22.

O'Nions, R.K. & Tolstikhin, I.N. 1994 Behaviour and residence times of lithophile and rare gas tracers in the upper mantle. *Earth Planet. Sci. Lett.* **124**, 131–138.

Peltier, W.R. & Jarvis, G.T. 1982 Whole mantle convection and thermal evolution of the Earth. *Phys. Earth Planet. Interiors* **29**, 281–304.

Poirier, J.-P. 1991 *Introduction to the Physics of the Earth's Interior.* Cambridge University Press, 264 pp.

Rasenat, S., Busse, F.H. & Rehberg, I. 1989 A theoretical and experimental study of double-layer convection. *J. Fluid Mech.* **199**, 519–540.

Ray, J.S. & Pande, K. 1999 Carbonatite alkaline magmatism associated with continental flood basalts at stratigraphic boundaries: cause for mass extinctions. *Geophys. Res. Lett.* **26**, 1917–1920.

Lord Rayleigh 1916 On convection currents in a horizontal layer of fluid when the higher temperature is on the under side. *Phil. Mag.* (6) **32**, 529–546.

Renardy, Y. & Joseph, D.D. 1985 Oscillatory instability in a Bénard problem of two fluids. *Phys. Fluids* **28**, 788–793.

Renardy, M. & Renardy, Y. 1985 Perturbation analysis of steady and oscillatory onset in a Bénard problem with two similar liquids. *Phys. Fluids* **28**, 2699–2708.

Ribe, N.M. 1998 Spouting and planform selection in the Rayleigh-Taylor instability of miscible viscous fluids. *J. Fluid Mech.* **34**, 315–336.

Richards, M.A., Duncan, R.A. & Courtillot, V.E. 1989 Flood basalts and hot-spot tracks: plume heads and tails. *Science* **246**, 103–107.

Richards, M.A. & Entgebretson, D.C. 1992 Large scale mantle convection and the history of subduction. *Nature* **355**, 437–440.

RICHTER, F.M. & JOHNSON, C.E. 1974 Stability of a chemically layered mantle. *J. Geophys. Res.* **79**, 1635–1639.

RICHTER, F.M. & McKENZIE, D.P. 1981 On some consequences and possible causes of layered convection. *J. Geophys. Res.* **86**, 6133–6142.

RICHTER, F.M., NATAF, H.C. & DALY, S.F. 1983 Heat transfer and horizontally-averaged temperature of convection with large viscosity variations. *J. Fluid Mech.* **129**, 173–192.

RITSEMA, J., NI, S., HELMBERGER, D.V. & CROTWELL, H.P. 1998 Evidence for strong shear velocity reductions and velocity gradients in the lower mantle beneath Africa. *Geophys. Res. Lett.* **25**, 245–248.

ROBERSTON, G.S. & WOODHOUSE, J.H. 1996 Ratio of relative S to P velocity heterogeneity in the lower mantle. *J. Geophys. Res.* **101**, 20041–20052.

ROMANOWICZ, B. & GUNG, Y. 2002 Superplumes from the core-mantle boundary to the lithosphere: implications for heat flux. *Science* **296**, 513–516.

SAMUEL, H. & FARNETANI, C.G. 2001 A denser and relatively undegassed lower mantle reservoir: geochemical and seismological model predictions. *Eos Trans. AGU* **82**, Fall Meet. Suppl., Abstract T21A-0874.

SAMUEL, H. & FARNETANI, C.G. 2002 Thermochemical convection and helium concentrations in mantle plumes. submitted to *Earth Planet Sci. Lett.*

SCHMELING, H. 1988 Numerical models of Rayleigh-Taylor instabilities superimposed upon convection. *Bull. Geol. Inst. Univ. Uppsala* **14**, 95–109.

SCHUBERT, G., ANDERSON, C. & GOLDMAN, P. 1995 Mantle plume interaction with an endothermic phase change. *J. Geophys. Res.* **100**, 8245–8256.

SCHUBERT, G., TURCOTTE, D.L. & OLSON, P. 2001 *Mantle convection in the Earth and Planets.* Cambridge University Press.

SCHUBERT, G., YUEN, D.A. & TURCOTTE, D.L. 1975 Role of phase transitions in a dynamic mantle. *Geophys. J. R. Astron. Soc.* **42**, 705–735.

SHERIDAN, R.E. 1983 Phenomena of pulsation tectonics related to the breakup of the eastern north american continental margin. *Tectonophysics* **94**, 169–185.

SIDORIN, I. & GURNIS, M. 1998 Geodynamically consistent seismic velocity predictions at the base of the mantle. in *The Core Mantle Boundary Region.* Gurnis, M., Wysession, M., Knittle, E., & Buffett, B., eds. American Geophysical Union, Washington, D.C. 209–230, 1998.

SOLOMATOV, V.S. & STEVENSON, D.J. 1993 Nonfractional crystal-lization of a terrestrial magma ocean. *J. Geophys. Res.* **98**, 5391–5406.

SOTIN, C. & LABROSSE, S. 1999 Three-dimensional thermal convection of an isoviscous, infinite-Prandtl-number fluid heated from within and from below: applications to heat transfer in planetary mantles. *Phys. Earth Planet. Inter.* **112**, 171–190.

SOTIN, C. & PARMENTIER, E.M. 1989 On the stability of a fluid layer containing a univariant phase transition: application to planetary interiors. *Phys. Earth Planet. Inter.* **55**, 10–25.

STAUDIGEL, H., PARK, K.-H., PRINGLE, M., RUBENSTONE, J.L., SMITH, W.H.F. & ZINDLER, A. 1991 The longevity of the South Pacific isotopic and thermal anomaly *Earth Planet Sci. Lett.* **102**, 24–44.

STEIN, M. & HOFMANN, A.W. 1994 Mantle plumes and episodic crustal growth. *Nature* **372**, 63–68.

STEINBACH, V. & YUEN, D.A. 1997 The influences of temperature- and pressure-dependent lower-mantle rheology on the interaction of upwellings with phase transitions. *Phys. Earth Planet. Int.* **103**, 85–100.

STENGEL, K.C., OLIVIER, D.S. & BROKER, J.R. 1982 Onset of convection in a variable-viscosity fluid. *J. Fluid Mech.* **120**, 411–431.

STEVENSON, D. J. 1981 Models of the Earth's core. *Science* **214**, 611–619.

STROM, R.G., SCHABER, G.G. & DAWSON, D.D. 1994 The global resurfacing of Venus. *J. Geophys. Res.* **99**, 10899–10926.

Su, W. & Dziewonski, A.M. 1997 Simultaneous inversion fro 3-D variations in shear and bulk velocity in the mantle. *Phys. Earth Planet. Interiors* **100**, 135–156.

Sumita, I. & Olson, P. 1999 A laboratory model for convection in the Earth's core driven by a thermally heterogeneous mantle. *Science* **286**, 1547–1549.

Tackley, P.J. 1995 On the penetration of an endothermic phase transition by upwellings and downwellings. *Science* **100**, 15477–15488.

Tackley, P.J. 1998 Three-dimensional simulations of mantle convection with a thermochemical CMB boundary layer: D"? in *The Core Mantle Boundary Region.* Gurnis, M., Wysession, M., Knittle, E., & Buffett, B., eds. American Geophysical Union, Washington, D.C. 231–253, 1998.

Tackley, P.J. 2000*a* Mantle convection and plate tectonics: toward an integrated physical and chemical theory. *Science* **288**, 2002–2007.

Tackley, P.J. 2000*b* Self-consistent generation of tectonic plates in time-dependent, three-dimensional mantle convection simulations. *Geochemistry, Geophysics, Geosystems* **1**.

Tackley, P.J. 2002 Strong heterogeneity caused by deep mantle layering. *Geochemistry, Geophysics, Geosystems* **3**.

Tackley, P.J., Stevenson, D.J., Glatzmaier, G.A. & Schubert, G. 1993 Effects of an endothermic phase transition at 670 km depth in a spherical model of convection in the Earth's mantle. *Nature* **361**, 699–704.

Tait, S. & Jaupart, C. 1989 Compositional convection in viscous melts. *Nature* **338**, 571–574.

Tanaka, K.L. & Chapman, M.G. 1992 Kasei Valles, Mars: interpretation of canyon materials and flood sources. *Proc. Lunar Planet. Sci. Conf.* **22**, 73–83.

Turner, J.S. 1979 *Buoyancy Effects in Fluids.* Cambridge University Press, 368 pp.

Utsunomiya, A., Suzuki, N. & Maruyama, S. 2002 The history of the Pacific superplume. *Superplume Workshop Tokyo 2002*, at Tokyo Institute of Technology.

VAN DER HILST, R.D. & KÁRASON, H. 1999 Compositional heterogeneity in the bottom 1000 kilometers of Earth's mantle : toward a hybrid convection model. *Science* **283**, 1885–1891.

VAN DER HILST, R.D., WIDIYANTORO, S. & ENGDAHL, E.R. 1997 Evidence for deep mantle circulation from global tomography. *Nature* **386**, 578–584.

VAN KEKEN, P.E., HAURI, E.H. & BALLENTINE, C.J. 2002 Mantle mixing: the generation, preservation and destruction of chemical heterogeneity. *Ann. Rev. Earth Planet. Sci. Lett.* **30**, 493–525.

VAN KEKEN, P.E & ZHONG, S. 1999 Mixing in a 3D spherical model of present day mantle convection. *Earth Planet. Sci. Lett.* **171**, 533–547.

VERONIS, G. 1968 Effect of a stabilizing gradient of solute on thermal convection. *J. Fluid Mech.* **34**, 315–336.

VIDALE, J.E., SCHUBERT, G. & EARLE, P.S. 2001 Unsuccessful initial search for a midmantle chemical boundary layer with seismic arrays. *Geophys. Res. Lett.* **28**, 859–862.

VINE, F. J. & MATTHEWS, D. H. 1963 Magnetic Anomalies over Oceanic Ridges. *Nature* **199**, 947–949.

VINNIK, L., CHEVROT, S. & MONTAGNER, J-P. 1997 Evidence for a stagnant plume in the transition zone? *Geophys. Res. Lett.* **24**, 1007–1010.

WANG, Y. & WEIDNER, D.J. 1996 $(\partial\mu/\partial T)_P$ of the lower mantle. *Pure Appl. Geophys.* **146**, 533–549.

WEGENER, A. L. 1912 Die Entstehung der Kontinente und Ozeane. *Geologische Rundschau.* **3**, 276–292.

WEINSTEIN, S.A. 1993 Catastrophic overturn of the Earth's mantle driven by multiple phase changes and internal heat generation. *Geophys. Res. Lett.* **20**, 101–104.

WHITE, R. & MCKENZIE, D. 1989 Magmatism at rift zones: the generation of volcanic continental margins and flood basalts. *J. Geophys. Res.* **94**, 7685–7729.

WHITEHEAD, J.A. & LUTHER, D.S. 1975 Dynamics of laboratory diapir and plume models. *J. Geophys. Res.* **80**, 705–717.

WILSON, J.T. 1963 Evidence from islands on the spreading of the ocean floor. *Nature* **197**, 536–538.

WILSON, J.T. 1966 Did the Atlantic close and then re-open? *Nature* **211**, 676–681.

WINTERER, E.L., NTLAND, J.H., VAN WAASBERGEN, R.J., DUNCAN, R.A., MC-NUTT, M.K., WOLFE, C.J., PREMOLI SILVA, I., SAGER, W.W. & SLITER, W.V. 1993 Cretaceous guyots in the northwest Pacific: an overview of their geology and geophysics. in The Mesozoic Pacific: geology, tectonics and volcanism. *Geophysical Monograph* **77**, 307–334.

YEGANEH-HAERI, A., WEIDNER, D. J. & ITO, E. 1989 Elasticity of MgSiO3 in the perovskite structure. *Science* **243**, 787–789.

YUEN, D.A., CADEK, O., CHOPELAS, A. & MATYSKA, C. 1993 Geophysical inferences of thermal-chemical structures in the lower mantle. *Geophys. Res. Lett.* **20**, 899–902.

YUEN, D.A., REUTELER, D.M., BALACHANDAR, S., STEINBACH, V., MALEVSKY, A.V. & SMEDSMO, J.L. 1994 Various influences on three-dimensional mantle convection with phase transitions. *Phys. Earth Planet. Inter.* **86**, 185–203.

ZERR, A., DIEGELER, A. & BOEHLER, R. 1998 Solidus of Earths deep mantle. *Science* **281**, 243–246.

ZHAO, M., YUEN, D.A. & HONDA, S. 1992 Multiple phase transitions and the style of mantle convection. *Phys. Earth Plan. Inter.* **72**, 185–210.

ZINDLER, A. & HART, S. 1986 Chemical geodynamics. *Annu. Rev. Earth Planet. Sci.* **14**, 493–571.